Graphene-Based nanostructures and colloidal silver coatings for flexible cellulose substrates

Original Citation:
Graphene-Based nanostructures and colloidal silver coatings for flexible cellulose substrates / Grandolfo, Adriana. - ELETTRONICO. - (2025).

Availability:
This version is available at http://hdl.handle.net/11589/282260 since: 2025-01-14

Published version
DOI:

Publisher: Politecnico di Bari

Politecnico
di Bari

Department of Electrical and Information Engineering
INDUSTRY 4.0
Ph.D. Program
SSD: CHIM/02–PHYSICAL CHEMISTRY

Final Dissertation

Graphene-Based Nanostructures and Colloidal Silver Coatings for Flexible Cellulose Substrates

by

Grandolfo Adriana

Adriana Grandolfo

Referees:

Prof. Dimitrios Gournis

Prof.Leonardo Scarabelli

Supervisors:

Prof. Elisabetta Fanizza

Elisabetta Fanizza

Prof. Maria Lucia Curri

Dr. Chiara Ingrosso

Chiara Ingrosso

Coordinator of Ph.D Program:

Prof. Caterina Ciminelli

Course n°37, 01/11/2021-31/01/2025

Abstract

Growing global critical concerns around public health and environmental protection demand for more even more effective and innovative technologies to mitigate these issues. Specifically, the rise of antibiotic-resistant bacteria and emerging microbial threats highlight the need for advanced antimicrobial solutions, while the widespread environmental presence of pharmaceutical contaminants introduces new monitoring challenges. To address these objectives, the scientific community is prioritizing zero-impact approaches in materials engineering, guided by sustainable and green chemistry principles. These adaptable and functional solutions are designed to perform effectively across diverse applications, aligning with Industry 4.0's commitment to environmentally responsible and high-performance manufacturing.

In this frame, the research activity of this PhD thesis focuses on developing innovative sustainable nanostructured and, as far as possible, Eco friend materials with multifunctional capabilities for fulfilling health and environmental concerns.

This work introduces a novel hybrid nanocomposite based on Reduced Graphene Oxide (RGO), functionalized with the biocompatible amino acid histidine, and decorated with silver (Ag) nanostructures. By leveraging *in situ* and *ex situ* colloidal synthesis methods, and finely adjusting synthesis parameters, this research achieves a nanocomposite material, whose properties—including antimicrobial efficacy, thermal conductivity and SERS plasmonic properties—can be accurately tuned by controlling size and shape of the Ag nanostructures (nanoparticles - NPs - and nanowires – NWs -). Remarkably, these processes allow for solution-based integration of these nanocomposites into cellulose-based substrates like paper and cotton textiles.

The development and application of the engineered nanocomposites is explored across three key fields: 1) antimicrobial coatings for textile, aimed at combating bacterial resistance, 2) flexible paper sensors for real-time monitoring of pharmaceuticals and pollutants in both environmental and biomedical settings, and 3) thermally conductive coatings for cotton fabrics, evaluating their suitability for use in wearable and flexible devices. Together, these applications highlight the versatile potential of nanocomposites in advancing sustainable, high-performance solutions for health and environmental challenges.

The materials developed in this study highlight the integration embody of nanotechnology and sustainable chemistry, demonstrating how nanoscale modifications of structural and functional properties can greatly enhance versatility and performance. This approach not only advances adaptable, high-performing solutions but also emphasizes the critical role of nanoscience in fostering safer and more sustainable technologies, aligning with the United Nations Sustainable Development Goals (SDGs), particularly SDG 3 (Good Health and Well-being), SDG 6 (Clean Water and Sanitation), and SDG 12 (Responsible Consumption and Production). By addressing key health and environmental challenges, this research contributes to a safer, more sustainable technological landscape, supporting societal goals for resilience, well-being, sustainability, and public well-being.

Table of contents

Abstract

Experimental Results

Conclusions

Appendix 1

Appendix 2

Appendix 3

Introduction

Nowadays, nanotechnologies represent a burgeoning area of scientific research focused on exploring the outstanding chemical-physical properties exhibited by materials at the nanoscale, for fundamental research, and for applications in diverse technology fields.

The unique properties of nanostructured materials, which depend on their size, crystalline structure and shape, have driven many efforts of the scientific community towards the development of preparative procedures of nano-objects providing a fine tuning of such parameters with a reproducible control. Besides, the high number of active sites on the nanoparticles' (NPs) surface makes them extremely promising for chemical sensing, photocatalysis, electrocatalysis and as antimicrobial agents.[1]

NPs synthesized via colloidal methods exhibit well-defined surface chemistry, influenced by capping molecules used to control their morphology and prevent aggregation. These molecules binding the NP surface during growth, enhance their stability and enable their processability. Indeed, capping agents coordinating the NP surface, facilitate their dispersion in organic solvents and integration into polymer matrices. Additionally, capping agents can be replaced with proper bifunctional ligands or (bio)molecules such as nucleic acids, proteins and enzymes[1], enables the formation of assemblies of NPs which exhibit novel properties due to collective interactions among proximal particles[2]. Such functionalities, in fact, are being exploited to manufacture complex hierarchical structures integrated into micro- or nano-architectures, resulting in a new generation of solid-state materials demonstrated promising for diverse advanced applications. [3]

Prominent interest within nanotechnology, is the synthesis and investigation of hybrid nanocomposites, which combines colloidal nanostructured inorganic materials with different carbon allotropic forms (i.e. carbon nanotubes, fullerenes, diamond, graphene derivatives and so on), showing not only enhanced the properties of the pristine materials, but also interesting novel functionalities not present in the pristine individual components, and deriving from the synergistic combination of their intrinsic properties.

Graphene, a bidimensional material formed of sp^2 carbon atoms organized in a honeycomb structure, is among the most suited scaffold for such a purpose, due to its large area and its high chemical reactivity [4]. These properties make it ready to be modified by a plethora of chemical approaches, also those encompassing supramolecular chemical interactions with functional aromatic linkers, which do not add defects to its carbon structure, and hence are not detrimental for its intrinsic chemical and physical properties, and that, concomitantly, can chemically bind functional NPs anchoring them onto its basal plane.

The large area and chemical reactivity of graphene derivatives on one hand, and the high surface to volume ratio and chemical processability of the surface of inorganic colloidal NPs on the other, have prompted the scientific research to focus on the design and implementation of new ecofriendly and sustainable procedures for the preparation of novel hybrid nanocomposites exhibiting intriguing characteristics for a variety of applications, as for the fabrication of functional hybrid nanostructures onto flexible, cost-effective, and ecofriendly substrates for detection purposes, for the manufacturing of antimicrobial or passive cooling coatings onto natural textiles, among others. [5]

An emerging focus within nanotechnology is the development of sustainable, innovative solutions for detecting trace pollutants on low-cost, flexible, biocompatible, and biodegradable substrates. The sensitivity and selectivity of nanomaterials in sensing pollutants or drug molecules can be fine-tuned by altering their intrinsic optical and electrical properties, offering promising alternatives to conventional analytical methods (i.e. extraction, purification, HPLC/MS, and chromatographic analysis). In this context, Surface-Enhanced Raman Spectroscopy (SERS) has gained attention for its high sensitivity and specificity in pollutant detection.[6]

Surface-Enhanced Raman Spectroscopy (SERS) is a powerful technique for ultrasensitive and selective biochemical detection, capable of providing molecular "fingerprint" information at low concentrations. The enhancement in SERS is primarily due to the high localized electromagnetic field on noble metal surfaces, caused by the excitation of localized surface plasmon resonances and enhanced chemical interactions between the adsorbate molecules and metal NPs. [6, 7]

In particular, the regions where such local electromagnetic field is highly enhanced, known as "hot spots," play a crucial role in Raman signal enhancement. This enhancement depends on the arrangement and morphology of the metal surface, with roughened or aggregated surfaces (like flower-like or dendritic structures) showing significant enhancement factors. Substrates featuring many hot spots and uniformly distributed nanostructures provide strong Raman enhancement and high measurement reproducibility. These resonance effects are influenced by the size, shape, composition, and spacing of the nanostructures, as well as the surrounding medium.[8]

The sensitivity of nanostructures is linked to the degree of localized surface plasmon resonance, which depends on the coupling between the electromagnetic wave and anisotropic metal nanostructures, such as rods, bipyramids, stars, or urchin-like particles. Capping agents or ligands, such as polyvinyl pyrrolidone (PVP), are essential for precise fabrication, reducing surface energy, preventing aggregation, and controlling the morphology of nanostructures.

SERS-based methods for molecule identification require highly specific substrates, like metal NPs decorated with molecular imprinted polymers or non-specific markers modulated by the target molecule. While nanomaterial fabrication is key for SERS sensors, chemical modification of the metal surface through organic functionalization is equally important for detecting challenging pollutants, such as pesticides or pharmaceuticals, and for adding extra functionalities to nanodevices used in molecular detection.[9]

Nanostructures based on Ag NPs are the most widely used for SERS applications due to the highly desired plasmonic properties of Ag NPs, low cost and easy fabrication/synthesis with respect to other metals. For instance, the use of Ag NPs has been very useful in sensing of molecules, because offers the highest enhancement factors (EFs).[8] However, reproducibility and stability of their signal remains a challenge due to their tendency to oxidize, aggregate and dissolve in presence of atmospheric oxygen and water vapor [10]. This limitation can be overcome by coating Ag NPs with a protective layer that does not interfere with their SERS activity while preventing oxidation. Besides, to further improve their enhancement factors, the SPR of Ag nanostructures have been coupled with other nanomaterials, to merge their EM effect with the chemical enhancement mechanisms (CE) [9].

For this purpose, single layer graphene and its derivatives have attracted as SERS substrates for accomplishing Raman enhancement [12]. Graphene oxide (GO) and reduced graphene oxide (RGO) have been, in fact, widely used in such applications for their large surface area, low production cost, and high surface reactivity that open the venue to the preparation of a variety of novel nanocomposites with (bio)molecules and nanostructures, exhibiting interesting chemical physical functionalities. GO and RGO are desirable materials for fabricating SERS substrates, because of their fluorescence quenching, high adsorption capacity of analyte molecules by aromatic π-π stacking and hydrophobic interactions, and especially for their stable SERS signals[9] originated from charge-transfer-induced mechanisms (CE) [8]. Due to these interesting properties, recent research has focused on the fabrication of GO/RGO composites with noble metal NPs to enhance SERS performance by combining CE and EM effects.

Particularly interesting is the integration of SERS active materials into natural substrates such as cotton, silk and wool fabrics, that have showed exceptional performances as supporting scaffolds for sensors [11], thanks to their surface reactivity, mechanical flexibility, biodegradability and biocompatibility, all properties extremely promising for the fabrication of sustainable wearable and flexible sensors.

In addition to their sensing capabilities, these nanostructured materials can also serve as effective antimicrobial agents. The spread of pathogenic bacteria resistant to antibiotics has encouraged the study of novel, cost-effective and sustainable antimicrobial solutions. Microorganisms forming harmful biofilms on surfaces cause severe hygienic issues and transmit infectious diseases. Thus, applying antimicrobial materials to textiles is essential to prevent the growth of biofilms, ensuring that these surfaces remain hygienic and safe for use in healthcare and everyday environments.

Therefore, there is an urgent need for innovative strategies in engineering textiles for conveying to them antimicrobial and self-cleaning properties, overcoming the lack of such functionalities in traditional ones.

For such a purpose, one of the most sustainable and scalable approaches relies on modifying natural fibres with functional NPs. Despite its limitations like wrinkle formation, hydrophilicity and microbial degradation, among the natural fibres, cotton is an ideal fabric due to its biocompatibility, biodegradability, flexibility and breathability. The use of coating techniques (i.e., dipping, impregnation, spray coating) to modify fabrics with nanostructures is a scalable and sustainable approach to impart novel functionalities to traditional textiles (such as antiwrinkle, antistatic, UV radiation shielding, hydrophobicity) while preserving their comfort, flexibility, lightness, breathability and texture.

Ag NPs are widely used in the antimicrobial field, because of their broad spectrum biocidal effect against diverse populations of bacteria, fungi, and viruses [12] and their effective bioactivity against multi-drug resistance pathogens [13]. Ag NPs have been widely applied to prevent formation of fouling biofilms, as these can have adverse effects in industrial processes limiting heat transfer, corroding metallic surfaces, and blocking flow of fluids [14].

The antibacterial activity of Ag NPs has been accounted to the release of Ag^+ ions, that, interacting with the negatively charged cell membrane of microorganisms lead to the generation of intracellular reactive oxygen (ROS) species, inducing oxidative stress that compromises its integrity, resulting also in cells death. [15] The biocidal effect of Ag NPs depends on the NPs size [16] and shape, pH and ionic strength of the NPs solution, light exposure conditions [17], and surface ligand chemistry (e.g. capping agent density, coordinating atom, carbon chain length and terminal group) [18]. Due to their large surface area to volume ratio, smaller Ag NPs have the highest antimicrobial effect, but their tendency to oxidase and aggregate to minimize surface energy, significantly reduces their biocidal effect [19], limiting their practical application. To circumvent such an inconvenient, chemical immobilization of Ag NPs onto surfaces bearing chemical functional groups capable to coordinate their surface, as the graphene basal plane, has been performed, enhancing their potential for antimicrobial applications.

Concerning the effects of graphene derivatives on the viability of bacterial cells, the literature is controversial, [20] and the contradictory explanations are ascribed to the diverse intrinsic physicochemical properties of graphene samples. Some works report on the dependence of bacteria cell viability on the graphene preparation method, its thickness, size, surface area, charge, functionalization, roughness, hydrophilicity, oxidation capacity and dispersibility, and hence it varies from sample to sample.[20] In these works, the antibacterial effect is caused by production of reactive oxygen species (ROS) that oxidase vital cellular components [21] and by the direct contact of the atomic-thick sharp edges of the graphene sheets, that, functioning as “cutters”, interrupt and damage cell membrane, causing outflow of the intracellular content. Some other studies, instead, report on the capability of graphene derivatives in promoting bacterial growth and biofilm formation, and such nanostructures are exploited in applications where bacterial metabolism increases, as in biofuel production by anaerobic digestion or in generation of renewable bioelectricity power in microbial fuel cells, where graphene derivatives are used as mediators of electron transfers in metabolic processes.

Nanostructured materials and their composites with graphene are optimal also for effectively conveying to fabrics other functionalities, such as hydrophobicity, electrical and thermal conductivity [22]. Suited for such an application, are in fact, the exceptional electrical and thermal conductivity, the mechanical flexibility and hydrophobicity of graphene and its derivatives. Textiles featuring advanced thermoregulatory properties have been regarded as original solutions for accomplishing human thermal comfort for sports, medical and aerospace, or for addressing the even more pressing need of fulfilling individual physical and physiological human wellbeing in diverse work environments and conditions [23]. Also, the interest for such textiles originates from the evidence that the regulation of the individual microclimate has been demonstrated more effective than the use of heating, ventilation, and air conditioning (HVAC) systems, because of differences of subjective thermal sensation,[24] thus resulting in a huge saving energy of building HVAC systems which account for about 40% of their total energy consumption.

In literature, cotton has been modified by impregnation with carbon nanotubes [25], with polymer formulations based on epichlorohydrin based resin modified by thermally conductive nanostructures like carbon nanotubes, boron nitride nanosheets (BNNSs), and graphene derivatives [26] , and with graphene nanoplatelets and BNNSs embedded in thermoplastic polyurethane (PU) [27-29]. Despite the significant boast of thermal conductivity of these approaches, scaling up is challenged because of the use of the unsafe carbon nanotubes, hazardous precursors in PU synthesis and toxic byproducts from epichlorohydrin-based resins [30]. As an alternative, polymer formulations heavily loaded with high thermally conductive nanofillers have been used but limited to the fabrication of patches. Polymer nanocomposites based on BNNs embedded into polyvinyl alcohol (PVA)/dimethyl sulfoxide solutions have been fabricated into fibers through a hot-drawn 3D printing process, and the resulting patches have a thermal conductivity increased up to 0.078 W $m^{-1} \cdot K^{-1}$, which is 2.2 times higher than cotton and 1.6 times higher than neat PVA fabrics [31]. Other efforts have focused on avoiding toxic solvents and fossil-based polymers by using biodegradable polymers with high thermally conductive nanofillers. Patches of cellulose/alkaline/urea solutions modified with 60 wt.% edge-selective hydroxylated BNNSs achieved through wet-spinning and weaving have reached a thermal conductivity increase from 0.86 W m^{-1} K^{-1} to 2.914 W m^{-1} K^{-1}[32]. Additionally, silk fibroin patches loaded with 50 wt.% exfoliated BNNs reached 1.77 W m^{-1} K^{-1} using vacuum filtration[33]. Despite being eco-friendly, these methods necessitate costly fabrication technologies and a high concentration of nanofillers, which exhibit chemical inertness and strong interlayer interactions. Consequently, this limits the sustainability and scalability of the approach.

In this thesis work, new hybrid nanocomposites formed of Reduced Graphene Oxide (RGO) sheets, functionalized with the biocompatible and water soluble aminoacidic histidine (His), and then decorated with Ag nanostructures, having different morphology (nanospheres and nanowires), were synthesized by diverse sustainable approaches for the manufacturing of novel antimicrobial cotton fabrics, thermally conductive cooling cotton textiles, and SERS active nanostructures for the detection of drug molecules onto flexible paper.

His was selected as intercalating, exfoliating and functionalizing agent of RGO, for its capability to bind its basal plane by aromatic π-π stacking interactions. Its water solubility allows the dispersion of RGO sheets in aqueous solutions by liquid-phase exfoliation (LPE), approach that would be not practicable in absence of His due to the high hydrophobicity of RGO and the high surface tension of water (72 mJ m^{-2}) inducing RGO aggregation, and that would require toxic organic solvents (i.e. N-methyl-2-pyrrolidone, N,N-dimethylformamide, ortho-dichlorobenzene etc.) with a lower surface tension (40 mJ m^{-2}).[34]

His strongly interacts with the RGO sheets concomitantly grafting a high density of -COOH and $-NH_2$ groups, that were exploited in our synthesis routes, as heteronucleation and growth sites in the *in situ* formation of the Ag nanostructures. The synthesis mechanisms of the designed nanocomposites were investigated and explained by systematically tuning the experimental conditions, and concomitantly studying the morphology and spectroscopy properties of the achieved nanostructures, also through a series of preliminary control experiments aimed at systematically evaluating the chemical behaviour of each chemical specie involved in the synthesis of the nanocomposites when His-RGO is present in the reaction solution.

This thesis is structured as follows:

In Chapter 1, the focus is on the properties, synthesis, and functionalization of nanostructured materials, with particular attention to colloidal Ag nanostructures, such as NPs and NWs. The chapter discusses how their unique chemical and physical properties depend on parameters such as size, shape, and crystalline structure. The different synthesis methods, including chemical reduction and UV-light photo-reduction, are described in detail, along with strategies to control NP morphology and prevent aggregation. Additionally, the applications of these nanomaterials in sensing, catalysis, and antimicrobial fields are explored.

Chapter 2, on the other hand, focuses on graphene and its derivatives, such as GO and RGO. This chapter highlights the synthesis and functionalization of graphene-based materials and their role in hybrid nanocomposites. Special attention is given to combining graphene with Ag nanostructures to develop multifunctional materials. These nanocomposites are discussed in the context of technological applications, including antimicrobial coatings, SERS-active substrates, and thermally conductive textiles. Sustainable approaches to fabricating these nanocomposites, particularly on natural fabrics like cotton, are emphasized for their potential in wearable sensors and environmental monitoring.

The Research finding section deals with the synthesis of the His-RGO/Ag NPs/Ag NWs nanocomposite, along with the techniques employed for its chemical and physical characterization. The section delves into the optimization of the synthesis process, systematically varying experimental conditions while simultaneously characterizing the spectroscopic and morphological properties of the resulting nanocomposites. The underlying mechanisms driving these processes are explained, and the chapter also explores the various applications of these hybrid nanocomposites, accompanied by the corresponding results.

This chapter is divided into three parts, each focusing on the use of the RGO-based nanocomposite with colloidal Ag in different applications:

Chapter 3: *In Situ decoration of reduced graphene oxide with silver nanoparticles: cotton fabric functionalization with a thermally conductive coating.* A thermally conductive nanocomposite coating for cotton, formed of His-RGO and decorated by Ag NPs, here named as Cot-His-RGO/Ag, was prepared in another work, by synthesizing Ag NPs, *in situ*, on the coordinating sites of cotton fabrics modified by impregnation with His-RGO, and then impregnated by aqueous methanol solutions of the $AgNO_3$ precursor, under UV-light exposure, without using chemical reductants. This method, proven successful in decorating cotton with Ag NPs for commercial antimicrobial textiles [22,23], demonstrated its viability in terms of scalability and sustainability. RGO was selected because it possesses the thermal conductivity closest to that of monolayer graphene, and compared to BNNs, it has higher chemical reactivity affording superior exfoliation and chemical modification capability. Furthermore, RGO was decorated with NPs of Ag, which exhibits high thermal conductivity (429 WmK^{-1}) [20], as able in principle to improve interlayer heat diffusion, bridging adjacent graphene sheets.

Chapter 4: *Novel hybrid nanocomposite based on Ag Nanoparticles decorated Reduced Graphene Oxide sheets: synthesis, characterization and assessment of the long-term antimicrobial activity towards textiles coating applications*. In this work, in one study, a nanocomposite based on Ag NPs and His-RGO, here called His-RGO/Ag NPs, was synthesized, in aqueous solutions and at low temperature, by reduction of the $AgNO_3$

precursor, *in situ*, onto the sheets of the His-RGO complex, in presence of sodium borohydride ($NaBH_4$) and trisodium citrate tribasic dehydrate ($Na_3C_6H_5O_7 \times 2H_2O$), the reducing and coordinating agents, for the manufacture of an antimicrobial coating for cotton. The His-RGO/Ag NPs hybrid nanocomposite was purposely designed with a high density of small Ag NPs to have a strong antimicrobial activity. In particular, the experimental synthetic parameters, $AgNO_3$, His-RGO, $NaBH_4$ and citrate relative concentrations, as well as the pH of the reaction solution, were systematically tuned and the spectroscopic and morphological properties of the achieved nanostructures were comprehensively investigated, to study their effect on the nanocomposite coating density and NPs size, and hence suitably engineering the nanocomposite. The achieved nanocomposite presents spherical Ag NPs of 24 ± 4 nm, densely coating the His-RGO sheets, and it has been used to modify cotton, by impregnation. Its biocidal effect was tested by the quantitative standardized ISO protocol method (ISO 20743:2021), and *Escherichia coli* (*E. coli*) was considered as model bacterium representative of the Gram negative bacteria

Chapter 5*: Innovative Green Synthesis of Ag Nanowire-Decorated Nanocomposites via Combined In Situ-Ex Situ Approach on Reduced Graphene Oxide for drug molecule SERS detection on flexible paper substrates.* This study involved the preparation of another nanocomposite, formed of RGO sheets decorated with Ag nanowires (NWs), synthesized using $AgNO_3$ as a precursor, sodium chloride (NaCl) to buffer concentration of Ag+ ions in the reaction environment, ethylene glycol (EG) serving as the green reducing agent and solvent, and polyvinylpyrrolidone (PVP) acting as a biocompatible coordinating ligand and stabilizing agent able to direct anisotropic growth of the NWs and disperse the resulting hybrid composite, here called His-RGO/Ag NWs, in water or alcohol. Under optimal experimental conditions, the implemented synthesis approach yielded Ag NWs with an average length of 5±3 μm and an average diameter of 0.10±0.03 μm. The intrinsic mechanical flexibility of both the RGO sheets and the Ag NWs make them materials suited for the modification of flexible substrates, to integrate in wearable devices and sensors. The novel His-RGO/Ag NWs hybrid nanocomposite was tested against neat Ag NWs, as a substrate for the Surface-Enhanced Raman Spectroscopy (SERS) detection of target molecules having a different chemical structure, namely 1-naphthalenethiol (1-Nat), rhodamine 6G(R6G), benzo[a]pyrene and tested for the SERS detection of propranolol hydrochloride (PRNL), a pharmaceutical molecule of interest. To increase the SERS signal, removal of PVP was also investigated implanting treatments with $NaBH_4$, KI and O_2/Ar and H_2/Ar plasma. $NaBH_4$ and KI treatments did not significantly improve performance, while plasma etching effectively enhanced the SERS signal of R6G.

The plasma treatment performed by cycles with O_2/Ar and H_2/Ar, although changed the sample's morphology, as evidenced by SEM analysis, improved the R6G signal decreasing its LOD by one order of magnitude compared to the untreated nanocomposite. SERS spectra of PRNL deposited on both plasma-treated and untreated His-RGO/Ag NW substrates showed that the treated sample exhibited more intense characteristic peaks (e.g., the peak at 1384 cm^{-1}) achieving a LOD of 10^{-7} M [17].

The obtained LOD of 10^{-7} M results lower than the allowed limit recognized by legislation, set at 5.21×10^{-4} M (135 mg/kg) demonstrating feasibility of the nanocomposite as SERS active material for the detection of drug molecules. These tests were designed and conducted in collaboration with the FunNanobio Group of the Departamento de Química Física y CINBIO Universidade de Vigo, led by Jorge Perez Juste.

Chapter 1

1.1 Properties of Nanostructured Materials

In recent years the terms “nanoscience” and “nanotechnology” have almost monopolized the scientific language. The interest for this branch of science moves from the fact that at the nanometre length scale, the materials present new and peculiar properties.[35] When a material exhibits at least one of its three dimensions within the range of 1-100 nm, [36]it demonstrates properties that are influenced by size and shape, and that are intermediate between those of bulk solids and individual atoms or molecules.[36, 37] The properties of bulk materials typically depend on the type of the chemical bound on which is based their structure, and hence, are independent on size and shape. Conversely, such parameters determine and modulate the characteristics of the materials when their size goes down to 10 nm.[35] At present, such a peculiar dependence of the properties of the nanomaterials on their morphology have tremendously advanced potentialities of material science.

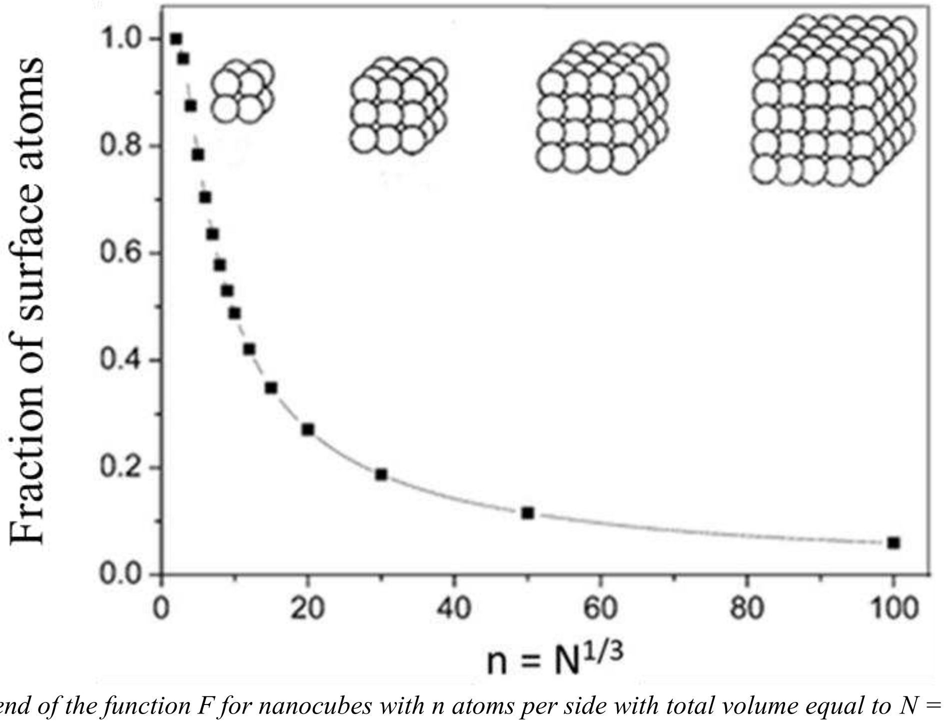

Fig. 1.1: *Trend of the function F for nanocubes with n atoms per side with total volume equal to N =* n^3*.[38]*

Two effects are typically observed in nanostructured materials: modulation of their thermodynamic properties with the variation of the surface atom fraction and the so called ‘quantum effects’.Nanostructured materials can be zero-, one-, two-, and three-dimensional (0D, 1D, 2D, and 3D), and may have different chemical compositions, such as metals, semiconductors, or metal oxides. They can exist in various crystalline phases or be amorphous. A class of nanostructured materials of significant interest comprises nanocrystals (NCs), which are crystalline NPs with at least one dimension ranging between 1 and 100 nm.[36, 38]

At the nanoscale, the fraction of surface atoms of the NP increases as the size decreases, following a function referred to as the F dispersion (Fig. 1.1). Since the surface atoms of NPs have fewer adjacent atoms compared to bulk ones, resulting in a lower coordination number, smaller-sized NPs possess higher surface free energy and increased chemical reactivity.[39]Thus, the fraction of surface atoms significantly contributes also to the total free energy of the NPs and the increase in surface free energy in smaller NPs leads to changes in some fundamental thermodynamic properties following scaling laws that vary inversely with $N^{1/3}$ or the inverse of the radius (r^{-1}) and diameter (d^{-1})[36], following the so-called "scale laws", such as the decrease in melting temperature and the increase in pressure required to induce phase transitions. [40]

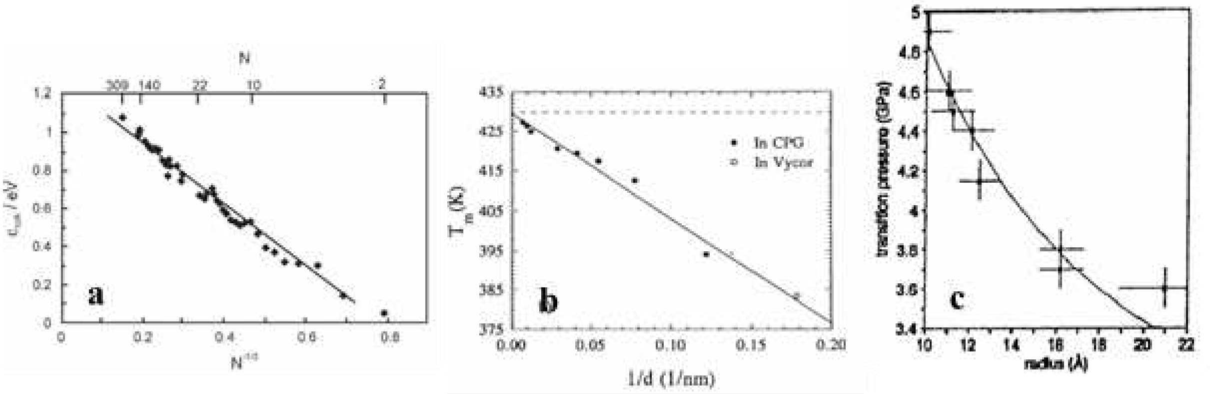

Fig. 1.2:*(a) Calculated cohesive energies of various sized magnesium clusters versus $N^{-1/3}$. (b) Melting temperature for indium confined in controlled pore glass and Vycor, as a function of the inverse of the pore diameter d^{-1}. The dash line represents the bulk melting point. (c) Dependence of the transition pressure on the radius for the pressure-induced structural transformation of CdSe NPs from wurtzite to rock salt.[40]*

As for example, the decrease of the NPs size provides the lowering of the cohesive energy. In a solid, such an energy is defined as the bound energy for atom. On the surface of a NP, the atoms possess several free valences having typically fewer direct neighbour atoms than in the bulk phase, and hence the cohesive energy scales with $N^{-1/3}$, as reported in Figure 1.2 (panel a). Another consequence of the unsaturation of the valences of the surface atoms is the accumulation of the energy on the surface of the NPs which leads to a decrease of the intrinsic melting temperatures of the materials (Figure 1.2, panel b).[40]

Additionally, at the nanoscale, NPs may exhibit properties that are absent in the corresponding bulk material, such as catalytic activity in Au NPs or superparamagnetism in ferromagnetic NPs.

As nanostructured materials represent a state of matter intermediate between bulk solids and atoms or molecules, the density of their electronic states lies in between a discrete and a continuous distribution of states, and the density of states (DOS) function differs from that of the reference bulk material. One approach used to calculate the DOS is based on applying principles of general physics used for solids with dimensions of few nanometres. [41]

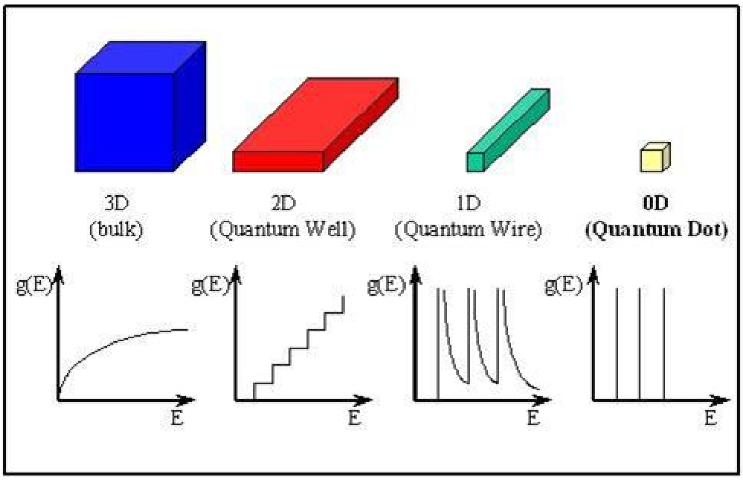

Fig. 1.3: *Idealized density of states (DOS) function for a semiconductor in 3, 2, 1, and 0 dimensions. In the 3-dimensional case, the energy levels are continuous, while in the 0-dimensional solids, the energy levels are discrete.[42]*

As the material's size becomes comparable to the exciton Bohr radius, a free charge in the material is treated as a particle confined in a potential well with the same dimensions as the material. Based on this model, the DOS of NPs should exhibit ideal variations predicted by the quantum mechanics model of a particle in a box, described as an intermediate function between the discrete levels of an atom and the band structure of a bulk solid. This model is based on solving the Schrödinger equation with boundary conditions for a particle confined in a box, where the electronic states are represented by a discrete distribution of levels. This distribution changes significantly when the dimensions of the solid approach few nanometres, resulting in size-dependent intrinsic properties. [41]

In a three-dimensional (3D) material, no spatial restrictions are imposed to the movement of the charge carriers which can thus move along tree dimensions. As shown in Figure 1.3, the resolution of the Schrödinger equation without any boundary conditions leads to density state function g(E) which scales with $E^{1/2}$ and provides a quasi-continuous of possible energy states for charge carriers.[36, 42]

When the charge carriers are confined in a two-dimensional electronic system (2D), the so-called quantum well, the DOS assumes the trend of a step-function and fewer discrete levels are available. In the case of a one-dimensional system (1D, quantum wire), the density of states is proportional to $E^{-1/2}$ exhibiting singularities near the band edges. Finally, in the limiting case in which the size of a solid becomes comparable to the De Broglie wavelength associated to its charge carriers, all dimensions shrink, and electrons and holes are confined in a zero-dimensional solid (0D) or quantum dot (QD). Herein, the DOS is represented by a delta function, meaning that the bands converge to atom-like energy states.[42]

Because of this quantisation of the charge carriers, a zero-dimensional particle is often called also as artificial atom, pseudo-atom or superatom.[43] Therefore, while the DOS in a 3D system is a function of energy $E^{1/2}$, for a 2D system, it is a "step-like" function with steps positioned at the energies of quantized levels. In a 1D system, there is a relationship $E^{-1/2}$, and in a 0D system, it is a δ-function of E, indicating that charges are confined in discrete energy levels (Fig. 1.3). As a result of the quantization effect [42] in nanostructured materials, the DOS exhibits a discrete level structure at the band edge. For a specific dimension characteristic of the material, the spacing between energy levels exceeds the thermal energy, and their fundamental physical, optical, magnetic, and electrochemical properties depend on size [36], unlike in bulk materials, where chemical and physical properties depend solely on the chemical composition [44].

1.1.2 Colloidal nanoparticles (NPs): synthesis, morphology control, and surface functionalization

In recent years, there has been an extraordinary growth in nanoscience and technology, mainly devoted to the development of new approaches for synthesizing nanomaterials, as well as the accessibility of tools for their investigation, classification and manipulation. Besides, the production of NPs requires understanding the fundamental properties of nanoscale chemistry and physics, as well as the know-how to commercialize them.[45]

Generally, metal NPs can be prepared by chemical, physical and biological methods; the chemical approaches encompass chemical reduction, electrochemical techniques, photochemical reduction and pyrolysis, physical methods can use arc-discharge and physical vapor condensation (pvc), and biological methods utilize microbial enzymes, plant extracts, or biomolecules, as reducing and stabilizing agents to reduce Ag^+ ions into Ag NPs. This process is also known as "green synthesis" and avoids the use of toxic chemicals. [46]

Studies have shown that the size, morphology, stability, and properties (both chemical and physical) of metal NPs are strongly influenced by experimental conditions, such as the kinetics of interaction between metal ions and reducing agents, and the adsorption processes of stabilizing agents to the metal NPs' surface. Thus, designing a synthesis method that controls these factors has become a major field of interest.

The most used chemical approaches are *bottom-up* methods which consist of the chemical reduction of Ag precursors in presence of reducing and coordinating agents and are performed at room temperature, or at high temperatures for increasing reaction rates, especially when mild reducing agents are used. Such procedures, known as hot injection, are most frequently applied for the preparation of stable, colloidal dispersions of NPs in water or organic solvents.[47] Typical reducing agents include polyols, $NaBH_4$, N_2H_4, sodium citrate and N,N-dimethylformamide, and in order to prevent aggregation of the NPs during the synthesis, surfactant such as sodium dodecyl sulphate (SDS), polyvinyl pyrrolidone (PVP) and tri-sodium citrate are used.

The *hot-injection* technique involves rapid injection, under stirring, of NP precursors into a hot solvent, heated to a temperature that induces their decomposition and provides the thermal energy necessary to trigger the nucleation of clusters and growth of the NPs in solution. The nucleation and subsequent growth occur in presence of one or more surfactants (e.g., acids, amines, phosphines) that act as stabilizing agents, as present polar heads coordinating the clusters and alkyl chains contributing to their dispersion in solvents. The chemical structure of coordinating agents plays a crucial role in controlling morphology and crystalline structure of NPs, along with other experimental parameters such as growth time, precursor injection speed and growth temperatures, molar ratios between precursors and coordinating agents, and pH of the reaction mixture.[45]

The choice of the coordinating agent is particularly crucial for controlling NP morphology, as ligands can specifically interact with certain crystal faces of growing clusters, limiting growth perpendicular to these faces. This results in preferential growth along specific crystal directions, leading to the formation of anisotropic nanostructures, such as nanorods and nanowires.[46]

NP morphology can also be influenced by the growth regime in which the synthesis is conducted, which can be either kinetic or thermodynamic. In the kinetic growth regime, there is a high concentration of monomer at the surface of the growing NPs and hence it deposits on each face of the NPs, preferably on those with higher energy and more sterically accessible. In contrast, the thermodynamic growth leads to the formation of the thermodynamically most stable particle shape. This growth regime occurs when the concentration of monomer in the solution is low, for example, when in solution occurs a reaction comprising the slow release of monomer, or when the monomer is injected drop-by-drop or at a controlled low speed in the synthesis solution, for example, by using a peristaltic pump. [46]

The temperature is another parameter that can control the crystalline phase of the initial core in polymorphic materials, and consequently, the morphology of the nanostructures. For example, Sarkar et al. synthesized both 2D and 3D Ag nanostructures with disk and globular morphologies using the silver-mirror reaction in the presence of an anionic surfactant.[46] Successful experiments using tri-sodium citrate, as an initial surfactant and reducing agent, followed by sodium formaldehyde sulfoxylate (SFS) addition, established a large-scale method for preparing Ag nanopowder with particle sizes less than 50 nm.

In another example, ascorbic acid was used as the reducing agent to develop flower-like Ag nanoarchitectures at room temperature with sizes of ca. 20 nm, while citric acid played a key role in the nanostructure formation. In 2009, Janardhanan et al. synthesized Ag NPs by an aqueous chemical method with an organic base and without adding capping agents. Ag NPs of 40-80 nm were formed through the oxidation of glucose to gluconic acid by amine in the presence of $AgNO_3$, with gluconic acid acting as the capping agent. [46]

Ag NPs can also be synthesized using various irradiation methods. For example, laser irradiation of an aqueous solution of Ag salt and surfactant can produce well-defined Ag NPs without the need for a reducing agent. In 2007, Ag NPs with narrow size distribution were synthesized in ethylene glycol-water mixtures without a stabilizer using the pulse radiolysis method. Remita et al. demonstrated that X-ray irradiation of metal salt aqueous solutions without a stabilizer can also lead to the synthesis of spherical NPs with a radius of about 14 nm.

Microwave irradiation has also been employed, providing a faster heating rate than conventional methods. Yanagida, Komarneni, and Liu reported synthesizing Pt and Ag NPs using fixed frequency microwave (2.45 GHz).[48]

Finally, coordinating agents are essential for controlling the surface chemical reactivity of NPs for their conjugation to biomolecules, their binding to surfaces, polymers or other nanostructures or their self-assembly. This can be achieved by implementing procedures to exchange the pristine coordinating agent of the nanoparticle surface while preserving their morphological and structural properties. Capping exchange procedures typically use a coordinating agent that binds more strongly to the NPs surface than the pristine ligand or use an excess of the new ligand to displace the existing one through mass action. Other strategies involve utilizing hydrophobic interactions between the coordinating agents at the NPs surface and amphiphilic molecules, such as lipids or phospholipids, or the hydrophobic cavity of host molecules[47, 49].

1.1.3 Size dependence of optical properties

Nanostructured metals, such as Ag, Au, and Cu, are of significant interest due to their unique optical properties, which are attributed to their plasmonic absorption. This phenomenon arises from the resonance interaction between the frequency of an electromagnetic incident radiation and the oscillation frequency of the coherent motion of the conduction electrons which are in the metal's conduction band, leading to the so-called Localized Surface Plasmon Resonance (LSPR) effect [50]. In the classical model of a spherical NP, the incident light wave polarizes the conduction electrons, generating dipolar oscillations in phase with the radiation (Fig. 1.4).[50] Specifically, when the NP diameter is smaller than the wavelength of the incident light, electron polarization occurs in the conduction band, leading to energy absorption and charge separation. This happens when the electromagnetic radiation has enough energy to displace the electron cloud relative to the nuclei, resulting in a Coulomb force that drives the electrons back to the minimum distance from the nuclei, causing oscillatory motion of the conduction band electrons, in accordance with the electric field of the incident radiation (Fig. 1.4). This oscillation is what produces the LSPR absorption [50].

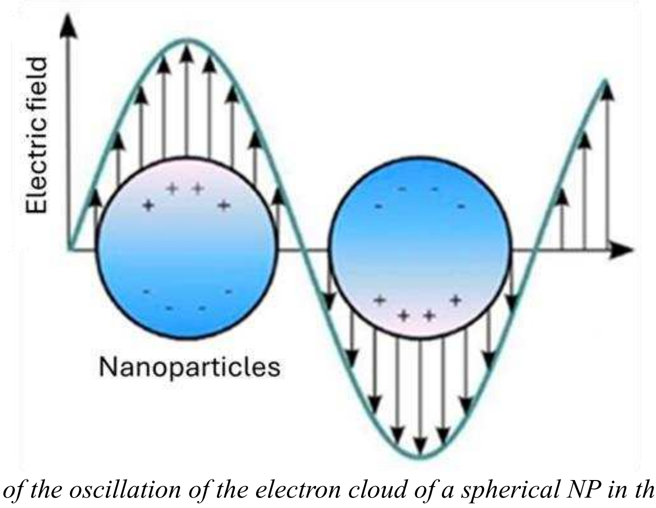

Fig. 1.4: *Representation of the oscillation of the electron cloud of a spherical NP in the LSPR process. [50]*

The oscillations of the electron cloud, known as plasmons, resonate at specific frequencies determined by factors such as electron density, NP shape, surface chemistry [9], and the dielectric constant of the surrounding medium[51].

In noble metal NPs, intense absorption occurs in the near UV-Visible region, and the frequency, shape, and width of the plasmon excitation are directly dependent on the NP's characteristics, as observed through UV-Vis absorption spectroscopy (Fig. 1.5).

For Ag NPs, the plasmonic peak can vary significantly with the size (Fig.1.5). [52]In the intrinsic size region (d < 5 nm), noble metal NPs (such as Au) may not show plasmon absorption.

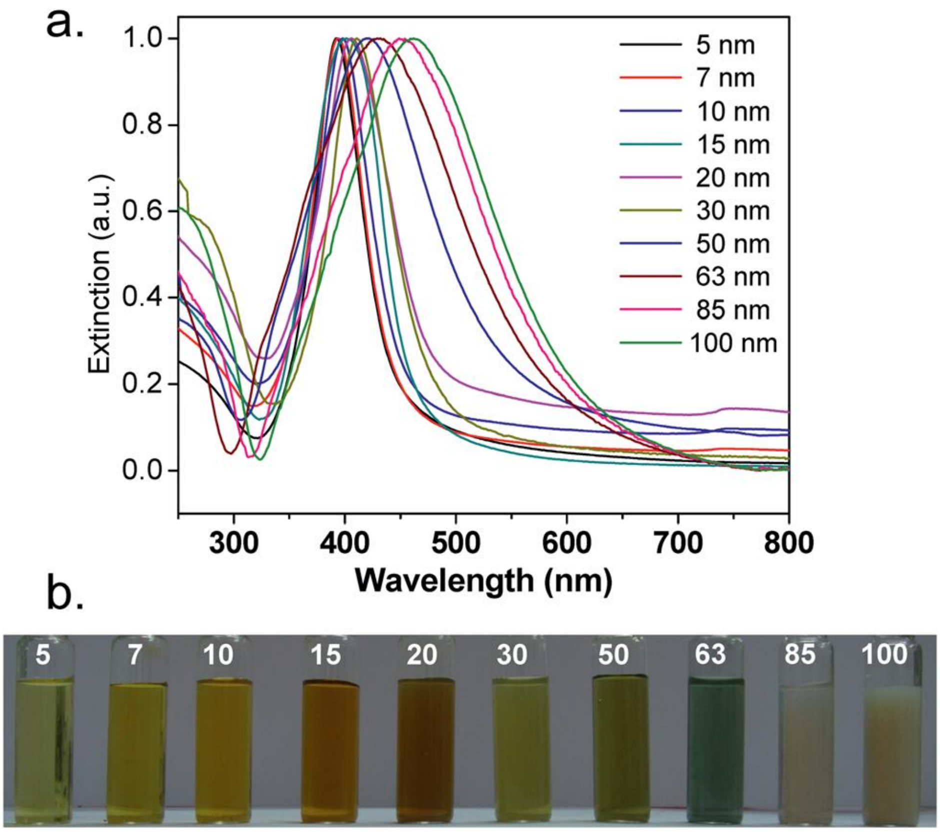

Fig. 1.5 : *In a) UV-Vis extinction spectra and (b) the distinctive colour of different sized Ag NPs. [52]*

However, Ag NPs of this size can still exhibit a plasmonic peak. For larger NPs (above 50-60 nm), the absorption peak becomes broad, covering most of the entire visible spectrum. This size-dependent behaviour is critical for their application across various fields, including medicine, electronics, and environmental science.[52]

For spherical NPs, absorption spectra can be predicted using Mie theory[50], which allows calculating the extinction coefficient *Cext*, or the extinction cross-section, providing information about absorbed and scattered radiation, according to the following equation:

$$Cext = -\left[\frac{24(\pi^2)(R^3)\left(\xi m^{\frac{3}{2}}\right)}{\lambda}\right] * \left[\frac{c''}{[(\xi' + 2\xi m)^2 + \xi''^2]}\right]$$

where λ is the wavelength of the incident radiation, *Cext* is the extinction coefficient, ξm is the dielectric constant of the surrounding medium, and $\varepsilon = \varepsilon'(\lambda) + i\varepsilon''(\lambda)$ is the complex dielectric function of the metal.

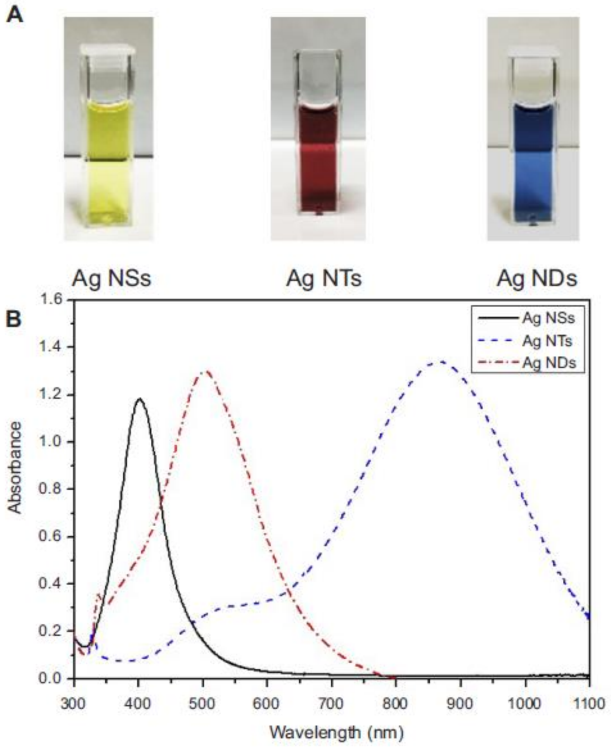

Fig.1.6: *(A) Solution color and (B) UV-VIR-NIR absorption spectra of Ag NPs with different shapes. Abbreviations: Ag NDs, Ag NSs and Ag NTs are respectively Ag NPs with disk, spherical and triangular plate morphology. [53]*

Spherical NPs typically display a single LSPR absorption, which is associated with a dipole resonance, while anisotropic particles can exhibit additional bands corresponding to quadrupole and higher-order multipole resonances.

For example, Ag nanoprisms with truncated edges show a strong in-plane dipole resonance at 670 nm, with additional minor peaks at 470 nm and 370 nm, and a shoulder at 410 nm, corresponding to in-plane and out-of-plane quadrupole and dipole resonances, respectively.[53]

1.2 Ag NPs properties, synthesis and applications

1.2.1 Properties of Ag NPs

Ag NPs possess a wide range of unique physical, chemical, and optical properties that arise from their nanoscale size and high surface area. These characteristics make Ag NPs distinct from Ag bulk and suitable for various scientific and technological applications. Key properties of Ag NPs include high electrical and thermal conductivity, plasmonic behaviour, antibacterial activity, and surface chemical reactivity, all of which can be finely tuned by controlling their size, shape, and surface chemistry during synthesis.

Ag nanostructures are particularly promising for their antimicrobial properties. In fact, different shapes of Ag NPs, such as spherical, rod, triangular, and cubic, exhibit varied levels of antibacterial efficacy. For instance, spherical Ag NPs generally demonstrate superior antibacterial activity compared to their triangular counterparts due to their larger surface area-to-volume ratio, which facilitates better interaction with microbial cells.

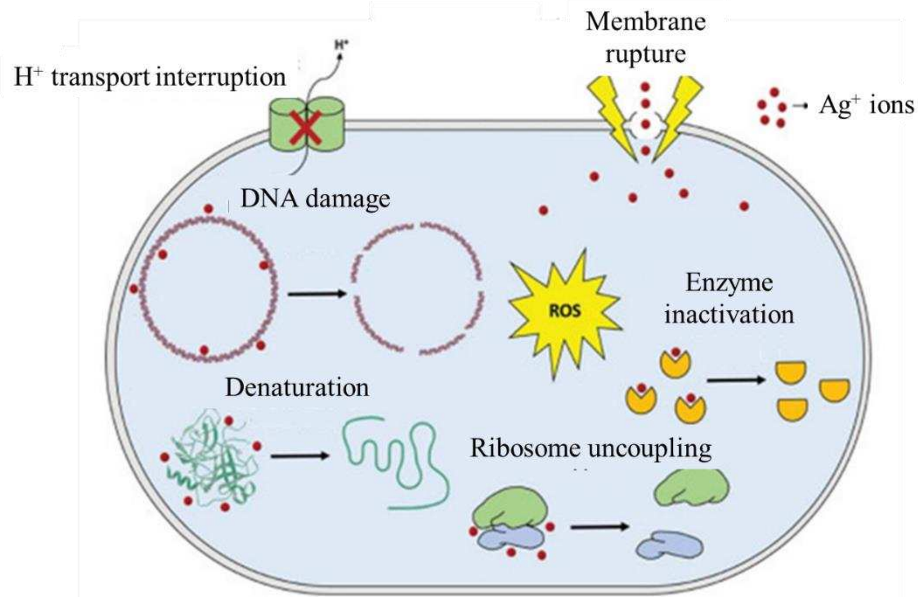

Fig. 1.7: *Schematic illustration of the antibacterial mechanism of Ag nanostructures. [54]*

Additionally, the edges and corners of anisotropic NPs like rods and cubes can lead to enhanced localized surface plasmon resonance (LSPR), contributing to their antimicrobial action by photocatalytic processes.[55]

The antibacterial activity of Ag NPs is largely attributed to their ability to release Ag^+.These ions interact with bacterial cell membranes, causing structural damage and interfering with vital processes, leading to cell death. The antibacterial efficacy of Ag NPs is closely tied to their size, with smaller particles exhibiting stronger activity due to their higher surface area, which facilitates greater ion release. This makes Ag NPs effective against a wide range of bacteria, including antibiotic-resistant strains, and has led to their use in medical coatings, wound dressings, and antimicrobial surfaces.

Three potential mechanisms of action for the antimicrobial activity of Ag NPs have been inferred. The first mechanism involves the generation of Ag^+ ions through the oxidation of the metallic Ag atoms constituting the

Ag Nanostructures. Compared to other nanostructures, Ag NWs have a high surface area, leading to greater Ag^+ ion production. Once released, these ions damage the bacterial cell membrane, bind to DNA denaturing it and inhibiting its replication, denature proteins, and decouple ribosomal subunits (Fig. 1.7), preventing nucleic acid transcription. Ag^+ ions also have a strong affinity for thiol groups in cysteine residues, facilitating interaction with respiratory chain proteins. [56]

Specifically, the interaction of Ag^+ ions with proton pumps blocks H^+ ion transfer and reduces the proton gradient within the cell, inhibiting ATP synthesis (Fig. 1.7). Additionally, Ag^+ ions can cause ion efflux and detachment of the cell membrane, leading to cell lysis. The second mechanism involves the formation of Reactive Oxygen Species (ROS) through the interaction of Ag^+ ions with thiol groups in the electron transport chain or by inhibiting enzymes that eliminate free radicals (Fig. 1.7). The third proposed mechanism is the mechanical action of Ag nanostructures adhering to the bacterial surface, causing membrane rupture by piercing effects (Fig. 1.7). [56, 57]

In addition to their antibacterial properties, Ag NPs demonstrate enhanced mechanical properties due to their small size and surface effects. At the nanoscale, materials like Ag NPs often show increased hardness and strength compared to their bulk counterparts, a phenomenon known as the Hall-Petch effect. This increased mechanical resilience makes Ag NPs suitable for their use in flexible materials and devices without compromising their structural integrity. Moreover, their small size allows them to be incorporated into various matrices, enhancing the mechanical properties of composite materials.

One of the key physical properties of Ag NPs is their high electrical conductivity, which remains remarkable even at the nanoscale. Although the conductivity may decrease slightly compared to bulk Ag due to increased surface electron scattering, they still exhibit exceptional conductivity, making them highly desirable for various electronic applications. The particle size and the presence of surface stabilizers, which prevent agglomeration, are crucial factors in preserving these conductive properties.

Another critical property is their thermal conductivity, which is similarly high like their electrical properties. However, this depends heavily on the quality of the NPs' crystalline structure. Defects such as grain boundaries or voids can reduce thermal conductivity, but well-synthesized Ag NPs with minimal imperfections exhibit superior heat transfer capabilities. This makes them particularly valuable for applications where efficient heat dissipation is required.

The LSPR effect in Ag NPs leads to strong light absorption and scattering, giving Ag NPs with unique optical characteristics, such as vibrant colors and the ability to enhance electromagnetic fields at their surface. The wavelength at which LSPR occurs is size-dependent, with smaller NPs resonating at shorter wavelengths and larger or shaped NPs (such as rods or triangles) shifting the resonance to longer wavelengths. This tunability of optical properties is highly useful for applications in sensing and imaging, where fine control over light interaction is required.

The chemical reactivity is another notable property, driven by their high surface area. As particle size decreases, the ratio of surface atoms increases, making Ag NPs highly reactive. This enhanced surface activity is especially beneficial for catalysis, where Ag NPs act as catalysts for a variety of chemical reactions. Furthermore, the surface of Ag NPs can be easily functionalized with different ligands, allowing their reactivity to be tailored for specific applications. Surface functionalization also plays a role in stabilizing the NPs preventing unwanted aggregation, thus preserving their reactive properties over time.

Lastly, their chemical stability is influenced by their size and surface environment. Although Ag is generally resistant to corrosion, NPs are more prone to oxidation, especially in the presence of air and moisture. However, this issue can be mitigated by using surface stabilizers or capping agents, which help protect the NPs from oxidation and aggregation, thereby extending their stability and functionality. Well-controlled synthesis methods can produce Ag NPs with enhanced chemical stability, allowing them to retain their beneficial properties over extended periods.

In conclusion, Ag NPs possess a unique combination of electrical, thermal, optical, chemical, and antibacterial properties, all of which are influenced by their nanoscale dimensions. Their high surface area and tuneable characteristics make them ideal for a wide range of applications, from electronics and catalysis to medical and sensing technologies. As research continues to advance, the ability to precisely control the synthesis of Ag NPs will further enhance their properties, opening the door to even more specialized uses.

1.2.2 Synthesis of colloidal Ag NPs: shape and size control

1.2.2a Synthesis of Ag NPs by colloidal approach. Among the various synthesis methods, chemical reduction remains one of the most effective and widely used techniques for the synthesis of Ag NPs. This method involves the reduction of Ag^+ to metallic Ag^0 in presence of a reducing agent, leading to the formation of NPs. The characteristics of the resulting Ag NPs, including their size, shape, and stability, are heavily influenced by the choice of the reducing agents, stabilizers, and reaction conditions. One common method to synthesize Ag NPs is by borohydride-mediated reduction, which produces Ag NPs. $NaBH_4$ is known for its strong reducing strength, which facilitates the rapid reduction of Ag^+ ions to metallic Ag, forming small, spherical NPs almost instantaneously. The concentration of $NaBH_4$ and the conditions under which it is introduced to the $AgNO_3$ solution can be manipulated to control the size and distribution of the NPs.[58] However, achieving NPs with high monodispersity and stability using this method has proven challenging, because $NaBH_4$ presents only a temporary stabilizing effect in forms of borohydride ions, specifically in the first step of the growth, evolving in borate ions by side reactions with water, detaching from the surface of the clusters and leading to aggregative/coalescence events.[59]

Another classical approach to synthesize Ag NPs is the citrate reduction method, which employs trisodium citrate (TSC) as both a reducing agent and stabilizer. [60]The weaker reducing agent TSC tends to produce relatively larger NPs with a broader size distribution and variations in shape, including undesired rods, cubes, and triangles. Dong et al. (2009) investigated this method in depth, focusing on how varying the pH of the reaction medium affects the size and morphology of the Ag NPs. Their research demonstrated that at higher pH levels, from 7.8 to 11.1, the reduction of $AgNO_3$ by citrate is more rapid, leading to the formation of spherical and rod-like particles. Conversely, at lower pH, from 5.7 to 7.8, the reduction is slower, resulting in the formation of triangular or polygonal NPs. They proposed a stepwise reduction strategy, where nucleation occurs under high pH conditions and growth under low pH, to achieve better control over NPs shape and size.[60]

To overcome the limitations encountered in the use of single reducing agents, a dual-reduction method employing both $NaBH_4$ and TSC has been developed. This co-reduction strategy offers better control over the nucleation and growth of NPs. By varying the reaction conditions, such as temperature and pH, it is possible to synthesize Ag NPs in a wide size range from 5 to 100 nm. For instance, an initial reduction using $NaBH_4$ at 60°C generates many Ag nuclei. At this stage, the primary process is the reduction of Ag^+, forming new nuclei, while Ostwald ripening is minimal. In the subsequent growth phase at higher temperatures, TSC-mediated reduction of unreacted Ag^+ occurs, further contributing to NPs growth. This approach ensures a better balance and control between nucleation and growth phases, leading to size-controlled synthesis of Ag NPs. The proposed dual thermal treatment encourages fast nucleation, followed by growth of Ag NPs at approximately the same rate, resulting in relatively monodispersed NPs. [61]

Analysing the reaction conditions for different sized Ag NPs, $NaBH_4$ demonstrated its predominant role for the synthesis of Ag NPs in the size range of 5–20 nm. On the other hand, TSC was the predominant reducing agent for the synthesis of Ag NPs in the range of 60–100 nm. For NPs in the size range of 25–60 nm, both $NaBH_4$ and TSC may work concurrently to reduce Ag^+ and form NPs. By varying the temperature, the reducing ability of $NaBH_4$ and TSC could be controlled to produce the most stable “initial” and “final” sols at 60°C and 90°C, respectively. The co-reduction approach provided a better balance between nucleation and growth of Ag NPs, thus enabling the synthesis of size-controlled Ag NPs. Moreover, the size and morphology could be precisely tuned by controlling the reduction rate during the second stage with an optimal pH of 10.5, which was maintained throughout for the synthesis of Ag NPs of various sizes.[61]

Overall, the synthesis of Ag NPs is a complex process that hinges on a delicate interplay between reduction and stabilization mechanisms. The choice of reducing agents, such as citrate and $NaBH_4$, and coordinating agents like PVP, alongside the optimization of reaction conditions, are critical in tailoring the properties of the NPs to meet specific application requirements. These studies underscore the importance of a nuanced understanding of the synthesis parameters to harness the full potential of Ag NPs.[62]

1.2.2b Synthesis of Ag NPs by photo-reduction under UV-light irradiation. The synthesis of Ag NPs through photo-reduction under UV-light irradiation is an efficient and environmentally friendly method. This process leverages the photoexcitation of electrons and the generation of free radicals when UV energy photons interact with water molecules or other reactants, facilitating reduction of Ag^+ ions to Ag in the presence of stabilizing agents.

UV light acts as a high-energy source, promoting electron transfer reactions that initiate reduction of Ag^+ ions without the need for chemical reducing agents. A key advantage of this method is its ability to control NP size, shape, and dispersion, by adjusting parameters such as wavelength, intensity, and exposure duration. This versatility allows the synthesis of Ag NPs not only in solutions, but also on surfaces for various applications.[63]

For instance, UV-light induced synthesis of Ag NPs on solid supports can create functional surfaces with enhanced properties. Huang et al. demonstrated this by successfully depositing Ag NPs onto a layered inorganic laponite clay matrix. The clay acted as both a stabilizing agent and a support structure, resulting in uniformly distributed NPs (10-30 nm), preventing agglomeration of the NPs thanks to the clay's layered structure, yielding to materials ideal for catalysis and antimicrobial applications.

Similarly, Ghosh et al. synthesized Ag NPs on polymer matrices by using Triton X-100 as a surfactant. UV-light irradiation promoted the formation of uniformly dispersed Ag NPs (10-20 nm), encapsulated by the polymer surfactant, making the system suitable for coatings of flexible electronic devices.

In another study, Sato-Berrú et al. explored the deposition of Ag NPs on silica and titania films, among other nanostructures. They investigated how different UV-light wavelengths influenced size and morphology of the NPs, finding that shorter wavelengths produced smaller, more uniform NPs (~15 nm), ideal for applications such as surface-enhanced Raman scattering (SERS) due to their plasmonic properties.

Additionally, UV-light induced reduction has been applied to organic polymer networks such as polyvinyl alcohol (PVA) and poly (acrylic acid) (PAA). Ag NPs were synthesized within a PVA matrix, where the resulting nanocomposites exhibited excellent stability and mechanical integrity, making them suitable for flexible electronics and antimicrobial coatings. Similarly, Ag NPs have been synthesized onto chitosan-based polymers; in these materials, the biocompatibility of chitosan, combined with the antimicrobial activity of Ag NPs, result in nanocomposites with potential use in biomedical applications, such as wound dressings and antibacterial surfaces.

The UV-light induced photo-reduction of Ag precursors in Ag NPs has been applied also in the modification of natural fibres like cotton. Cotton fabrics are cellulosic materials which have a negative zeta potential in neutral and alkali aqueous solutions owing to the carboxyl or hydroxyl groups in their chemical structure.[64] When the cotton fabrics were immersed into an Ag precursor solution, the Ag^+ ions adsorb and diffuse into the cotton fibre due to electrostatic interactions with the Ag^+ ions and negatively charged alcoholate and/or carboxylate groups in the cellulose chain. These attraction forces decrease the mobility of Ag^+ ions, enhance the formation of Ag nuclei and control their growth [65]. UV-light irradiation can directly induces photoreduction of Ag^+ onto the cotton fabrics functional groups ($OH^-$and COOH) which behave as coordinating sites and Ag NPs form by "heterogeneous nucleation".

Rehan et al. developed another UV-light irradiation technique to incorporate Ag NPs directly into cotton fabrics. By impregnating the cotton in an alcoholic $AgNO_3$ solution (100-500 ppm) and exposing it to UV light, Ag^+ ions were reduced *in situ* onto the cotton fibers. The use of alcoholic solution (10% methanol) is strictly required because methanol acts as a reducing agent. The formation of Ag NPs was confirmed by the fabric's color change, from bright to dark brown, indicating the reduction of Ag^+ and the formation of NPs. Increasing the Ag^+ concentration led to particle sizes between 50-100 nm, with aggregation dependent on the specific synthesis conditions. The overall reaction mechanism is shown below.[65]

$$Ag^{+} + H_2O + h\nu \rightarrow Ag^{0} + H^{+} + OH\bullet$$

$$OH\bullet + –CH2\ (OH) \rightarrow –CH\bullet\ (OH) + H_2O$$

$$Ag^{+} + –CH\bullet\ (OH) \rightarrow Ag^{0} + –CH{=}O + H^{+}$$

$$(Ag^{0})_{n} + Ag^{+} + –CH\bullet\ (OH) \rightarrow (Ag^{0})\ n_{+1} + –CH{=}O + H^{+}$$

$$(Ag^{0})\ n + (Ag^{0)\ m} \rightarrow (Ag^{0})\ n_{+m}$$

In other possible mechanisms, the cellulose monomer (glucose ring) can oxidize under UV-light, forming aldehyde groups that could reduce Ag^{+} ions into Ag evolving into carboxyl groups[65]. Yang and Freeman have reported that the UV-light irradiation is able to penetrate through the cotton fabric and causes photo-oxidation in its bulk and second layer. However, the surface of the cotton fabric that is exposed to UV-light irradiation shows the highest level of oxidation.[66] According to Yang and Freeman, the reduction process continues, leading to Ag NPs on both the surface and within the cotton fabric. Nevertheless, the reduction of Ag^{+} ions and the formation of Ag NPs are expected to be more concentrated near the surface than in deeper inside the fabric.

1.2.3 Applications of Ag NPs.

Among Ag nanostructures, Ag NPs, have widespread applications due to their exceptional physical and chemical properties, such as high thermal and electrical conductivity, antibacterial properties, and plasmonic effects.

The synthesis of Ag NPs can be controlled to achieve specific particle sizes and morphologies, making them highly suitable for diverse applications.

In electronic packaging, Ag NPs are utilized as bonding materials due to their ability to provide excellent thermal and electrical conductivity at relatively low sintering temperatures. One of the critical applications of Ag NPs is in the development of thermal interface materials (TIMs) for high-power electronic devices, where Ag NPs provide superior thermal and electrical conductivities essential for devices operating above 250°C, surpassing traditional solder materials like Sn-based alloys.

Controlled synthesis techniques, such as chemical reduction and thermal decomposition, yield Ag NPs with diameters between 13 and 30 nm, allowing for controlled agglomeration. In TIM applications, controlled agglomeration promotes low-temperature interconnection and results in sintered structures with properties akin to Ag bulk, such as high thermal conductivity and excellent shear strength.

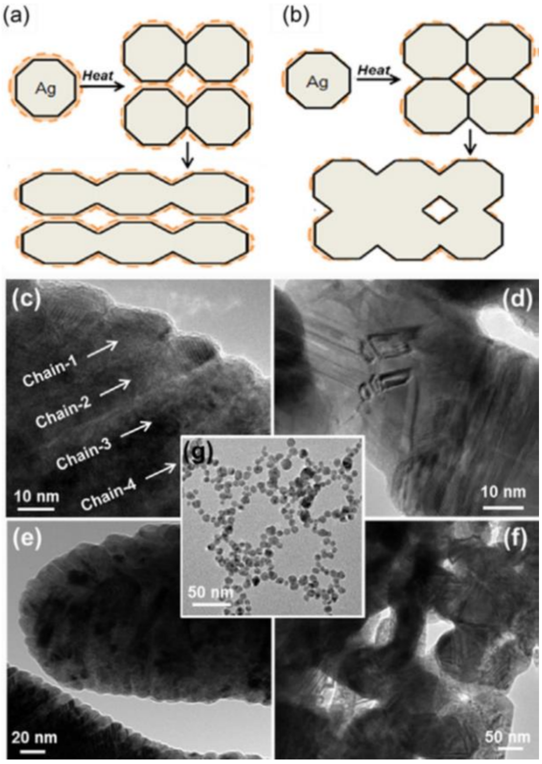

Fig 1.8.: *Schematic diagrams of the sintering process of Ag NPs with (a) thick organic shells and (b) thin organic shells. TEM images of Ag NPs sintered at 200°C for 20 min with (c) thick organic shells and (d) thin organic shells. (e) and (f) low magnification TEM images of (c) and (d), respectively. (g) TEM image of pristine Ag NPs.[67]*

Wang et al. (2013) demonstrated a sintering approach using Ag NPs with a mean diameter of 13 nm, achieving a thermal conductivity of 229 W/m·K.[67] However, challenges remain in addressing crystallographic defects like large- angle grain boundaries, which can negatively impact the thermal performance of sintered Ag NPs scattering phonon transfer.(Fig.1.8) *[67].*Research on bimodal Ag NP pastes has focused on combining small and large particles to improve stacking density, mechanical strength and thermal conductivity, helping to mitigate crystallographic defects and stabilize the structure under high-temperature operation. A bimodal Ag NPs paste, was synthesized by ultrasonic mixing of two types of unimodal Ag NPs, one with a diameter of 10 nm and the other 50 nm. The bimodal distribution optimizes the paste's properties, where smaller NPs act as fillers to enhance the initial packing density, while larger ones form a stable framework to reduce crystallographic defects. After sintering at 250°C for 30 min, the resulting structure exhibits high thermal conductivity of 278.5 W/m·K, reaching about 65% of the theoretical bulk Ag value (Fig.1.9). [68]

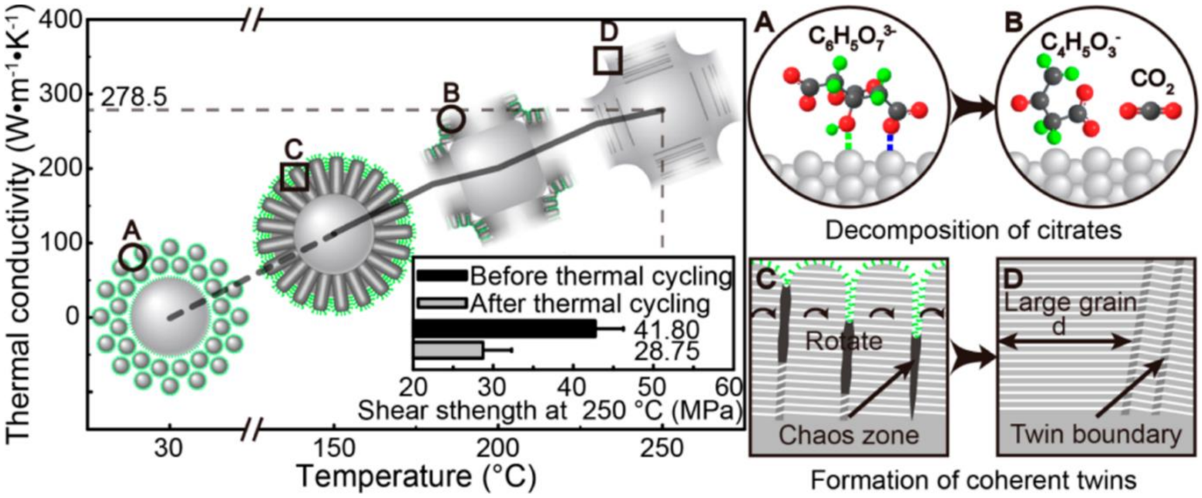

Fig 1.9: *Thermal conductivities of the three types of Ag NPs after sintering at 30−250 °C for 30 min (left panel). Shear strengths of sandwiched Ag NPs samples after initially sintering at 150−250 °C for 30 min and subsequently undergoing thermal cycling from 50 to 200 °C for 1000 cycles (insertion); Sintering evolution model of Ag NPs in Ag NP-BM paste:(a) before sintering and after sintering at (b) 120−180 °C, (c) 180−230 °C and (d) 230−250 °C.[68]*

The paste also demonstrates impressive shear strength, maintaining a shear strength of 28.75 MPa, even after 1000 thermal cycles between 50°C and 200°C, which ensures its structural integrity and performance under extreme conditions. This combination of high thermal conductivity and mechanical strength makes the Ag NPs paste particularly suitable as a thermal interface material (TIM) for high-temperature power devices, addressing limitations of traditional TIMs in electronic applications where operating temperatures exceed 250°C (Fig.1.9).[68]

In addition to these uses, Ag NPs have found significant application in photovoltaic devices due to their plasmonic properties embedded within the active layers of solar cells, Ag nanostructures trap light more effectively like antennas, improving power

conversion efficiency. NPs synthesized via chemical reduction methods have been employed in various types of solar cells, including dye-sensitized solar cells (DSSCs) and organic photovoltaic cells, where they enhance the absorption of light and improve charge transport across the device.

The great versatility of Ag NPs is also shown by their use in conductive inks for printed electronics. [69]Here, Ag NPs are synthesized to achieve very small particle sizes (typically below 10 nm) and are then dispersed in a solvent to create conductive inks that can be printed onto various substrates, including flexible plastics and papers. These inks, once sintered at low temperatures, form conductive pathways suitable for producing RFID tags, flexible circuits, and wearable sensors. The use of organic stabilizers during the synthesis ensures that the NPs remain well-dispersed, but as shown in Wang et al.'s study, these organic shells must be carefully controlled or removed during sintering to achieve the desired electrical properties without compromising the film's performance.

Paper-based electronics have gained significant interest recently, particularly due to their potential applications in flexible electronics. To achieve ultra-low resistivity, high concentrations of Ag NPs (up to 80 wt%) are essential. Recent work has demonstrated conductive inks based on Ag NPs treated by optimized sintering processes. After sintering at 120°C under 25 MPa pressure for 20 min, Ag NP based conductive tracks on paper exhibited a resistivity of 3.92×10^{-8} Ω·m, only 2.45-folds higher than bulk Ag, showcasing excellent electrical performance. [69]

These conductive tracks also retained strong mechanical flexibility, showing only a minor increase in resistivity, from 4.01×10^{-8} to 5.08×10^{-8} Ω·m after 1000 bending cycles. Paper-based substrates, which are lightweight, biodegradable, and foldable, have potential applications in flexible displays, RFID tags, batteries, solar cells, and biomedical devices. The integration of metal NPs conductive inks, especially Ag NPs, has been crucial for large-area flexible electronics due to their high electrical conductivity, resistance to oxidation and compatibility with low-temperature processing requirements.

Various methods for preparing and depositing nano-Ag inks nano-Ag have been explored, including inkjet printing, airbrush spraying, and sputter coating. However, these techniques have several limitations, such as high costs and environmental concerns. To address these challenges, innovative approaches like the pen-on-paper method have been developed. Innovative approaches like Lewis et al.'s pen-on-paper method provided a low-cost, portable fabrication technique for printed electronics and optoelectronic device

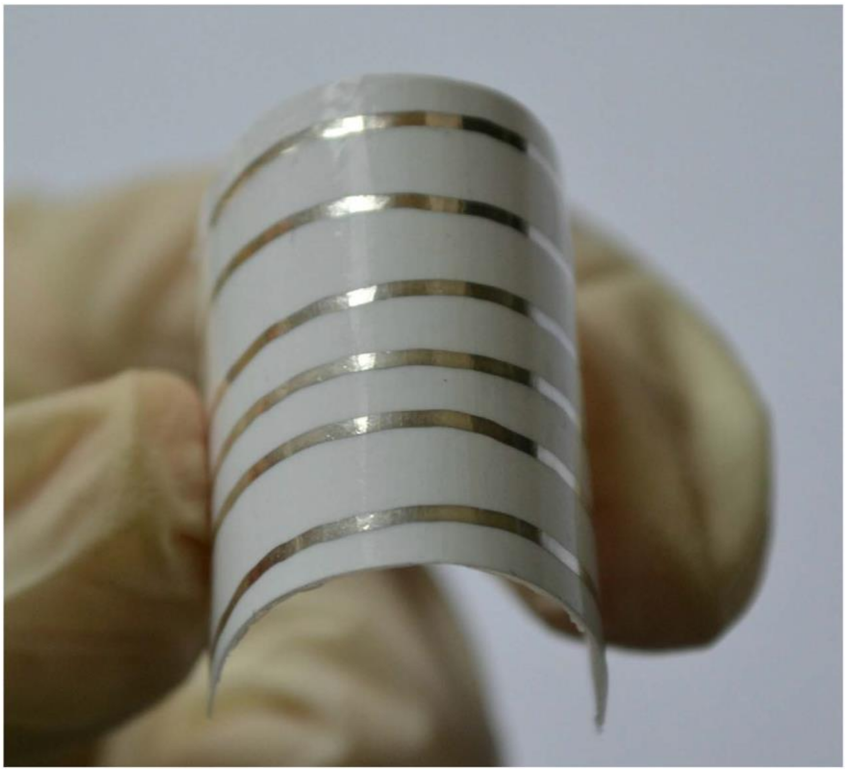

Fig. 1.10: *Digital image of a pattern written on paper substrate bending outwards by nearly 90° at the hot pressure sintering condition with the temperature of 120 °C, pressure of 25 MPa, and sintering time of 15 min.[69]*

Building upon this, Yang et al. (2012) developed an Ag NPs ink with 20 wt% solid loading, achieving a resistivity of 3.26×10^{-6} Ω·m after sintering at 200°C for 60 min. Liu et al. (2013) further improved the process, writing Ag nano-ink on sulfuric acid paper and sintering it at 180-220°C, achieving a resistivity of 2.1×10^{-6} Ω·m.

These innovations highlight the growing potential of Ag NP-based inks in creating high-performance, low-resistivity paper-based electronics suitable for flexible circuits, antennas, and sensors (Fig.1.10).

Ag NPs have also been employed in life sciences as therapeutic agents in photodynamic therapy for cancer treatment, [70] where they act as photocatalysts to produce ROS [71]. This broad-spectrum activity makes them suitable for applications in wound dressings, coatings for medical devices, and water filtration systems.

Due to their antimicrobial properties, Ag nanostructures are key components in various cosmetic and pharmaceutical formulations, such as creams and ointments for treating acne and dandruff, oral hygiene products, and deodorants that inhibit microbial growth, as well as in the production of sterile antimicrobial dressings.[62] The shape, synthesis method, and choice of capping agents are critical factors that influence the antimicrobial activity of Ag nanostructures. The effectiveness of these nanostructures in medical and environmental applications, therefore, depends on the careful design and precise control of synthesis parameters.

For example, capping agents like PVP and trisodium citrate not only stabilize NPs, but also control their growth into specific shapes. PVP commonly leads to the formation of rod-shaped NPs, which exhibit different antimicrobial properties compared to spherical or triangular NPs synthesized with other agents. Studies have shown that spherical Ag NPs, synthesized using $NaBH_4$ and trisodium citrate, demonstrate higher antibacterial activity against *Escherichia coli* and *Staphylococcus aureus* compared to triangular Ag nanoplates. [62] Ag NPs synthesized through a chemical reduction method using sodium citrate as a stabilizing agent have been shown to be highly effective against both *Gram-positive* and *Gram-negative* bacteria. This broad-spectrum activity makes them suitable for applications in wound dressings, coatings for medical devices, and water filtration systems.

Moreover, Ag NPs find large applications in sensing technologies, especially in Surface-Enhanced Raman Spectroscopy (SERS). The localized surface plasmon resonance (LSPR) of Ag NPs significantly enhances the Raman scattering of nearby molecules, making them extremely sensitive for detecting trace amounts of chemicals or biomolecules. SERS substrates created using Ag NPs synthesized via reduction methods have been successfully employed in environmental monitoring and medical diagnostics. The uniform distribution of NPs and the control over their size are essential for maximizing the enhancement effect, with smaller, well-dispersed particles providing better sensitivity.

1.3 Ag nanowires (NWs): properties, synthesis and applications

1.3.1 Properties of Ag NWs

Ag NWs are unidimensional (1D) structures characterized by diameters typically between 10 and 200 nm and lengths from 5 to 100 µm, [72]with aspect ratios ranging from 10 to 10^4 [45] which exhibit unique optical, electrical, and mechanical properties that make them highly valuable in numerous advanced technological applications,[73] such as transparent conductive films (TCFs), flexible electronics, sensors, and photovoltaic cells.[74, 75] These properties are largely determined by the NW's aspect ratio (the ratio of length to diameter), which is a critical parameter influencing both their electrical and thermal conductivity and transparency. The ability to synthesize Ag NWs with controllable diameters, from ultra-thin (17 nm) to thicker variants (up to 100 nm), allows for tuning these properties to match specific applications.

The optical properties of Ag NWs are governed by the phenomenon of LSPR, which arises from the collective oscillation of conduction electrons in response to an incident electromagnetic radiation.[76]This behaviour is especially pronounced in metallic nanostructures due to their high electron density. When light interacts with Ag NWs, the conduction electrons are polarized and oscillate in resonance with the electric field of the incident light, generating two key plasmonic modes: transverse plasmon resonance and quadrupole resonance.[77, 78]

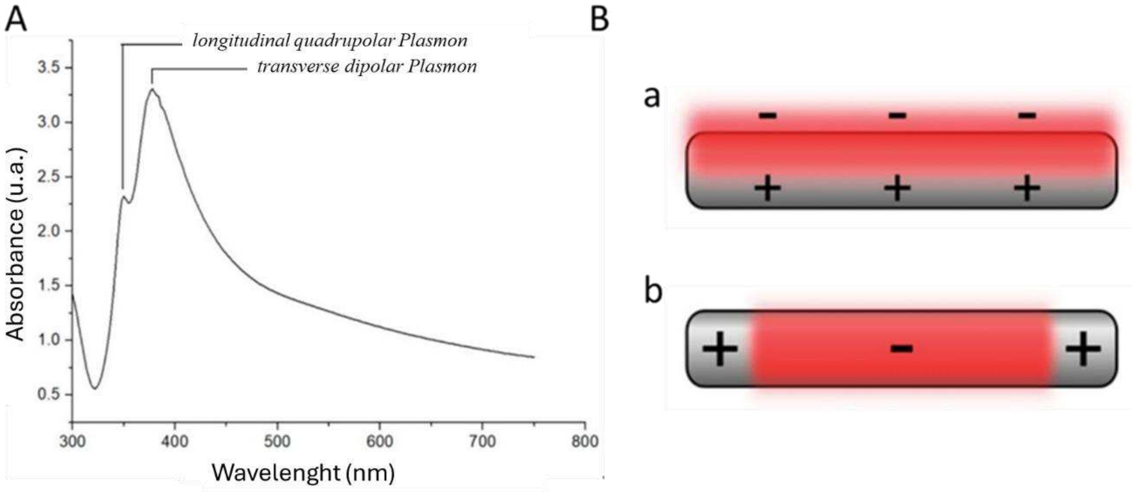

*Fig. 1.11: (A) UV-Vis absorption spectrum characteristic of Ag NWs. **(B)** General scheme of the electron cloud oscillation modes for **(a)** the transverse dipolar plasmon and **(b)** the longitudinal quadrupolar plasmon in NWs. The red area represents the electron cloud. [79]*

These modes are responsible for the strong light absorption observed in the UV-Vis spectrum, characterized by two distinct peaks in the UV region, typically with a narrow full width at half maximum, associated with the transverse plasmon, and a second peak at lower wavelengths, associated with the longitudinal quadrupolar plasmon (Fig. 1.11A).

In the excitation of the transverse dipolar plasmon, the electron cloud moves along the NW diameter, forming a transversely oscillating dipole (Fig. 1.12B).[79] In contrast, in the excitation of the transverse quadrupolar plasmon, half of the electron cloud moves parallel to the incident electric field while the other half moves antiparallel, creating a longitudinal oscillation along the NW (Fig. 1.11B). The resonance frequency of these two plasmonic peaks can be tuned by varying the diameter and length of the nanostructures.

The position and intensity of these peaks are directly related to the NW's geometry. The transverse plasmon resonance peak (λ_max) corresponds to the oscillation of electrons along the diameter of the nanowire, while the quadrupole resonance peak (λ_weak) results from higher-order oscillations along its length. The difference between these two peaks (Δλ = λ_max - λ_weak) serves as a key indicator of the NW's diameter. Empirical studies have shown that this relationship follows an exponential trend, which can be described mathematically as:

$$D_{nanowire} = 7{,}8409 \cdot e^{0.0651(\lambda_{max} - \lambda_{weak})}$$

where $D_{nanowire}$ represents the NW's diameter in nanometres. This equation provides a cost-effective method for estimating the diameter of Ag NWs, bypassing the need for high-resolution imaging techniques such as Transmission Electron Microscopy (TEM) or Scanning Electron Microscopy (SEM), which are both expensive and time-consuming. By analysing the UV-Vis spectra of Ag NW suspensions, researchers can quickly determine the NW diameter, making this technique highly useful for real-time process monitoring during synthesis.(Fig.1.12)[80]

Moreover, the absorption coefficient (ξ) of Ag NWs, which measures the efficiency of light absorption at a given wavelength, is found to decrease with increasing NW diameter. This effect can be attributed to enhanced light scattering by larger NWs, which causes a reduction in absorbance.*[80]* The relationship between the absorption coefficient and the Δλ value from the plasmonic peaks is given by the linear equation:

$$\xi = -0.6641(\lambda_{max} - \lambda_{weak}) + 31.66$$

Using this equation in conjunction with the Beer-Lambert Law (A = ξ bc), where A is the absorbance, b is the optical path length, and c is the concentration, it is possible to calculate the concentration of Ag NWs in solution. This information is critical for determining the yield of NWs synthesis and optimizing the process. For instance, by dividing the calculated concentration by the initial amount of Ag precursor, the reaction yield can be estimated with high accuracy *.[80]*

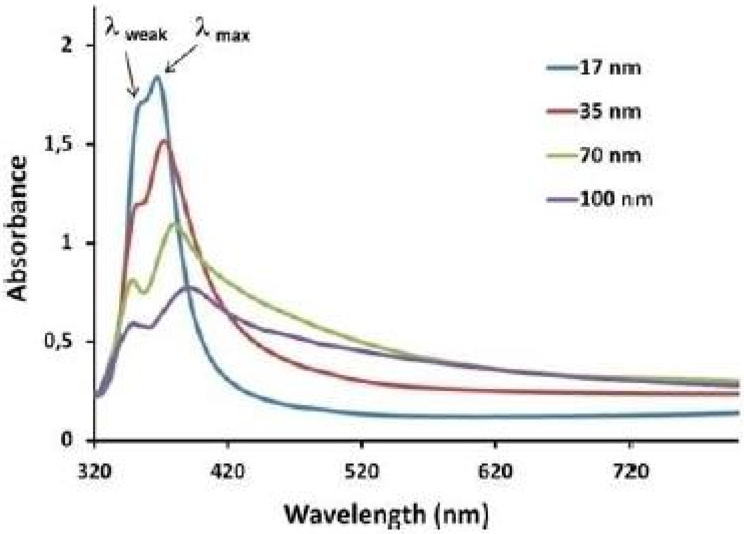

Fig. 1.12: *UV-Vis spectra of aqueous suspensions of Ag NWs with uniform diameters of average size of 17, 35, 70 and 100 nm.[80]*

Additionally, the mechanical properties of Ag NW networks, such as flexibility and stretchability, are also influenced by the diameter and aspect ratio of the NWs. Networks composed of ultra-thin NWs exhibit superior mechanical robustness, making them suitable for use in flexible electronics and wearable devices. The high aspect ratio ensures that a small number of NWs can form conductive paths across large areas, reducing the amount of Ag required and decreasing the overall cost of the material.

1.3.2 Synthesis of Ag NWs

The interesting chemical-physical properties of Ag NWs, which are closely dependent on the aspect ratio modulated by the synthesis approach, have led to the development of various synthesis procedures over the past two decades.

Historically, the synthesis of Ag NWs began with the reduction of Ag^+ ions on highly oriented pyrolytic graphite electrodes, though this method yielded NWs with low uniformity and aspect ratios. This led to the development of methods using hard and soft templates.[81] Hard templates, such as nanoporous membranes and carbon nanotubes, ensure the formation of highly ordered NWs by growing nanostructures within the template's pores through chemical or electrochemical reduction of Ag^+ ions. For example, X. Martin et al. utilized nanoporous alumina membranes to prepare NWs by coating them with a metallic Ag film, which was then used as a cathode in an electroplating process.[82] Similarly, D. Ugarte et al. filled carbon nanotubes with $AgNO_3$, which was converted to metallic Ag through electron beam irradiation, generating Ag NWs via thermolysis.[43, 83]

However, the removal of hard templates can be complex and might compromise the integrity of the NWs. To address this, soft template strategies have been developed, using surfactants, micelles, and polymers. These methods are generally conducted in water with ascorbic acid or $NaBH_4$ as a reducing agents[84]. Surfactants or polymers adsorb onto the surface of Ag clusters, controlling their growth through continuous adsorption and desorption. For example, X. Murphy et al. [84]proposed the use of cylindrical CTAB micelles as soft templates, while C. Wang et al. [85]synthesized Ag NWs using sodium dodecyl sulfate (SDS) micelles dispersed in 1-octanol. After adding $AgNO_3$ and irradiating the mixture with UV light, the resulting nanostructures were purified and dried, yielding NWs with lengths of approximately 2.5 μm and diameters between 20 and 30 nm.

DNA also serves as a soft template, owing to its unique structure and ability to facilitate supramolecular interactions. X. Braun et al. employed DNA to direct Ag NW synthesis by immobilizing Ag^+ ions on the helices through ion exchange and subsequent reduction.[86-88]

Despite these advancements, the soft template approach still encounters challenges such as irregular morphology, polycrystallinity, and low aspect ratios of the nanostructures. Template removal is often complex, and the yield of NWs is typically low, which limits the scalability of the process.

As an alternative, one among the most prominent method is the solvothermal process,[89] known for its simplicity, scalability, high yield, and ease of controlling reaction conditions. This method involves synthesis in water or alcohol within an autoclave heated up to temperatures between 80°C and 200°C under controlled pressure. For instance, B. Bari et al. [55]applied this method by injecting a NaCl solution dropwise into a mixture of $AgNO_3$, PVP, and glucose, and then letting the reaction to proceed in an autoclave at 160°C for 22 h. The resulting NWs exhibited high aspect ratios, with lengths between 200 and 500 μm and diameters between 45 and 65 nm.

1.3.2a Polyol synthesis of Ag NWs. The polyol synthesis is one of the most widely used methods for the large-scale preparation of Ag NWs with high crystallinity. This method was originally developed by Xia's group to produce Ag nanostructures with controllable morphologies, including cubes, wires, and spheres.[37, 88]

The process is conducted at elevated temperatures, utilizing polyols—multivalent alcohols with high boiling points—as reducing agents for the metal precursor. The most used polyol is ethylene glycol (EG), which serves both as a solvent and reducing agent. In addition, a polymeric coordinating agent such as poly(vinylpyrrolidone) (PVP) is used to induce the anisotropic growth of nanostructures and to stabilize the final NWs, preventing their aggregation[90].

The use of polyols offers significant advantages. [91]Their high boiling points enable the synthesis of nanostructures at high temperatures without the need for high-pressure equipment. Polyols also act as chelating agents, allowing controlled nucleation and growth of NPs, leading to monodisperse NPs with uniform shapes and sizes. Moreover, the high reducing strength of EG at elevated temperatures facilitates the rapid reduction of $AgNO_3$, the primary source of Ag^+ ions, into Ag atoms.

This method can also accommodate the use of simple and economical metal precursors, further increasing its appeal for large-scale synthesis.

In X. Xia et al.'s approach[90] , ethylene glycol (EG) was used both as a solvent and as a reducing agent, PVP as a stabilizing agent, and $AgNO_3$ as the source of Ag^+ ions. In the early stages of this research, Pt NPs were used as seeds for the heterogeneous nucleation of Ag NWs [92]. Specifically, the process involves two stages: in the first stage, Pt nuclei generate by reduction of platinum (II) chloride ($PtCl_2$) with EG at 160°C, and in the second stage, the Ag precursor is added into the reaction solution, and it is then reduced by EG. X. Xia et al. hypothesized that Pt seeds separate from the nanostructures as Ag reacts during nucleation and growth, while PVP promotes anisotropic growth by selectively binding to certain faces of the growing clusters. However, the high cost of Pt and the two-stage approach limit the applicability of this strategy on an industrial scale.

To overcome these limitations, Xia et al. later developed a self-seeding process, where the concentration of $AgNO_3$ was kept low, and its injection rate was carefully controlled using a syringe pump.[93] This approach resulted in the slow and controlled nucleation of Ag NWs, eliminating the need for expensive Pt seeds.

Recent studies have shown that the addition of inorganic salts such as Fe(II) or Fe(III) salts, Cu(I) or Cu(II) chlorides, potassium bromide (KBr) or sodium bromide (NaBr), and sodium chloride (NaCl) can further optimize the growth and morphology of Ag NWs by stabilizing the nanoclusters and slowing down the reduction kinetics.[94, 95] In these syntheses, $AgNO_3$ is the primary source of Ag^+ ions, which are reduced to metallic Ag by EG at temperatures above 150°C, as shown in the reaction:

$$2HOCH_2CH_2OH+O_2\rightarrow 2HOCH_2CHO+2H_2O$$

And the generation of glycolaldehyde from EG at these temperatures is crucial for reducing Ag^+ ions to Ag atoms.

According to Wiley et al. [90], who introduced a standard procedure for polyol synthesis of Ag NWs, chloride ions (Cl^-) from NaCl facilitate the growth of Ag NWs in two ways: first, by stabilizing clusters through electrostatic interactions, and second, by reducing the concentration of Ag^+ ions and thus Ag metal cluster monomers in the reaction environment by forming AgCl, which is poorly soluble in polyols. This eliminates the need for the syringe pump used by Xia et al. and regulates the release of Ag^+ ions into the reaction environment preventing the rapid supersaturation of the solution and promoting the growth of high aspect ratio NWs. Studies have demonstrated that the optimal NaCl concentration for this process is 12 μM, which allows the formation of well-defined Ag NWs while minimizing the production of undesired byproducts, such as micrometer-sized Ag particles.

Although the details of this procedure have been subjected to further modifications by various researchers, two fundamental factors have proven crucial for producing Ag NWs in high-yields. First, measures must be taken to prevent the reaction medium from becoming rapidly supersaturated with Ag seeds. Second, oxidative etching on the surfaces of growing Ag NWs must be prevented. This modified method has been widely adopted by many research groups for the synthesis of Ag NWs.

Furthermore, the rate of injection of Ag^+ into the solution significantly affects the morphology of the resulting nanostructures. At lower injection rates (around 5 mL/h), Ag^+ ions are slowly introduced into the reaction, limiting the number of the formed nuclei, and promotes the growth of longer and thinner NWs.[96] Conversely, higher injection rates lead to the rapid formation of Ag nuclei, resulting in shorter, thicker NWs or irregular particles due to supersaturation.

In addition to injection rate, the temperature plays a pivotal role in determining the final NW dimensions. As shown by the parametric study, increasing the reaction temperature from 150°C up to 200°C leads to longer NWs, with an optimal temperature of 170°C for achieving high yields of NWs with diameters around 62 nm and lengths up to 50 μm.

Stirring rate is another critical factor, as it affects the homogeneity of the solution. A stirring rate of 1000 rpm ensures uniform distribution of Ag^+ ions throughout the solution, leading to the consistent formation of NWs. Lower stirring rates result in larger diameters due to localized accumulation of Ag atoms, which form larger particles. However, excessively high stirring can cause fragmentation of the NWs, reducing their length and uniformity.

For example, by maintaining the temperature at 130°C and controlling the stirring speed, it was possible to achieve NWs exceeding 60 microns in length. The research showed that slower stirring favoured the formation of longer NWs, while higher speeds disrupted the one-dimensional growth and resulted in shorter wires. At extremely slow speed or no stirring, wires as long as 100 microns were produced, with consistent diameters of around 60 nm. This study also highlighted that maintaining a stable growth environment without excessive mechanical disruption facilitated the uniform deposition of Ag atoms along the wire's length, thereby avoiding the formation of NPs or other unwanted shapes.[55]

In a study, a seedless, surfactant-free polyol process where Ag salt was reduced using sodium citrate in the presence of sodium hydroxide (NaOH) was reported. The addition of NaOH played a pivotal role in directing the growth of NWs instead of spherical particles by stabilizing specific facets of the Ag, yielding Ag NWs up to 12 microns long. It was observed that the NaOH concentration strongly influenced the morphology of the Ag structures: without NaOH, irregular particles formed, while higher NaOH concentrations led to fewer but longer NWs. This suggests that the hydroxide ions not only participate in reducing Ag but also control the crystal growth direction.[97]

A variation of the polyol method, reported in another study, used a hydrothermal synthesis approach to produce very-long Ag NWs, up to 500 microns in length with diameters in the range of 45-65 nm. This method employed glucose as a reducing agent and AgCl as the Ag source. The slow reduction of Ag^+ ions by glucose allowed for controlled one-dimensional growth, while the presence of Cl^- ions helped to regulate the reaction kinetics. PVP was used as a surfactant to cap the NWs and prevent them from aggregating during the reaction. The slow, steady release of Ag^+ ions in the reaction was crucial in promoting elongation of the NWs, as the gradual deposition of Ag atoms facilitated continuous growth along a single axis. This method produced NWs with remarkably high aspect ratios, suitable for applications requiring both high conductivity and transparency.[96]

Another work reports a modification of the polyol process, with the addition of copper chloride ($CuCl_2$) to further control the growth of Ag NWs by acting as a co-catalyst. The $CuCl_2$ helped to mediate the reduction of Ag^+ ions, resulting in more uniform NWs with controlled diameters and lengths. The introduction of halides like Cl^- ions has been shown to significantly influence the aspect ratio of Ag NWs by controlling the nucleation rate and slowing the reduction process, allowing for more precise growth.[98]

In conclusion, the polyol method offers several advantages for the synthesis of Ag NWs, including scalability, cost-effectiveness, and the ability to fine-tune NWs morphology by adjusting parameters such as temperature, injection rate, salt concentration, and stirring rate. These factors are crucial for producing Ag NWs with the desired aspect ratio and crystallinity, making them suitable for applications in transparent conductive films, flexible electronics, and antimicrobial coatings.

1.3.3 Applications of Ag NWs

Ag NWs have a broad range of applications, thanks to their unique properties such as high electrical conductivity, optical transparency, and remarkable plasmonic properties. These characteristics make Ag NWs ideal for use in flexible electronics, touchscreens, optoelectronic devices, and Surface-Enhanced Raman Spectroscopy (SERS) sensors.[79]

A significant application in which Ag NWs are utilized is in transparent conductive films, which are essential for devices like touchscreens, organic photovoltaic cells, and OLED displays. Ag NW-based films offer high transmittance (over 90%) and low sheet resistance (below 10 Ω/sq), while also being more flexible and cost-effective than traditional materials like indium tin oxide (ITO). Their mechanical flexibility makes them particularly suited for next-generation bendable electronics, where maintaining performance under deformation is critical. In solar cells, Ag NWs serve as transparent conductive electrodes, offering enhanced durability compared to ITO and making them ideal for flexible solar panels.

A key advantage of using long Ag NWs is that they minimize the number of junctions between individual wires, directly enhancing the electrical conductivity of the films. In contrast, shorter NWs typically require more intensive post-synthesis treatments—such as high-temperature annealing, mechanical pressing, or laser welding—to fuse these junctions and reduce contact resistance. Post-synthesis treatments like thermal annealing or mechanical pressing are generally used to further improve the contact between wires, enhancing the overall performance of Ag NW networks in flexible electronics. However, the synthesis of longer NWs significantly reduces the need for such treatments, streamlining the manufacturing process. [55]

Hydrothermal synthesis methods enable the production of long Ag NWs (over 200 microns), which form conductive networks without the need for additional post-processing. This capability not only simplifies large-scale production but also helps maintain the integrity of Ag NW networks, making it a cost-effective solution for the development of flexible electronic materials. The reduced reliance on post-synthesis treatments ensures that both conductivity and transparency remain high, without compromising the structural performance of the NWs films (Fig.1.13).[55]

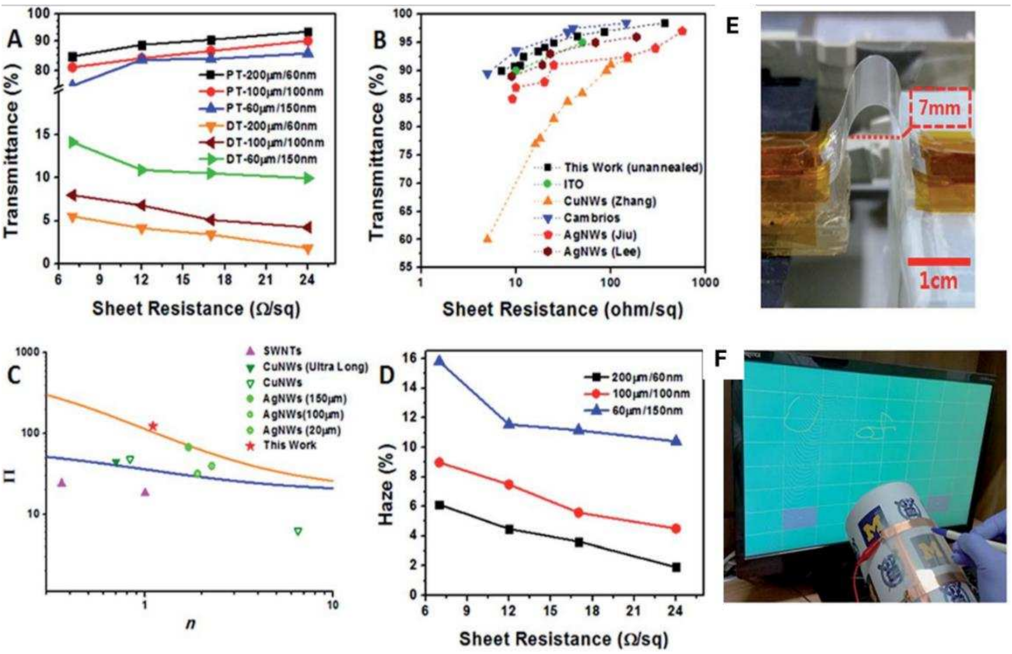

Fig.1.13: *(A) Parallel and diffusive transmittance of various Ag NW transparent electrodes. (B) Comparison of opto-electrical properties of the fabricated Ag NW network with recently published results on ITO, Cu NW, Cambrios, Ag NW and Ag NW. (C) Percolative figure of merit (Π), plotted against conductivity exponents (n). The solid lines indicate the value of Π required to give certain combinations of T and Rs. Blue and orange color lines represent 100 Ω sq^{-1} with 90% transmittance and 10 Ω sq^{-1} with 90% transmittance. (D) Haze analysis of various Ag NW transparent electrodes. (E) DC image of the bending test; (F) flexible touch panel on a cylindrical surface.[55]*

The benefit of using long NWs is particularly relevant in flexible and stretchable electronics, where Ag NW networks are integrated into substrates like polyethylene terephthalate (PET) or polyimide (PI). These substrates allow devices to maintain electrical performance even when subjected to mechanical deformations such as bending, twisting, or stretching. This capability is critical for wearable technologies and bioelectronic devices, where the durability and functionality of the device depend on the Ag NWs' ability to form stable conductive pathways that remain intact under mechanical stress. By maintaining conductivity and flexibility, Ag NW-based films offer a robust solution for the next generation of flexible electronic devices.

However, at high concentrations and in suited deposition conditions, Ag NWs exhibit a LSPR absorption over a wide spectral range, from UV to IR,[54] [99] resulting from light-trapping phenomena caused by hotspots formed at the intersections of overlapping Ag NWs [100] making them interesting in the detection of (bio)molecules [76, 77]by SERS with single-molecule sensitivity. Ag NWs create "hot spots" where the electromagnetic field is significantly amplified, thus increasing the sensitivity of the SERS technique. Another effective method to enhance SERS performance and generate additional active hot spots is through chemical etching of plasmonic nanostructures. The number of SERS-active hot spots is critical for achieving high sensitivity in SERS-based sensing. One promising approach is to increase the surface roughness of Ag NWs by applying a targeted chemical etching process, designed to create more SERS-active hot spots along their length. In this method, Ag NWs are first synthesized using the polyol process and then etched with a mixture of NH_4OH and H_2O_2. This etching creates "beads on a string" features, significantly enhancing their surface roughness[101] while preserving the NWs' crystallinity (Fig.1.14). Single-NWs SERS mapping shows that this method overcomes the limitations of conventional one-dimensional Ag NWs, which typically have SERS activity only at the tips, by producing etched NWs with an increased number of hot spots and polarization-independent SERS signals over tens of micrometers in length.

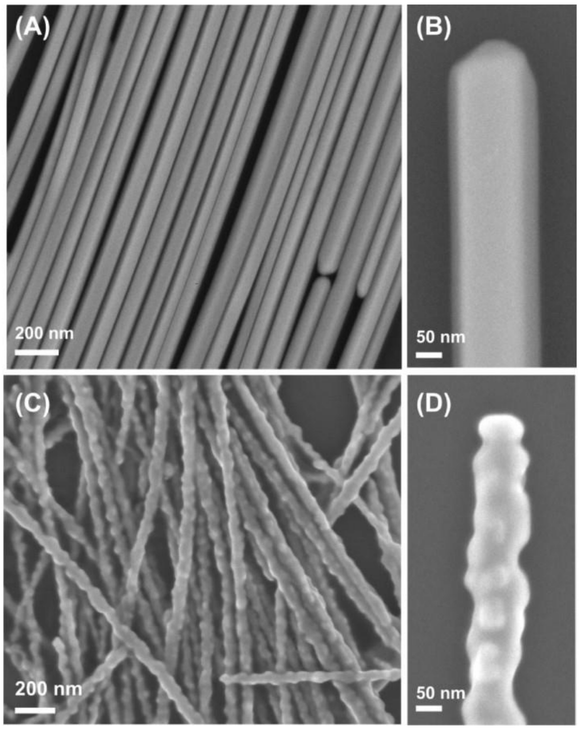

Fig. 1.14: *SEM images of (A, B) as-synthesized and (C, D) chemically etched Ag* NWs.[101]

Additionally, Ag NWs have found applications in biosensing and biomedical devices,[56] particularly for creating conductive and biocompatible surfaces. Ag NWs are incorporated into flexible sensors that can monitor physiological parameters like body temperature, heart rate, or glucose levels in real time. Their high conductivity and flexibility make them ideal for use in wearable sensors that require constant contact with the human body.[102] Furthermore, Ag NWs have been explored for use in antibacterial coatings due to Ag's well-known antimicrobial properties. Ag NWs synthesized by the polyol approach, starting from the reduction of $AgNO_3$ by EG, in presence of sodium chloride (NaCl) and PVP, present enhanced antibacterial activity due to their unique morphology and large aspect ratio, facilitating better interaction with bacterial membranes. Specifically, these Ag NWs show significant antimicrobial efficacy against *Pseudomonas aeruginosa*. The incorporation of Ag NWs into medical devices or wound dressings could provide a dual function—both monitoring and reducing bacterial infections.

Ag NWs are effective electrocatalysts for the reduction or oxidation of molecules in which their electrical conductivity enhances electrocatalytic performance of the electrodes.[94, 103] The advantage of their application in this field comes from their high surface-to-volume ratio, which, combined with the catalytic action of nanostructured metallic Ag in specific electrochemical processes, leads to a significant increase in reaction kinetics. [76] An example of this application is presented by X. Linge et al. [104] who developed a carbon electrode decorated with Ag NWs for catalysing oxygen reduction reaction, a critical process in fuel cells.

Chapter 2

2.1 Graphene: properties and preparation synthesis

The discovery of graphene and its properties in 2004 earned the physicists Andre Geim and Konstantin Novoselov the Nobel Prize in Physics in 2010. Graphene has attracted intense interest across multiple scientific disciplines, including physics, chemistry, and materials science, due to its unique exceptional physical, chemical, and mechanical properties.[105] With a theoretical surface area of approximately 2630 m^2g^{-1}, graphene's high intrinsic mobility (up to 200,000 $cm^2v^{-1}s^{-1}$), Young's modulus (~1.0 TPa), and remarkable thermal conductivity (~5000 $Wm^{-1}K^{-1}$) set it apart from other materials. These characteristics, coupled with its high optical transmittance (97.7%) in the visible spectral range and excellent electrical conductivity, make graphene a promising material for applications ranging from transparent conductive electrodes to high-performance sensors and capacitors, energy storage devices, membranes, and batteries. [106-108]

Graphene is a two-dimensional monoatomic layer of sp^2-hybridized carbon atoms arranged in a crystalline honeycomb structure, which has a planar conformation with a thickness of about 0.34 nm. In this lattice, each carbon atom is bonded to its adjacent atom via strong σ bonds and has a π orbital perpendicular to the plane, contributing to the network of delocalized electrons that give to graphene remarkable properties.

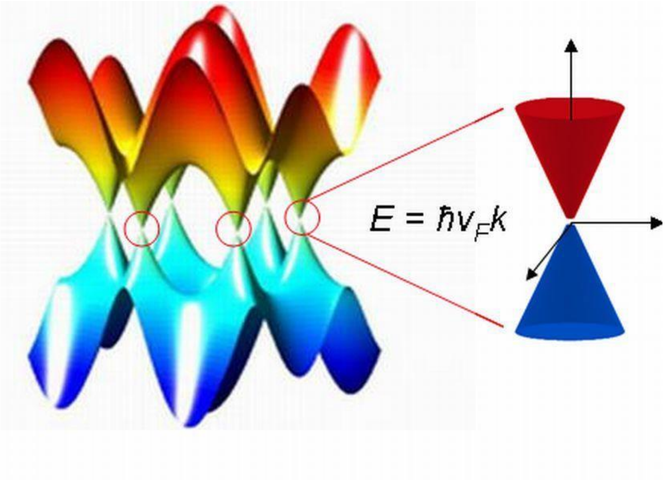

Fig. 2.1*: Energy bands associated with the sublattices intersect at zero and give rise to conical sections of the energy spectrum.*

However, despite graphene's theoretically perfect structure, real graphene often contains various defects such as topological defects, vacancies, adatoms, and cracks. These defects can be intentionally introduced through techniques like electron irradiation, or they can occur naturally during the synthesis process.

Graphene's electronic properties are governed by its unique band structure, which is a direct consequence of its planar geometry and electronic configuration of the carbon atoms. In pristine graphene, electrons behave as relativistic particles, following a linear dispersion relation near the Dirac points (the K and K' points in the Brillouin zone). [4]

The energy dispersion relation is described by:

$$E(k)= \pm \hbar \nu_F |k|$$

where E is the energy of the charge carriers, k is the wave vector, ν_F is the Fermi velocity, approximately 1×10^6m/s, $\hbar$ is the reduced Planck constant.

At the charge-neutral points, known as Dirac points, its electronic properties exhibit a linear energy-momentum relationship, which results in massless Dirac fermions. The tight-binding model provides a description of this band structure, which leads to extraordinary electron mobility and ambipolar field effects.

In fact, near the Dirac points, the conduction band, which results completely empty, and the valence band, which is completely full, touch at a single point, resulting in a zero bandgap and the graphene density of states (DOS) [4] near this point follows a linear relation with energy as in the following:

$$D(E)= 2|E| / \pi(\hbar \nu_F)^2$$

These properties lead to unique electronic properties such as ballistic charge transport, where electrons can move through the material without scattering over relatively long distances, and high carrier mobility, which can reach values exceeding 200.000 $cm^2V^{-1}s^{-1}$ at low temperatures (Bolotin et al., 2008) and values of up to 15.000 $cm^2 V^{-1} s^{-1}$ at room temperature (Novoselov et al., 2004). [4]

Conventionally, the Fermi Energy E_F in graphene is dependent on the charge carrier density n and is given by:

$$E_F = \hbar \nu_F (\pi \mid n \mid)^{1/2}$$

These properties allow graphene to function as a semimetal or a zero-bandgap semiconductor, enabling applications in field-effect transistors (FETs) where charge carriers can be tuned between electrons and holes.

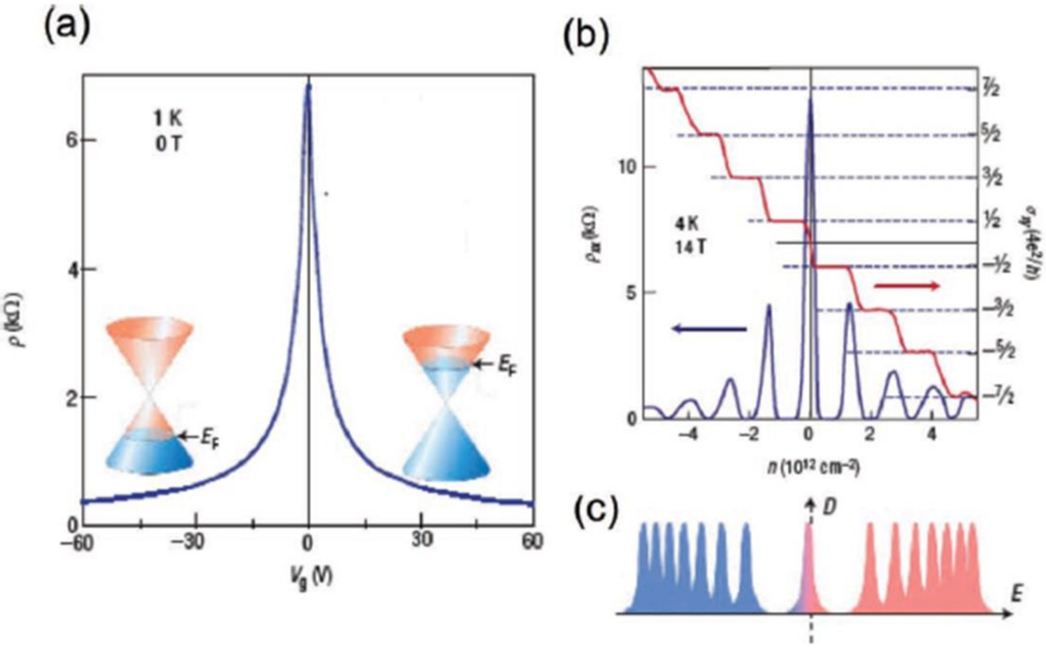

Fig. 2.2: *(a) Ambipolar electric field effect in monolayer graphene. The insets show the changes in the position of the Fermi level energy* E_F *with changing gate voltage* V_g *; (b) The hallmark of massless Dirac fermions is QHE plateau in* σ_{xy} *at half integers of* $4e^2/h$ *; (c) Landau levels in the density of states D in graphene are described by* $E_N \alpha \sqrt{N}$ *for massless Dirac fermions.*

This ambipolar electric field effect consists of the inversion of the charge carrier sign based on the applied gate voltage in field-effect transistors (FETs) or the charge transferred to graphene, and mobility values that do not decrease at high carrier concentrations, as they are not scattered over sub-micrometric distances (up to ~0.3 mm at 300K).

The conductivity of graphene as a function of the gate voltage V_g is given by:

$$\sigma(Vg) = \frac{e^2 \mid n(Vg) \mid}{h\mu}$$

where e is the elementary charge, h is Planck's constant, $n(V_g)$ is the charge carrier density, which can be tuned by the gate voltage, μ is the mobility of the charge carriers. [4]

Graphene's thermal properties are equally impressive, with a reported thermal conductivity of up to 5000 $Wm^{-1}K^{-1}$ for suspended monolayer graphene. This value is much higher than that of traditional materials like copper and makes graphene an excellent candidate for heat dissipation in electronic devices. The high thermal conductivity is attributed to phonon transport, due to the low density of electronic states near the Fermi level. Heat transport in graphene is primarily governed by acoustic phonons, with thermal conductivity showing a ballistic transport regime at low temperatures and a diffusive regime at higher temperatures. The thermal conductivity κ can be estimated using the Boltzmann transport equation:

$$\mathrm{k} = \frac{1}{A}\sum_{\lambda}\int \hbar\omega_{\lambda}v_{\lambda}(q)v_{\lambda}(q)\tau_{\lambda}(q)\frac{\partial f_0}{\partial T}dq$$

where λ represents the phonon mode, ω_λ is the phonon frequency, $v_\lambda(q)$ is the group velocity, $\tau_\lambda(q)$ is the phonon relaxation time, f_0 is the Bose-Einstein distribution. [4]

One of the most notable observations of graphene's electronic behavior is the quantum Hall effect (QHE), which can be observed even at room temperature, a phenomenon attributed to the material's massless Dirac fermions. The half-integer QHE has been confirmed experimentally, providing further insight into graphene's potential as a material for quantum devices. The Hall conductivity in graphene is quantized and can be expressed as:

$$\sigma_{xy} = \frac{\pm 4e^2}{h(N + \frac{1}{2})}$$

where *N* is the Landau level index. The half-integer quantization is a direct consequence of the massless Dirac fermions and their two-fold valley degeneracy. [4]

Graphene also demonstrates exceptional mechanical properties. Nanoindentation experiments using atomic force microscopy (AFM) have shown that defect-free monolayer graphene possesses a Young's modulus of approximately 1.0 TPa and a fracture strength of 130 GPa. The strength of graphene arises from the covalent sp^2 bonds that form between carbon atoms in the hexagonal lattice. Tensile strain can be applied to graphene without causing rupture until reaching strain levels of up to 20% (Lee et al., 2008). These mechanical properties are further enhanced when graphene is chemically modified, such as through hydrogenation or functionalization with NPs, leading to potential applications in flexible electronics and ultra-strong composites. Raman spectroscopy is often used to characterize graphene, providing insights into its defect density, number of layers, and strain. The Raman spectrum of graphene includes distinct G and 2D peaks, which are sensitive to changes in graphene's structure and environment. These peaks shift in response to mechanical strain and electron-phonon coupling, offering a non-invasive method for analysing graphene's mechanical and electronic properties. [4]

Its optical properties are characterized by a constant high-frequency conductivity and transparency across the visible spectrum. The material's high optical transmittance (~97.7%) makes it an ideal candidate for transparent conductive films, a key component in touch screens, solar cells, and other optoelectronic devices. Graphene's transparency decreases linearly with the number of layers, making it possible to fine-tune the optical properties of multilayer graphene structures for specific applications.

Several methods have been developed to produce high-quality graphene, each with distinct advantages and limitations. The synthesis approach of graphene and its derivatives significantly impacts the resulting material's properties, including number of layers, size, defect density, and surface chemistry, which in turn affect its suitability for specific uses. Graphene can be synthesized through various methods, including micromechanical exfoliation of graphite, chemical vapor deposition (CVD) on polycrystalline catalytic substrate, epitaxial growth on SiC substrate (known as SiC graphitization) and the reduction of graphene oxide.

Micromechanical exfoliation of graphite, commonly known as the "Scotch tape method", is the simplest method used to isolate monolayer graphene flakes. This technique involves applying a force of about 300 nN lm^{-2}, greater than the van der Waals force (2 eV/nm^2) that binds the graphite sheets, to the surface of highly ordered pyrolytic graphite (HOPG) crystals to detach and exfoliate the crystalline layers until a single layer is obtained. Initially, the interaction of AFM (Atomic Force Microscopy) and STM (Scanning Tunnelling Microscopy) tips with the HOPG surface was exploited to provide sufficient energy to overcome the interplanar attraction forces and remove a monolayer of polycrystalline graphene. Subsequently, K. Geim et al. developed the method based on the use of the scotch tape, in which an adhesive tape is used to exfoliate HOPG.[107] The technique involves placing an adhesive tape on the surface of a graphite crystal, peeling off the tape along with several layers of material, and repeating the process to obtain thinner layers, until thin flakes adhered to the tape can be transferred to an insulating substrate. This method allows for the isolation of monolayer graphene with high crystalline quality, but only on a micro- and nanometric scale. Therefore, the graphene obtained is generally used for fundamental studies. The samples prepared in this way exhibit the best electrical and mechanical properties, but due to limited scalability, this method is less suitable to produce graphene for industrial electronic applications.

Chemical vapor deposition (CVD) is one of the most promising techniques for scalable graphene production. In this process, hydrocarbons such as methane are decomposed at high temperatures on metal substrates like copper or nickel, leading to the growth of large-area graphene films.[81] The choice of the substrate is crucial in determining the quality and number of graphene layers. Copper is commonly used due to its low carbon solubility, which promotes the growth of monolayer graphene. In contrast, nickel tends to produce multilayer graphene as carbon atoms dissolve into the metal at high temperatures and precipitate out during cooling.

Notably, Bae et al. (2010) demonstrated the large-scale production of 30-inch graphene films using CVD on copper, which were subsequently transferred onto flexible substrates for use in touchscreens. This method involves growing graphene on a catalytic substrate at high temperatures (800-1000°C) in a controlled atmosphere using a gaseous hydrocarbon precursor. The use of copper sheets as a catalyst has been shown to yield polycrystalline graphene with high crystalline quality and charge mobility, with a 95% yield of monolayer graphene. While the process is complex and costly, it is currently the most widely used method for the large-scale production of macroscopic graphene sheets, making it highly suitable for industrial electronic applications.

Chemical approaches are, in principle, more accessible, less expensive, and highly versatile, because they allow for the deposition of graphene from solution onto various substrates. They also enable chemical decoration of its basal plane or incorporation into polymers for the preparation of multifunctional hybrid materials and nanocomposites. The main challenge of these processes lies in isolating single atomic layers, which requires time consuming exfoliation and separation techniques leading typically to low yields of mono layer graphene.

Liquid-phase exfoliation is another method that has gained attention for its scalability and cost-effectiveness. In this process, bulk graphite is exfoliated into graphene sheets in a liquid medium using ultrasonic energy.

[109]Surfactants or solvents such as N-methyl-2-pyrrolidone (NMP) are typically used to stabilize the exfoliated graphene and prevent reaggregation. Liquid-phase exfoliation can produce large quantities of graphene, although the resulting flakes are often small and contain a mixture of monolayer and few-layer graphene. Nevertheless, this method is suitable for applications where large-scale production is more important than achieving perfect monolayers, such as in conductive inks, coatings, and composite materials. Hernandez et al. (2008) demonstrated the production of high-concentration graphene dispersions using this method, which were subsequently used to create conductive films with potential applications in flexible electronics and transparent electrodes.

One of the most significant chemical methods for synthesizing graphene is the chemical reduction of graphene oxide (GO), obtained by expansion and oxidation of graphite.[110] GO shows the same layered structure as graphite, but exhibits carbon atoms bonded to hydroxyl, epoxide, and carboxyl groups, that increase the interplanar distance in GO due to the steric hindrance of oxygen. GO [110]consists of stacked layers held together by supramolecular aromatic π-π stacking interactions, and the exfoliation, which is performed by ultrasonication, takes advantages by the solvent interactions with the graphite layers, and hence it is favoured in solvents (water, ethanol, dimethyl sulfoxide (DMSO), N-methyl-2-pyrrolidone (NMP), N,N-Dimethylformamide (DMF) and acetone) whose surface tension matches the surface energy of GO. Given the presence of oxygenated groups, GO is highly hydrophilic, and during sonication, intercalation of water molecules allows for almost complete exfoliation (~90%) of the material into single layers.

To restore the aromatic system of graphene, GO is reduced to Reduced Graphene Oxide (RGO). Despite RGO still having residual oxygen functionalities and structural defects, it possesses chemical, electrical, and thermal properties very similar to those of graphene, it is less hydrophilic than GO [110]and may aggregate in aqueous solutions over time, but offers the advantage of being dispersible in solution following appropriate surface functionalization.

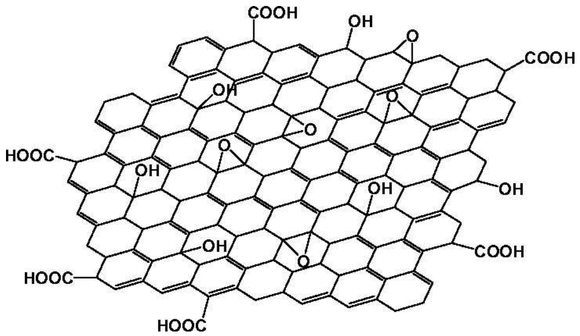

Fig.2.3: *Schematic representation of the structure of RGO highlighting the presence of both aromatic (C sp^2) and aliphatic (C sp^3) domains with –COOH, -OH, and epoxide functionalities.[110]*

2.2 Covalent and non covalent routes to graphene based nanocomposites

The unique chemical and physical properties of graphene make it a highly promising material for numerous advanced applications in electronics, energy, biomedicine, (photo)catalysis, optoelectronics, and sensing technologies. However, challenges such as its poor dispersibility in solvents and the difficulty of scalable production hinder its full utilization. [110]To address these issues, functionalization of graphene is crucial.

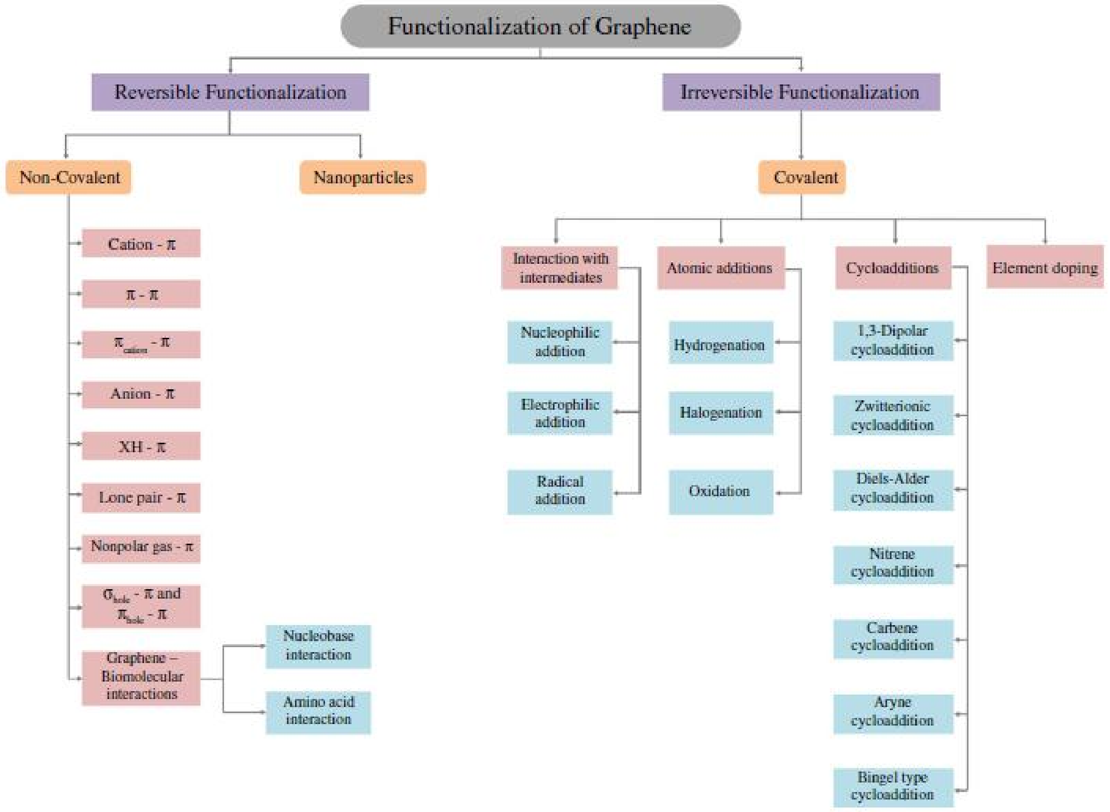

Fig. 2.4: *Schematic representation of different types of functionalization of graphene.*

By carefully selecting the appropriate functionalization technique it is possible to tailor graphene’s properties to meet the specific requirements of various applications, whether enhancing its dispersibility, electrical conductivity, introducing chemical reactivity, or modifying its interaction with other materials.

Two principal methods of graphene functionalization are commonly employed: covalent and non-covalent approaches (Fig. 2.4). Covalent functionalization involves the formation of covalent bonds between the functional groups of the new molecules and the C sp^2 atoms of the basal plane of graphene disrupting its extended π-conjugation, or with the oxygenated groups at the basal plane and edges of GO or the residual oxygen based functionalities of RGO.[111] While covalent functionalization provides a robust chemical modification and new chemical groups are grafted onto the basal plane, its carbon hybridization state is modified passing from sp^2 to sp^3, reducing the π conjugation of the aromatic system, which in turn decreases the material's electrical conductivity, thermal conductivity, and mechanical flexibility. [111]

One of the most common covalent functionalization techniques involves the addition of free radicals or the covalent attachment of molecules to GO. These processes introduce functional groups that can enhance graphene's solubility in organic solvents, improve its compatibility with polymers, or alter its electronic properties by opening a bandgap.

Tour et al. demonstrated that graphene can be covalently functionalized using diazonium salts, which generate nitrophenyl radicals that covalently bind to the graphene basal plane. This reaction disrupts the graphene's π-conjugation, transforming the sp^2 hybridized carbons into sp^3 hybridized carbons, thereby introducing a tuneable bandgap that makes the material more suitable for electronic devices such as transistors.

Another versatile method for covalent functionalization is cycloaddition reactions. One of the most widely studied cycloaddition reactions in graphene functionalization is the Diels-Alder reaction. This reaction involves the addition of conjugated dienes to graphene's double bonds, forming six-membered rings on the graphene surface. Haddon et al. (2011) demonstrated that graphene could undergo Diels-Alder cycloaddition with maleic anhydride and tetracyanoethylene, which resulted in significant alterations to its electronic properties. These types of functionalization reactions are particularly valuable in developing polymer-graphene composites, where the introduction of new chemical groups onto graphene allows for stronger interactions with polymer matrices, enhancing the mechanical and electrical properties of the composite material.

GO has also been widely used as a starting material for covalent functionalization due to its rich surface chemistry. The presence of oxygen-containing functional groups, such as hydroxyl, epoxy, and carboxyl groups, provides reactive sites for covalent attachment. This makes GO an ideal candidate for functionalization with organic molecules and polymers, which can significantly enhance its performance in various applications. For example, the covalent attachment of oligothiophenes to GO has been shown to create a donor-acceptor system with excellent optical properties. Liu et al. demonstrated that oligothiophene-functionalized GO exhibits significant fluorescence quenching, making it a promising material for optoelectronic applications, including solar cells. Similarly, the functionalization of GO with biocompatible polymers such as poly (ethylene glycol) (PEG) has been shown to improve the material's dispersibility in aqueous media, enabling its use in biomedical applications such as drug delivery. Yang et al. highlighted the use of PEGylated GO as a nanocarrier for hydrophobic drugs like camptothecin (Fig. 2.5), demonstrating its potential in targeted cancer therapies.

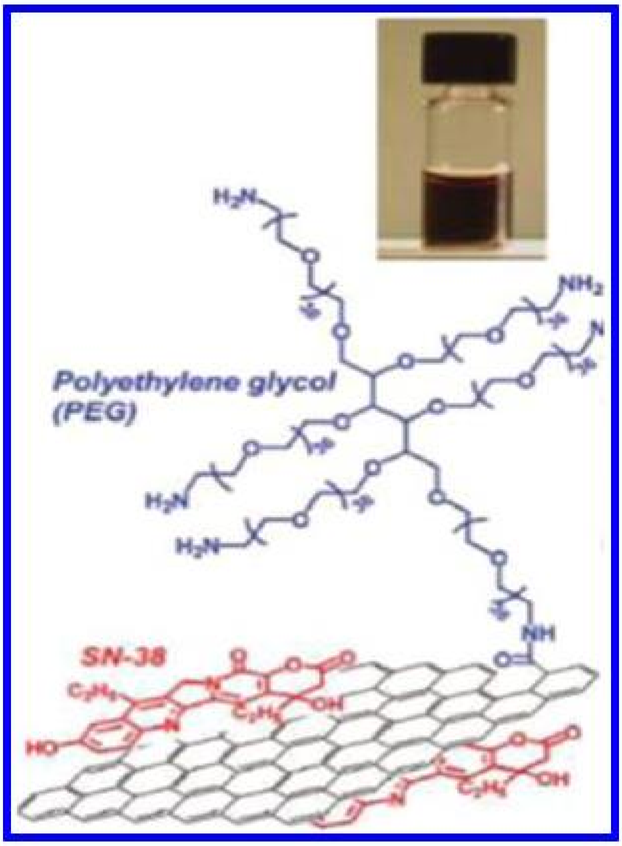

Fig. 2.5: *Immobilization of SN38 camptothecin on PEG-GO.*

Another important reaction of covalent functionalization involves hydrogenation and halogenation of graphene, which alters its fundamental electronic properties. Sofo et al. theoretically predicted the existence of graphene, a fully hydrogenated derivative of graphene. Graphene retains the honeycomb lattice of graphene but transforms from a semimetal to an insulator due to the conversion of sp^2 carbons into sp^3 carbons. The process of hydrogenation opens a bandgap in graphene, making it suitable for applications that require insulating materials. Elias et al. (2009) demonstrated that hydrogenation can be reversed by annealing the material at high temperatures, allowing it to regain its conductive properties. However, in most cases, hydrogenation creates stable, irreversible changes that can be exploited in applications such as hydrogen storage and catalysis, where controlled reactivity is desired. Partial hydrogenation, as reported by Sun et al. (2016), has even been used to introduce magnetic properties into graphene, a discovery that could open new avenues in spintronics and magnetic storage devices.

While covalent functionalization is effective in modifying graphene's intrinsic properties, non-covalent functionalization is preferred when the preservation of graphene's electrical or thermal conductivity is crucial, for example in (bio)sensors, conductive films, and energy storage devices. Non-covalent interactions such as aromatic π-π stacking, Van der Waals forces, hydrogen bonds, dispersion forces, donor-acceptor charge transfer complexes, and electrostatic interactions, allow functional groups to interact with the basal plane of graphene without disrupting its graphitic structure, thereby preserving its electronic properties, and introducing new functional groups. These electronic characteristics make graphene versatile in complexation reactions with organic compounds or transition metals through π-π, H-π, and metal-π interactions. The associated π* antibonding orbitals can accept electrons, favouring interactions between graphene and electron-rich particles such as ions and alkali metals. The systems mostly used in this context include hexabenzocoronenes, porphyrin derivatives, pyrene derivatives, anthracene, and others.

One of the most widely studied non-covalent functionalization methods is aromatic π-π stacking, where aromatic molecules interact with graphene through Van der Waals forces. This type of interaction preserves graphene's extended π-conjugation, ensuring that its electrical properties remain largely unaffected. For instance, the non-covalent attachment of conjugated molecules like porphyrins and phthalocyanines to graphene has been shown to improve its light harvesting capability in the visible spectra range, making it suitable for use in photovoltaic devices. Zhang et al. demonstrated that porphyrin-functionalized graphene exhibits enhanced light absorption and fluorescence quenching, which can be exploited in organic solar cells and light-emitting devices.

Another important route of non-covalent functionalization is the deposition of NPs onto the graphene's basal plane. This approach has been used to enhance graphene's catalytic properties, particularly in the field of fuel cells and sensors. Noble metal NPs, such as Pt and Ag, can be deposited onto graphene via non-covalent interactions, enhancing its catalytic activity. Kim et al. reported that Pt NPs [112]deposited on graphene exhibited superior catalytic performance in fuel cells compared to other carbon-based supports. This enhancement is due to the high surface area and excellent electrical conductivity of graphene, which facilitate electron transfer during catalytic reactions.

In addition to π-π stacking and NPs deposition, non-covalent functionalization using polymers has also been widely explored. By wrapping graphene in polymer chains, its solubility and processability can be significantly improved. For example, polyvinyl alcohol (PVA) has been used to non-covalently functionalize graphene, enhancing its dispersibility in water and organic solvents without compromising its electrical properties. Sun et al. demonstrated that polystyrene-functionalized graphene could be effectively dispersed in organic solvents, making it suitable for use in flexible electronic devices and coatings.

Graphene's interaction with biomolecules, such as DNA and proteins, is another promising area of non covalent functionalization. Sastry et al. (2020) explored the binding of DNA nucleobases, such as adenine, guanine, cytosine, and thymine, to graphene. They found that guanine exhibited the strongest interaction due to its higher π-electron density. This finding is crucial for biosensing applications, where graphene could serve as a platform for detecting biomolecular changes in real time. Similarly, graphene's interaction with aromatic amino acids like tryptophan and tyrosine allows for its use in detecting proteins or other biological markers, further broadening its application in biomedicine.

Among the most important graphene ligands, those with higher affinity due to reversible aromatic interactions include histidine and polycyclic aromatic hydrocarbon derivatives like pyrene. These molecules act as molecular wedges, intercalating between the different planes of graphene, enabling its exfoliation from bulk graphite. This mechanism allows to produce stable colloidal dispersions of graphene flakes in certain organic solvents.[113]

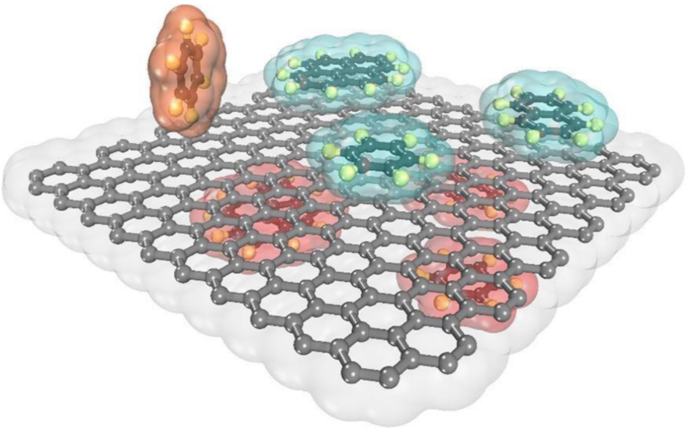

Fig. 2.6: *Schematic representation of the π-π and C-H π interactions between benzene, naphthalene, and pyrene molecules on both sides of the aromatic surface of graphene [111].*

Another key non-covalent interaction used in functionalizing graphene is the cation-π interaction. In this case, graphene interacts with positively charged species, which can have a significant effect on its surface chemistry and physical properties. Hussain et al. (2018) demonstrated how cation-π interactions between graphene and various onium ions, such as ammonium and phosphonium, could significantly alter the stability and performance of graphene-based materials. The strength of this interaction depends on factors like size and charge of the cation, making it possible to tailor graphene's properties for specific applications, such as gas separation membranes or chemical sensors. These interactions are particularly useful in enhancing the structural stability of graphene-based systems by providing cross-linking effects that reinforce the material, without permanently modifying its surface.[110]

In conclusion, both covalent and non-covalent functionalization methods provide powerful tools for tailoring graphene's properties to suit a wide range of applications. The continued development of novel functionalization strategies promises to further unlock the vast potential of graphene in science and technology[5, 110]

2.3 Applications of graphene and its derivatives

Graphene's unique properties have unlocked a vast array of applications, spanning electronics, optoelectronics, (photo)catalysis, energy storage, sensors, and biomedicine. Its derivatives, such as GO and RGO, are similarly versatile, with functional groups that enable chemical modifications, enhancing their incorporation into various composites and biological systems. For instance, GO's oxygenated groups make it highly compatible with polymers, as demonstrated in applications like polymer nanocomposites where GO's functionalization enhances dispersion in organic solvents (Stankovich et al., 2006). This has led to innovations in material science, especially in the production of flexible, durable composites.

Energy storage is another area where graphene has shown remarkable promise, particularly in lithium-ion batteries (LIBs) and supercapacitors. The high surface area and conductivity of graphene allow for rapid electron transfer, enhancing the performance of electrode materials. For instance, graphene anodes in LIBs have been shown to achieve significantly higher capacities compared to conventional graphite anodes, as graphene can store lithium ions on both sides of its two-dimensional structure. Wang et al. (2009) reported the use of RGO as an anode material surpassing the capacity of traditional graphite anodes with a reversible capacity of 540 mAh/g. In supercapacitors, Stoller et al. (2008) reported that graphene-based electrodes achieved a specific capacitance of 135 F/g in aqueous electrolytes, demonstrating high energy and power density. The material retained 98% of its capacitance after 10,000 cycles, making it ideal for long-term applications like electric vehicles and portable electronics.

Graphene's potential as a replacement for indium tin oxide (ITO) in transparent conductive films (TCFs) is another area of interest, particularly in flexible electronics. Graphene TCFs exhibit high electrical conductivity and transparency, coupled with mechanical flexibility, making them ideal for flexible displays, solar cells, and touchscreens (Bae et al., 2010). Bae et al. demonstrated that large-area graphene films, fabricated using CVD, exhibited a sheet resistance of 125 Ω/sq at 97.4% transmittance. These films were applied as transparent electrodes in flexible touchscreens, highlighting graphene's ability to enable lightweight, flexible electronic devices. This offers a significant advantage over ITO, which is both brittle and expensive, particularly for large-scale or flexible applications.[4, 109]

The incorporation of graphene into polymer matrices has also been extensively explored, with studies demonstrating its ability to enhance the mechanical properties of polymers. Even at low loadings, graphene significantly improves the tensile strength, elastic modulus, and thermal stability of the composites (Young et al., 2012). This enhancement is due to graphene's high aspect ratio and large interfacial area, which facilitates load transfer within the polymer matrix. Applications of these graphene-polymer composites range from structural materials to flexible electronics and thermal management systems, further broadening the utility of graphene in advanced material science.

In high-speed electronics, graphene's high electron mobility and low resistivity make it a strong candidate for field-effect transistors (FETs). Unlike silicon, graphene allows for faster electron transport, leading to high-frequency operation in electronic devices. Lin et al. (2010) demonstrated graphene-based FETs operating at frequencies exceeding 100 GHz, making them suitable for RF communications. Although the absence of a bandgap in graphene presents challenges for digital logic circuits, graphene nanoribbons (GNRs) have been shown to induce a bandgap through quantum confinement, making graphene viable for digital circuits. Additionally, researchers at IBM developed a graphene-based RF integrated circuit (IC) that incorporated a graphene transistor and frequency mixer. This IC operated at frequencies up to 10 GHz, outperforming traditional silicon-based mixers in terms of speed and efficiency (Lin et al., 2011), showcasing graphene's potential for faster, more efficient electronics.[114]

Graphene has also made significant strides in biomedical applications, particularly in drug delivery and tissue engineering. GO's high surface area and ability to form non-covalent interactions with various molecules make it an excellent platform for drug delivery. A study by Liu et al. (2008) demonstrated that GO-doxorubicin complexes exhibited enhanced anticancer activity *in vitro* compared to free doxorubicin, due to the higher drug loading capacity onto the GO surface thanks to the π-π stacking interactions between GO and doxorubicin, and targeted delivery to cancer cells by controlled release in response to specific stimuli such as pH changes.

Additionally, graphene-based scaffolds have been developed for tissue engineering, leveraging graphene's mechanical strength, conductivity, and biocompatibility. Park et al. (2011) showed that graphene scaffolds promoted the growth of neuronal cells, indicating their potential in neural tissue engineering.

In sensing applications, graphene's large surface area and high sensitivity to charge transfer processes make it ideal for detecting low concentrations of gases and biomolecules. Graphene-based materials have been successfully employed to detect analytes such as ammonia (NH_3) and carbon dioxide (CO_2), as well as biological molecules like DNA and proteins (Schedin et al., 2007). For example, Schedin et al. demonstrated the use of a graphene gas sensor capable of detecting individual gas molecules such as NO_2, NH_3, and CO. Ohno et al. (2010) developed a graphene field-effect transistor (GFET) biosensor for the detection of glucose, achieving a detection limit of 10 pM. Similarly, a study by He et al. (2010) showed that GO could be functionalized with antibodies to detect specific cancer biomarkers with high sensitivity, highlighting graphene's potential in the field of point-of-care diagnostics. This sensitivity is unparalleled by conventional metal-oxide-based sensors, making graphene an invaluable material for environmental monitoring and industrial safety applications. [4, 109, 114]

In addition to (bio)sensing, graphene has also been used in pressure sensors and strain sensors. Its high mechanical strength and flexibility allow graphene to respond to minute mechanical deformations, making it highly sensitive to changes in pressure or strain. Flexible graphene-based pressure sensors have been integrated into wearable electronics for health monitoring, where they can detect physiological signals such as heart rate and respiration (Zang et al., 2015). These sensors offer high sensitivity, flexibility, and biocompatibility, making them ideal for next-generation wearable health devices.

In conclusion, graphene and its derivatives have demonstrated remarkable versatility and potential across a wide range of applications, from high-speed electronics and energy storage to advanced sensors and biomedical devices. The continuous development of scalable production methods and the ongoing research into graphene's properties and functionalization are expected to further expand its impact in science and technology.

2.4 Colloidal inorganic NPs decorated graphene derivatives based nanocomposites: synthesis and applications

The functional groups of molecules, which are used as molecular wedges in the exfoliation and functionalization of graphene and its derivatives can be used to bind colloidal NPs and nanocrystals (NCs) onto their basal plane, to prepare hybrid nanocomposites that synergistically combine the properties of both kinds of materials. This typically enhances the properties of the individual components and/or introduces new functionalities that the pristine materials do not possess.

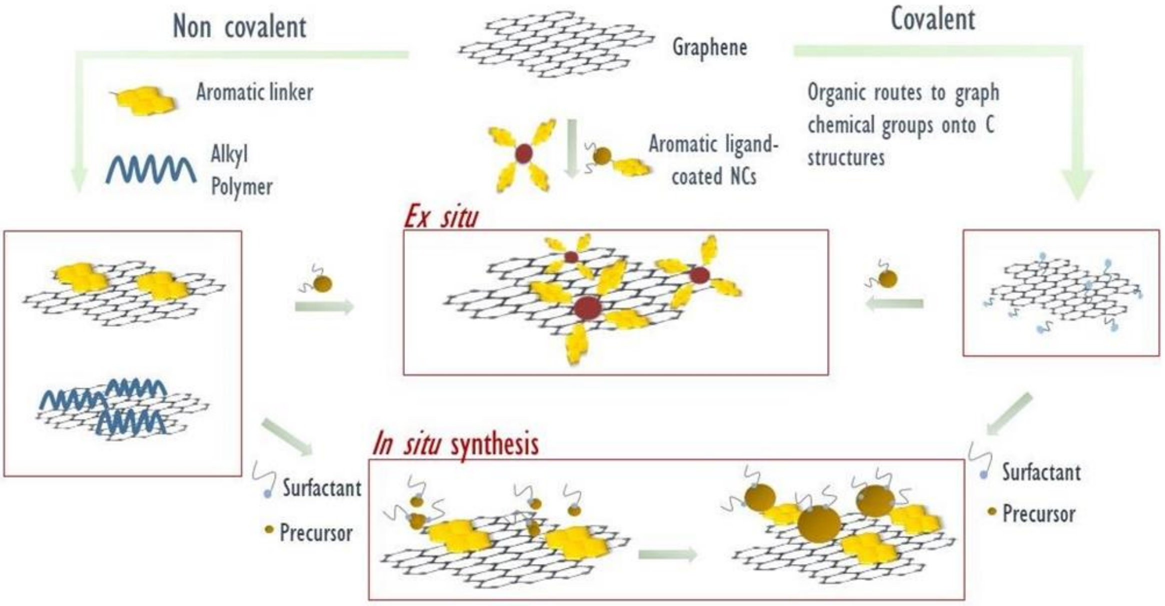

Fig. 2.7: *Schematic of the preparation of hybrids based on graphene (G) and colloidal NP with covalent and non-covalent functionalization approaches, both in situ and ex situ.*

The approaches for preparing these nanocomposites can be classified into two types: *ex situ* approaches, which involve by direct immobilization of pre-synthesized NPs onto the aromatic platform of graphene, and *in situ* methods, which utilize pre-existing functionalities of graphene or those of grafted groups or immobilized molecules as coordinating sites for NP heteronucleation and growth (Fig. 2.7).

The *in situ* synthesis method provides a powerful approach for the preparation of graphene-based nanocomposites. In this case, the NPs are formed and grown in place, or "*in situ*," onto the GO/RGO sheets, which have been pre-functionalized. [115]The functionalization step introduces reactive groups that serve as anchoring points for the nucleation and growth of the NPs, offering enhanced control over NPs' coating density, size and shape, and hence overall nanocomposite's functionalities. Additionally, the direct formation of NPs onto the graphene basal plane enhances the overall stability of the nanocomposite and leads to stronger coupling interaction between the two materials. This contrasts with the *ex situ* methods, where NPs are simply mixed with graphene leading to weaker physical and chemical interactions. Other *ex situ* approaches instead consist of functionalizing pre-synthesized NPs by coordinating agents that can bind directly to the graphene basal plane by aromatic π- π stacking interactions, or that can bind through coordination, covalent chemical bonding, or electrostatic interactions to a bifunctional linker, which is anchored to the graphene surface via π-π, hydrophobic, or electrostatic interactions (Fig. 2.7).

A kind of hybrid nanocomposite of significant fundamental and practical interest is based on graphene oxide (GO) flakes decorated, by a *in situ* colloidal approaches, with Au NPs.[116] Some of these nanocomposites were synthesized by heteronucleating and growing small Au NPs, 2-3 nm in size, directly onto GO sheets in aqueous solutions, starting from $HAuCl_4$ as the precursor, which is reduced to Au^0 by the strong reducing agent $NaBH_4$. [117]Larger Au NPs, 10-20 nm in size, chemically bonded to GO, were obtained by reducing $HAuCl_4$ with weaker reducing agents such as citrate or ascorbic acid. This approach was used by the research group conducting the thesis work to prepare hybrids based on nanographene oxide (NGO) flakes, decorated with a high density of *in situ* synthesized Au NPs, using citrate as the reducing agent.[118]

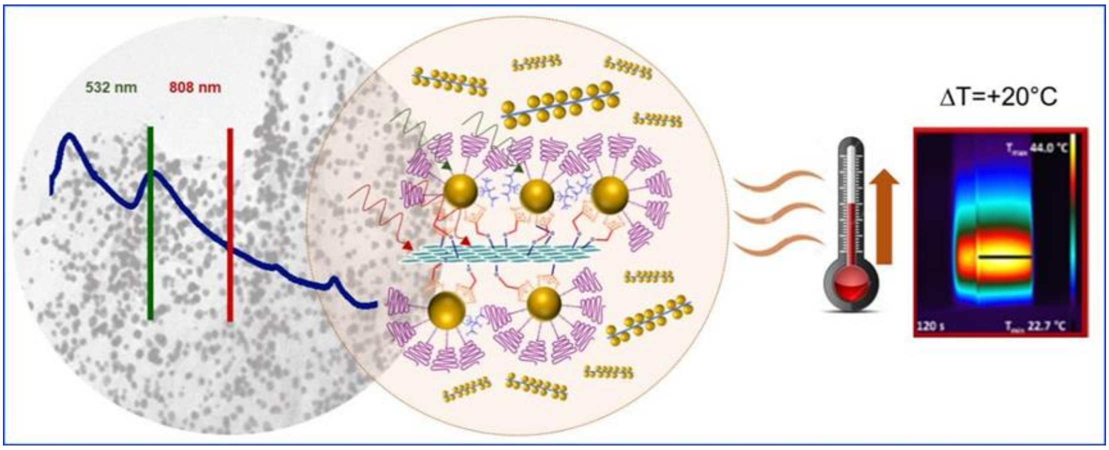

Fig. 2.8: *TEM image, UV-Vis-NIR absorption spectrum, and schematic of Au nanoparticle attachment to GO for photothermal applications [118].*

This method provides an excellent control on the morphology of the NPs anchored onto the GO sheets and a high coating density, making the nanocomposite suitable for photothermal applications. The attachment of the Au NPs onto GO allows for the combination of the photothermal properties of the NPs, which absorb in the visible spectral range (520-530 nm), with those of graphene, which absorbs in the NIR (700-900 nm) resulting in a superior photothermal activity compared to the individual components (Fig. 2.8). The nanocomposite resulted biocompatible as well, and hence suitable for applications in photothermal ablation of cancer cells. [118]

Another approach recently developed by the research group in which this thesis work was conducted, involves functionalizing RGO sheets with 1-pyrenecarboxylic acid to achieve the complex PCA-RGO, whose -COOH functionalities are utilized as coordinating sites for the *in situ* synthesis of the Au NPs (Fig. 2.9A),[119] that was performed by modifying the Brust's procedure. In this approach, the $HAuCl_4$ precursor is reduced, in presence of the PCA-RGO complex, from Au^{3+} to Au^{+} by an aromatic thiol and then from Au^{+} to Au^{0} by $NaBH_4$. Since the thiol is a strong coordinating agent and $NaBH_4$ is a strong reducing agent, the resulting NPs are small, 2-3 nm in size (Fig. 2.9A) with a plasmonic absorption peak at 564 nm (Fig. 2.9B).

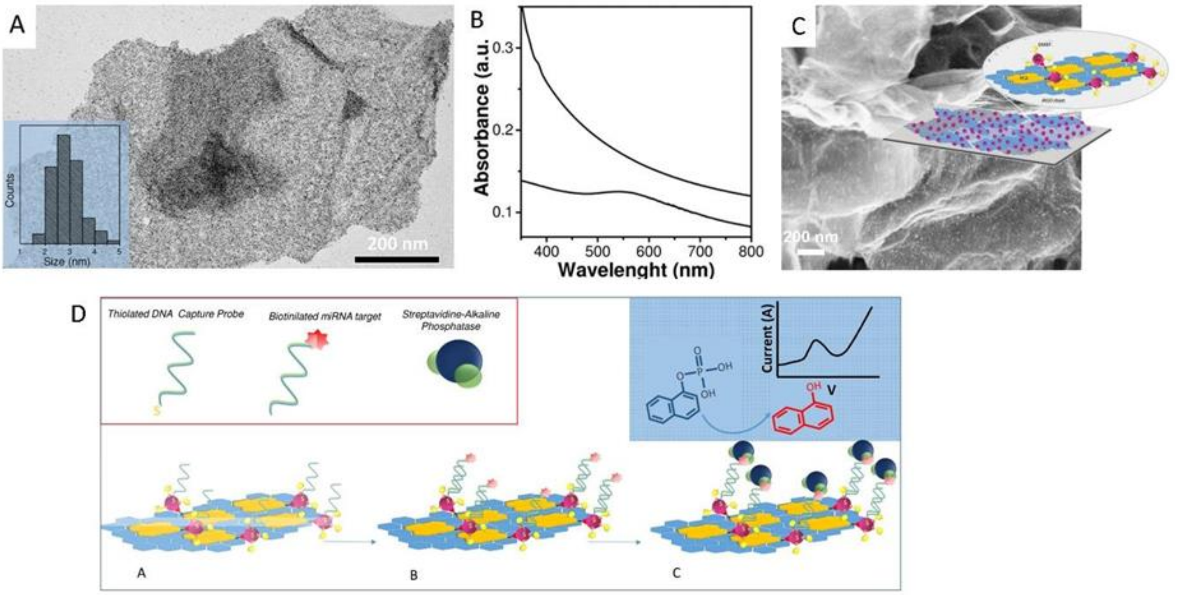

Fig. 2.9:* *(A)* *TEM micrograph*, (B)* *UV-Vis-NIR spectrum, and* ***(C) *SEM image of the PCA-RGO/Au NP hybrid nanocomposite. Functionalization of the SPCE electrode with PCA-RGO/Au NP for the detection of mRNA [119]*

The use of the aromatic thiol slows down and controls the reduction process of the NPs while simultaneously binding the NPs to the RGO basal plane through π-π interactions (Fig. 2.9C), enabling its electronic coupling with the NPs. This hybrid nanocomposite was used to modify a Screen-Printed Carbon Electrode (SPCE). After appropriate functionalization with a DNA capture probe, the modified SPCE was used for the detection of mRNA-221, a cancer biomarker, using differential pulse voltammetry (Fig. 2.9D).

The hybrid modified electrode exhibited sensitivity comparable to the most advanced sensors reported in the literature, owing to its excellent electrical conductivity, high kinetics of heterogeneous charge transfer, reduced charge transfer resistance at the electrode/electrolyte interface, high electroactivity, and large surface area of the nanostructured electrode. [119]

Another hybrid nanocomposite synthesized using the same strategy involves RGO flakes functionalized with 1-aminopyrene (PA), which are then decorated with Au NPs (PA-RGO/Au NPs) (Fig. 2.10A). [120]In this material, the Au NPs heteronucleate and grow on the amine functionalities of PA anchored onto RGO through π-π interactions (Fig. 2.10A). The $HAuCl_4$ precursor is reduced to Au^{0} on PA-RGO by a long-chain alkylamine, oleylamine (OLEAM), which also acts as a solvent, reductant and coordinating agent, stabilizing the hybrid in organic solvents. This material was used to modify Screen-Printed Carbon Electrodes (SPCE) (Fig. 2.10B) that were treated by spin-coating with a mixture of methanol and acetic acid ($CH_3OH/AcOH$) to remove the surface OLEAM dielectric layer and were used for the detection of dopamine (DA) (Fig. 2.10C), a neurotransmitter[121] whose abnormal levels indicate brain diseases such as Parkinson's and Huntington's disease.[122]

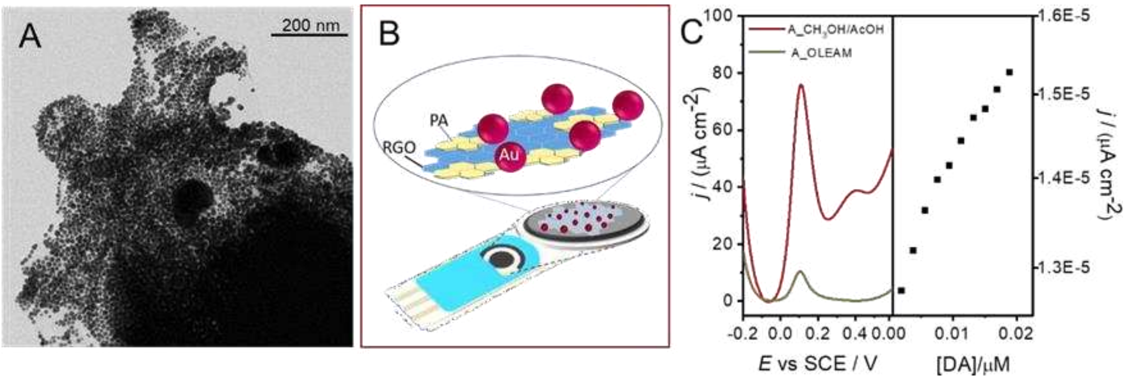

Fig. 2.10: ***(A)*** *TEM image of PA-RGO/Au NPs.* ***(B)*** *Schematic of SPCE modification.* ***(C)*** *(Right panel) DPV of SPCE modified with PA-RGO/Au NPs (A_OLEAM) and after treatment by spin-coating with $CH_3OH/AcOH$ (A_$CH_3OH/AcOH$), following the addition of 10^{-5} M DA. (Left panel) Calibration curve of A_$CH_3OH/AcOH$. [120]*

The limit of detection (LOD) reached by using the hybrid modified SPCEs was 0.0025 μM (RSD < 1%), that, to the best of our knowledge, is among the lowest reported for this class of graphene/Au nanocomposites based electrochemical sensors, thus envisioning their potential for innovative point-of care technology in the clinical diagnosis of DA.

Hybrid nanocomposites based on PCA-RGO complex, decorated with TiO_2 nanorods (NRs) (PCA_RGO/TiO_2 NRs), have been synthesized using the same *in situ* colloidal approach, starting from the titanium tetraisopropoxide precursor in presence of the oleic acid coordinating agent. These materials can be employed for the degradation of organic pollutants under UV illumination. In these structures, UV light absorption by TiO_2 NRs, a wide bandgap nanocrystalline semiconductor, promotes the generation of electron-hole pairs, which are effectively separated with by electron transfer to graphene, acting as a charge sink. This process enhances the photocatalytic activity of the hybrid compared to the TiO_2 NRs alone. The photo-generated charges in the hybrid react with water molecules, promoting the formation of reactive oxygen species (ROS) responsible for the photodegradation of pollutants.

Among the hybrid materials based on graphene derivatives and colloidal inorganic NPs synthesized via an *ex situ* approach, there is also nanocomposite recently developed in the research group where this thesis work was conducted, based on CVD graphene decorated with PbS colloidal NCs [106]. The NCs were functionalized with pyrenyl butyric acid (PBA) through a ligand exchange procedure, replacing the pristine oleic acid used as a capping agent in the NC synthesis. Subsequent incubation of monolayer CVD graphene films in the PBA-coordinated NCs solution facilitated their anchoring onto graphene via aromatic π-π stacking interactions [106]. PbS NCs were chosen to transfer absorption properties in the visible (Vis) and enhance near-infrared (NIR) spectral range due to their high absorption coefficient and tunable band gap with size. PbS NCs exhibit low charge mobility, but when combined with graphene, photogenerated holes on the photoexcited NC semiconductor are transferred to graphene through the aromatic linker PBA, delocalizing them in the aromatic system. When appropriately integrated into an external electrical circuit, under white LED illumination, the hybrid converts the incident light into an electrical signal, demonstrating a 3% reduction of the graphene sheet resistance [106].

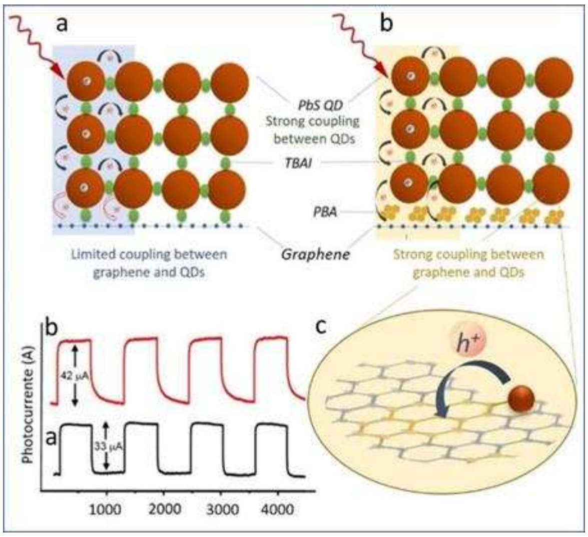

Fig. 2.11: *Schematic of charge transfer NC-NC and NC-graphene and photocurrents of PbS NC multilayers coordinated by TBAI (a) and TBAI-coordinated NC multilayers having PBA at the interface with graphene (b). Schematic of the transfer of photo-generated holes from PbS to graphene (c).*

As a further evidence of the effectiveness of the PBA linker in promoting strong electron coupling interactions between the PbS QDs and monolayer CVD graphene, recent studies, which were conducted in the group of this thesis work, have shown that graphene CVD-based photodetectors modified with multilayers of PbS QDs, where the first layer of QDs is coordinated with PBA molecules, exhibit higher photoresponse efficiency compared to photodetectors where the first layer of QDs is surface coordinated with oleic acid (OLEA) or other short-chain ligands such as tetrabutylammonium iodide (TBAI) (Fig. 2.11). The procedure of preparation of the nanocomposite material in this work, begins with the synthesis of the PbS QDs using a colloidal method, followed by ligand exchange of OLEA, the pristine surfactant used in the synthesis, with PBA. PBA binds to graphene through non-covalent π–π interactions, while its carboxyl group coordinates the PbS QDs surface. The ligand exchange is critical, as it enhances the QDs-graphene electron coupling. The devices are fabricated respectively, by spin-coating i. multilayers of OLEA-PbS QDs onto graphene followed by ligand exchange using TBAI for each layer to improve NC-NC coupling, and ii. the first layer of PBA-PbS QDs followed by the deposition of multilayers of OLEA-PbS QDs each treated by TBAI. The hybrid graphene/PbS QDs photodetectors integrating PBA at the QDs-graphene heterojunction exhibited a significant enhancement of the photoresponse, with up to a 30% increase in photocurrent compared to conventional devices using only TBAI as a linker. This improvement is attributed to the strong electron coupling between the QDs and graphene, which is mediated by the PBA,[123] facilitating more efficient charge transfers and resulting in improved photodetection properties.

Another hybrid nanocomposite synthesized using the same *ex situ* strategy involves the decoration of monolayer graphene, grown via CVD, with TiO_2 NCs that are coordinated by PBA at the surface. [124](Fig. 2.12 A). The TiO_2 NCs are initially capped with oleic acid (OLEA), the ligand used during the synthesis for endowing the NCs with stability and size uniformity. The NCs are then subjected to ligand exchange with PBA, enabling them to bind to graphene. The resulting hybrid is prepared by immersing CVD-grown graphene into a solution containing PBA-coated TiO_2 NCs. This approach leverages the aromatic π-π stacking interactions between the pyrene moiety and the graphene surface, allowing the TiO_2 NCs to assemble in highly interconnected multilayered structures onto graphene (Fig. 2.12 B-C). The achieved TiO_2/graphene hybrid exhibits significant improvements in photocurrent generation and charge transport when exposed to UV light, with an increase of up to 50% in the photoelectrochemical activity compared to bare graphene. These properties are attributed to the effective electron coupling between TiO_2 and graphene, facilitated by the PBA linker, which enhances the photoresponse and prolongs exciton recombination times of the nanocomposite, making it suitable for various applications such as solar cells, photodetectors, and biosensors.

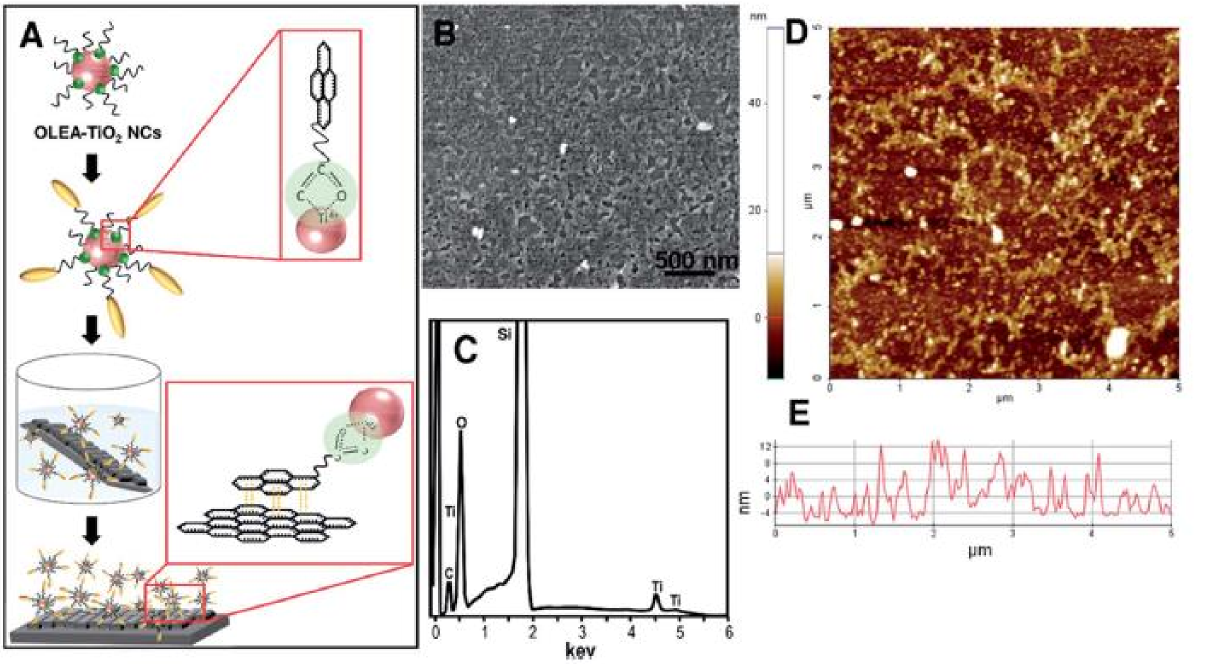

Fig. 2.12 *(A) Sketch of the functionalization of CVD grown monolayer graphene with PBA-coated TiO_2 NCs, with close-up views of the chemical coordination of PBA at the NCs surface and of the aromatic π-π stacking chemical interactions of PBA and graphene. (B) SEM picture, (C) EDS spectrum in the range of 0–6 keV, (D) AFM 2-D topography image and (E) cross-sectional line profile taken along the red line of panel (D) of CVD monolayer graphene functionalized with PBA-capped TiO_2 NCs.[124]*

2.5 Nanocomposites based on Ag NPs and graphene derivatives: synthesis and integration into flexible, eco-friendly substrates for advanced applications

The combination of RGO with functional inorganic NPs, such as AgNPs, creates a novel class of hybrid nanocomposites that synergistically merge the unique properties of both materials. RGO offers exceptional mechanical strength, high electrical conductivity, and flexibility, making it ideal for flexible substrates. Meanwhile, Ag nanostructures contribute strong antimicrobial properties and excellent conductivity. Depending on their morphology, such as nanospheres or NWs, Ag structures enhance the composite in different ways: NWs provide superior conductive pathways and mechanical flexibility, while spherical Ag NPs offer a larger surface area for chemical interactions. Together, these features make RGO-Ag nanocomposites particularly useful for applications in photocatalysis, sensing, optoelectronics, and flexible electronics.

The mechanical flexibility of the RGO/Ag NP hybrid nanocomposites allows them to conform to different shapes and surfaces, making them ideal for wearable sensors that can detect strain, pressure, or temperature changes. In biomedical applications flexibility is crucial because it enables the integration of devices into fabrics or allows direct skin contact, maintaining comfort without sacrificing performance. Furthermore, suitably engineered graphene/Ag NP hybrid nanocomposites exhibit low cytotoxicity, making them suitable for direct contact with biological tissues, whether as diagnostic tools.

In addition to flexibility, the environmental sustainability of these materials makes them extremely convenient for applications. Graphene is derived from carbon, a naturally abundant element, while efforts to reduce the environmental impact of Ag NPs synthesis process have pushed towards green chemistry methods, which minimize the use of hazardous chemicals, aligning with the global demand for sustainable materials in advanced technologies.

Kim et al. reported the development of a multifunctional fabric fabricated by coating a knitted textile with RGO and Ag NWs via supersonic cold spraying to apply in wearable electronics. The unique combination of conductivity, stretchability, washability, hydrophobicity, and antibacterial properties makes the fabricated fabrics ideal for applications in healthcare monitoring, energy storage, and soft robotics, opening new avenues for e-textile development (Fig.2.13).[112]

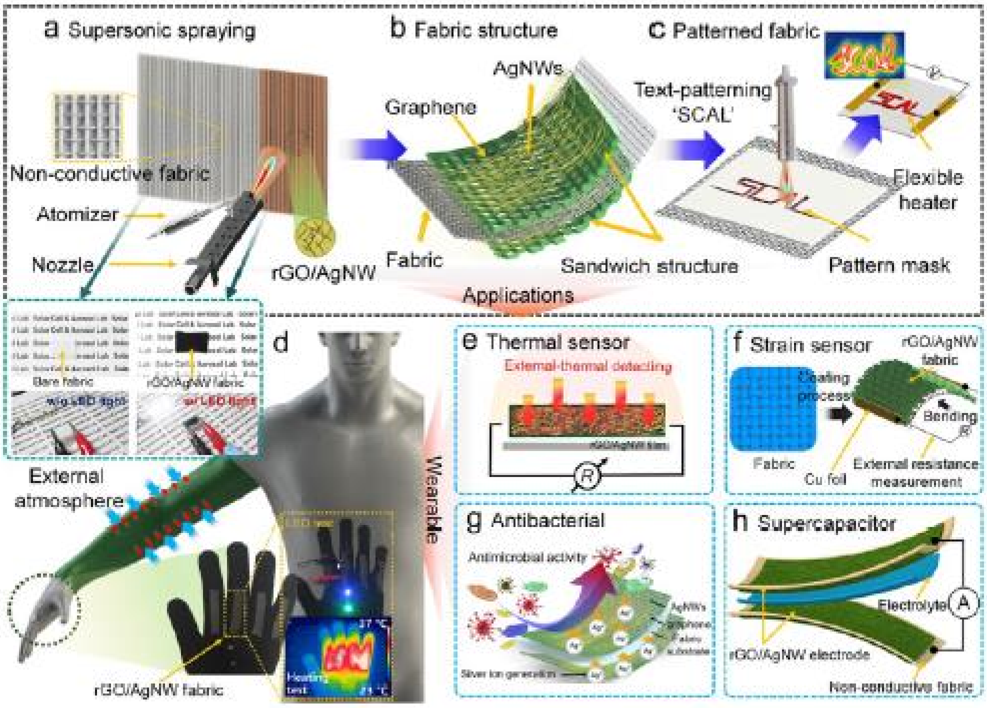

Fig.2.13: *Sketch of the fabrication process of the multifunctional RGO/Ag NW modified fabric sensor. (a) Supersonic spraying for depositing RGO/Ag NW. (b) RGO/AgNW-coated fabrics. (c) Different patterned coatings through supersonic spraying (d−h) Wearable RGO/AgNW fabric as a thermal sensor, strain sensor, antibacterial fabric and supercapacitor.[112]*

The preparation of the fabric involves the use of RGO for its large surface area and high adhesion to the fabric, while Ag NWs enhance the electrical conductivity and impart antibacterial properties. The RGO and Ag NW mixture is supersonically sprayed onto a nylon-polyurethane knitted fabric, ensuring strong adhesion with the conductive material without the need for post-processing. The supersonic cold spray process uses a gas stream to atomize the dispersion, evaporating the solvent and depositing RGO and Ag NW solids onto the fabric. This technique provides a scalable and cost-effective method for producing conductive fabrics with strong adhesion and durability.[112]

This multifunctional fabric demonstrates excellent performance in several applications. As a heater, it can reach temperatures of up to 56 °C under 3.5 V, showing stable thermal cycling and repeatable performance over multiple cycles. The fabric also functions as a thermal sensor, with resistance changes correlating to ambient temperatures. When tested as a strain sensor, the fabric exhibited high sensitivity with a gauge factor of 0.56

over strains of up to 170%, maintaining stable performance even after 3000 cycles of stretching. As a supercapacitor, the fabric displayed specific capacitance values up to 46 mF·cm^{-2} at a current density of 0.2 mA·cm^{-2}. The capacitance was stable over 10,000 charge-discharge cycles, demonstrating the durability of the material for energy storage applications. The fabric's hydrophobicity and antibacterial properties further enhance its suitability for wearable devices, with a water contact angle (WCA) of 120° and an antibacterial reduction rate of 99.9% for *E. coli* and *S. aureus*.

A flexible, conductive fabric was fabricated by coating a cotton with RGO and Ag/Cu NPs through a supersonic cold spraying method. The synthesis involved the chemical reduction of GO to RGO, followed by the deposition of Ag and Cu NPs onto the fabric substrate. [125]The supersonic cold spraying technique ensured strong adhesion of the NPs to the fibres, resulting in a highly conductive and durable material.

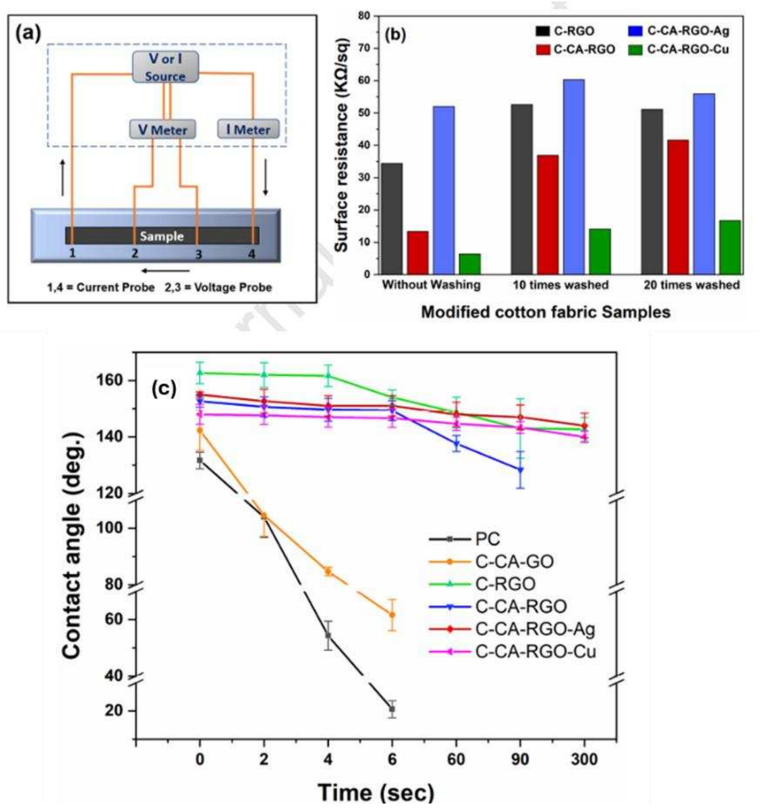

Fig. 2.14: *(a) Sketch of the surface resistance measurement setup of fabric samples by the four-point probe method. (b) Surface resistance of modified cotton fabrics after different washing cycles. (c) WCAs of different cotton fabric samples with a different over time[125]*

SEM and energy-dispersive X-ray spectroscopy (EDX) confirmed the successful deposition of the NPs onto the fabric surface, while electrical conductivity measurements showed that the material retained its conductivity even after multiple washing cycles. The fabric was also characterized for its hydrophobic properties using WCA measurements, demonstrating its suitability for outdoor and wearable applications. The antibacterial effects of the Ag and Cu NPs were tested against common pathogens, showing nearly complete inhibition of microbial growth. This hybrid fabric was designed as a wearable sensor capable of detecting strain and temperature changes, making it highly applicable in smart textiles for healthcare monitoring and environmental sensing. The flexibility, durability, and multifunctionality of the fabric underscore its potential for real-world applications in wearable electronics and biomedical devices (Fig.2.14).

In another work [126], medical-grade polyviscose fabrics were modified by RGO/Ag NP nanocomposite coatings for the preparation of medical textiles. The developed materials represent a simple, scalable, and eco-friendly solution for producing reusable and durable antimicrobial medical fabrics, making them highly suitable for use in hospitals, particularly in reducing healthcare-associated infections (HAIs). This synthesis process involves a two-step in situ reduction approach. Initially, the polyviscose fabric substrate, composed of a non-woven structure with high porosity, was pre-treated with a $NaBH_4$ solution. The role of $NaBH_4$ is critical as it creates reactive sites on the fabric surface by inducing defects in the polymeric structure. This step prepares the fabric for the subsequent incorporation of AgNPs and RGO. Following pre-treatment, the fabric was immersed in a mixture containing $AgNO_3$ and GO, where Ag^+ ions were reduced *in situ* to form Ag NPs, while GO was simultaneously reduced to RGO. The reduction process facilitated by $NaBH_4$ that rapidly leads to the nucleation of Ag NPs both on the surface and within the porous matrix of the fabric. Notably, the wrinkled surface and microvoids of the polyviscose fabric act as micro-reactors that allow controlled nucleation and prevent excessive agglomeration of Ag NPs, thus regulating the size of the NPs.(Fig.2.15) The use of RGO as a co-reducing and stabilizing agent further enhanced the distribution of the Ag NPs across the fabric surface. Upon reduction to RGO, the interaction between the Ag NPs and RGO sheets increased the overall stability and loading of the Ag NPs onto the fabric. Scanning electron microscopy (SEM) analyses revealed that the Ag NPs were well dispersed and adhered effectively to the RGO network, forming a uniform coating onto the textile fibres.[126]

The resulting RGO/Ag NP nanocomposites demonstrated exceptional antimicrobial activity, achieving 100% bacterial inhibition against *E.coli* within 6 h of exposure. This antimicrobial efficacy was maintained even after 12 laundering cycles, with a minor reduction to 90.1%, indicating high wash fastness. The enhanced durability is attributed to the strong binding between the Ag NPs and the RGO matrix, which minimized NP leaching during washing, as confirmed by inductively coupled plasma optical emission spectroscopy (ICP-OES) tests. These tests measured Ag leaching in saline solution and found that the RGO/Ag NP nanocomposite leached significantly less Ag compared to fabrics treated solely with Ag NPs. Furthermore, the study found that the incorporation of RGO improved the oxidative stability of the Ag NPs. The graphene sheets acted as a barrier, reducing the likelihood of Ag oxidation, which is a common issue with Ag NPs. The surface plasmon resonance

(SPR) observed in the UV–Vis spectra further confirmed the presence of stable, well-formed Ag NPs in the nanocomposite, with the SPR signal remaining strong even after multiple washing cycles.

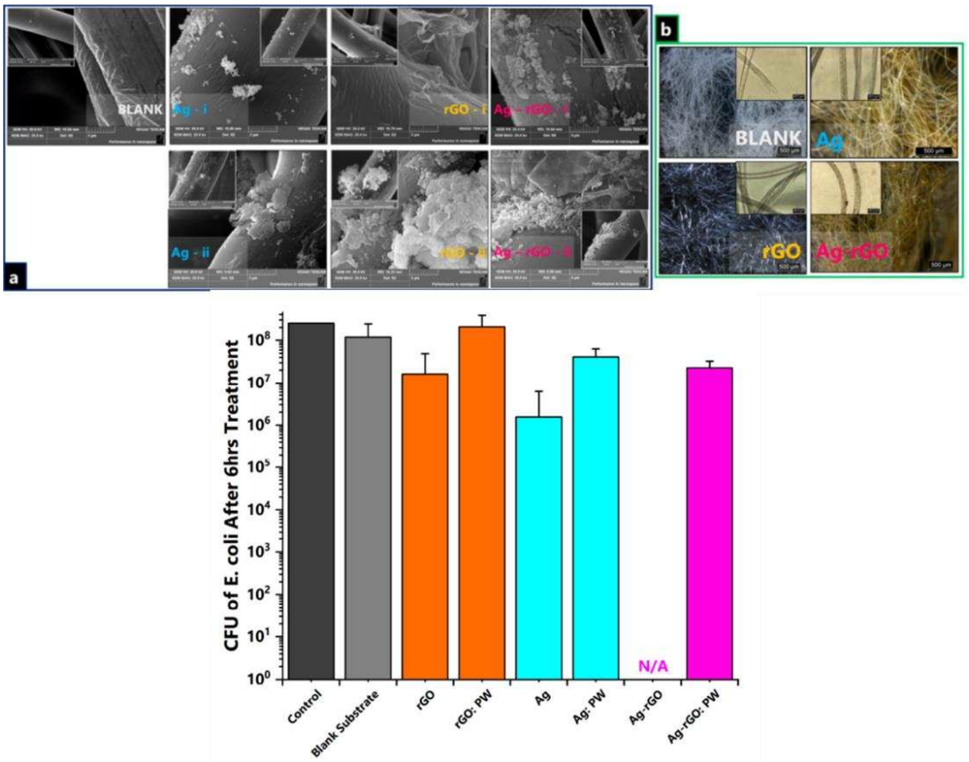

Fig.2. 15: *(a) SEM images of nanocomposite-incorporated polyviscose fibres, both (i) before laundering, and (ii) after laundering. (b) Dark-field optical microscope images of nanocomposite-incorporated polyviscose fibres with longitudinal microscopy images in the inset; c) Viable E. coli counts after 6 h of treatment in the dark at 37°C on non-woven polyviscose fabrics, both unmodified (Control) and modified with RGO, Ag, and RGO-Ag, before and after laundering (PW: post-wash)[126]*

References

[1] J.W. Mcbain, C.S. Salmon, "Colloidal Electrolytes. Soap Solutions and Their Constitution," Journal of the American Chemical Society, 1920, 42: pp. 426-460.

[2] Y.D. Smet, et al., "On the Determination of Ostwald Ripening Rates from Dynamic Light Scattering Measurements," Langmuir, 1999, 15: pp. 2327-2332.

[3] Y. Yin, A.P. Alivisatos, "Colloidal Nanocrystal Synthesis and the Organic–Inorganic Interface," Nature, 2005, 437(7059): pp. 664-670.

[4] F. Bonaccorso, et al., "Graphene Photonics and Optoelectronics," Nature Photonics, 2010, 4(9): pp. 611-622.

[5] Y.B. Kumar, et al., "Chapter 7 - Reversible and Irreversible Functionalization of Graphene," in Theoretical and Computational Chemistry, T. Dinadayalane and F. Hagelberg, Editors, 2022, Elsevier, pp. 157-189.

[6] X. Chen, et al., "Optik - International Journal for Light and Electron Optics," Optik, 2022.

[7] L. Fu, et al., "Adsorption Behavior of Organic Pollutants on Microplastics," Ecotoxicology and Environmental Safety, 2021, 217: p. 112207.

[8] C.M. Muntean, et al., "Gold vs. Silver Colloidal Nanoparticle Films for Optimized SERS Detection of Propranolol and Electrochemical-SERS Analyses," Biosensors, 2023, 13, DOI: 10.3390/bios13050530.

[9] C. Wang, et al., "A Longitudinal Study on the Mental Health of General Population During the COVID-19 Epidemic in China," Brain, Behavior, and Immunity, 2020, 87: pp. 40-48.

[10] J. Yang, et al., "Flexible and Reusable SERS Substrate for Rapid Conformal Detection of Residue on Irregular Surface," Cellulose, 2021, 28(2): pp. 921-936.

[11] W. Liu, et al., "A Review of the Removal of Microplastics in Global Wastewater Treatment Plants: Characteristics and Mechanisms," Environment International, 2021, 146: p. 106277.

[12] T. Xiu-Zhi, et al., "Synthesis of Graphene Decorated with Silver Nanoparticles by Simultaneous Reduction of Graphene Oxide and Silver Ions with Glucose," Carbon, 2013, 59: pp. 93-99.

[13] R. Khojasteh-Taheri, et al., "Green Synthesis of Silver Nanoparticles Using Salvadora Persica and Caccinia Macranthera Extracts: Cytotoxicity Analysis and Antimicrobial Activity Against Antibiotic-Resistant Bacteria," Applied Biochemistry and Biotechnology, 2023, 195(8): pp. 5120-5135.

[14] R.A.N. Chmielewski, J.F. Frank, "Biofilm Formation and Control in Food Processing Facilities," Comprehensive Reviews in Food Science and Food Safety, 2003, 2(1): pp. 22-32.

[15] Y. Xiong, et al., "The Role of Surface Chemistry on the Toxicity of Ag Nanoparticles," Small, 2013, 9(15): pp. 2628-38.

[16] R. Weiner, et al., "Assessment of Mass Transfer from Poly(ethylene) Nanocomposites Containing Noble-Metal Nanoparticles: A Systematic Study of Embedded Particle Stability," ACS Applied Nano Materials, 2018, 1.

[17] Y. Li, et al., "Surface-Coating-Dependent Dissolution, Aggregation, and Reactive Oxygen Species (ROS) Generation of Silver Nanoparticles Under Different Irradiation Conditions," Environmental Science & Technology, 2013, 47(18): pp. 10293-10301.

[18] B. Le Ouay, F. Stellacci, "Antibacterial Activity of Silver Nanoparticles: A Surface Science Insight," Nano Today, 2015, 10(3): pp. 339-354.

[19] Y.M. Long, et al., "Surface Ligand Controls Silver Ion Release of Nanosilver and Its Antibacterial Activity Against Escherichia coli," International Journal of Nanomedicine, 2017, 12: pp. 3193-3206.

[20] H.M. Hegab, et al., "The Controversial Antibacterial Activity of Graphene-Based Materials," Carbon, 2016, 105: pp. 362-376.

[21] S. Liu, et al., "Antibacterial Activity of Graphite, Graphite Oxide, Graphene Oxide, and Reduced Graphene Oxide: Membrane and Oxidative Stress," ACS Nano, 2011, 5(9): pp. 6971-80.

[22] Y. Zheng, et al., "Intelligent Textiles for Visual and Smart Interaction," Advanced Fiber Materials, 2024, 6(4): pp. 946-948.

[23] Y. Peng, Y. Cui, "Advanced Textiles for Personal Thermal Management and Energy," Joule, 2020, 4(4): pp. 724-742.

[24] Z. Wang, et al., "Individual Difference in Thermal Comfort: A Literature Review," Building and Environment, 2018, 138: pp. 181-193.

[25] M.J. Rahman, T. Mieno, "Conductive Cotton Textile from Safely Functionalized Carbon Nanotubes," Journal of Nanomaterials, 2015, 2015(1): p. 978484.

[26] A. Abbas, et al., "Cooling Effect of MWCNT-Containing Composite Coatings on Cotton Fabrics," The Journal of The Textile Institute, 2013, 104(8): pp. 798-807.

[27] M. Dai, et al., "A Green Approach to Preparing Hydrophobic, Electrically Conductive Textiles Based on Waterborne Polyurethane for Electromagnetic Interference Shielding with Low Reflectivity," Chemical Engineering Journal, 2021, 421: p. 127749.

[28] Y. Wang, et al., "Flexible, Durable and Thermal Conducting Thiol-Modified rGO-WPU/Cotton Fabric for Robust Electromagnetic Interference Shielding," Chemical Engineering Journal, 2019, 360: pp. 817-828.

[29] Y.-C. Soong, C.-W. Chiu, "Multilayered Graphene/Boron Nitride/Thermoplastic Polyurethane Composite Films with High Thermal Conductivity, Stretchability, and Washability for Adjustable-Cooling Smart Clothes," Journal of Colloid and Interface Science, 2021, 599: pp. 611-619.

[30] R.J. Slocombe, et al., "Phosgene Derivatives. The Preparation of Isocyanates, Carbamyl Chlorides and Cyanuric Acid," Journal of the American Chemical Society, 1950, 72: pp. 1888-1891.

[31] T. Gao, et al., "Three-Dimensional Printed Thermal Regulation Textiles," ACS Nano, 2017, 11(11): pp. 11513-11520.

[32] T. Gao, et al., "Three-Dimensional Printed Thermal Regulation Textiles," ACS Nano, 2017, 11(11): pp. 11513-11520.

[33] L.-H. Zhao, et al., "Simultaneously Improved Thermal Conductivity and Mechanical Properties of Boron Nitride Nanosheets/Aramid Nanofiber Films by Constructing Multilayer Gradient Structure," Composites Part B: Engineering, 2022, 229: p. 109454.

[34] Y. Hernandez, et al., "High-Yield Production of Graphene by Liquid-Phase Exfoliation of Graphite," Nature Nanotechnology, 2008, 3(9): pp. 563-568.

[35] M.A. Gatoo, et al., "Physicochemical Properties of Nanomaterials: Implication in Associated Toxic Manifestations," Biomed Research International, 2014, 2014: p. 498420.

[36] A.P. Alivisatos, "Perspectives on the Physical Chemistry of Semiconductor Nanocrystals," The Journal of Physical Chemistry, 1996, 100(31): pp. 13226-13239.

[37] H. Ha, et al., "Mini Review of Synthesis Strategies of Silver Nanowires and Their Applications," Colloid and Interface Science Communications, 2022, 50: p. 100663.

[38] A.P. Alivisatos, "Perspectives on the Physical Chemistry of Semiconductor Nanocrystals," The Journal of Physical Chemistry, 1996, 100: pp. 13226-13239.

[39] E. Roduner, "Size Matters: Why Nanomaterials Are Different," Chemical Society Reviews, 2006, 35(7): pp. 583-592.

[40] S.D. Huber, E. Altman, "Bose Condensation in Flat Bands," Physical Review B, 2010, 82(18): p. 184502.

[41] N.W. Ashcroft, N.D. Mermin, Solid State Physics, 2021: Cengage.

[42] X.M. Lin, et al., "Formation of Long-Range-Ordered Nanocrystal Superlattices on Silicon Nitride Substrates," The Journal of Physical Chemistry B, 2001, 105(17): pp. 3353-3357.

[43] D. Ugarte, et al., "Nanocapillarity and Chemistry in Carbon Nanotubes," Science, 1996, 274(5294): pp. 1897-9.

[44] C. Burda, et al., "Chemistry and Properties of Nanocrystals of Different Shapes," Chemical Reviews, 2005, 105(4): pp. 1025-1102.

[45] J. Chang, E.R. Waclawik, "Colloidal Semiconductor Nanocrystals: Controlled Synthesis and Surface Chemistry in Organic Media," RSC Advances, 2014, 4(45): pp. 23505-23527.

[46] H. Ghorbani, et al., "Biological and Non-Biological Methods for Silver Nanoparticles Synthesis," Chemical and Biochemical Engineering Quarterly, 2011, 25.

[47] A. Dong, et al., "A Generalized Ligand-Exchange Strategy Enabling Sequential Surface Functionalization of Colloidal Nanocrystals," Journal of the American Chemical Society, 2011, 133(4): pp. 998-1006.

[48] S. Bhakya, et al., "Biogenic Synthesis of Silver Nanoparticles and Their Antioxidant and Antibacterial Activity," Applied Nanoscience, 2016, 6(5): pp. 755-766.

[49] N. Depalo, et al., "α-Cyclodextrin Functionalized CdS Nanocrystals for Fabrication of 2/3 D Assemblies," The Journal of Physical Chemistry B, 2006, 110(35): pp. 17388-17399.

[50] C.M. Cobley, et al., "Shape-Controlled Synthesis of Silver Nanoparticles for Plasmonic and Sensing Applications," Plasmonics, 2009, 4(2): pp. 171-179.

[51] W. Xiong, et al., "Chapter 2 - Noble Metal–Based Nanosensors for Environmental Detection," in Advanced Nanomaterials for Pollutant Sensing and Environmental Catalysis, Q. Zhao, Editor. 2020, Elsevier, pp. 39-78.

[52] S. Agnihotri, et al., "Size-Controlled Silver Nanoparticles Synthesized Over the Range 5–100 nm Using the Same Protocol and Their Antibacterial Efficacy," RSC Advances, 2014, 4(8): pp. 3974-3983.

[53] J.Y. Cheon, et al., "Shape-Dependent Antimicrobial Activities of Silver Nanoparticles," Int J Nanomedicine, 2019, 14: pp. 2773-2780.

[54] X. Huang, et al., "Gold Nanorods: From Synthesis and Properties to Biological and Biomedical Applications," Adv Mater, 2009, 21(48): pp. 4880-4910.

[55] B. Bari, et al., "Simple Hydrothermal Synthesis of Very-Long and Thin Silver Nanowires and Their Application in High Quality Transparent Electrodes," Journal of Materials Chemistry A, 2016, 4(29): pp. 11365-11371.

[56] J. Mejía Méndez, et al., "Activities Against Lung Cancer of Biosynthesized Silver Nanoparticles: A Review," Biomedicines, 2023, 11: p. 32.

[57] X. Huang, et al., "Gold Nanorods: From Synthesis and Properties to Biological and Biomedical Applications," Advanced Materials, 2009, 21.

[58] K. Mavani, M. Shah, "Synthesis of Silver Nanoparticles by Using Sodium Borohydride as a Reducing Agent," 2013. doi:10.13140/2.1.3116.8648

[59] D.L.V. Hyning, et al., "Characterization of Colloidal Stability During Precipitation Reactions," Langmuir, 2001, 17: pp. 3120-3127.

[60] Q. Zhang, et al., "A Systematic Study of the Synthesis of Silver Nanoplates: Is Citrate a 'Magic' Reagent?" Journal of the American Chemical Society, 2011, 133(46): pp. 18931-18939.

[61] X. Dong, et al., "Shape Control of Silver Nanoparticles by Stepwise Citrate Reduction," Journal of Physical Chemistry C, 2009, 113: pp. 6573-6576.

[62] C. Iwuji, et al., "Synthesis and Characterization of Silver Nanoparticles and Their Promising Antimicrobial Effects," Chemical Physics Impact, 2024: p. 100758.

[63] S. Iravani, et al., "Synthesis of Silver Nanoparticles: Chemical, Physical and Biological Methods," Res Pharm Sci, 2014, 9(6): pp. 385-406.

[64] A.C. Ferrari, J. Robertson, "Interpretation of Raman Spectra of Disordered and Amorphous Carbon," Physical Review B, 2000, 61(20): pp. 14095-14107.

[65] M. Rehan, et al., "Towards Multifunctional Cellulosic Fabric: UV Photo-Reduction and In-Situ Synthesis of Silver Nanoparticles into Cellulose Fabrics," International Journal of Biological Macromolecules, 2017, 98: pp. 877-886.

[66] K. Chandrasekaran, J.K. Thomas, "The Mechanism of the Photochemical Oxidation of Water to Oxygen with Silver Chloride Colloids," Chemical Physics Letters, 1983, 97(4): pp. 357-360.

[67] S. Wang, et al., "Rapid Pressureless Low-Temperature Sintering of Ag Nanoparticles for High-Power Density Electronic Packaging," Scripta Materialia, 2013, 69(11): pp. 789-792.

[68] M. Li, et al., "Bimodal Sintered Silver Nanoparticle Paste with Ultrahigh Thermal Conductivity and Shear Strength for High Temperature Thermal Interface Material Applications," ACS Applied Materials & Interfaces, 2015, 7(17): pp. 9157-9168.

[69] F. Wang, et al., "Dispensing of High Concentration Ag Nanoparticles Ink for Ultra-Low Resistivity Paper-Based Writing Electronics," Scientific Reports, 2016, 6(1): p. 21398.

[70] A. Barucci, et al., "Label-Free SERS Detection of Proteins Based on Machine Learning Classification of Chemo-Structural Determinants," Analyst, 2021, 146(2): pp. 674-682.

[71] J.L. Mejía-Méndez, et al., "Activities Against Lung Cancer of Biosynthesized Silver Nanoparticles: A Review," Biomedicines, 2023, 11(2).

[72] H. Alam, S. Ramakrishna, "A Review on the Enhancement of Figure of Merit from Bulk to Nano-Thermoelectric Materials," Nano Energy, 2013, 2(2): pp. 190-212.

[73] S. Kim, B. Hwang, "Ag Nanowire Electrode with Patterned Dry Film Photoresist Insulator for Flexible Organic Light-Emitting Diode with Various Designs," Materials & Design, 2018, 160: pp. 572-577.

[74] L.F. Gerlein, et al., "High-Performance Silver Nanowires Transparent Conductive Electrodes Fabricated Using Manufacturing-Ready High-Speed Photonic Sinterization Solutions," Scientific Reports, 2021, 11(1): p. 24156.

[75] S.I. White, et al., "Electrical Percolation Behavior in Silver Nanowire–Polystyrene Composites: Simulation and Experiment," Advanced Functional Materials, 2010, 20.

[76] G. Barbillon, "Latest Novelties on Plasmonic and Non-Plasmonic Nanomaterials for SERS Sensing," Nanomaterials, 2020, 10, DOI: 10.3390/nano10061200.

[77] Y.-J. Zhang, et al., "Plasmonic Core–Shell Nanomaterials and Their Applications in Spectroscopies," Advanced Materials, 2021, 33.

[78] D. Tan, et al., "Recent Advances in MXene-Based Force Sensors: A Mini-Review," RSC Advances, 2021, 11(31): pp. 19169-19184.

[79] M.K. Francis, et al., "Ag Nanowires Based SERS Substrates with Very High Enhancement Factor," Physica E: Low-Dimensional Systems and Nanostructures, 2022, 137: p. 115080.

[80] M.R. Azani and A. Hassanpour, "Synthesis of Silver Nanowires with Controllable Diameter and Simple Tool to Evaluate Their Diameter, Concentration and Yield," ChemistrySelect, 2019.

[81] M. Mazur, “Electrochemically prepared silver nanoflakes and nanowires,” Electrochemistry Communications, 2004. 6(4): p. 400-403.

[82] G. Riveros, et al. “Silver nanowire arrays electrochemically grown into nanoporous anodic alumina templates,” Nanotechnology, 2006. 17(2): p. 561.

[83] C.R. Martin, “Nanomaterials: A Membrane-Based Synthetic Approach,” Science, 1994. 266: p. 1961-1966.

[84] N.R. Jana, et al., “Wet chemical synthesis of silver nanorods and nanowires of controllable aspect ratio,” Chemical Communications, 2001(7): p. 617-618.

[85] J. Liu, et al, “Nanoscale metal−organic frameworks for combined photodynamic & radiation therapy in cancer treatment,”Biomaterials, 2016. 97: p. 1-9.

[86] B. El, et al., “DNA-Templated Assembly and Electrode Attachment of a Conducting Silver Wire,” Nature, 1998. 391: p. 775-8.

[87] L. Berti, et al., “DNA-Templated Photoinduced Silver Deposition,” Journal of the American Chemical Society, 2005. 127(32): p. 11216-11217.

[88] J. Lu, et al., “DNA-templated photo-induced silver nanowires: Fabrication and use in detection of relative humidity,” Biophysical Chemistry, 2009. 145(2): p. 91-97.

[89] T. Muhmood, et al., “Silver nanowires: a focused review of their synthesis, properties, and major factors limiting their commercialization,” Nano Futures, 2022. 6.

[90] B. Wiley, et al., “Polyol Synthesis of Silver Nanoparticles: Use of Chloride and Oxygen to Promote the Formation of Single-Crystal, Truncated Cubes and Tetrahedrons,” Nano Letters, 2004. 4(9): p. 1733-1739.

[91] S. Coskun, et al., “Polyol Synthesis of Silver Nanowires: An Extensive Parametric Study,” Crystal Growth & Design, 2011. 11(11): p. 4963-4969.

[92] C. Ducamp-Sanguesa, et al.,“Synthesis and characterization of fine and monodisperse silver particles of uniform shape,” Journal of Solid State Chemistry, 1992. 100(2): p. 272-280.

[93] Y. Sun and Y. Xia, “Shape-Controlled Synthesis of Gold and Silver Nanoparticles,” Science, 2002. 298(5601): p. 2176-2179.

[94] T. Muhmood, et al., “Silver nanowires: a focused review of their synthesis, properties, and major factors limiting their commercialization,” Nano Futures, 2022. 6(3): p. 032006.

[95] K.E. Korte, et al., “Rapid synthesis of silver nanowires through a CuCl- or CuCl2-mediated polyol process,” Journal of Materials Chemistry, 2008. 18(4): p. 437-441.

[96] J. Jiu, et al., “Facile synthesis of very-long silver nanowires for transparent electrodes,” Journal of Materials Chemistry A, 2014. 2(18): p. 6326-6330.

[97] K.K. Caswell, et al., “Seedless, Surfactantless Wet Chemical Synthesis of Silver Nanowires,” Nano Letters, 2003. 3(5): p. 667-669.

[98] K.E. Korte, et al., “Rapid synthesis of silver nanowires through a CuCl- or CuCl2-mediated polyol process,” Journal of Materials Chemistry, 2008. 18: p. 437-441.

[99] C. Amicucci, et al, “Cost Effective Silver Nanowire-Decorated Graphene Paper for Drop-On SERS Biodetection,” Nanomaterials (Basel), 2021. 11(6).

[100] S.X. Leong, et al., “Chapter 2 - Nanoplasmonic materials for surface-enhanced Raman scattering, in Principles and Clinical Diagnostic Applications of Surface-Enhanced Raman Spectroscopy,” Elsevier Y. Wang, Editor, 2022, p. 33-79.

[101] M.S. Goh, et al., “A chemical route to increase hot spots on silver nanowires for surface-enhanced Raman spectroscopy application,” Langmuir, 2012. 28(40): p. 14441-9.

[102] Y. Ahn, et al., “Highly Conductive and Flexible Silver Nanowire-Based Microelectrodes on Biocompatible Hydrogel,” ACS Applied Materials & Interfaces, 2014. 6(21): p. 18401-18407.

[103] S. Ye, et al., “Metal nanowire networks: the next generation of transparent conductors.,” Adv Mater, 2014. 26(39): p. 6670-87.

[104] J.M. Linge, et al., “Silver Nanowire-Based Catalysts for Oxygen Reduction Reaction in Alkaline Solution,” ChemCatChem, 2021. 13.

[105] B. Martín-García, et al., “Electronic Supplementary Information Efficient Charge Transfer in Solution-Processed PbS Quantum Dot-Reduced Graphene Oxide Hybrid Materials,” 2015.

[106] C. Ingrosso, et al., “Photoactive Hybrid Material Based on Pyrene Functionalized PbS Nanocrystals Decorating CVD Monolayer Graphene,” ACS Applied Materials & Interfaces, 2015. 7(7): p. 4151-4159.

[107] K.S. Novoselov, et al., “Electric field effect in atomically thin carbon films,” Science, 2004. 306(5696): p. 666-9.

[108] C. Gómez-Navarro, et al., “Electronic transport properties of individual chemically reduced graphene oxide sheets,” Nano Lett, 2007. 7(11): p. 3499-503.

[109] K.S. Novoselov, et al., “A roadmap for graphene,” Nature, 2012. 490(7419): p. 192-200.

[110] V. Georgakilas, et al., “Functionalization of Graphene: Covalent and Non-Covalent Approaches, Derivatives and Applications,” Chemical Reviews, 2012. 112(11): p. 6156-6214.

[111] F. Porta, et al., “New Au(0) Sols as Precursors for Heterogeneous Liquid-Phase Oxidation Catalysts,”Journal of Catalysis, 2002. 211(2): p. 464-469.

[112] T. Kim, et al., “Supersonically Sprayed Washable, Wearable, Stretchable, Hydrophobic, and Antibacterial rGO/AgNW Fabric for Multifunctional Sensors and Supercapacitors,” ACS Appl Mater Interfaces, 2021. 13(8): p. 10013-10025.

[113] X. An, et al., “Stable Aqueous Dispersions of Noncovalently Functionalized Graphene from Graphite and their Multifunctional High-Performance Applications,” Nano Letters, 2010. 10(11): p. 4295-4301.

[114] W. Kong, et al., “Path towards graphene commercialization from lab to market,” Nature Nanotechnology, 2019. 14(10): p. 927-938.

[115] C. Ingrosso, et al., “Solvent dispersible nanocomposite based on Reduced Graphene Oxide and in-situ decorated gold nanoparticles,” Carbon, 2019.

[116] M. Brust, et al., “Synthesis of thiol-derivatised gold nanoparticles in a two-phase Liquid–Liquid system,” Journal of the Chemical Society, Chemical Communications, 1994(7): p. 801-802.

[117] M. Wuithschick, et al., “Turkevich in New Robes: Key Questions Answered for the Most Common Gold Nanoparticle Synthesis,” ACS Nano, 2015. 9(7): p. 7052-7071.

[118] F. Vischio, et al., “Au nanoparticles decorated nanographene oxide-based platform: Synthesis, functionalization and assessment of photothermal activity,” Biomaterials advances, 2022. 145: p. 213272.

[119] C. Ingrosso, et al., “Au nanoparticle in situ decorated RGO nanocomposites for highly sensitive electrochemical genosensors,” Journal of Materials Chemistry B, 2019. 7(5): p. 768-777.

[120] H.H. and F.E. Osterloh, “A Simple Large-Scale Synthesis of Nearly Monodisperse Gold and Silver Nanoparticles with Adjustable Sizes and with Exchangeable Surfactants,” Chemistry of Materials, 2004. 16: p. 2509-2511.

[121] A.A. Grace, “Phasic versus tonic dopamine release and the modulation of dopamine system responsivity: a hypothesis for the etiology of schizophrenia,” Neuroscience, 1991. 41(1): p. 1-24.

[122] D. Chaudhury, et al., “Rapid regulation of depression-related behaviours by control of midbrain dopamine neurons,” Nature, 2013. 493(7433): p. 532-6.

[123] S. Ahn, et al., “π–π Interactions Mediated Pyrene Based Ligand Enhanced Photoresponse in Hybrid Graphene/PbS Quantum Dots Photodetectors,” Advanced Electronic Materials, 2022. 8(1): p. 2100672.

[124] C. Ingrosso, et al., “Enhanced photoactivity and conductivity in transparent TiO2 nanocrystals/graphene hybrid anodes,” Journal of Materials Chemistry A, 2017. 5(19): p. 9307-9315.

[125] S. Bhattacharjee, et al., “Nanoparticles incorporated graphene-based durable cotton fabrics,” Carbon, 2020. 166: p. 148-163.

[126] N. Noor, et al., “Durable Antimicrobial Behaviour from Silver-Graphene Coated Medical Textile Composites,” Polymers (Basel), 2019. 11(12).

Experimental results

In this section, I report on the synthesis and development of novel hybrid nanocomposites composed of RGO sheets functionalized with the biocompatible and water-soluble amino acid histidine (His), and subsequently decorated with Ag nanostructures of varying morphologies (NPs and NWs). These hybrid materials are synthesized using sustainable *in situ* and *ex situ* colloidal approaches, with the objective of engineering multifunctional nanocomposites for diverse applications, such as antimicrobial and thermally conductive coatings for cotton fabrics and Surface-Enhanced Raman Spectroscopy (SERS)-active substrates for the detection of pharmaceutical molecules on flexible substrates.

The synthesis of the His-RGO/Ag NPs and His-RGO/Ag NWs nanocomposites, respectively, is investigated, exploring the effect of the experimental conditions on the resulting materials, that are then thoroughly characterized integrating different complementary techniques for their elucidating their chemical and physical properties. This section delves into the optimization of the synthesis process, systematically varying experimental conditions, such as precursor concentrations, reducing agents, and reaction pH, to fine-tune the size and shape of the Ag nanostructures, while simultaneously characterizing spectroscopic and morphological properties of the resulting nanocomposites. The reaction mechanisms driving their synthesis are explained, finally exploring the performances of the hybrid nanocomposites for the different targeted applications.

The experimental work presented here is, therefore, divided into three chapters, each focusing on different applications of the His-RGO/Ag nanocomposites:

Chapter 3: *In Situ Decoration of Reduced Graphene Oxide (RGO) with AgNPs: Cotton Fabric Functionalization with a Thermally Conductive Coating*. A thermally conductive nanocomposite coating for cotton, formed of His-RGO sheets decorated by Ag NPs, here named as Cot-His-RGO/Ag, was prepared by synthesizing Ag NPs, *in situ*, on the coordinating sites of cotton fabrics modified by impregnation with His-RGO, and then impregnated by aqueous methanol solutions of the $AgNO_3$ precursor, under UV-light exposure, without the need of chemical reducing agents. RGO was selected for its high thermal conductivity, and its decoration with Ag NPs was designed to enhance intersheet heat diffusion. This method demonstrates potential scalability and sustainability to produce thermally conductive textiles. The research activity presented in this chapter was performed in the frame of the TRANSISTOR project (BRIC, ID:33-2019) funded by INAIL, working in collaboration with the groups of Prof. Carola Corcione and Dr. Claudio Mele, both at the University of Salento (Italy) Prof. Antonella Milella at Dept. of Chemistry (University of Bari) (Italy) and with Dr. Giuseppe Bianco at CNR-NANOTEC, Bari (Italy).

Chapter 4: *Silver Nanoparticle-Decorated RGO Hybrid Nanocomposites: Synthesis, Characterization, and Durable Antimicrobial Efficacy for Textile Coatings*. This chapter reports on the synthesis, characterization, and long-term antimicrobial performance of a nanocomposite based on His-RGO sheets decorated by spherical Ag NPs (His-RGO/Ag NPs). The nanocomposite was synthesized, in aqueous solutions and at low temperature, by reduction of the $AgNO_3$ precursor, *in situ*, onto the sheets of the His-RGO complex, in presence of sodium borohydride ($NaBH_4$) and trisodium citrate tribasic dehydrate ($Na_3C_6H_5O_7 \times 2H_2O$), the reducing and coordinating agents, for the manufacture, by impregnation, of an antimicrobial coating for cotton fabrics. The antimicrobial efficacy was assessed using the standardized ISO 20743:2021 method, with *Escherichia coli (E. coli)* employed as a model Gram-negative bacterium. This research activity was performed in the frame of the PON (2014-2020) ECOTEC (ARS 01_00951) project, working in collaboration with Dr. Ilaria De Pasquale at CNR-IPCF Bari (Italy), Prof. Antonella Milella at Department of Chemistry (University of Bari, Italy), and Dr. Giuseppe Bianco at CNR-NANOTEC Bari (Italy).

Chapter 5*: Green synthesis of Ag NW-decorated RGO nanocomposites via a combined in situ–ex situ approach deposited on paper for SERS detection of drugs and pollutants.* This study involves the development of a hybrid nanocomposite composed of His-RGO and Ag NWs, synthesized via an *in situ-ex situ* approach. This nanocomposite was evaluated as a flexible substrate for SERS-based detection of pharmaceutical molecules, such as propranolol hydrochloride (PRNL), with enhanced detection sensitivity following plasma treatments. The research activity presented in this chapter was conducted in collaboration with the FunNanobio research Group of the Departamento de Química Física y CINBIO, led by Professor Jorge Perez Juste at the University of Vigo (Spain), where I spent a period of six months from January to July 2024, to develop, test and validate the nanocomposite for SERS detection of drug.

Chapter 3

In Situ Decoration of Reduced Graphene Oxide (RGO) with AgNPs:Cotton Fabric Functionalization with a Thermally Conductive Coating

The application of thermally conductive materials as coatings on fiber surfaces represents an innovative technology solution for conveying heat dissipation capability to IR-opaque textiles. In this work, a sustainable and scalable approach to manufacture a thermally conductive hybrid nanocomposite coating for cotton, formed by RGO sheets functionalized by histidine (His) and decorated by Ag NPs, is reported. Tens nm in size Ag NPs were synthesized, *in situ,* at the coordinating sites of the His-RGO modified cotton impregnated by H_2O/CH_3OH solutions of the $AgNO_3$ precursor, under UV-light exposure, without using chemical reductants. The physical chemical properties of the nanocomposite modified fabrics were comprehensively investigated integrating chemical and structural analysis, as UV-Vis absorption, XPS, and Raman spectroscopies, SEM-EDS technique, AFM, and functional characterization by thermal, electrical, oxygen permeability and surface wettability measurements and mechanical tests. The resulting coating exhibits a thermal conductivity, which was twice as high as untreated cotton, maintaining its oxygen permeability, increasing its flexibility, while simultaneously reducing its wettability. This notable enhancement can be attributed to the synergistic effect of the conductive Ag nanostructures and His-RGO sheets within the nanocomposite, and it matches the thermal conductivity achieved by state-of-the-art methods, while offering additional advantages of being more eco-friendly, scalable, and sustainable. The reported characterization of the structural properties of the achieved coating opens the venue to interesting perspectives towards its application in passive conducting cooling textiles for an effective personal thermal comfort management.

3.1 Introduction

Recently, increasing attention has been devoted to innovative strategies aiming to engineer textiles to fulfill technological demands to overcome lack of functionalities of traditional ones and conveying additional properties, like hydrophobicity, flame retardancy, self-cleaning, antimicrobial, electric and thermal conductivity, antiwrinkle, antistatic and UV radiation shielding [1-4]. Nanostructured materials and nanocomposites, showing high surface to volume ratio, along with original chemical and physical properties depending on morphology and chemical composition [5-6], are optimal candidates for effectively conveying to fabrics novel functionalities, without detrimentally affecting their breathability or texture.

In this frame, textiles featuring advanced thermoregulatory characteristics have been regarded as original solutions for accomplishing human thermal comfort, addressing the need of high-performance textiles in industries such as sports, medical, and aerospace, where thermal management is crucial [7-8]. Among these, passive cooling textiles, which are designed to enhance human body heat dissipation through the fabrics without consuming extra energy [9], manage personal thermal comfort by regulating heat exchange between skin and surrounding environment, by enhancing transmission of mid infrared radiation, decreasing near infrared radiation absorption, and increasing human body heat loss by thermal conduction [10].

To the best of our knowledge, few studies have focused on engineering textiles and patches for fulling such a challenge, and each one offers an innovative solution, exhibiting concomitantly, however, limitations as well. Among these, some approaches report on the fabrication of textiles with high thermal conductivity, where heat conduction inside an IR-opaque textile is the primary heat dissipation pathway; some routes consist of coating, by impregnation, natural textiles as cotton, which is favored for its softness, wear comfort and breathability, with high thermally conductive nanofillers or their formulations with polymers. As for example, cotton has been modified by impregnation with carbon nanotubes [11], with polymer formulations based on epicholorohydrin based resin modified by thermally conductive nanostructures like carbon nanotubes, boron nitride nanosheets (BNNSs), and graphene derivatives [12-14], and formulations formed of graphene nanoplatelets and BNNSs embedded in polyurethane (PU) [15-17]. Although these routes are the simplest and the most scalable ones, accomplishing a significant improvement in thermal conductivity, their scaling up is challenged, because of the unsafe use of hazardous precursors in the PU synthesis and toxic byproducts from epichlorohydrin-based resins [18]. As an alternative to these issues, few approaches have used formulations of biocompatible polymers heavily loaded with high thermally conductive nanofillers but are however limited to the fabrication of patches and use of fossil-fuel based polymers, and, in some cases, also toxic organic solvents. As an example, polymer nanocomposites based on BNNs embedded into polyvinylalcohol (PVA)/dimethyl sulfoxide formulations have been fabricated into fibers through a hot-drawn 3D printing process, and the resulting patches have a thermal conductivity increased up to 0.078 $W\ m^{-1}\cdot K^{-1}$, which is 2.2 times higher than cotton and 1.6 times higher than neat PVA fabrics [19]. As an alternative, few other works have focused on fabricating patches formed of biodegradable polymers heavily loaded with high thermally conductive nanostructures. In this regard, patches of cellulose/alkaline/urea solutions modified with 60 wt% edge-selective hydroxylated BNNSs, achieved through wet-spinning and weaving, have reached a thermal conductivity increase from 0.86 $W\ m^{-1}\ K^{-1}$ up to 2.914 $W\ m^{-1}\ K^{-1}$ [20]. Also, silk fibroin patches, loaded with 50 wt% exfoliated BNNs reached 1.77 $W\ m^{-1}\ K^{-1}$ using vacuum filtration, have been developed [21]. Despite being eco-friendly, these last methods necessitate costly fabrication technologies and a high concentration of nanofillers, which exhibit chemical inertness and strong interlayer interactions, limiting sustainability and scalability of the approach.

From this picture it therefore emerges that the development of passive cooling textiles by ecofriendly and sustainable approaches is still an unsolved challenge. In this work, a thermally conductive coating based on modified cotton was prepared by impregnation with a nanocomposite formed of histidine functionalized Reduced Graphene Oxide (His-RGO) *in situ* decorated with Ag NPs. RGO possesses the thermal conductivity closest to that of monolayer graphene, which ranges from 370−600 $W\ mK^{-1}$ when supported onto a substrate [22], and compared to BNNs, it has a higher chemical reactivity affording superior exfoliation and chemical modification capability, opening the venue to technologies that do not solely encompass a good conductivity, but exploit also the functionalities of molecular species anchored onto its basal plane.

His was selected as a biocompatible exfoliating agent of RGO, enabling its dispersion in water [23-24]. His binds RGO by aromatic π-π stacking interactions, without introducing additional structural defects, detrimental for its thermal and electrical conductivity [25], and grafts RGO with -COO$^-$ and imidazole nitrogen functionalities, effective in coordinating nanostructures [26].

RGO sheets were decorated with NPs of Ag, which is characterized by high thermal conductivity (429 WmK^{-1}) [27], as able in principle to improve interlayer heat diffusion, bridging adjacent RGO sheets [28]. These coatings were achieved through *in situ* photoreduction via UV-light irradiation of His-RGO coated fabrics soaked in $AgNO_3$ aqueous methanol solutions [29,30], a method proven successful in decorating cotton with Ag NPs for commercial antimicrobial textiles [29,30], demonstrating viability in terms of scalability and sustainability. This approach circumvents the requirement of using strong and hazardous reductants (e.g., $NaBH_4$) or even milder alternatives (e.g., citrate, ascorbic acid), which all necessitate time-consuming washing steps to optimize thermal conduction.

3.2 Materials and methods

Chemicals and Materials. Reduced Graphene Oxide (RGO) was purchased from Graphene Supermarket (1.6 µm thick flakes), histidine (His) from Alpha Aesar, methanol ($CH_3OH \geq 99.9\%$), acetone (99.9%) and silver nitrate ($AgNO_3$, > 99%) from Sigma Aldrich. All these chemicals were used as received without further purification. Aqueous solutions were prepared by using Milli-Q water (18.2 MΩ·cm, organic carbon content ≥ 4 µg L^{-1}) achieved by a Milli-Q gradient A-10 system.

Exfoliation and functionalization of RGO by His. 100 mg of RGO powder were stirred in 100 mL of His aqueous solutions (1.6 mg mL^{-1}), at room temperature, for allowing its intercalation among and functionalization of the sheets [23,24]. Then, the His-RGO dispersion was purified from the excess of His by four cycles of ultracentrifugation (45000 rpm for 30 min), sonicated in water at pH 11 in an ice cooled US bath for 5 h, and then purified by two and four cycles of ultracentrifugation (45000 rpm for 30 min). Finally, the isolated His-RGO powder was dispersed in water at neutral pH, at a concentration of 4 mg ml^{-1} and sonicated for 6 h.

Pre-treatment of cotton (Cot). Cot fabrics were washed to remove contaminants from the fibers by stirring in acetone for 8 h, followed by three cycles of washing in water at 40°C, alternated each one by a drying step onto a hotplate at 50°C [31].

Modification of Cot fabrics with His-RGO (Cot/His-RGO). Cot fabrics were impregnated with 4 mg/ml His-RGO aqueous dispersions at neutral pH, by two dipping steps of 3 h, followed by overnight dipping, and finally, by others two dipping steps of 3 h. Each dipping step was followed by drying at 50°C onto a hotplate. These samples are called Cot/His-RGO (Table 1).

Preparation of the Ag NPs coated Cot/His-RGO fabrics (Cot/His-RGO/Ag). The *in situ* synthesis of the Ag NPs onto the Cot/His-RGO fabrics was performed soaking overnight the fabrics in 0.1 g mL^{-1} $AgNO_3$ water/methanol mixed solutions, where two different water/methanol volume ratio were tested, namely 9:1 v/v and 1:1 v/v, and then, the Ag^+ ions were allowed to reduce onto the wet Cot/His-RGO fabrics in air and under UV-light irradiation [29,30] (λ = 254 nm, 0.2 mW cm^{-2}) for 30 min. The samples were placed 10 cm orthogonally from the UV-light lamp source. These samples were named Cot/His-RGO/Ag$_{\_9:1,UV}$ and Cot/His-RGO/Ag$_{\_1:1,UV}$, respectively (Table 1). As a purpose of comparison, Cot/His-RGO samples wet in 9:1 v/v and 1:1 v/v water/methanol mixtures and exposed to UV-light irradiation, as well as Cot/His-RGO samples impregnated by 0.1 g mL^{-1} AgNO$_3$ 1:1 v/v water/methanol mixed solutions dried in dark conditions at ambient atmosphere, were investigated. These samples are named Cot/His-RGO$_{\_9:1,UV}$, Cot/His-RGO$_{\_1:1,UV}$ and Cot/His-RGO/Ag$_{\_1:1}$, respectively (Table 3.1).

Table 3.1. Samples investigated in the work.

Sample	**UV-light exposure**	**AgNO$_3$ (g mL^{-1})**	**H$_2$O (mL)**	**CH$_3$OH (mL)**
Cot/His-RGO	No	---	---	---
Cot/His-RGO$_{\_1:1,UV}$	Yes	---	5	5
Cot/His-RGO/Ag$_{\_1:1}$	No	0.1	5	5
Cot/His-RGO/Ag$_{\_1:1,UV}$	Yes	0.1	5	5
Cot/His-RGO$_{\_9:1,UV}$	Yes	---	9	1
Cot/His-RGO/Ag$_{9:1,UV}$	Yes	0.1	9	1

Characterization techniques.

UV-Vis absorption spectra in reflectance mode were collected at room temperature by means of a Cary 5000 (Varian) UV/Vis/NIR spectrophotometer equipped with an integration sphere to measure the Diffuse Reflectance. Raman spectra were recorded by using a LabRAM HR Horiba-Jobin Yvon spectrometer with an excitation wavelength of 532 nm. Measurements were carried out under ambient conditions at low laser power (1 mW) to avoid laser-induced damage of the sample. The Raman signal from the silicon wafer at 520 cm^{-1} was used to calibrate the spectrometer and accuracy of the spectral measurement was 1 cm^{-1}. X-Rays Photoelectron Spectroscopy (XPS) analyses were carried out with a Scanning XPS Microprobe (PHI 5000 Versa Probe II, Physical Electronics) equipped with a monochromatic Al Kα X-ray source (1486.6 eV), operating at 15 kV and 24.8 W, with a spot size of 100 µm. Survey (0–1200 eV) and high-resolution spectra (C1s, O1s, N1s and Ag3d) were recorded in FAT (Fixed Analyser Transmission) mode at a pass energy of 117.40 eV and 29.35 eV, respectively. All spectra were collected at an angle of 45° with respect to the sample surface. Charging was compensated using a dual beam charge neutralization system with a flux of low energy electrons (~1 eV) combined with very low energy positive Ar$^+$ ions (10 eV). The hydrocarbon component of C1s spectrum was used as internal standard for charging correction and it was fixed at 285.0 eV. Best-fitting of the high-resolution spectra was carried out with MultiPak data processing software (Physical Electronics). Attenuated Total Reflection Fourier Transform Infrared (ATR-FTIR) spectroscopy was carried out by a 670 FTIR spectrometer (Varian, Palo Alto, CA, USA) equipped with a diamond ATR accessory of 2 mm and a deuterated tryglicine sulfate (DTGS) detector. Samples were drop-cast on the internal reflection element and solvent was allowed to evaporate. Spectra were recorded in the range of 4000–400 cm^{-1}, acquiring 16 scans with a nominal resolution of 1 cm^{-1}. Transmission Electron Microscopy (TEM) analyses were performed by a Jeol Jem-1011 microscope operating at 100 kV, equipped by a high-contrast objective lens and a W filament as electron source, with an ultimate point resolution of 0.34 nm. Images were acquired by a Quemesa Olympus CCD 11 Mp Camera. Samples were prepared dipping a 300 mesh amorphous carbon-coated Cu grid in aqueous dispersions of His-RGO, then leaving the solvent to evaporate at room temperature. Field Emission Scanning Electron Microscopy (FE-SEM) measurements were performed by a Zeiss Sigma microscope (Carl Zeiss Co., Oberkochen, Germany) operating in the range of 0.5–20 KV and equipped with an in-lens secondary electron detector and an INCA Energy Dispersive Spectroscopy (EDS) detector. Samples were mounted onto stainless-steel sample holders by double-sided conductive carbon tape and grounded by silver paste. Size statistical analysis of the Ag nanostructures average size was performed by the ImageJ analysis software.

Thermal conductivity measurements.

Thermal conductivity (TC) was estimated by Differential Scanning Calorimetry (Mettler Toledo TGA/DSC1 Stare System). A sensor material, i.e. Indium (Tm= 156.6°C) was placed onto the fabrics and heated from 20°C to 200°C at 10°C min^{-1} in nitrogen atmosphere (N_2 flow: 60ml min^{-1}). Averaged values were obtained by at least three measurements for each sample. For calculating TC, the Flynn and Levin's method [32] was employed, and the thermal resistance of the fabric sample (Rs) was defined according to Eq. (1):

$$R_s = R' - R \qquad (1)$$

where R′ and R are the thermal resistances determined by the slope of the Indium melting peak with and without the fabric sample, respectively.

TC was estimated according to Eq. (2):

$$TC = \frac{L}{A(R'-R)} = \frac{L}{AR_S} \qquad (2)$$

where L is the sample thickness and A is the contact area between the sample and Indium sensor.

Tensile Tests.

Mechanical properties of the untreated and treated cotton samples were characterized by a dynamometer (Lloyd LR5K) equipped with a load cell of 100N, displacement speed of 10 mm min^{-1} and jaw length 40mm. The fabrics were cut along the texture with size of 120 x 13 x 0.2 mm. Five replicates were performed for each sample. The achieved mean values of tensile strength (σ), strain at break (ε) and tensile modulus (E) were measured.

Static water contact angle analysis.

Static water contact angle (WCA) measurements of untreated and treated cotton fabrics were performed using bi-distilled water (surface tension γ= 72.1 mN m^{-1}). The analyses were performed at room temperature by means of the sessile drop technique according to NORMAL Protocol 33/89 [33]. Five measurements of each specimen were performed to achieve average values and standard deviation.

Surface Resistivity measurements.

Surface Resistivity of cotton fabric was measured according to the American Association of Textile Chemists and Colorists (AATCC) Test Method n. 76-2005 [34]. A parallel plate electrodes configuration was used. The fabric was placed in contact with the electrodes and covered with a corning glass onto which a weight was positioned to apply a constant pressure between the fabric and the electrodes. Resistance between electrodes was measured in both length and width directions of the fabric sample. Surface resistance (Rs) was estimated as:

$$R_s = \frac{R \times W}{D}$$

where R is the measured resistance, W is the width of the fabric and D is the distance between the electrodes.

Washing durability.

Durability of the Cot/His-RGO/$Ag_{\_1:1,UV}$ samples was assessed by measuring the TC and the static WCA mean values upon 5, 10 and 20 washing cycles of the fabrics with tap water, which were performed by using a centrifuge at the speed of 2000 rpm for 15 min and drying the samples at 60°C for 3 hr 3 h.

Oxygen permeability tests

Oxygen permeability of the neat Cot and of the Cot/His-RGO/$Ag_{\_1:1,UV}$ samples were measured by means of the Multiperm ExtraSolution instrument (PermTech Srl). The tests were carried out on 2 cm^2 samples at 23 °C with 0% relative humidity.

Atomic Force Microscopy (AFM) analyses

The surface topography and roughness of the specimens were examined using a Bruker Multimode 8 atomic force microscope (AFM) in tapping mode under ambient conditions. The images were obtained with scan sizes of 5 × 5 μm^2, and a scan rate of 0.5 Hz. The cantilever employed was a Scanasyst-air with a resonance frequency of 70 kHz and a spring constant of 0.4 N m^{-1}. Nanoscope Analysis software version 1.5 was utilized for data processing.

3.3 Results and discussion

3.3.1 His-RGO functionalization of cotton fabrics

Commercial Reduced Graphene Oxide (RGO) was exfoliated and functionalized with histidine (His) in water at pH 11 under sonication (Fig.3.1a). A purification procedure of the His-RGO dispersion was further performed by ultracentrifugation cycles to remove His in excess (see Materials and methods) [23,24]. The absorption spectra of the supernatants collected after each ultracentrifuge step of the His-RGO dispersion show that the intensity of the absorption shoulder at 275 nm, which is ascribed to the n-π* transition of the His imidazole ring [35] (Appendix 1,Fig. 1 of Supplementary material), becomes almost negligible after the third ultracentrifugation cycle, assessing the nearly complete removal of free His from the His-RGO dispersion.

His is expected to intercalate between the RGO multilayers [26,36] and binds its basal plane via aromatic π–π stacking interactions with the imidazole ring (Fig.3.1a) [23,24]. The structures of the His-RGO complex achieved after exfoliation appear nearly electron transparent in the TEM micrographs, are few µm in lateral size, and present higher image contrast features, reasonably due to folded edges and wrinkles (Fig.3.1b). Also, few layers of His-RGO have been observed in the sample. UV-Vis absorption spectra of the His-RGO aqueous dispersions show an absorption peak at 275 nm, which is ascribed to the characteristic π-π* transition of the -C=C- bond of RGO (Fig.3.1c), that superimposes that of His, which is expected at ca. 263 nm and reasonably ascribed to intramolecular π-π* transitions of the His imidazole ring [37], likely because of its low concentration in the His-RGO complex. Typical UV-Vis absorption features of molecular linkers functionalizing by aromatic π-π interactions the basal plane of RGO, as pyrene molecules, were observed at RGO:pyrene w/w significantly lower (1:17) [36,38] than that one used here in the preparation of the His-RGO complex, that is 1:1.6. This high w/w was purposely selected to limit the decrease of the thermal conductivity of RGO, that is induced by the organic His coating layer [39].

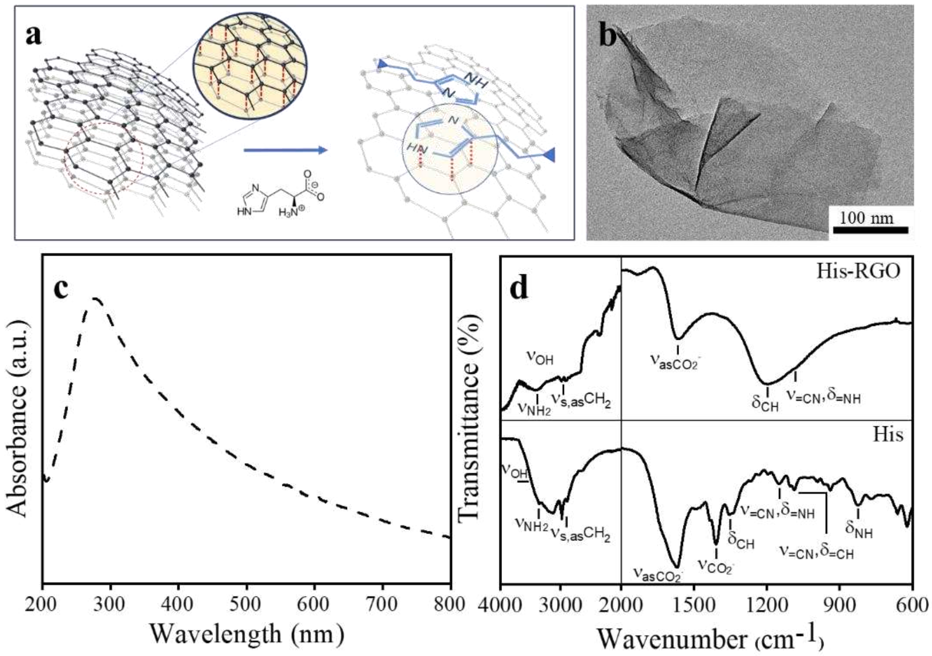

Fig. 3.1: *(a) Sketch of the exfoliation and functionalization of RGO in His solutions at pH 11. (b) TEM micrograph of His-RGO. (c) UV-Vis absorption spectra of 0.04 mg mL^{-1} His-RGO aqueous dispersions. (d) ATR-FTIR spectra of powders of His-RGO and His, deposited respectively from 4 mg mL^{-1} aqueous dispersions and solutions at pH 11. (The sketch is not drawn to scale).*

The successful functionalization of the RGO basal plane by His is provided by the Attenuated Total Reflection Fourier Transform Infrared (ATR-FTIR) spectra of powders of the His-RGO complex. Such infrared spectra, in fact, evidence, in the high wavenumber region, the stretching vibration of -NH$_2$ (υ_{NH2}) groups at 3394 cm^{-1}, as well as the symmetric and asymmetric stretching modes of $-CH_2$ moieties ($\upsilon_{s,asCH2}$) at 2988 cm^{-1} and 2901 cm^{-1}, respectively, observed also in the neat His (Fig. 1d). The His-RGO spectra show also the $-COO^-$ (νCOO^-) asymmetric stretching at 1564 cm^{-1} and a broad band between ca. 1380-695 cm^{-1}, originating from the overlapping of the aliphatic -CH bending (δ_{CH}), imidazole =CN stretching ($\upsilon_{=CN}$), =NH bending ($\delta_{=NH}$) and =CH bending ($\delta_{=CH}$), evident in the infrared spectrum of His at 1193 cm^{-1}, 1149 cm^{-1} and 1086 cm^{-1} [40], respectively, definitely assessing the modification of RGO with His.

Cotton (Cot) impregnation was performed by dipping in 4 mg ml^{-1} His-RGO aqueous dispersions at neutral pH. In such a condition, imidazole nitrogen atoms and carboxylate side chain groups in His are expected to favor chemisorption of His-RGO onto Cot, due to their hydrogen bond interactions (Fig.3.2a) with the hydroxyl groups of the textile (Appendix 1, Fig. 2). Cot modified by His-RGO (Cot/His-RGO) presents in its absorption spectrum the peak of RGO at 275 nm (Appendix 1,Fig.3).

Scanning Electron Microscopy (SEM) micrographs show the barely smooth and bright in image contrast surface morphology of the neat Cot fabrics (Fig.3.2b), that significantly changes, becoming darker in the image contrast, rough, and coated by a dense layer of flakes after modification with the His-RGO sheets (Fig.3.2c).

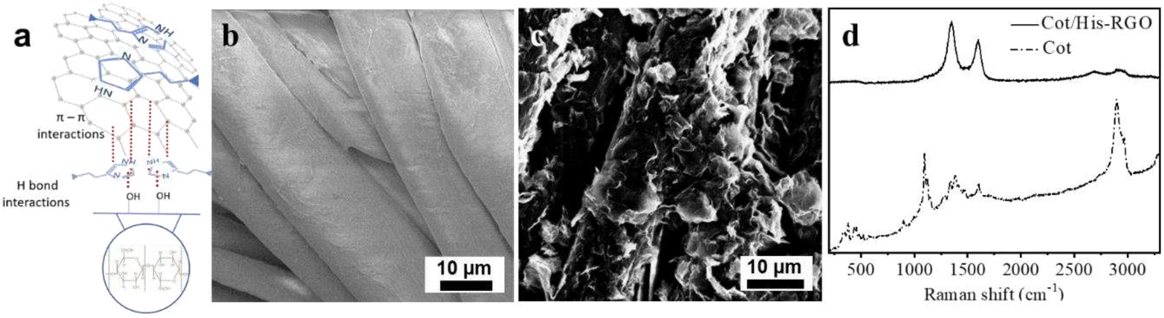

***Fig.3.2**: (a) Sketch of the chemisorption of His-RGO onto Cot. (b-c) SEM images and (d) Raman spectra of Cot fabrics as neat (b) and impregnated by dipping into 4 mg ml^{-1} His-RGO aqueous dispersions (c). (The sketch is not drawn to scale).*

The Raman spectrum of the sample shows at 1340 cm^{-1} and 1591 cm^{-1} the typical D and G peaks, respectively of graphitic materials [41] (Fig.3.2d), that are not visible in the Raman spectrum of neat Cot [42], and hence, can be ascribed to the His-RGO coating (Fig.3.2d). It is worth noticing that the Raman signals of His, expected at 1320 cm^{-1} [43], are not evident in the Raman spectrum of His-RGO, because superimposed by the D mode of RGO. The strong resonant Raman signal of RGO also suppresses Raman signatures of neat Cot fabric (Fig.3.2d).

3.3.2 Preparation of the Cot/His-RGO/Ag fabrics.

Cot/His-RGO fabrics were modified with Ag NPs by dipping in 0.1 g mL^{-1} Ag precursor solutions formed of H_2O and CH_3OH at two different volume ratios, namely 9:1 v/v (9:1$_{v/v}$) and 1:1 v/v (1:1$_{v/v}$), and by exposing the wet fabrics to UV-light (λ≥254 nm) to induce Ag$^+$ photoreduction [29,30] (Fig.3.3). Although methanol is an unsafe solvent, it has been used in textile industry for formulating coatings based on silicates, plant extracts and essential oils, on cellulose based substrates. This includes the production of functional and biocompatible cotton fabrics, cotton gauzes and wound dressing for biomedicine applications [44-46]. Such a procedure, in fact, has been reported in literature for the manufacture of antimicrobial commercial Cot fabrics, specifically using the Ag precursor 9:1$_{v/v}$ solution [29,30].

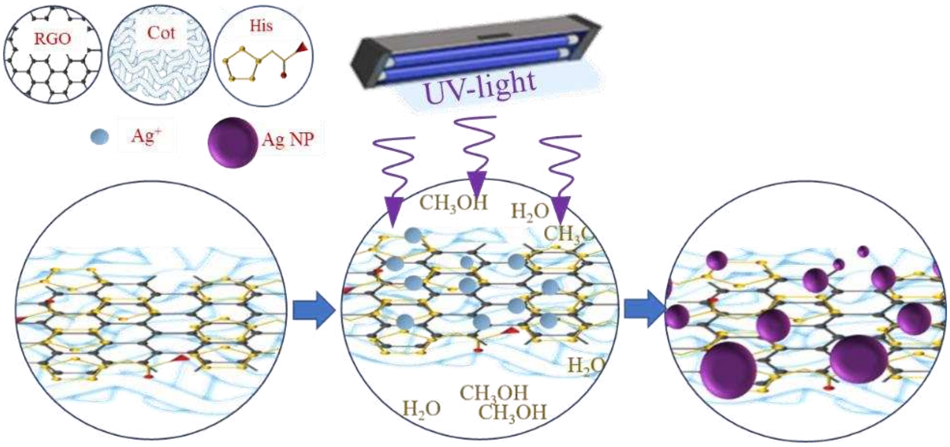

***Fig. 3. 3.**: Sketch of the UV-light induced photoreduction of Ag$^+$ ions in Ag NPs onto the Cot/His-RGO fabrics. (The sketch is not drawn to scale).*

Fig.3.4 reports the SEM-EDS investigation and Raman spectrum of the Cot/His-RGO/Ag fabrics manufactured starting from the Ag precursor 1:1$_{v/v}$ solution, under UV-light irradiation (Cot/His-RGO/Ag$_{\_1:1,UV}$). The SEM images collected by secondary electrons evidence fibers densely coated by bright microstructures (Fig.3.1.4a, left panel), showing bright image contrast also in the same SEM image recorded by back scattered electrons (Fig.3.4a, right panel). The microstructures can be mostly ascribed to Ag, as assessed by the EDS spectrum of the sample that shows its 2.984 keV Lα line (Fig.3.4f), and the chemical mapping, recorded at the same Ag line, evidencing the uniform distribution of the metal onto the fabrics (Fig.3.4e). Furthermore, the UV-Vis absorption spectrum of the manufactured Cot/His-RGO/Ag samples show the typical Localized Surface Plasmon Resonance (LSPR) absorption peak of Ag NPs [47] at 360 nm (Appendix 1,Fig.3), thus confirming the presence of the metal nanostructures in the experimental conditions investigated. The Raman spectrum of Cot/His-RGO/Ag$_{\_1:1,UV}$ (Fig.3.4b) exhibits the D and G peaks of RGO, that maintain the same intensity ratio and positions as in Cot/His-RGO (Fig.3.2d), assessing that Raman spectroscopy does not detect the addition of structural defects to RGO in the *in situ* photoreduction of Ag$^+$ ions.

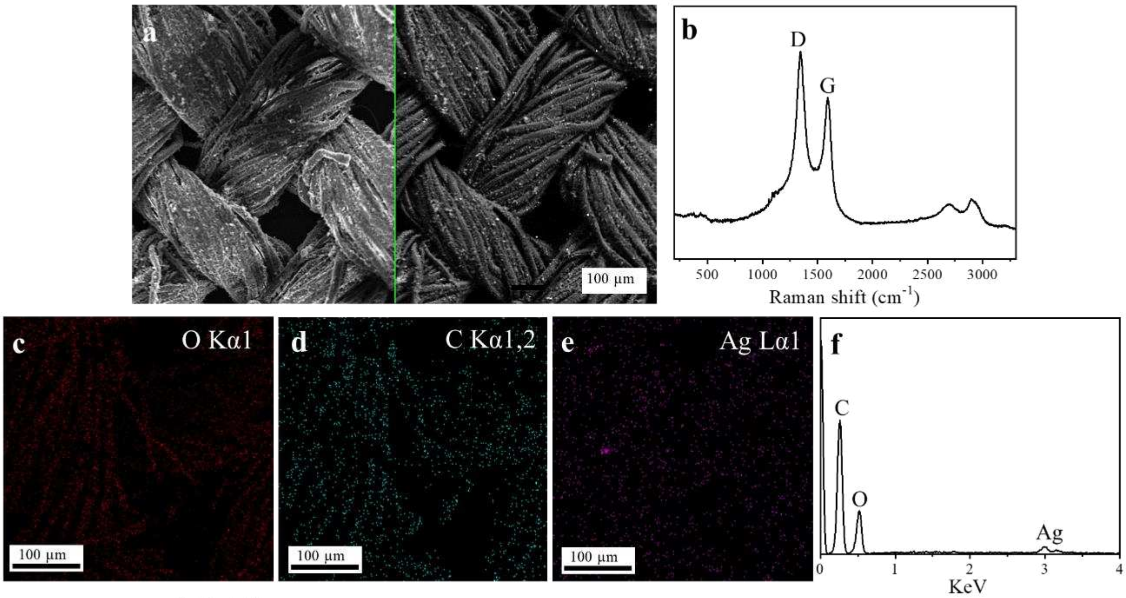

Fig. 3.4*: (a) SEM images collected by secondary (left panel) and back scattered electrons (right panel), (b) Raman spectrum, (c-e) chemical mapping images collected at the (c) O Kα line at 0.525 eV, (d) C Kα line at 0.277 eV, and (e) Ag 2.984 keV Lα line, and (f) EDS spectrum of Cot/His-RGO/Ag*$_{\_1:1,UV}$.

Ag NPs and microstructures were observed to form also after dipping the Cot/His-RGO fabrics in 0.1 g mL^{-1} Ag precursor 1:1 v/v solutions, and then letting the samples dry in dark conditions, at ambient atmosphere (Cot/His-RGO/Ag$_{\_1:1}$). In such experimental conditions, though electron transfers from RGO provide galvanic reduction of the Ag$^+$ ions [48], the Ag NPs concentration is lower than that achieved under UV-light exposure, as indicated by the lower absorption intensity of the spectrum of Cot/His-RGO/Ag$_{\_1:1}$ with respect to Cot/His-RGO/Ag$_{\_1:1,\mathrm{UV}}$ (Appendix 1,Fig.3).

When the Ag precursor 9:1 $_{v/v}$ solution was used for impregnating Cot, and the reduction of Ag$^+$ was performed under UV-light irradiation, the SEM-EDS investigation of Cot/His-RGO/Ag$_{\_1:9,\mathrm{UV}}$ shows uniformly distributed the bright in contrast micrometer sized structures (Fig.3.5a, left panel) of Ag, appearing bright also in the SEM image collected with the signal of the back-scattered electrons (Fig.3.5a, right panel), and evidences the Lα line of Ag at 2.984 keV in the EDS spectrum (Fig.3.5f) and the chemical mapping recorded at the Lα line of Ag (Fig.3.5e), along those of the Kα line of O and Kα line of C (Fig.3.5c-d). Also, in this sample the Raman investigation does not detect the addition of defects to the graphitic structure of RGO after the *in situ* photoreduction of the Ag$^+$ ions (Fig. 5b).

In Cot/His-RGO/Ag$_{\_9:1,\mathrm{UV}}$, the micrometer sized Ag structures (Fig.3.5a) appear larger and brighter than those obtained in Cot/His-RGO/Ag$_{\_1:1,\mathrm{UV}}$ (Fig.3.4a), and Ag NPs featuring a LSPR peak at 372 nm, form onto Cot, with a lower concentration with respect to that in the Cot/His-RGO/Ag$_{\_1:1,UV}$ samples, as assessed by the comparison of their absorbance intensities (Appendix 1,Fig.3)

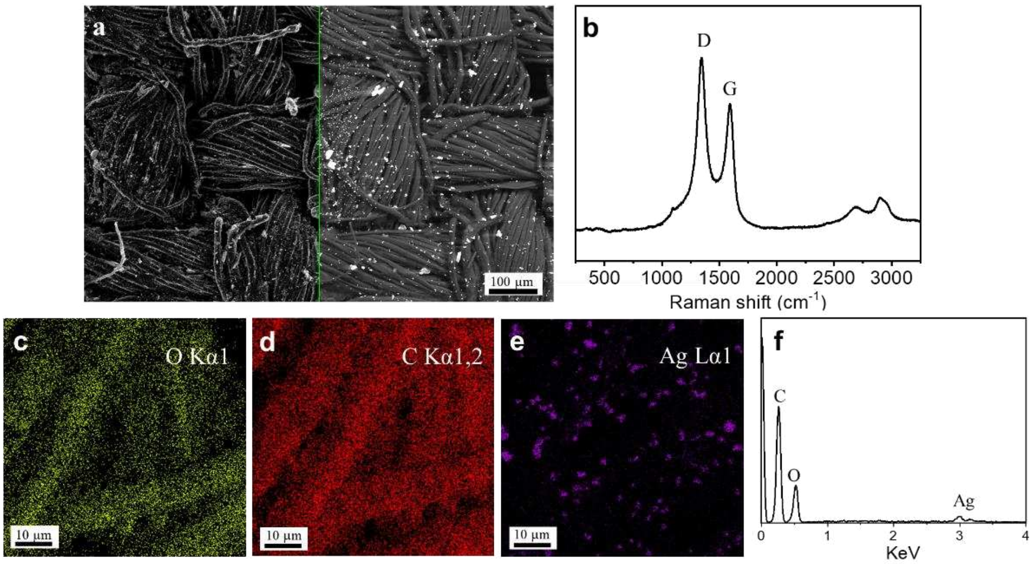

Fig.3.5 *: (a) SEM images collected by secondary (left panel) and back scattered electrons (right panel), (b) Raman spectrum, (c-e) chemical mapping recorded at the (c) O Kα line at 0.525 eV, (d) C Kα line at 0.277 eV and (e) Ag 2.984 keV Lα line, and (f) EDS spectrum of Cot/His-RGO/Ag$_{\_1:9,UV}$.*

The formation of Ag nano and microstructures can be accounted for by absorption and diffusion of Ag^+ ions into the Cot/His-RGO fabrics, induced by electrostatic and coordinating interactions between Ag^+ ions and the oxygen and nitrogen based functionalities of His-RGO, respectively, followed by heteronucleation and growth (Fig.3.3). Under UV-light exposure the reaction is expected to evolve via generation of formaldehyde from reduction of the Ag^+ ions to Ag^0 by $^{\cdot}CH_2OH$ radicals, originated the latter, from reaction between CH_3OH and $^{\cdot}OH$ radicals that form from the solvent mixture under UV-light, [49] as follow:

$$\cdot OH + CH_3OH \rightarrow -\cdot CH_2(OH) + H_2O$$

$$Ag^+ + {}^{\cdot}CH_2(OH) \rightarrow Ag^0 + CH_2{=}O + H+$$

$$(Ag^0)_n + Ag^+ + {}^{\cdot}CH_2\,(OH) \rightarrow (Ag^0)_{n+1} + CH_2{=}O + H^+$$

$$(Ag^0)_n + (Ag^0)_m \rightarrow (Ag^0)_{n+m}$$

XPS investigation was performed to study the surface chemistry of the Cot/His-RGO/Ag$_{\_1:1,UV}$ against the Cot/His-RGO and Cot/His-RGO$_{\_1:1,UV}$ reference samples (Fig.3.6), and the same study was carried out for Cot/His-RGO$_{\_9:1,UV}$ and Cot/His-RGO/Ag$_{\_9:1,UV}$ (Appendix 1,Fig.4).

All the C1s spectra of Cot/His-RGO, Cot/His-RGO$_{\_1:1,UV}$ and Cot/His-RGO/Ag$_{\_1:1,UV}$ were fitted with six components (Fig.3.6), specifically at 284.5 eV, 285.6 eV, 286.8 eV, 288.0 eV, 289.4 eV and 291.1 eV, that were ascribed to sp^2 C, sp^3 C, C-OH/R, C=O, C(O)OH/R and to π-π*, respectively. The contribute of His to some peaks of the C1s spectrum is expected, namely the C-N bond to the peak at 285.6 eV, while the N=C-NH group is expected to contribute to the C-OH/R peak and the carboxyl group falls underneath the peak at 289.4 eV, respectively.

The C1s spectrum of Cot/His-RGO (Fig.3.6a) with its narrow and highly asymmetrical shape and the π-π* satellite peak, is typical of graphitic materials and confirm the presence of RGO at the surface of the Cot fabrics. Upon impregnation with the solvent mixture (Fig.3.6b) and with the Ag precursor addition (Fig.3.6c), after UV-light exposure, the spectra broaden, and the high binding energy shoulder associated with oxygenated groups and sp^3 carbon increases, thus pointing out to a more functionalized RGO surface. This is confirmed by the oxygen concentration which increases from 5.5 at.% in the pristine Cot/His-RGO, up to 13.5 and 18.0 at.%, in the Cot/His-RGO$_{\_1:1,UV}$ and Cot/His-RGO/Ag$_{\_1:1,UV}$ samples, respectively.

The N1s high-resolution spectrum reported in Fig.3.6d confirms the presence of His at the surface of the Cot fabrics. The N1s spectrum was curve-fitted with three peaks, namely at 399.0 eV, at lower binding energy, assigned to imidazole nitrogen ($\underline{N}$=C-NH), at 400.0 eV ascribed to N=C-$\underline{N}$H and the last component at 401.1 eV, due to the protonated His amine group (NH_3^+) [50]. In the N1s spectrum of the Cot/His-RGO$_{\_1:1,UV}$ sample, these peaks shift to lower binding energies, namely 398.5 eV, 399.6 eV and 400.9 eV, respectively (Fig.3.6e). With the addition of $AgNO_3$ and heteronucleation of the Ag NPs, the imidazole nitrogen shifts to 398.8 eV ($\underline{N}$=C-NH) and 399.2 eV (Fig.3.6f), likely due to the coordination with the metal NPs and microstructures [51]. Coordination is anticipated to occur also at the -COO$^-$ functionalities of His [51]. However, the complex chemistry of the C1s component, due to overlapping signals from RGO and His, prevents distinguishing changes in the C(O)OH/R component during Ag structures formation.

The same trend in the C1s and N1s components can be observed in the XPS spectra of Cot/His-RGO$_{\_9:1,UV}$ and Cot/His-RGO/Ag$_{\_9:1,UV}$ (Appendix 1,Fig.4).

Moreover, the XPS investigation of the Cot/His-RGO/Ag$_{\_1:1,UV}$ and Cot/His-RGO/Ag$_{\_9:1,UV}$ samples confirms that the Ag precursor 1:1v/v solutions lead to a higher atomic concentration (at.%) of Ag$^+$ photoreduced on the fabrics surface (Fig.3.6g), and assesses, on the basis of the Ag3d high-resolution spectra, similar line shapes and peak positions of the Ag3d5/2 component at 368.4 ± 0.1 eV, indicative of metallic Ag NPs (Fig.3.6h) in both samples [52], as also confirmed by the UV-Vis spectra (Appendix 1,Fig.3).

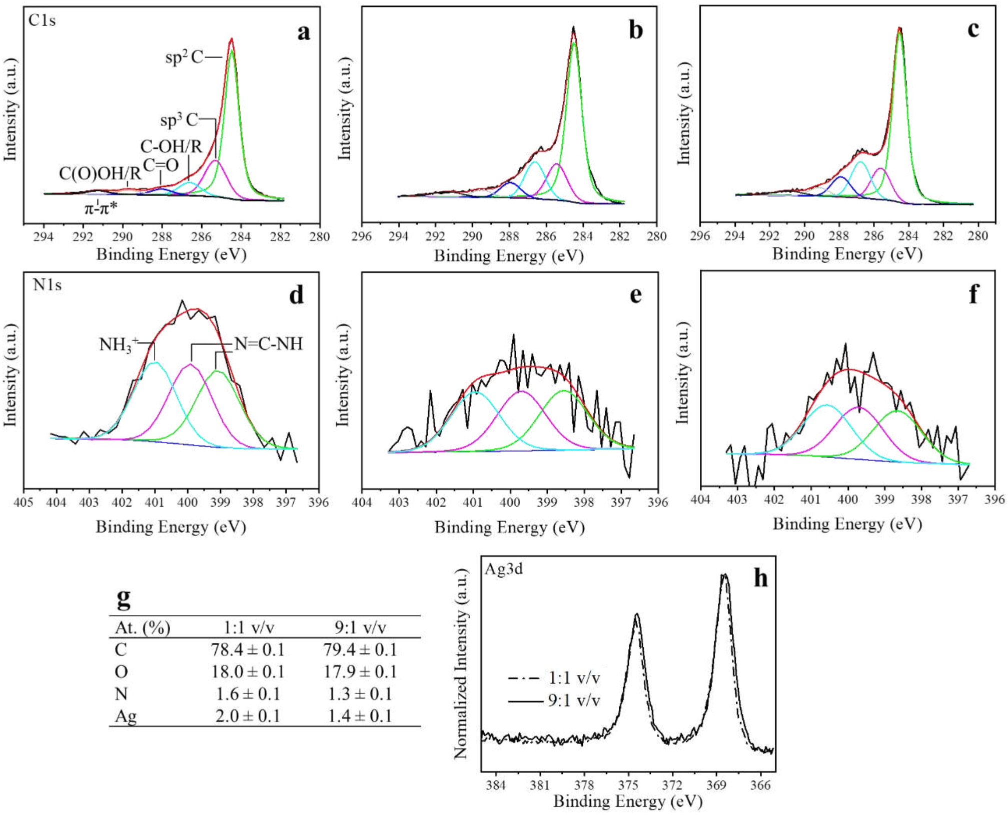

At. (%)	1:1 v/v	9:1 v/v
C	78.4 ± 0.1	79.4 ± 0.1
O	18.0 ± 0.1	17.9 ± 0.1
N	1.6 ± 0.1	1.3 ± 0.1
Ag	2.0 ± 0.1	1.4 ± 0.1

***Fig.3.6**: XPS (a,b,c) C1s and (d,e,f) N1s high-resolution spectra of (a,d) Cot/His-RGO , (b,e) Cot/His-RGO$_{\_1:1,UV}$ (c,f) Cot/His-RGO/Ag$_{\_1:1,UV}$. (g) At.% and (h) XPS Ag3d high-resolution spectra of Cot/His-RGO/Ag$_{\_1:1,UV}$ and Cot/His-RGO/Ag$_{\_9:1,UV}$.*

3.3.3 Thermal conductivity and surface resistivity measurements of the fabrics.

Thermal conductivity (TC) of the manufactured fabrics was estimated by Differential Scanning Calorimetry (DSC), as described in Materials and methods. Typical DSC curves of neat Cot and Cot/His-RGO, which were purified from the excess of His by four ultracentrifuge washing steps, are reported in Appendix 1,Fig.5, and their TC are 1.1 ± 0.1 W m^{-1}K^{-1} and 1.7 ± 0.2 W m^{-1}K^{-1} (Fig.3.7a), respectively. It is worth noticing that the TC of Cot differs from the values reported in literature which are in between 0.026-0.065 W m^{-1}K^{-1} [53-54], due to the cleaning pre-treatment performed in acetone and water to remove contaminants [31]. Besides, the TC of Cot/His-RGO fabrics, which were purified from the excess of His by two ultracentrifuge steps, is lower, 1.3 ± 0.2 W m^{-1}K^{-1} (Appendix 1,Table 1, Fig. 1), than Cot/His-RGO fabrics purified by four ultracentrifuge steps (Fig.3.7a), because of the excess of organic His residual from the second purification step, that decreases the thermal conduction capability of the fabrics [39].

Regarding the TC of the UV-light exposed samples, the TC of neat Cot remained constant and equal to 1.1 ± 0.1 W m^{-1}K^{-1} after UV-light irradiation. In contrast, the TC of Cot/His-RGO$_{\_1:1,UV}$ was measured at 1.6 ± 0.1 W m^{-1}K^{-1} (Fig.3.7a). This value slightly increases up to 1.7 ± 0.4 W m^{-1}K^{-1} in Cot/His-RGO/Ag$_{\_1:1}$ (Fig.3.7a), and significantly enhances up to 2.1 ± 0.2 W m^{-1}K^{-1} (Fig.3.7a) in the Cot/His-RGO/Ag$_{\_1:1,UV}$ samples. The DSC curve of Cot/His-RGO/Ag$_{\_1:1,UV}$ is shown in Appendix 1, Fig.5.

For the samples prepared with the 9:1 v/v solutions, the TC significantly dropped to 0.9 ± 0.1 W m^{-1} K^{-1} in Cot/His-RGO$_{\_9:1,UV}$ (Appendix 1,Table 1), and increased up to 1.6 ± 0.4 W m^{-1} K^{-1} in Cot/His-RGO/Ag$_{\_9:1,UV}$ (Appendix 1,Table 1).

The increase of TC of the Cot/His-RGO/Ag$_{\_1:1,UV}$ fabrics is in line with the thermal transport capability reported for patches formed of polymer formulations based on toxic solvents, loaded with high nanofillers concentrations and fabricated by less scalable approaches [19,21].

a

Sample	$AgNO_3$ (g mL^{-1})	TC (W mK^{-1})	Rs (×10^4 Ω sq^{-1})	σ (MPa)	ε (%)	E (MPa)
Cot	---	1.1 ± 0.1	---	33.53 ± 1.97	22 ± 3	272.32 ± 8.97
Cot/His-RGO	---	1.7 ± 0.2	4.0	32.98 ± 3.06	22 ± 1	262.12 ± 23.04
Cot/His-RGO$_{\_1:1,UV}$	---	1.6 ± 0.1	1.6	---	---	---
Cot/His-RGO/Ag$_{\_1:1}$	0.01	1.7 ± 0.4	---	---	---	---
Cot/His-RGO/Ag$_{\_1:1,UV}$	0.01	2.1 ± 0.2	1.2	25.65 ± 0.90	26 ± 3	181.43 ± 9.80

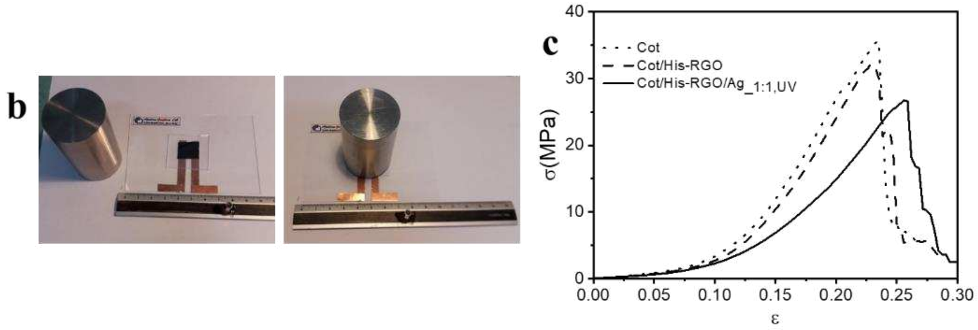

***Fig.3.7**: (a) TC of Cot, Cot/His-RGO, Cot/His-RGO$_{\_1:1,UV}$, Cot/His-RGO/Ag$_{\_1:1}$ and Cot/His-RGO/Ag$_{\_1:1,UV}$. R_s of Cot/His-RGO, Cot/His-RGO$_{\_1:1,UV}$ and Cot/His-RGO/Ag$_{\_1:1,UV}$. Tensile strength (σ), strain at break (ε) and tensile modulus (E) of Cot, Cot/His-RGO and Cot/His-RGO/Ag$_{\_1:1,UV}$. (b) Experimental set-up for the measurement of R_s. (c) Strain-stress curves of Cot, Cot/His-RGO and Cot/His-RGO/Ag$_{\_1:1,UV}$.*

Surface resistivity (R_s) of the modified Cot fabrics was also measured according to the method reported in [34] (Fig.3.7b), as described in Materials and methods.

R_s of the Cot/His-RGO fabrics is ca. 4.0 × 10^4 Ω sq^{-1} and it decreases in Cot/His-RGO$_{\_1:1,UV}$ and Cot/His-RGO/Ag$_{\_1:1,UV}$ down to 1.6 × 10^4 Ω sq^{-1} and 1.2 × 10^4 Ω sq^{-1} (Fig.3.7a), respectively. On the contrary, Cot/His-RGO$_{\_9:1,UV}$ and Cot/His-RGO/Ag$_{\_9:1,UV}$ have a R_s slightly lower, namely 1.3 × 10^4 Ω sq^{-1} and 1.0 × 10^4 Ω sq^{-1}, respectively (Appendix 1,Table 1).

It is worthwhile considering that, a noticeable increase of thermal conductivity was accomplished, although the C/O ratio of the Cot/His-RGO/Ag$_{\_1:1,UV}$ sample is ca. 2 (Appendix 1,Table 2), attesting its low conductivity, which is likely due to the high density of oxygen based functionalities of the immobilized His molecules necessary [55], however, to process RGO from aqueous dispersions for modifying cotton by impregnation.

A plausible explanation for the observed trends in TC and Rs is the interplay between i. the formation of $^{\cdot}CH_2OH$ species from reaction of $^{\cdot}OH$ radicals, which generate from water under UV-light irradiation, and CH_3OH, that lead to the formation of Ag NPs filling the gaps among the His-RGO sheets, and hence increasing both TC and reducing R_s [56] (Fig.3.7a), and ii. the reaction of $^{\cdot}OH$ radicals with RGO that grafts -C-OH and -C=O groups onto its basal plane, as assessed by XPS analyses (Fig.3.6b,c,Appendix 1,Fig. 4b,c) [56,57], leading to a p-doping effect of His-RGO that decreases R_s [57] and concomitantly provides phonon scattering phenomena that reduce TC [58]. These hypotheses can reasonably explain the evidence that for the Cot/His-RGO/$Ag_{\_1:1,UV}$ fabrics, which were achieved under UV-light exposure from the Ag precursor $1:1_{V/V}$ solution in which the photogenerated $^{\cdot}OH$ radicals could be scavenged mostly by methanol, instead of reacting with RGO, leading to $^{\cdot}CH_2OH$ species favoring formation of Ag NPs in a larger concentration (Appendix 1,Fig.3), higher TC and R_s were observed (Fig.3.7a).

3.3.4 Atomic Force Microscopy (AFM) investigation of the fabrics.

In order to go in depth into the factors that lead to the observed increase of TC in the Cot/His-RGO/$Ag_{\_1:1,UV}$ fabric samples, their surface morphology was investigated by AFM and compared to that of neat cotton to achieve information concerning quality and effectiveness of the applied coating. The AFM phase imaging, combined with topography, is particularly suited for such a purpose, as given that AFM phase imaging is capable of sensing variations in stiffness, it is possible to distinguish between parts of the fibers surface that are exposed, from those that are fully covered with the nanocomposite [59].

Fig.3.8 reports the AFM height images of the cotton fibers, before and after applying the His-RGO/$Ag_{\_1:1,UV}$ coating, as well as the corresponding AFM phase images. The topography images of the uncoated sample show irregularities of the cotton fibers (Fig.3.8a), that are confirmed by phase images (Fig.3.8b), whereas the absence of cracks in both the topography and phase images of the Cot/His-RGO/$Ag_{\_1:1,UV}$ samples (Fig.3.1.8c-d) is an indication of the uniform surface coverage of the textile, thus explaining its good thermal conductivity values. In addition, the height profile recorded along lines of the topography image of the Cot/His-RGO/$Ag_{\_1:1,UV}$ sample (Fig.3.8e) shows the formation of Ag NPs having size of tens nm. Finally, surface roughness measurements were determined by evaluating the root mean square roughness (Rq) values of the investigated areas. The measured Rq values are 47.2 nm and 14.2 nm, respectively for the neat Cot and the Cot/His-RGO/$Ag_{\_1:1,UV}$ fabric samples, confirming the presence of a smooth and continuous nanocomposite coating.

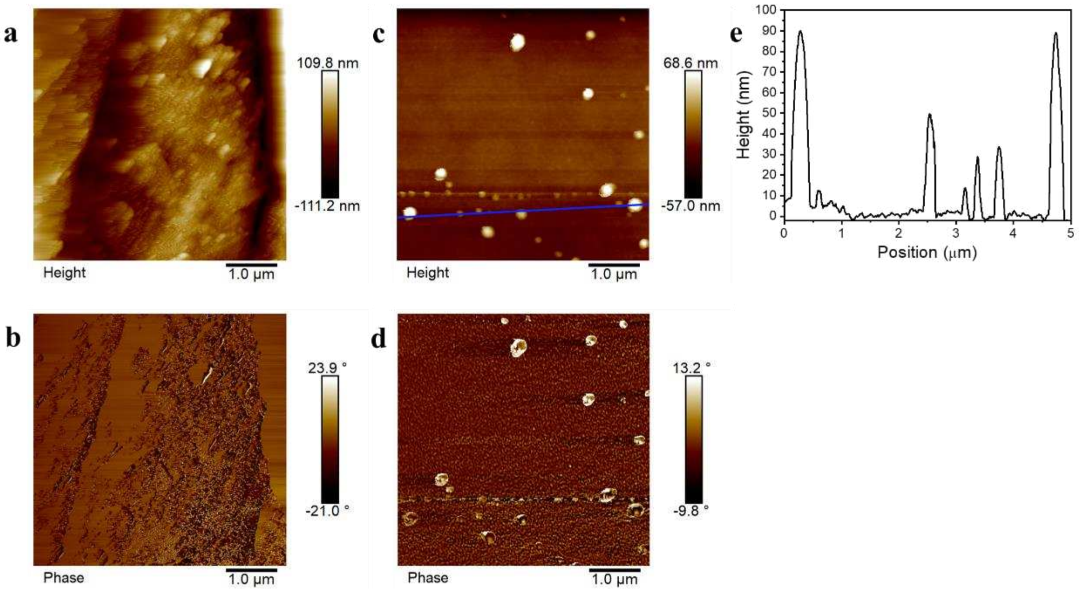

***Fig.3.8**: (a,c) Tapping- and (b,d) phase-mode 2D-view AFM images of the (a,b) Cot and (c,d) Cot/His-RGO/Ag$_{\_1:1,UV}$ samples. In (e) cross sectional profile taken along the blue line marked in (c).*

3.3.5 Mechanical properties, water contact angle analyses, oxygen permeability and durability of fabrics.

Tensile tests were performed to investigate the effect of the coating of Cot with His-RGO and His-RGO/Ag$_{\_1:1,UV}$ on its mechanical properties. The results show that the mean values estimated for strength (σ) and strain at break (ε) do not statistically differ in Cot and Cot/His-RGO samples (Fig.3.7a), while a slight decreases of the tensile modulus (E) with the treatment with His-RGO was noticed (Fig.3.7a). After treatment with His-RGO/Ag$_{\_1:1,UV}$, the mean value of σ decreases of ca. 20%, as well as E, which decreases of ca. 33%, while ε increases of 13% (Fig.3.7a). These results assess that the nanocomposite coating treatment enhances the intrinsic flexibility of Cot, letting to infer an improvement in wear comfort [60], moderately reducing its tensile strength, evidence that could be likely be due to the local heating of the fabric generated under UV-light irradiation [61].

Besides, oxygen permeability tests of the Cot/His-RGO/Ag$_{\_1:1,UV}$ fabric samples showed that the coating does not modify the breathability of the textiles (data not shown), likely because it preserves the spaces among the yarns of the fabric texture [62], as also assessed by the SEM images (Fig3.4a and Fig.3.5a).

Cot is characterized by a very fast absorption of water due to capillary effects requiring long times and high energy consumption for its drying, and hence, additional finishes are often used to convey hydrophobicity properties [63]. In this regard, water absorption behaviour of the Cot/His-RGO$_{\_1:1v/v}$ fabrics was investigated by contact angle (WCA) measurements, and while bare Cot absorbs water, Cot/His-RGO/Ag$_{\_1:1v/v,UV}$ presents a lower absorption capability with WCA of 100 ± 10, likely due to the increased roughness of the coating [64] and to the moisture barrier and hydrophobic properties of RGO [65].

The washing durability of the His-RGO/Ag$_{\_1:1,UV}$ coating was investigated by monitoring the mean values of TC and static WCA after 5, 10 and 20 laundering cycles (Fig.3.9). As it can be noticed, the washing durability is low, in fact, the TC of Cot/ His-RGO/Ag$_{\_1:1,UV}$ reaches almost the same values as the Cot/His-RGO sample, passing from 2.1± 0.2 W m^{-1} K^{-1}, to 2.0 ± 0.1 W m^{-1} K^{-1} after 5 cycles, 1.9 ± 0.1 W m^{-1} K^{-1} after 10 cycles and 1.6 ± 0.2 W m^{-1} K^{-1} after 20 cycles. Concomitantly, the WCA decreases from 100 ± 10, to 74 ± 2, 64 ± 3 and to 31 ± 2, assessing a reduction of the hydrophobicity of ca. 70%. Therefore, further investigation is necessary to overcome this limitation, for instance by means of the use of a self-polymerizable and flexible biocompatible polymer coating as polydopamine, a 'molecular glue', [66] able to sustain the alkaline washing environment of detergents and acting as an adhesive of the nanocomposite onto the textile.

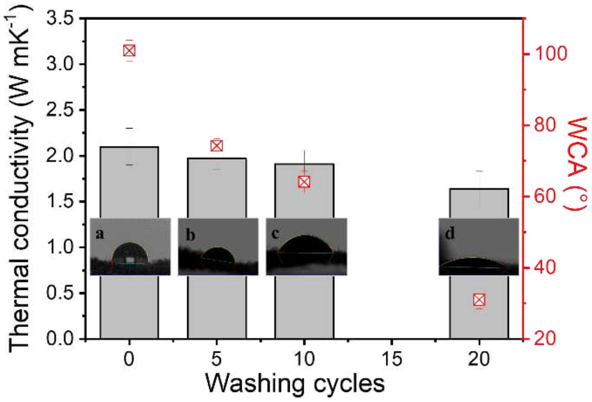

Fig.3.9: *TC and WCA values of the Cot/His-RGO/Ag$_{\_1:1,UV}$ sample, as prepared and after 5, 10 and 20 washing cycles. (In the insets) Water droplet image on Cot/His-RGO/Ag$_{\_1:1,UV}$ before (a) and after 5 (b), 10 (c) and 20 (d) washing cycles.*

3.4 Conclusions

A new thermally conductive hybrid nanocomposite coating for cotton (Cot), formed by histidine functionalized Reduced Graphene Oxide (His-RGO), decorated with tens nm in size Ag NPs and microstructures, has been manufactured by an ecofriendly, scalable, and sustainable approach. The strategy consists of impregnating Cot by dipping in His-RGO aqueous dispersions, and then, in $AgNO_3$ solutions, 1:1 v/v in H_2O:CH_3OH, followed by UV-light irradiation, in air, inducing the *in situ* photoreduction of the Ag NPs onto the textile from $AgNO_3$. His has been selected because of its biocompatibility, water solubility, and capability to bind RGO by aromatic π-π stacking interactions allowing its dispersion in water, and concomitantly, coordinate the Ag NPs, also favoring chemisorption of the His-RGO coating to Cot by hydrogen interactions. The preliminary results of the thermal conductivity of the coating are promising, as it is found twice that of the neat Cot, due to the bare components' contribution to the resulting textile thermal transport capability, and to the establishment of more extended heat conduction percolation paths among the photogenerated Ag NPs and the RGO sheets. The thermal transport capability of the manufactured coating is, indeed, in line with those reported in literature for patches fabricated by expensive technologies, formed of polymer formulations heavily loaded by high thermally conductive nanofillers and that use, in some works, also toxic solvents, that, in fact, result in less sustainable and scalable methodologies. The nanocomposite coating preserves oxygen permeability and increases flexibility of Cot, letting to infer an improvement in wear comfort, while only moderately reduces its strength, and decreases its water absorption capability. The next steps should focus on improving the adhesion of the nanocomposite coating to cotton, and ensuring its durability through washing, particularly under the alkaline conditions of detergents. Finally, although further investigation is necessary for assessing textile's radiative heat dissipation capability, the reported preliminary study of the coating makes it promising for the development of natural IR-opaque passive cooling textiles.

References

[1] Y. Zhang, et al., “Functional Textiles with Smart Properties: Their Fabrications and Sustainable Applications,”Adv. Funct. Mater., 2023. 33: 2301607.

[2] G. Li, et al., “Autonomous Electroluminescent Textile for Visual Interaction and Environmental Warning,” Nano Lett., 2023. 23: 8436-8444.

[3] M. Li, et al., “Recent Progress of the Active Materials with Various Micro-structures for Flexible Textile-Based Supercapacitors for Flexible,” Adv. Fiber Mater., 2022. 4: 1005–1026.

[4] R. Xu, et al., “Breathable Kirigami-Shaped Ionotronic e-Textile with Touch/Strain Sensing for Friendly Epidermal Electronics,” Adv. Fiber Mater., 2022. 4: 525–1534.

[5] C. Ingrosso, et al., “Photoelectrochemical properties of Zn(II) phthalocyanine/ZnO nanocrystals heterojunctions: Nanocrystal surface chemistry effect,” Appl. Surf. Sci., 2005. 246: 367–371.

[6] M.L. Curri, et al., “Emerging methods for fabricating functional structures by patterning and assembling engineered nanocrystals,” Phys. Chem. Chem. Phys., 2010. 12: 11197-11207.

[7] H. Yu, et al., “Electronic Textile with Passive Thermal Management for Outdoor Health Monitoring,” Adv. Fiber Mater., 2024. 6: 1241–1252.

[8] J. Wang, et al., “High temperature thermally conductive nanocomposite textile by “green” electrospinning,” Nanoscale, 2018. 10: 16868.

[9] Y. Peng, Y. Cui, “Advanced Textiles for Personal Thermal Management and Energy,” Joule, 2020. 4: 724–742.

[10] X. Lan, et al., “Designing heat transfer pathways for advanced thermoregulatory textiles,” Mater. Today Phys., 2021. 17: 100342-100370.

[11] M.J. Rahman, T. Mieno, “Conductive Cotton Textile from Safely Functionalized Carbon Nanotubes,” J. Nanomater., 2015. 10: 978484.

[12] H. Zhou, et al., “One-Way Water-Transport Cotton Fabrics with Enhanced Cooling Effect,” Adv. Mater. Interfaces, 2016. 3: 1600283.

[13] A. Abbas, et al., “Cooling effect of MWCNT-containing composite coatings on cotton fabrics,” J. Text. I., 2013. 104: 798–807.

[14] A. Abbas, et al., “Improving Thermal Conductivity of Cotton Fabrics Using Composite Coatings Containing Graphene, Multiwall Carbon Nanotube or Boron Nitride Fine Particles,” Fibers and Polym., 2013. 14: 1641-1649.

[15] M. Dai, et al., “A green approach to preparing hydrophobic, electrically conductive textiles based on waterborne polyurethane for electromagnetic interference shielding with low reflectivity,” Chem. Eng. J., 2021. 421: 127749-127759.

[16] Y. Wang, et al., “Flexible, durable and thermal conducting thiol-modified RGO-WPU/cotton fabric for robust electromagnetic interference shielding,” Chem. Eng. J., 2019. 360: 817-828.

[17] Y.C. Soong, et al., “Multilayered graphene/boron nitride/thermoplastic polyurethane composite films with high thermal conductivity, stretchability, and washability for adjustable-cooling smart clothes,” J. Colloid Interface Sci., 2021. 599: 611–619.

[18] R.J. Slocombe, et al., “Phosgene Derivatives. The Preparation of Isocyanates, Carbamyl Chlorides and Cyanuric Acid,” J. Am. Chem. Soc., 1950. 72: 1888–1891.

[19] T. Gao, et al., “Three-Dimensional Printed Thermal Regulation Textile,” ACS Nano, 2017. 11: 11513−11520.

[20] K. Wu, et al., “Green Production of Regenerated Cellulose/Boron Nitride Nanosheet Textiles for Static and Dynamic Personal Cooling,” ACS Appl. Mater. Interfaces, 2019. 11: 40685−40693.

[21] J. Xi, et al., “High Thermal Conductivity and Radiative Cooling Designed Boron Nitride Nanosheets/Silk Fibroin Films for Personal Thermal Management,” ACS Appl. Mater. Interfaces, 2024, 16, 7732−7741.

[22] T. Y. Kim, et al., “The Electronic Thermal Conductivity of Graphene,” Nano Lett., 2016, 16, 2439−2443.

[23] S. Elumalai, et al., “An Experimental and Steered Molecular Dynamics Simulation Approach to Histidine Assisted Liquid-Phase Exfoliation of Graphite into Few-Layer Graphene,” Phys. Chem. Chem. Phys., 2020, 22, 9910−9914.

[24] L. Zhang, et al., “Surface-Assisted Assembly of a Histidine-Rich Lipidated Peptide for Simultaneous Exfoliation of Graphite and Functionalization of Graphene Nanosheets,” Nanoscale, 2019, 11, 2999−3012.

[25] Z. G. Fthenakis, et al., “Effect of Structural Defects on the Thermal Conductivity of Graphene: From Point to Line Defects to Haeckelites,” Phys. Rev. B, 2014, 89, 125421.

[26] C. Ingrosso, et al., “PbS Nanocrystals Decorated Reduced Graphene Oxide for NIR Responsive Capacitive Cathodes,” Carbon, 2021, 182, 57−69.

[27] M. Rycenga, et al., “Controlling the Synthesis and Assembly of Silver Nanostructures for Plasmonic Applications,” Chem. Rev., 2011, 111, 3669−3712.

[28] Y. Li, et al., “Incorporating Ag Nanowires into Graphene Nanosheets for Enhanced Thermal Conductivity: Implications for Thermal Management,” ACS Appl. Nano Mater., 2020, 3, 6061−6070.

[29] M. Rehan,et al., “Towards Multifunctional Cellulosic Fabric: UV Photo-Reduction and In-Situ Synthesis of Silver Nanoparticles into Cellulose Fabrics,” Int. J. Biol. Macromol., 2017, 98, 877−886.

[30] F. Paladini, e al., “Antibacterial and Antifungal Dressings Obtained by Photochemical Deposition of Silver Nanoparticles,” J. Appl. Polym. Sci., 2014, 131, 40326−40334.

[31] S. Bhattacharjee, et al., “Nanoparticles Incorporated Graphene-Based Durable Cotton Fabrics,” Carbon, 2020, 166, 149−163.

[32] J. H. Flynn, D. M. Levin, “A Method for the Determination of Thermal Conductivity of Sheet Materials by Differential Scanning Calorimetry (DSC), Thermochim,” Acta, 1988, 126, 93−100.

[33] Normal Protocol 33/89, Contact Angle Determinations, 1993.

[34] AATCC Technical Manual, Vol. 85, pag. 97, Copyright © 2009 American Association of Textile Chemists and Colorists, www.aatcc.org.

[35] V. R. Preedy, “Food and Nutritional Components in Focus: Imidazole Dipeptides: Chemistry, Analysis, Function and Effects,” RSC, London, 2015.

[36] C. Ingrosso, et al., “Solvent Dispersible Nanocomposite Based on Reduced Graphene Oxide in Situ Decorated with Gold Nanoparticles,” Carbon, 2019, 152, 777−787.

[37] E. Satheeshkumar, et al., “One-Step Simultaneous Exfoliation and Covalent Functionalization of MoS2 by Amino Acid Induced Solution Processes,” ChemNanoMat, 2017, 3, 172−177.

[38] C. Ingrosso, et al., “Au Nanoparticle Decorated Reduced Graphene Oxide and Its Electroanalytical Characterization for Label-Free Dopamine Detection,” Mater. Adv., 2024, 5, 549−560.

[39] K. C. Chan, et al., “A Theoretical Model for the Effective Thermal Conductivity of Graphene Coated Metal Foams,” Appl. Therm. Eng., 2019, 161, 114112.

[40] J. G. Mesu,et al., “Infrared and Raman Spectroscopic Study of pH-Induced Structural Changes of L-Histidine in Aqueous Environment,” Vib. Spectrosc., 2005, 39, 114−125.

[41] A. C. Ferrari, J. Robertson, “Interpretation of Raman Spectra of Disordered and Amorphous Carbon,” J. Phys. Rev. B, 2000, 61, 14095−14107.

[42] D. Puchowicz, M. Cieslak, Raman Spectroscopy in the Analysis of Textile Structures, in: C. S. Pathak, S. Kumar (Eds), Recent Developments in Atomic Force Microscopy and Raman Spectroscopy for Materials Characterization, IntechOpen, 2021, https://doi.org/10.5772/intechopen.99731.

[43] G. Zhu, et al., “Raman spectra of amino acids and their aqueous solutions,” Spectrochimica Acta Part A 78 (2011) 1187–1195, https://doi.org/10.1016/j.saa.2010.12.079.

[44] M. Rehan, et al., “Functionalization strategy of carboxymethyl cotton gauze fabrics with zeolitic imidazolate framework-67 (ZIF-67) as a recyclable material for biomedical applications,” Internat. J. Biol. Macromol. 279 (2024) 135148, https://doi.org/10.1016/j.ijbiomac.2024.135148.

[45] H. E. Emam, et al., "Protective Cotton Textiles via Amalgamation of Cross-Linked Zeolitic Imidazole Frameworks," Ind. Eng. Chem. Res. 59 (2020) 10931−10944, https://doi.org/10.1021/acs.iecr.0c01384.

[46] A. Rehman, et al., "Green dyeing of modified cotton fabric with Acalypha wilkesiana leave extracts," Sust. Chem. Pharm. 21 (2021) 100432, https://doi.org/10.1016/j.scp.2021.100432.

[47] K. C. Lee, et al.; "Size effect of Ag nanoparticles on surface plasmon resonance," Surf. Coat. Technol. 202 (2008) 5339-5342, https://doi.org/10.1016/j.surfcoat.2008.06.080.

[48] Y. Park, et al., "Spontaneous Formation of Gold Nanoparticles on Graphene by Galvanic Reaction through Graphene," ACS Omega 4 (2019) 18423-18427, https://doi.org/10.1021/acsomega.9b02691.

[49] K. Chandrasekaran, J. K. Thomas, "The mechanism of the photochemical oxidation of water to oxygen with silver chloride colloids," Chem. Phys. Lett. 97 (1983) 357-360, https://doi.org/10.1016/0009-2614(83)80507-7.

[50] O. Kostko, et al., "Local electronic structure of histidine in aqueous solution," Phys. Chem. Chem. Phys. 23 (2021) 8847-8853, https://doi.org/10.1039/D1CP00361E.

[51] P. Budurua, et al., "Functionalization of silver nanoparticles with glutamine and histidine for simple and selective detection of Hg^{2+} ion in water samples," Sens. & Actuators B: Chem. 244 (2017) 972-982, https://doi.org/10.1016/j.snb.2017.01.041.

[52] I. Lopez-Salido, et al., "Ag nanoparticles on highly ordered pyrolytic graphite (HOPG) surfaces studied using STM and XPS," Surf. Sci. 588 (2005) 6–18, https://doi.org/10.1016/j.susc.2005.05.021.

[53] P. J. Rivero, et al., "The thermal conductivity of textiles," Nanoscale Res. Lett. 10 (2015) 501, https://doi.org/10.1088/0959-5309/58/1/310.

[54] O. I. Kalaoglu-Altan, et al., "Improving thermal conductivities of textile materials by nanohybrid approaches," iScience 25 (2022) 103825, https://doi.org/10.1016/j.isci.2022.103825.

[55] O. C. Compton, et al., ACS Nano 5 (2011) 4380–4391, https://doi.org/10.1021/nn1030725.

[56] E. J. Radich, P. V. Kamat, "Making Graphene Holey Gold-Nanoparticle-Mediated Hydroxyl Radical Attack on Reduced Graphene Oxide," ACS Nano 7 (2013) 5546-5557, https://doi.org/10.1021/nn401794k.

[57] R. Singla, A. Kottantharayil, "Stable hydroxyl functionalization and p-type doping of graphene by a non-destructive photo-chemical method, Carbon 152 (2019) 267-273, https://doi.org/10.1016/j.carbon.2019.06.021.

[58] S. Mann, et al., "Lattice thermal conductivity of pure and doped (B, N) Graphene," Mater. Res. Express 7 (2020) 095003, https://doi.org/10.1088/2053-1591/abb2cd.

[59] A. I. S. Neves, et al., "Towards conductive textiles: coating polymeric fibres with graphene," Scientific Reports 7 (2017) 1-10, https://doi.org/10.1038/s41598-017-04453-7.

[60] H. Jun Sim, et al., “Soft and elastic hygroelectric fiber for wearable human monitoring textiles,” Chem. Eng. J. 495 (2024) 153486, https://doi.org/10.1016/j.cej.2024.153486.

[61] L. Guardia, et al., “UV light exposure of aqueous graphene oxide suspensions to promote their direct reduction, formation of graphene–metal nanoparticle hybrids and dye degradation,” Carbon 50 (2012) 1014-1024, https://doi.org/10.1016/j.carbon.2011.10.005.

[62] M. G. Chakroun, et al., “Effect of knitting structure and dyeing process on drying time, air and vapor permeability,” Text. Res. J. 94 (2024) 1263–1278, https://doi.org/10.1177/0040517524122.

[63] B. Xu, Z. Cai, “Fabrication of a superhydrophobic ZnO nanorod array film on cotton fabrics via a wet chemical route and hydrophobic modification,” Appl. Surf. Sci. 254 (2008) 5899-5904, https://doi.org/10.1016/j.apsusc.2008.03.160.

[64] P. J. Rivero, et al., “Nanomaterials for Functional Textiles and Fibers,” Nanoscale Res. Lett. 10 (2015) 501, https://doi.org/10.1186/s11671-015-1195-6.

[65] Y. Su, et al., “Impermeable barrier films and protective coatings based on reduced graphene oxide,” Nat. Commun. 5 (2014) 4843, https://doi.org/10.1038/ncomms5843.

[66] C. Fu, et al., “Surface engineering for cellulose as a boosted Layered Double Hydroxide via controlled intercalation and a low-temperature synthesis,” Appl. Surf. Sci. 589 (2023) 153115, https://doi.org/10.1016/j.apsusc.2022.153115.

Chapter 4

Silver Nanoparticle-Decorated RGO Hybrid Nanocomposites: Synthesis, Characterization, and Durable Antimicrobial Efficacy for Textile Coatings

A new antimicrobial hybrid nanocomposite formed of RGO sheets functionalized with histidine (His) and decorated with Ag NPs, has been synthesized by a facile, *in situ*, colloidal approach, and has been tested as antimicrobial coating for cotton. The synthesis has been performed in water, at low temperature, starting from $AgNO_3$ precursor in presence of trisodium citrate and sodium borohydride reducing and capping agents. The NPs anchor onto the RGO basal plane by the aromatic His linker, that has been selected because of its capability to i. exfoliate the RGO sheets allowing their dispersion in aqueous solution, ii. bind the graphene platform by π-π aromatic stacking interactions, and iii. provide coordinating sites for the Ag NPs. The hybrid nanocomposite has been purposely engineered with the His-RGO sheets densely coated by small in size Ag NPs to optimize antimicrobial activity, by systematically investigating the role of the synthetic parameters, Ag precursor:citrate and Ag precursor:borohydride molar ratio, pH and Ag precursor:His-RGO w/w, on its morphology and spectroscopy properties. Ag NPs, 24 ± 4 nm in size, have been found to form uniformly onto the His-RGO sheets by an aggregative growth process, with a high density and narrow size dispersion. The antimicrobial properties of cotton textiles impregnated by the nanocomposite have been investigated by the standard quantitative ISO protocol (ISO 20743:2021) using *Escherichia coli* as a reference bacterium, against cotton textiles modified by neat Ag NPs purposely synthesized with same size and surface chemistry. The results show that the nanocomposite modified fabrics present a biocidal effect more durable over time than coatings based on neat Ag NPs, thanks to the gas and moisture barrier properties of RGO which protect the Ag NPs from oxidation, endowing them with a long-term biocidal efficacy.

4.1 Introduction

Given the overuse of antibiotics, there has recently been the alarming spread of multidrug resistant pathogenic bacteria strains [1]that has compromised the efficacy of conventional therapeutic treatments, encouraging the development of alternative antimicrobial approaches. Nanotechnologies offer promising solutions for addressing such a goal, proposing novel advanced functional materials with enhanced antimicrobial activity.

Nanostructures based on Ag nanoparticles (NPs) are among the most widely used, thanks to their broad spectrum biocidal effect against diverse populations of bacteria, fungi, and viruses, [2]and their effective bioactivity against multi-drug resistance pathogens.[3] Ag NPs have been widely applied to prevent formation of fouling biofilms, as these can have adverse effects in industrial processes limiting heat transfer, corroding metallic surfaces, and blocking flow of fluids [4]. Besides, biofilm microbial aggregates can be 10–10^4 times more resistive to antimicrobial agents compared to pristine microorganisms in suspension.[5]

The antibacterial activity of Ag NPs has been accounted to the release of Ag^+ ions, that, interacting with the negatively charged cell membrane of microorganisms lead to the generation of intracellular reactive oxygen (ROS) species, inducing oxidative stress that compromises its integrity, [6]resulting also in cells death. [7]The biocidal effect of Ag NPs depends on the NPs size [8]and shape, pH and ionic strength of the NPs solution, light exposure conditions [9], and surface ligand chemistry (e.g. capping agent density, coordinating atom, carbon chain length and terminal group [10]. Due to their large surface area to volume ratio, smaller Ag NPs have the highest antimicrobial effect, but their tendency to oxidase and aggregate to minimize surface energy, significantly reduces their biocidal effect [10], limiting their practical application. To circumvent such an inconvenient, chemical immobilization of Ag NPs onto surfaces bearing functional groups capable to coordinate their surface, has been performed, enhancing their potential for antimicrobial applications.

Graphene is among the most suited platforms for such a purpose, due to its large surface area and its high chemical reactivity [ref], that make it ready to be modified by a plethora of chemical approaches, also those encompassing the use of functional aromatic linkers that bind its basal plane by supramolecular interactions, concomitantly chemically binding the NPs.

Concerning the effects of graphene derivatives on the viability of bacterial cells, the literature is controversial, [11]and the contradictory explanations are ascribed to the diverse intrinsic physicochemical properties of graphene samples. Some works report on the dependence of bacteria cell viability on the graphene preparation method, its thickness, size, surface area, charge, functionalization, roughness, hydrophilicity, oxidation capacity and dispersibility, and hence it varies from sample to sample. In these works, the antibacterial effect is caused by production of reactive oxygen species (ROS) that oxidase vital cellular components [12] and by the direct contact of the atomic-thick sharp edges of the graphene sheets, that, functioning as "cutters", interrupt and damage cell membrane, causing outflow of the intracellular content. Some other studies, instead, report on the capability of graphene derivatives in promoting bacterial growth and biofilm formation, and such nanostructures are exploited in applications where bacterial metabolism increases, as in biofuel production by anaerobic digestion or in generation of renewable bioelectricity power in microbial fuel cells, where graphene derivatives are used as mediators of electron transfers in metabolic processes. [13]

In this work, a new hybrid nanocomposite formed of Reduced Graphene Oxide (RGO) functionalized with the aminoacidic histidine (His), and then decorated with colloidal Ag NPs, has been synthesized by reducing, *in situ*, the $AgNO_3$ precursor onto the RGO sheets, in presence of sodium borohydride ($NaBH_4$) and trisodium citrate tribasic dehydrate ($Na_3C_6H_5O_7 \times 2H_2O$), in water, at low temperature.

His has been selected as an intercalating, exfoliating and functionalizing agent of RGO, for its capability to bind its basal plane by aromatic π-π stacking interactions. Its water solubility allows the dispersion of RGO sheets in aqueous solutions by liquid-phase exfoliation (LPE), approach that would be not practicable in absence of His due to the high hydrophobicity of RGO and the high surface tension of water (72 mJ m^{-2}) inducing RGO aggregation, and that would require toxic organic solvents (i.e. N-methyl-2-pyrrolidone, N,N-dimethylformamide, ortho-dichlorobenzene etc.) with a lower surface tension (40 mJ m^{-2}).[14]

His strongly interacts with the RGO sheets, concomitantly grafting a high density of -COOH and $-NH_2$ groups, that behave as heteronucleation and growth sites in the *in situ* formation of the Ag NPs [15].

The hybrid nanocomposite has been designed with a high density of small Ag NPs to have a strong antimicrobial activity. For this purpose, the experimental parameters, $AgNO_3$, His-RGO, $NaBH_4$ and citrate relative concentrations, as well as pH of the reaction solution, have been systematically tuned and concomitantly the spectroscopic and morphological properties of the achieved nanostructures have been comprehensively investigated, to study their effect on the nanocomposite coating density and NPs size for suitably engineering the nanocomposite.

The achieved nanocomposite presents spherical Ag NPs of 24 ± 4 nm, densely coating the His-RGO sheets, and it has been used to modify cotton, by impregnation, and tested as an antimicrobial coating. Cotton is among the most popular natural fibres for clothing materials, for its flexibility, absorbency, versatility and breathability, but it has some limitations such as wrinkle formation, hydrophilicity, long drying times, and most of all, microbial degradation that has restricted its applications as apparel fabric. The use of coating techniques (i.e. dipping, impregnation, spray coating) to modify cotton fabrics with nanostructures is among the most scalable and sustainable approach, to convey novel functionalities to cotton textiles, preserving concomitantly wear comfort, flexibility, lightness, breathability, and texture.

Various standard tests have been developed and used to determine the antibacterial activity of fabrics. The mostly used are qualitative tests such as ISO 20645: 2004, AATCC 147: 2004,[16] and halo method of JIS L 1902: 2008, and quantitative tests such as AATCC 100: 2004 and JIS L 1902:2015. Qualitative tests are inadequate to accurately determine the antibacterial activity of fabric samples, while quantitative methods are more accurate, because the reduction of bacterial growth is calculated against that of a control sample.

Here, the quantitative standardized ISO protocol method (ISO 20743:2021) has been used for investigating the biocidal effect of the nanocomposite coating, and *Escherichia coli* (*E. coli*) has been considered as a model bacterium representative of the Gram negative bacteria. The antimicrobial properties have been investigated at different concentrations of the coating, over time, at different aging conditions, and against those of coatings based on pristine Ag NPs of comparable size and surface chemistry. Such a study goes behind the approaches reported in literature, in comparing the antimicrobial activity of the nanocomposite with that of pristine Ag NPs of same morphology, surface chemistry, and processed in the same experimental conditions, and going in-depth the correlation between the biocidal activity and the morphology and surface chemistry of the nanocomposite on cotton. The results show that the nanocomposite coating inhibits bacterial growth even at low concentrations and has a strong antibacterial activity that lasts longer than that of neat Ag NPs, regardless their aging conditions, thanks to the capability of His-RGO to prevent Ag NPs aggregation and oxidation.

4.2 Materials and methods

Chemicals and Materials. Reduced Graphene Oxide (RGO) was purchased from Graphene Supermarket (1.6 µm thick flakes), histidine (His) from Alpha Aesar and methanol, silver nitrate ($AgNO_3$, 99.9999%), sodium borohydride ($NaBH_4$), sodium hydroxide (NaOH) and trisodium citrate dihydrate ($Na_3C_6H_5O_7 \times 2H_2O$) from Sigma Aldrich. All these chemicals were used as received without further purification. Aqueous solutions were prepared by using Milli-Q water (18.2 MΩ·cm organic carbon content ≥ 4 µg L^{-1}) achieved by a Milli-Q gradient A-10 system.

Exfoliation and functionalization of Reduced Graphene Oxide (RGO) with Histidine (His). A dispersion of 100 mg mL^{-1} of RGO and 160 mg mL^{-1} of His in water was stirred at room temperature to allow intercalation of His among the RGO multilayers. Then, His-RGO was purified from the excess of His by four cycles of ultracentrifugation (40000 rpm for 30 min), sonicated in an ice cooled bath sonicator for 8 h, and purified again by four cycles of ultracentrifugation (40000 rpm for 30 min). The isolated His-RGO pellet was finally dispersed in water at pH 11, at the concentration of 4 mg mL^{-1}.

Synthesis of Silver Nanoparticles (Ag NPs). Ag NPs were prepared by reducing $AgNO_3$ in presence of $NaBH_4$ and $Na_3C_6H_5O_7 \cdot 2H_2O$ as both reducing and coordinating agents.[17] In a typical procedure, 1 mL of a 0.01 M $Na_3C_6H_5O_7 \cdot 2H_2O$ solution was added to 5.5 mL of a 10^{-3} M $AgNO_3$ solution in water and stirred for 30 min at room temperature. Then, 1 mL of a freshly prepared solution of 0.01 M $NaBH_4$ was slowly added, under vigorous stirring, and water was added to reach the final volume of 10 mL. Upon addition of $NaBH_4$, the colour of the reaction mixture turns from dark brown to pale yellow, and the reaction mixture was stirred for other 2.5 h, at room temperature, to complete the reduction. Then, the Ag NPs were purified by two cycles of centrifugation (10000 rpm for 20 min) and finally dispersed in water.

Synthesis of the Ag NPs decorated His-RGO hybrid nanocomposites (His-RGO/Ag NPs). In a typical experiment, hybrid nanocomposites based on His-RGO decorated with Ag NPs (His-RGO/Ag NPs) were synthesized, at ice bath temperature, by injecting 2 mL of His-RGO (4 mg mL^{-1}) previously sonicated 3 h, to an aqueous solution of $Na_3C_6H_5O_7 \cdot 2H_2O$ and $NaBH_4$ stirred for 30 min, followed by addition of an aqueous solution of $AgNO_3$. The reaction was left to proceed under vigorous stirring for 30 min. The investigated $AgNO_3$:His-RGO w/w were 1:1, 3:1 and 4:1, the $AgNO_3$:$NaBH_4$ molar ratio were 1:1.7, 1:5, 1:7, 3:3.5, 4:5 and 4.6 and the $AgNO_3$:$Na_3C_6H_5O_7 \cdot 2H_2O$ molar ratio were 1:2.5, 3:7.5, 4:10, 4:12.5 and 4:15, respectively. The synthesis was performed at pH 8 and pH 9, where the latter was reached by adding 100 µl of a 0.1 M NaOH solution to the synthesis reaction, soon after injection of $AgNO_3$. The synthesized His-RGO/Ag NPs hybrid nanocomposites were purified by two cycles of ultracentrifugation (40000 rpm for 20 min) and were dispersed in 2 mL water at the concentration of 4 mg mL^{-1} in His-RGO and 16 mg mL^{-1} in $AgNO_3$ for further characterizations.

Pre-treatment of cotton (Cot). Cot fabrics were pre-treated to remove contaminants by overnight stirring in acetone, followed by three cycles of washing in water at 40°C. [18]

Modification of Cot fabrics with His, His-RGO, Ag NPs and His-RGO/Ag NPs. Two types of Cot fabrics (3.8 cm in diameter, 0.4±0.05 g) were prepared by using the His-RGO/Ag NPs nanocomposite synthesized at pH 9. The former, Cot/His-RGO/Ag NPs_C1, was achieved treating the fabrics by four impregnation steps of 3 h each, and one overnight impregnation, in a nanocomposite dispersion 4 mg mL^{-1} in His-RGO and 16 mg mL^{-1} in $AgNO_3$. The latter, Cot/His-RGO/Ag NPs_C2, was prepared treating the fabrics by one impregnation step of 3 h in a nanocomposite dispersion, 0.4 mg mL^{-1} in His-RGO and 1.6 mg mL^{-1} in $AgNO_3$. A drying step at 50°C onto a hotplate was performed after each impregnation.

For the purpose of comparison, a set of samples was prepared by impregnating Cot with respectively, solutions of His and dispersions of His-RGO and Ag NPs, all at pH 9, here named Cot/His, Cot/His-RGO and Cot/Ag NPs. Cot/His-RGO_C1 were achieved treating Cot by four impregnation steps of 3 h each, and one overnight impregnation in 4 mg mL^{-1} His-RGO aqueous dispersions, while Cot/His-RGO_C2 were prepared modifying Cot by one impregnation step of 3 h, in 0.4 mg mL^{-1} His-RGO aqueous dispersions. Cot/His_C1 were prepared by four impregnation steps of 3 h each, and one overnight impregnation, in 6.4 M His aqueous solutions, while Cot/His_C2, by one impregnation step of 3 h in 0.64 M His aqueous solutions. Finally, Cot/Ag NPs were achieved by one impregnation step of 3 h with Ag NPs aqueous dispersions at the concentrations of 1.6 mg mL^{-1} in $AgNO_3$.

Characterization techniques.

UV−Vis Spectroscopy analysis. Steady state UV-Vis absorption spectra were collected in reflectance mode by a Cary 5000 (Varian) UV/Vis/NIR spectrophotometer at room temperature.

Raman analysis. Excitation of the Raman scattering was done in 180◦ backscattering geometry by a MicroRaman Xplora (Horiba) using a 532 nm laser (power 0.125 mW cm^{-2}), objective 10×, 10% filter and 1200 g/mm diffraction gratings. Spectral data were collected at room temperature (21 ± 2 °C) in the range between 100-3000 cm^{-1}, with 25 s acquisition time and 25 accumulations per spectrum. It is crucial to not exceed the laser power of 0.2 mW cm^{-2} to prevent fluorescence phenomena, and laser powers higher than 0.4 mW cm^{-2} to avoid substrate damaging induced by the Raman laser.

Attenuated Total Reflection Fourier Transform Infrared (ATR-FTIR) Spectroscopy. ATR-FTIR spectroscopy was carried out by a 670 FTIR spectrometer (Varian, Palo Alto, CA, USA) equipped with a diamond ATR accessory of 2 mm and a deuterated tryglicine sulfate (DTGS) detector. The samples were deposited by casting onto the internal reflection element and the solvent was allowed to evaporate. Spectra were recorded in the 4000–400 cm^{-1} range, by acquiring 16 scans with a nominal resolution of 1 cm^{-1}.

*X-rays Photoelectron Spectroscopy (XPS).*XPS analyses of UCot, Cot/His-RGO, Cot/Ag NPs and Cot/His-RGO/Ag NPs_C2,were carried out with a Scanning XPS Microprobe (PHI 5000 Versa Probe II, Physical Electronics) equipped with a monochromatic Al Kα X-ray source (1486.6 eV), operating at 15 kV and 24.8 W, with a spot size of 100 µm. Survey (0–1200 eV) and high-resolution spectra (C1s, O1s, and Ag3d) were recorded in FAT (Fixed Analyser Transmission) mode at a pass energy of 117.40 eV and 29.35 eV, respectively.

All spectra were collected at an angle of 45° with respect to the sample surface. Charging was compensated using a dual beam charge neutralization system with a flux of low energy electrons (~1 eV) combined with very low energy positive Ar^+ ions (10 eV). The C-C component of C1s spectrum was used as internal standard for charging correction and it was fixed at 284.8 eV. Best-fitting of the high-resolution spectra was carried out with MultiPak data processing software (Physical Electronics).

Transmission Electron Microscopy (TEM) investigation. TEM analyses were performed by a Jeol Jem-1011 microscope operating at 100 kV, and equipped by a high-contrast objective lens, and a W filament as an electron source, with an ultimate point resolution of 0.34 nm. Images were acquired by a Quemesa Olympus CCD 11 Mp Camera. Samples were prepared by dipping a 300 mesh amorphous carbon-coated Cu grid in aqueous dispersions of Ag NPs and His-RGO/Ag NPs, then leaving water to evaporate at room temperature.

Field Emission Scanning Electron Microscopy (FE-SEM). Field emission scanning electron microscopy (FE-SEM) analyses of Cot, Cot/His-RGO_C2, Cot/Ag NPs and Cot/His-RGO/Ag NPs_C2, were performed by using a Zeiss Sigma microscope (Carl Zeiss Co., Oberkochen, Germany) operating at 5 kV and equipped with an in-lens secondary electron detector and an INCA Energy Dispersive Spectroscopy (EDS) detector. The Cot/Ag NPs, Cot/His-RGO and Cot/His-RGO/Ag NPs_C2 samples were analysed after 24 h of incubation with *E. coli*, that was fixed using 2.5% glutaraldehyde in phosphate-buffered saline buffer (PBS) (0.2 M, pH 7.0) overnight at 4°C. Afterwards, the samples were washed several time with PBS, and were soaked in aqueous ethanol solutions, at increasing concentrations in ethanol from 20% to 100%, with a time lapse of 15 min between each soaking, to gradually dehydrated the bacterial cells, and finally left to dry overnight.

All the specimens were fixed onto silicon slides that were mounted onto stainless-steel sample holders by using a double-side carbon tape and were coated, by sputtering, with a thin layer of Au (10 nm) to avoid charging effects.

Antibacterial activity.

Antibacterial activity was assessed using a quantitative approach based on the Transfer Method from ISO 20743:2021 [*https://www.iso.org/standard/79819.html*], with some modifications. In detail, the antimicrobial activity was done against *E. coli* (ATCC 35218), Gram-negative bacteria purchased from ATCC (www.atcc.org). *E. coli* strain was propagated into Nutrient broth (NB) (Oxoid, Basingstoke, Hampshire, UK) and incubated at 37°C for 24 h. Cells were isolated by centrifugation (10,000 rpm, 10 min, 4°C), washed twice in 50 mM sterile potassium phosphate buffer (pH 7.0), and re-suspended in NB. Cell density was estimated using optical density at 620 nm, and the strain was used as an inoculum for antibacterial tests, after dilution in NB to a final concentration of ca. 6.0 log10 colony-forming unit (CFU) mL^{-1}. The ISO tests of Cot, Cot/His_C1/C2, Cot/His-RGO_C1/C2, and Cot/His-RGO/Ag NPs_C1/C2, were performed on six replicates of each sample. Cot fabrics were placed in a plate of nutrient agar containing 1 mL of the bacterial suspension at the concentration of ca. 6.0 $\log_{10}$ CFU mL^{-1}, to transfer bacteria from the plate to the specimens. Immediately after the inoculation, a neutralizing solution was added to 3 specimens of each type of sample. The vials were shaken out vigorously by a vortex mixer to remove attached cells. The resulting suspensions were subjected to serial dilution in physiological saline solution (0.9% NaCl) and a viable count was determined by the plate count method with nutrient agar, prepared in duplicate for each dilution. These specimens are referred to as the time 0 (t_0) group. The remaining 3 specimens of each type of fabrics were incubated at 37°C for 24 h after the inoculation in a high humidity chamber (> 70% RH atmospheric condition). Subsequently, these samples were processed in the same way as the t_0 group and referred to as the t_{24} group. The enumeration of bacteria was expressed in CFU mL^{-1}, that was calculated according to the dilution factor. Each experiment was repeated three times using three batches of samples.

Antibacterial activity (A) was calculated according to Eq. (1):

$$A = (logC_t \ - \ logC_0) - \ (logT_t \ - \ logT_0) = F - G \tag{1}$$

where C_t and C_0 are the Log CFU mL^{-1} of the Cot control samples at t_0 and after 24 h (t_{24}), respectively; t_t and t_0 are the Log CFU mL^{-1} of the Cot/His_C1/C2, Cot/His-RGO_C1/C2 and Cot/His-RGO/Ag NPs_C1/C2 samples at t_{24} and t_0, respectively; F is the growth value of the control Cot specimen and G is the cell density of the Cot/His_C1/C2, Cot/His-RGO_C1/C2 and Cot/His-RGO/Ag NPs_C1/C2 samples, respectively. According to the ISO, efficacy of the antibacterial properties of the fabrics can be considered as “low” when A<2, “significant” when $2 \leq A < 3$, and “strong” when $A \geq 3$.

The bacterial reduction percentage (R%) in number of viable/live bacteria after incubation [19] was also determined using Eq. (2):

$$R\ (\%) = \frac{logC_t - logT_t}{logC_t} * 100 \tag{2}$$

Study of the stability of bactericidal activity over time

Two kinds of experiments were performed to study the stability of the bactericidal effect of the His-RGO/Ag NPs nanocomposite, 0.4 mg mL^{-1} in His-RGO and 1.6 mg mL^{-1} in $AgNO_3$, over time.

In the first experiment, the same batch of the His-RGO/Ag NPs dispersion was divided into four aliquots and their antibacterial performance was respectively tested at day 0 and after 15, 30 and 60 days of aging, upon deposition onto Cot by one step of impregnation of 3 h.

In the second experiment, another batch of the His-RGO/Ag NPs dispersion, 0.4 mg mL^{-1} in His-RGO and 1.6 mg mL^{-1} in $AgNO_3$, was used to coat four Cot fabrics samples, by one impregnation of 3 h, and their antibacterial activity was respectively investigated on day 0 and after 15, 30 and 60 days of aging. For comparison, the antimicrobial activity of a 1.6 mg mL^{-1} in $AgNO_3$ Ag NPs dispersion was tested in the same experimental conditions as the nanocomposite. All the dispersions and the modified Cot fabric samples were stored at room temperature and under daylight exposure.

4.3 Results and discussion

4.3.1 Exfoliation and functionalization of Reduced Graphene Oxide (RGO) with histidine (His)

Commercial RGO was exfoliated and functionalized by liquid phase exfoliation (LPE) with Histidine (His), by stirring and sonication in aqueous solutions of His at pH 11, followed by cycles of purification by ultracentrifugation and redispersion in water. His intercalates between the RGO layers, [20] assembling onto the RGO basal plane by aromatic π–π stacking interactions through its imidazole ring (Fig.3.2.1 panel A), and peels off the sheets during sonication, facilitating exfoliation.[21, 22]

The condition of pH 11 was selected because His is in its deprotonation state having pKa ~ 9.1, [23]its dandling carboxylate and ammino groups allow RGO dispersion in water, with the negative charges of the carboxylate groups that limit RGO π–π re-stacking by electrostatic repulsion. The results of the spectroscopic and morphological characterization are reported in *Results and Discussion* of Chapter 3, paragrah 3.3.1. *His-RGO functionalization of cotton fabrics (*Fig.3.1).

4.3.2 Synthesis and characterization of the His-RGO/Ag NPs hybrid nanocomposite

An *in situ* synthesis colloidal approach was used for the preparation of the hybrid nanocomposite formed by the complex His-RGO decorated with Ag NPs, in water, by using silver nitrate ($AgNO_3$) precursor, in presence of sodium borohydride ($NaBH_4$) and sodium citrate tribasic dehydrate ($C_6H_5O_7Na_3 \times 2H_2O$).

To engineering the nanocomposite for antimicrobial applications, and purposely synthesize His-RGO sheets densely coated by small Ag NPs, the role of the chemical species involved in the synthesis on the coating density and size of the NPs was investigated, by tuning the experimental parameters, and concomitantly investigating morphology and spectroscopy properties of the achieved nanostructures. For this purpose, three preliminary control experiments were performed; in a first experiment, His-RGO and the silver precursor were mixed under stirring, in the other two experiments, citrate and borohydride were separately added to such a mixture. Afterwards, a systematic study of the effect of the Ag precursor, His-RGO, citrate and borohydride relative concentrations, and of the pH of the reaction solution, on the morphological and spectroscopic properties of the achieved hybrid nanocomposites, was carried out.

Control experiments

The series of control experiments was performed by stirring, at ice bath temperature, dispersions in water respectively of: i. His-RGO added by the Ag precursor without citrate and borohydride, ii. His-RGO added by the Ag precursor and then by borohydride without citrate, and iii. His-RGO added by citrate and then by the Ag precursor, without borohydride. The achieved samples were purified by multiple cycles of ultracentrifugation and redispersion in water, and UV-Vis absorption spectroscopy and morphology investigation of the isolated pellets and of the collected supernatants, was performed.

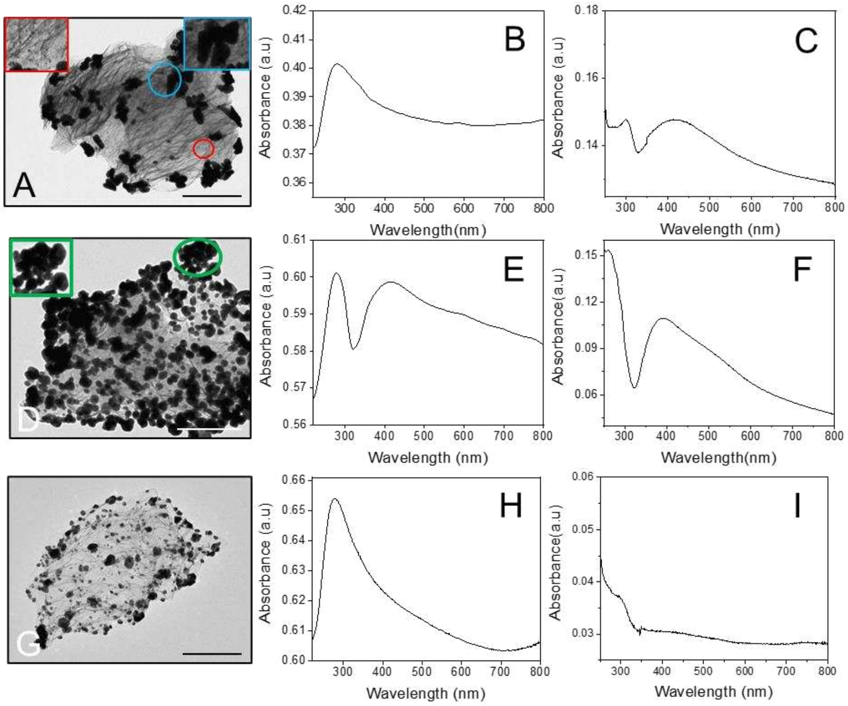

***Fig.4.1**: TEM images (A,D,G) with details of the NPs morphology (in the insets) and UV-Vis absorption spectra of the (B,E,H) hybrid samples obtained with the 1:1 Ag precursor:His-RGO w/w at ice-bath temperature, starting from 4 mg mL^{-1} RGO and 4 mg mL^{-1} AgNO$_3$, and of the (C,F,I) corresponding collected supernatants (scale bar 200 nm). The samples were prepared stirring His-RGO with the Ag precursor (A-C) without borohydride and citrate, (D-F) with 3 mM borohydride and without citrate and (G-I) with 3.7 mM citrate and without borohydride. In (D) the Ag precursor:borohydride molar ratio is 1:1.7 and in (G) the Ag precursor:citrate molar ratio is 1:2.5. In (B,E,H) UV-Vis absorption spectra were collected by diluting 1:100 the as-synthesized samples of panels (A,D,G).*

TEM micrographs of the sample of panel A show sheet like micrometer sized features exhibiting the folded edges, wrinkles and corrugations typical of RGO sheets [24](Fig.4.1,panel B), decorated with high image contrast polydisperse NPs, having size between 9 ± 4 nm and 96 ± 25 nm, also irregular and multifaceted in the morphology, with some of them showing a not uniform image contrast (Fig.4.1, panel A), likely due to the occurrence of coalescence and aggregation phenomena [26]. The UV-Vis absorption spectrum of this sample presents the strong absorption peak of RGO at 281 nm, which broadens towards the low energy side of the spectrum (Fig.4.1, panel B), likely including the signal of the polydisperse Ag nanostructures (Fig.4.1, panel A), with an increase of the absorption baseline, reasonably due to scattering processes originated from RGO multilayers. The absorption spectrum of the corresponding supernatant shows a peak at 300 nm [27] that is likely due to nitrate ions, and a broad peak at 415 nm ascribed to the Localized Surface Plasmon Resonance (LSPR) absorption peak originated from collective excitation of the free conduction band electrons of neat Ag

NPs [28], assessing the presence of unreacted precursor, as well as occurrence of homonucleation of Ag NPs in the reaction solution (Fig.4.1, panel C).

The Ag nanostructures observed in the sample of panel A can be reasonably explained by the spontaneous galvanic reduction of Ag^+ ions diffusing from the solution,[29] due to transfer of electrons from RGO, which electrostatically interact with the $-COO^-$ groups of His-RGO, heteronucleating and growing coordinated to the $-NH_2$ and $-COO^-$ sites of His []

The sample of panel D presents a significantly higher density of nanostructures than the sample of panel A, more spherical and partially also aggregated, with a not uniform image contrast and a mean size of 31 ± 7 nm (Fig.4.1, panel D). This sample shows, in the absorption spectrum, the peak of RGO at 281 nm and the LSPR peak of Ag NPs at 414 nm, that enlarges towards the low energy side of the spectral range, due to aggregation of Ag nanostructures (Fig.4.1, panel E). The corresponding supernatant shows the LSPR peak of Ag NPs at 391 nm, assessing occurrence of homonucleation also in this experimental condition (Fig.4.1, panel F).

The Ag nanostructures of panel D are supposed to form by combination of the rapid reduction of the Ag precursor by borohydride [30]and by the galvanic process[31]. The spherical shape of the NPs can be explained by the temporary stabilizing effect of the borohydride ions, that coordinate small Ag clusters at the early stages of the synthesis, contributing in controlling their morphology, and then evolve in borate ions by side reactions with water, [30]detaching from the surface of the clusters and leading to aggregative/coalescence events involving also the nanostructures preformed onto the RGO basal plane by galvanic reduction.

The sample of panel G presents few aggregated NPs with a size of ca. 50-100 nm, along with smaller NPs with a mean size of ca. 27 ± 7 nm, a spherical morphology and a coating density lower than the sample of panel D. The absorption spectrum shows the strong peak of RGO at 281 nm, that broadens towards the lower energy side of the spectral range, as it most likely includes the plasmon signal from polydisperse Ag NPs (Fig.4.1, panel H), and it is more intense than the signal of sample of panel A (Fig.4.1, panel B) and of panel C (Fig.4.1, panel E), addressing a higher exfoliation of RGO, likely due to repulsive interactions among citrate ions binding the surface $-COO^-$ and $-NH_2$ moieties of His-RGO by hydrogen bonds. The corresponding supernatant shows only a weak large LSPR shoulder between 350-600 nm and the peak at ca. 300 nm ascribed to nitrite ions [27](Fig.4.1, panel I). The evidence that homonucleation phenomena of NPs occur with a less extent in the supernatant, and that the coating density of the sample of panel G is lower than the sample of panel D, assess that part of the Ag precursor remains unreacted in solution, allowing to infer that, at the investigated low temperature of the process, sodium citrate behaves mostly as a strong coordinating ligand, [32] controlling morphology of the Ag clusters formed by reduction with His-RGO in the galvanic process.

This preliminary set of experiments demonstrates the behaviour of the species involved in the synthesis of the Ag NPs in presence of His-RGO in the investigated experimental conditions, assessing the role of: (i) His, in anchoring the Ag NPs to the RGO sheets by coordination to its $-COO^-$ and $-NH_2$ groups, and in mediating charge transfers between RGO and the Ag NPs [ref nostril], (ii) borohydride, as a strong reducing and temporary capping agent, accomplishing reduction of the Ag precursor to Ag clusters and contributing in controlling their morphology at the early stages of their synthesis, and (iii) citrate, as a strong coordinating ligand, [32] dictating morphology of the nanostructures formed by galvanic reduction.

Effect of the precursor and reactant molar ratio

The synthesis of the His-RGO/Ag NPs hybrid nanocomposite was performed by rapidly injecting the Ag precursor in a dispersion of His-RGO, citrate and borohydride, in water, at ice bath temperature. Such a low temperature was selected to slow down the reduction of the Ag precursor with borohydride, and for allowing a better control over the final NP morphology, avoiding aggregation and loss of colloidal stability.[33]

In the investigated experimental condition, as demonstrated by the preliminary control experiments, heteronucleation of the Ag clusters occurs mainly by reduction processes induced by borohydride and by transfer of electrons from His-RGO, while the growth, which is assisted mainly by citrate, evolves through aggregative/coalescence events among the Ag clusters with addition of Ag atoms diffusing from the solution, [29] until the formed NPs reach an optimal size at which electrostatic repulsions between the citrate coating molecules prevent further aggregation [34] and coalescence phenomena.

To adjust the concentration of borohydride and of citrate, aiming at achieving a high coating density of the His-RGO sheets with small Ag NPs, two experiments were performed, tuning separately the relative concentrations of borohydride and citrate, keeping constant all other synthesis parameters (Ag precursor:His-RGO w/w at 1:1, ice-bath temperature and pH) and investigating concomitantly the morphological and spectroscopic properties of the achieved nanocomposites. In the first, the relative concentration of borohydride was increased decreasing the Ag precursor:borohydride molar ratio from 1:1.7 up to 1:5 and keeping constant the Ag precursor:citrate molar ratio at 1:2.5. In the second, the relative concentration of citrate was increased by decreasing the Ag precursor:citrate molar ratio from 1:2.5 to 1:7 and keeping constant the Ag precursor:borohydride molar ratio at 1:1.7. In these experimental conditions, the pH of the synthesis solutions was measured after the Ag precursor injection, and it was found to be ca. 8.

The TEM micrographs and the UV-Vis absorption spectra of the obtained hybrid nanocomposites and corresponding supernatants are reported in Fig.4.2.

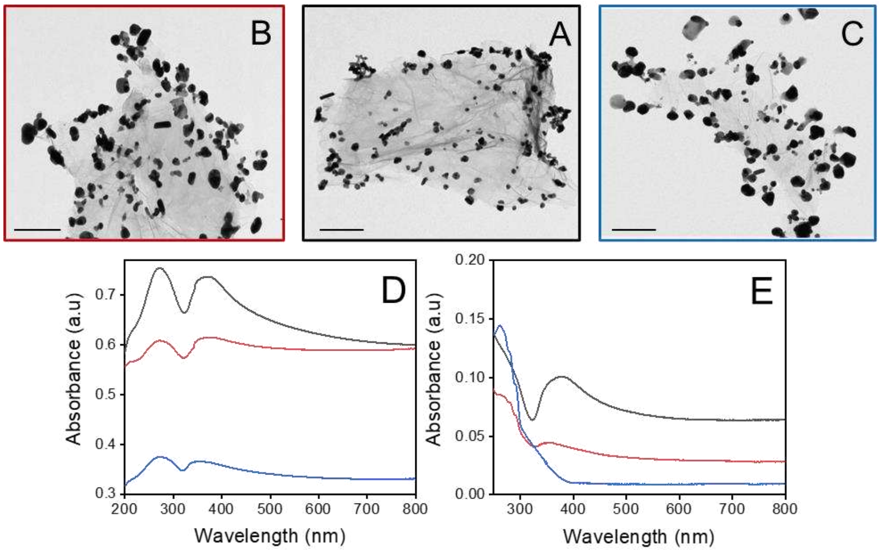

Fig.4.2 *:TEM images (A-C) of hybrid samples obtained starting from 4 mg* mL^{-1} *His-RGO and 4 mg* mL^{-1} $AgNO_3$*, at ice bath temperature, pH 8, and with the 1:1 Ag precursor:His-RGO w/w, at (A) 1:2.5 Ag precursor:citrate and 1:1.7 Ag precursor:borohydride molar ratio, (B) 1:2.5 Ag precursor:citrate and 1:5 Ag precursor:borohydride molar ratio, (C) 1:7 Ag precursor:citrate and 1:1.7 Ag precursor:borohydride molar ratio (scale bar 200 nm). (D) UV-Vis absorption spectra achieved by diluting 1:100 the as-synthesized hybrid samples of panels A-C and (E) corresponding supernatants.*

The sample reported in panel A of Figure 3.2.3 shows His-RGO sheets coated by irregular and few aggregated Ag nanostructures, and by spherical Ag NPs, 26 ± 7 nm in mean size. Its absorption spectrum has the LSPR peak of the Ag NPs at 372 nm (Fig.4.2, Panel D), more intense and narrower and shifted to lower wavelengths with respect to the LSPR peak of panel E of Figure 4.2, in which the hybrid was synthesized with only borohydride. This evidence assesses a higher control of the morphology of the NPs and a lower aggregation, which are due to the combined effect of citrate and borohydride in the formation of smaller NPs.

Passing from the Ag precursor:borohydride molar ratio of 1:1.7 to 1:5, the mean size of the nanostructures increases up to 45.8 ± 7.3 nm, as well as their aggregation (Fig.4.2, panel B), as confirmed by the shift of the absorption up to 374 nm, the enlargement of the LSPR peak, the increase of the baseline signal intensity for wavelengths higher than 450 nm (Fig.4.2, panel D), and the decrease of the LSPR peak intensity. In such a sample, the aggregation is likely induced by the increase of the ionic strength of the solution originated from the enhancement of the borohydride concentration. [30]

Passing from the Ag precursor:citrate molar ratio of 1:2.5 to 1:7, the NPs present a larger mean size of 69 ± 21 nm (Fig.4.2, panel C) with an increased polydispersion in the size. This evidence can be accounted for by the enhancement of the ionic strength of the solution due to the increase of the citrate concentration [35], inducing destabilizing effects and promoting coalescence phenomena among the clusters in growth. The LSPR peak is at 352 nm, less intense and shifted of 20 nm towards the higher energy size of the spectrum (Fig.4.2, panel D) with respect to the sample of panel A, even though the size of the Ag NPs is significantly larger. This evidence is due to the capability of citrate to reduce the oxide layer at the surface of the Ag NPs, shifting their LSPR peak. [36]

As far as the supernatants of the samples of panels A-C of Fig.4.2, the supernatant of the sample of panel A shows the LSPR peak at 379 nm, more intense than the LSPR peak of the supernatant of the sample of panel B, assessing higher Ag NPs homonucleation, while the supernatant of the sample of panel C does not show a structured LSPR feature, but only a shoulder between 300 and 400 nm likely due to nitrite ions and small Ag clusters [37](Fig.4.2, panel E). This evidence confirms that, in the investigated conditions, the increase of borohydride and citrate relative concentrations increases the extent of the unreacted Ag precursor, and this effect is more evident for citrate.

The lack of control of the NP morphology, and the tendency of the NPs to aggregate with the increase of the borohydride and citrate relative concentrations, prompted us to carry on the engineering of the nanocomposite working with the Ag precursor:borohydride and Ag precursor:citrate molar ratio of 1:1.7 and 1:2.5, tuning the other experimental parameters.

Effect of pH of the reaction solution

Since the citrate capping ligand has three carboxylic groups with pKa values respectively of 3.2, 4 and 6.4, and its coordinating capability increases when it is fully deprotonated,[38] the synthesis of the hybrid nanocomposite was performed also testing a pH of reaction higher than that investigated so far. Namely, the pH was brought to 9 by adding NaOH to the synthesis solution, soon after the Ag precursor injection, while keeping constant the 1:1 Ag precursor:His-RGO w/w, and the 1:2.5 and the 1:1.7 Ag precursor:citrate and Ag precursor:borohydride molar ratio, respectively.

The TEM images show the formation of spherical and monodisperse Ag NPs, well separated onto the His-RGO platform, with a size of ca. 20 ± 9 nm (Fig.4.3, panel A). The morphology, size and size distribution are found respectively more regular, smaller, and narrower than the nanocomposite achieved at pH 8 (Fig.4.2, panel A). The LSPR peak is at 358 nm, shifted towards the higher energy side of the investigated spectral range [29] and it is narrower and less intense than the sample synthesized at pH 8 (Fig.4.3, panel B). The LSPR peak of the supernatant (Fig.4.3, panel C) has an intensity comparable with that of the sample synthesized at pH 8 (Fig.4.2, panel E), assessing occurrence of homonucleation of the Ag NPs also in this condition of pH.

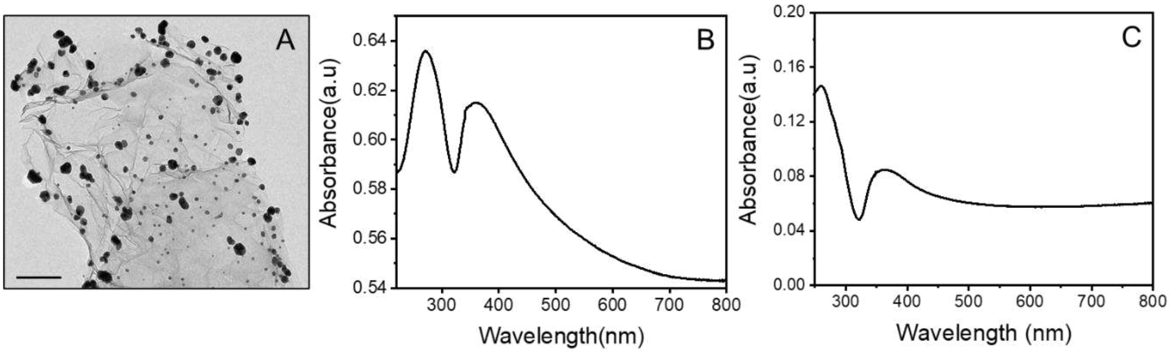

Fig.4.3 *: (A) TEM image and UV-Vis absorption spectrum of the (B) hybrid sample, obtained starting from 4 mg mL^{-1} His-RGO and 4 mg mL^{-1} $AgNO_3$, at ice bath temperature, pH 9, with the 1:1 Ag precursor:His-RGO w/w and 1:2.5 Ag precursor:citrate and 1:1.7 Ag precursor:$NaBH_4$ molar ratio and of the (C) corresponding supernatant (scale bar 200 nm). The concentration of sodium citrate and $NaBH_4$ were 0.05 M and 0.04 M, respectively. The UV-Vis absorption spectrum of panel B was collected by diluting of 1:100 the as-synthesized sample.*

The evidence that at pH 9 the size of the Ag NPs is lower than that at pH 8 can be likely ascribed to the increase of the aggregation energy barrier of the clusters in growth, due to the enhancement of their surface charge. For aggregative growth processes, in fact, the Derjaguin, Landau, Verwey, Overbeek (DLVO) theory considers that the aggregation barrier, the energy required for the aggregation of two particles, corresponds to the maximum of the interaction potential between two particles, resulting from the combination of their attractive van der Waals and repulsive electrostatic forces.[39] [40]The theory suggests that two particles can overcome their electrostatic repulsion and aggregate/coalesce, if their aggregation energy barrier is lower than the thermal energy, thus enabling particles growth. It is likely that at the low temperature of the synthesis, the increase of the negative charge of the citrate ligand molecules at pH 9 increases the repulsive electrostatic forces, slowing down the growth and reducing the size of the NPs. In view of these results, the condition of pH 9 was selected as the most suited to synthesize Ag NPs with the smallest size, and such a pH was used in the further experiments.

Effect of the $AgNO_3$:His-RGO w/w.

Another set of experiments was performed to increase the coating density of the His-RGO sheets, by increasing the $AgNO_3$:His-RGO w/w from 1:1, to 3:1 and 4:1, while fixing the pH at 9, and concomitantly tuning the Ag precursor:citrate and the Ag precursor:borohydride molar ratio to keep small the size of the NPs and narrow their size distribution.

Not an evident increase of the coating density was observed by increasing the Ag precursor:His-RGO w/w up to 3:1 and accordingly decreasing the Ag precursor:citrate and Ag precursor:borohydride molar ratio of three-folds, namely down to 3:7.5 and 3:5.1, respectively. In this condition, the His-RGO sheets are coated by monodisperse Ag NPs, 17 ± 5 nm in mean size (Fig.4.4, panel A). Conversely, an evident increase of the coating density was observed by increasing the Ag precursor:His-RGO w/w up to 4:1. In particular, with the Ag precursor:citrate and Ag precursor:borohydride molar ratio decreased of four-folds down to 4:10 and 4:6.8, the nanostructures are irregular and polydisperse with a size of ca. 61±18 (Fig.4.4, panel B), while with the Ag precursor:citrate and the Ag precursor:borohydride molar ratio decreased of five-folds down to 4:12.5 and 4:8.5, respectively they become monodisperse, with a smaller mean size of 42 ± 8 nm, showing a higher coating density. Finally, further decreasing only the Ag precursor:citrate of six-folds down to 4:15, but keeping constant the Ag precursor:borohydride molar ratio at 4:8.5, the mean size of the NPs decreases down to 24 ± 4 nm (Fig.4.4, panel D).

The Raman spectrum of the hybrid nanocomposite of panel D shows that the position of the D and G peaks of His-RGO, and their intensity ratio, do not change after decoration with the Ag NPs (Fig.4.4, panel E), assessing that the defect density of the graphitic structure of the sheets is not affected by the *in situ* synthesis of the NPs.

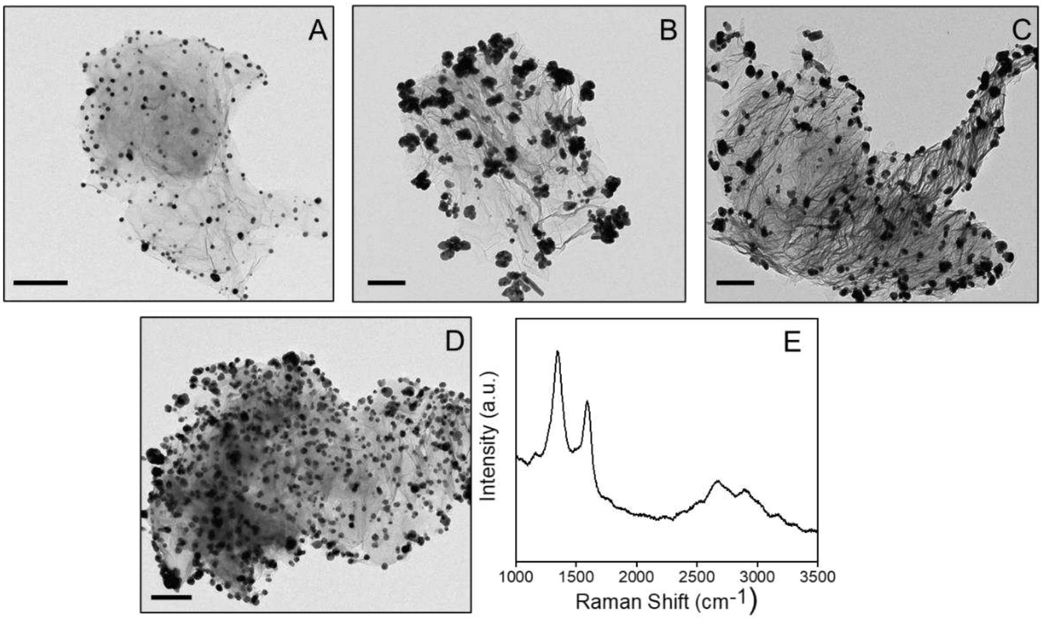

Fig.4.4: *TEM images of the hybrid samples synthesized at ice bath temperature and pH 9, obtained from (A) 4 mg mL^{-1} His-RGO and 12 mg mL^{-1} AgNO$_3$ at the 3:1 Ag:His-RGO w/w, with the 3:7.5 Ag precursor:citrate and 3:5.1 Ag precursor:borohydride molar ratio, (B) 4 mg mL^{-1} His-RGO and 16 mg mL^{-1} AgNO$_3$ at the 4:1 Ag:His-RGO w/w, with the 4:10 Ag precursor:citrate and 4:6.8 Ag precursor:borohydride molar ratio, (C) 4 mg mL^{-1} His-RGO and 16 mg mL^{-1} AgNO$_3$ at the 4:1 Ag:His-RGO w/w, with the 4:12.5 Ag precursor:citrate and 4:6.8 Ag precursor:borohydride molar ratio, (D) 4 mg mL^{-1} His-RGO and 16 mg mL^{-1} AgNO$_3$ at the 4:1 Ag:His-RGO w/w, with the 4:15 Ag precursor:citrate and 4:6.8 Ag precursor:borohydride molar ratio (scale bar 200 nm). (E) Raman spectrum of the sample of panel D.*

4.3.3 Spectroscopy and morphological properties of His-RGO/Ag NPs dispersion over time

Ag NPs are known to undergo physicochemical modifications over time, specifically dissolution, oxidation, aggregation, and ROS generation, depending on the light irradiation conditions, as well as on the properties of their coating layer (i.e. chemical structure, ionization, charge density and molecular weight) [ref], that can induce steric, electrostatic or electrosteric repulsive forces between the NPs, preventing aggregation.

In the case study of citrate coated Ag NPs, it is known that, although citrate decreases the amount of the released Ag^+ ions via chelation, [41] their release increases at lower pH,[41] and decreases with the aggregation of the Ag NPs. Dissolution with Ag^+ release and aggregation occur simultaneously, owing to the discontinuity of the citrate surface layer,[42] and could be also combined with oxidation, although citrate[41] reduces the oxide layer at the surface of the Ag NPs. [43]

In view of such properties of the Ag NPs, the morphological and spectroscopy properties of aqueous dispersions of the hybrid nanocomposite of panel D of Figure 3.2.5 were monitored over time and were compared to those of pristine citrate coated Ag NPs of same size and surface chemistry, aged in aqueous dispersions at the same pH 9 as the nanocomposite. The TEM micrographs show that the Ag NPs anchored onto His-RGO aggregate in time more slowly than the pristine Ag NPs, as they pass to be spherical with a size of 24 ± 4 nm, in the as synthesized nanocomposite, to 30 ± 8 nm after 18 days of aging, and start to aggregate after 22 days, reaching a size of 81 ± 25 nm, and 94 ± 31 nm after one month. The nanocomposite shows an extensive aggregation only after 60 days of aging (Appendix 2,Figure 1).

On the contrary, the Ag NPs show, in the same timeframe, a more extensive coalescence, as their size passes from 19 ± 3 nm to 35 ± 5 nm, 87 ± 15 nm and 157 ± 25 nm after respectively 18 and 22 days and one month. These results can be explained considering that the chemical immobilization of the Ag NPs onto the His-RGO platform prevents migration of the NPs, limiting their coalescence.

For completeness, the UV-Vis absorption spectra of the nanocomposite aqueous dispersion were collected after 32 days, and they show an enlargement of the LSPR peak of the Ag NPs over time, confirming their aggregation onto His-RGO[9]. The citrate-coated Ag NPs show an enlargement of the LSPR peak, with a decrease in intensity, as well as a 3 nm shift from 393 nm to 396 nm, that can be ascribed to their dissolution.

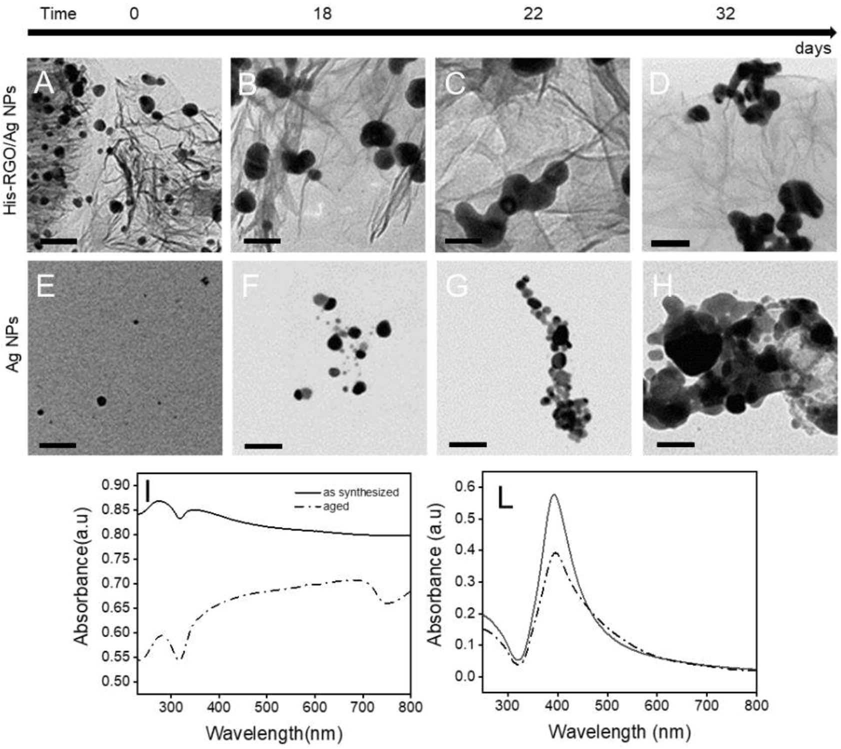

Fig.4.5: *TEM micrographs of (A-D) His-RGO/Ag NPs and (E-H) citrate coated Ag NPs, (A,E) as synthesized, and after (B,F) 18, (C,G) 22, and (D,H) 32 days (scale bar 100 nm). UV-Vis absorption spectra of (I) His-RGO/Ag NPs and (L) citrate coated Ag NPs as synthesized and after 32 days.*

4.3.4 Antimicrobial properties investigation

The standard and quantitative ISO 20743:2021 protocol was used to study, by the contact method, the antibacterial activity of the His-RGO/Ag NPs nanocomposite as a coating of Cot textiles against *E. coli* strain. Two typologies of nanocomposites coated Cot fabric samples, Cot/His-RGO/Ag NPs_C1 and Cot/His-RGO/Ag NPs_C2, were tested, differing in the concentration of the nanocomposite dispersion and in the number of impregnation steps of the textile. For purpose of comparison, control samples of untreated Cot, and Cot fabrics modified by His and His-RGO, respectively, were also tested at two different concentrations and number of impregnation steps, C1 and C2 (see Experimental Section).

According to the ISO 20743:2021, the antibacterial value (A) was calculated, where A is the efficacy of the antibacterial property of the tested fabrics. Moreover, also the growth reduction (R%) was calculated, where R% is the growth reduction of the tested specimens compared to the control samples Cot and the experimental specimens sets (Cot/His, Cot/His-RGO and Cot/His-RGO Ag NPs) after inoculation. [19]

The Cot control sample does not show antibacterial activity, but, as expected, bacterial growth, from 6.10 ±0.25 Log CFU mL^{-1} to 8.80±0.23 Log CFU mL^{-1} (Table 4.1) is observed, because of the capability of microorganisms to easily adhere, due to its large surface area and hygroscopicity,[44] and the tendency of the natural fibres to provide nutrients and energy sources in the form of carbohydrates. Likewise, Cot/His_C1 and Cot/His-RGO_C1 show a growth from 6.19±0.25 Log CFU mL^{-1} to 8.51±0.27 Log CFU mL^{-1}, and from 6.11±0.31 Log CFU mL^{-1} to 8.72±0.27 Log CFU mL^{-1}, respectively (Table 4.1). Conversely, the Cot/His-RGO/Ag NPs_C1 sample shows a 100% of abatement with a strong antibacterial efficiency with A of 9.1 (Table 4.3).

The same trend of the antibacterial activity is observed for the Cot/His-RGO/Ag NPs_C2 sample and the corresponding Cot/His_C2 and Cot/His-RGO_C2 specimens, which show a bacterial growth from 5.92±0.24 CFU mL^{-1} to 8.41±0.22 CFU mL^{-1} and from 6.63±0.27 CFU mL^{-1} to 8.90±0.29 CFU mL^{-1}, respectively.

These results assess that the biocidal effect of the nanocomposite is mainly ascribed to the Ag NPs. The latter realise Ag$^+$ ions that interact electrostatically with the negatively charged cell membrane of microorganisms, damaging it by strongly interacting with thiol groups of vital enzymes and sulphur proteins on the cellular wall surface. At the same time the bacterial envelope is disrupted, because when Ag$^+$ attach to the cell wall or cytoplasmic membrane, they enhance the permeability of the cell and ultimately lead to cell disruption. [45] Furthermore, free Ag$^+$ are uptake by cells, they deactivate respiratory enzymes generating ROS that lead to diverse dysfunctions in the lipid membrane, interfere with cell division, and attack enzymes and proteins, resulting in an irreversible damage to DNA replication. [46]

The evidence that the Cot/His-RGO samples show antibacterial growth can be explained considering that His molecules have not a biocidal effect, and, irrespectively of the intrinsic biocidal effect of RGO, which was not tested because the bare RGO is not dispersible in aqueous solution and hence not processable onto Cot. Having His a pKa of 9.1, it is likely that anchoring onto the RGO basal plane, its neat negative charge [23]induces the repulsion of bacteria cells, which also have a negative surface charge,[11] favouring their growth.

Table 4.1*. Antimicrobial results (Log CFU mL^{-1}) of the Cot, Cot/His_C1/C2, Cot/His-RGO_C1/C2, and Cot/His-RGO/Ag NPs_C1/C2, obtained according to the standard ISO 20743:2021.*

	Cell density (Log CFU mL^{-1})*	
Sample	**After inoculation (t=0 h)**	**After incubation (t=24 h)**
UCot	6.10±0.25	8.80±0.23
Cot/His_C1	6.19±0.25	8.51±0.27
Cot/His-RGO_C1	6.11±0.31	8.72±0.27
Cot/His-RGO/Ag NPs_C1	6.41±0.13	0.00±0.00
Cot/His_C2	5.92±0.24	8.41±0.22
Cot/His-RGO_C2	6.63±0.27	8.90±0.29
Cot/His-RGO/Ag NPs_C2	6.87±0.18	0.00±0.00

*CFU mL^{-1}: colony forming units mL^{-1}.

In view of the excellent biocidal effect of the Cot/His-RGO/Ag NPs_C2 samples, they were used, here on, for the further investigation of the antimicrobial properties of the nanocomposite.

4.3.5 Stability of the nanocomposite bactericidal performance over time

As assessed by Fig.4.5, the morphology of the His-RGO/Ag NPs slowly changes over time, and hence, the stability of its antimicrobial activity was tested also over time. Such a study was performed letting the nanocomposite aging both in aqueous dispersion and las a coating onto Cot and testing its biocidal effect at different times. For both kinds of tests, the times 0, 15, 30 and 60 days, were investigated (Table 4.2).
The same study was performed by using neat Ag NPs, 1.6 mg mL^{-1} in $AgNO_3$, that were aged and processed in the same conditions as the nanocomposite.

***Table 4.2**. Antimicrobial results (Log CFU mL^{-1}) obtained according to the standard ISO 20743:2021 of the Cot/Ag NPs and Cot/His-RGO/Ag NPs_C2, after 0, 15, 30 and 60 days of storage in aqueous dispersion and on Cot fabrics.*

		Cell density (Log CFU mL^{-1})*	
Storage condition	**Sample**	**After inoculation (t=0 h)**	**After incubation (t=24 h)**
	UCot	6.10±0.31	8.80±0.23
t=0 day			
In dispersion	Cot/Ag NPs	6.31±0.25	0.00±0.00
	Cot/His-RGO/Ag NPs_C2	6.44±0.22	0.00±0.00
On textile	Cot/Ag NPs	6.21±0.24	0.00±0.00
	Cot/His-RGO/Ag NPs_C2	6.18±0.26	0.00±0.00
t=15 days			
In dispersion	Cot/Ag NPs	6.19±0.31	0.00±0.00
	Cot/His-RGO/Ag NPs_C2	6.80±0.13	0.00±0.00
On textile	Cot/Ag NPs	6.21±0.30	0.00±0.00
	Cot/His-RGO/Ag NPs_C2	6.38±0.12	0.00±0.00
t= 30 days			
In dispersion	Cot/Ag NPs	6.22±0.24	7.81±0.42
	Cot/His-RGO/Ag NPs_C2	6.34±0.27	0.00±0.00
On textile	Cot/Ag NPs	6.02±0.29	6.80±0.17
	Cot/His-RGO/Ag NPs_C2	6.44±0.17	0.00±0.00
t= 60 days			
In dispersion	Cot/Ag NPs	6.11±0.31	7.91±0.32
	Cot/His-RGO/Ag NPs_C2	6.07±0.21	0.00±0.00
On textile	Cot/Ag NPs	6.31±0.21	7.03±0.18
	Cot/His-RGO/Ag NPs_C2	6.17±0.31	0.00±0.00

*CFU mL^{-1}: colony forming units mL^{-1}.

After 15 days of aging in dispersion and on textile, the Cot/Ag NPs and Cot/His-RGO/Ag NPs_C2 samples show a good antimicrobial activity. No growth, in fact, is observed for these specimens (Table 4.2), highlighting a strong antimicrobial activity (Table 4.3). After 30 days of aging in dispersion and on textile, the Cot/His-RGO/Ag NPs_C2 sample shows a good antimicrobial activity; indeed, after incubation, the cell density of E. coli is not detected (Table 4.2), and the antibacterial value A still shows a strong efficacy, namely 9.04 and 9.14, after aging in dispersion and on the textile, respectively (Table 4.3). On the contrary, for the Cot/Ag NPs specimens, where the Ag NPs were aged both in aqueous dispersion and on textile, a small increase of cell density has been observed (Table 4.2). After 60 days, irrespectively of the aging conditions, the antibacterial activity of the Cot/His-RGO/Ag NPs_C2 sample is still preserved (Table 4.2 and Table 4.3).

Table 4.3. *Antimicrobial activity (A=F-G) obtained according to the standard ISO 20743:2021, where F is the growth value on the control specimen (UCot; F=+2.7) and G is the cell density of Cot/Ag NPs and Cot/His-RGO/Ag NPs specimens.*

Sample	**Cell density (G)**	**Antimicrobial activity (A)**
Cot/His-RGO/Ag NPs_C1	-6.4	9.10
Cot/His-RGO/Ag NPs_C2	-6.8	9.50
Samples with different storage conditions		
t=0 days		
Cot/Ag NPs from dispersion	-6.31	9.01
Cot/His-RGO/Ag NPs_C2 from dispersion	-6.44	9.14
Cot/Ag NPs on textile	-6.21	8.91
Cot/His-RGO/Ag NPs_C2 on textile	-6.18	8.88
t=15 days		
Cot/Ag NPs from dispersion	-6.19	8.89
Cot/His-RGO/Ag NPs_C2 from dispersion	-6.80	9.50
Cot/Ag NPs on textile	-6.21	8.91
Cot/His-RGO/Ag NPs_C2 on textile	-6.80	9.50
t=30 days		
Cot/His-RGO/Ag NPs_C2 from dispersion	-6.34	9.04
Cot/His-RGO/Ag NPs_C2 on textile	-6.44	9.14
t=60 days		
Cot/His-RGO/Ag NPs_C2 from dispersion	-6.07	8.77
Cot/His-RGO/Ag NPs_C2 on textile	-6.17	8.87

The decrease of the antimicrobial activity of the Ag NPs aged in aqueous dispersion can be explained by their strong tendency to aggregate over time (Fig.4.5). The aggregation, in fact, decreases the surface area and surface energy of the NPs, slowing-down their dissolution and the Ag^+ ion release, [10] resulting in a decrease of their antimicrobial activity. Conversely, for the nanocomposite stored in dispersion, a long-term antimicrobial efficacy is observed over time, likely due to the capability of His-RGO to limit Ag NPs aggregation (Fig.4.5).

To go in-depth into and explain the biocidal effect of the nanocomposite aged on Cot, FE-SEM analyses were performed to study its morphology after 60 days, against that of the reference sample of Cot and of the Cot/Ag NPs and Cot/His-RGO_C2 samples, aged, for the same period, after inoculation and after 24 h of incubation of *E. coli*, concomitantly also investigating the morphology of the *E. coli* strain and its organization onto the surface of the fabrics.

Panels A-B of Fig.4.6 report representative FE-SEM images of Cot fabrics after inoculation (panel A) and after 24 h of incubation of *E. coli* (panel B), respectively. In detail, immediately after inoculation (6.10±0.25 CFU mL^{-1}), the FE-SEM micrographs show *E. coli* bacteria onto the rather smooth surface of Cot and evidence the growth of *E. coli* (8.80±0.23 CFU mL^{-1}), with a regular and smooth surface, after 24 h of incubation.

The FE-SEM analyses of the Cot/His-RGO fabrics show strain of *E. coli* wrapping bright contrast, multilayered and micrometer sized structures, reasonably ascribed to His-RGO sheets (Fig.4.6 panels C-C1), assessing that the presence of RGO sheets does not interfere with the growth of the cells (from 6.63±0.27 CFU mL^{-1} to 8.90±0.29 CFU mL^{-1}). In fact, the images confirm the presence of healthy *E. coli* cells, having morphology comparable with that observed in FE-SEM images of the Cot control sample (Fig.4.6, panel B).

The SEM images of the Cot/Ag NPs samples collected after 24 h of incubation, show that, although for such a sample a small increase of cell density of *E. coli* from 6.11±0.31CFU mL^{-1} up to 7.91±0.32 CFU mL^{-1} is observed (Table 4.2), some bacteria grow with aggregate cells formation, with intact morphological features for some cells, while for others, the cell wall is wrinkled, with the outer membrane collapsed [47](Fig.4.6, panels D-D1). As far as Cot/His-RGO/Ag NPs, instead, after 24 h of incubation, the SEM investigation demonstrates absence of cells on the textile (Fig.4.6, panels E-E1) confirming the results achieved by the plate count method, where no microbial growth is observed, as the cell density passes from 6.17±0.316 CFU mL^{-1} to 0.00±0.00 CFU mL^{-1} (Table 4.2). However, both Cot/Ag NPs and Cot/His-RGO/Ag NPs evidence grain-type coalesced nanostructures accountable for aggregates of Ag NPs, that are expected to detrimentally affect biocidal activity. Thus, to explain the motivation why the Cot/His-RGO/Ag NPs sample still shows a killing effect of bacteria after 60 days, its chemical composition was characterized by XPS and compared with that of the Cot/Ag NPs samples aged in the same conditions.

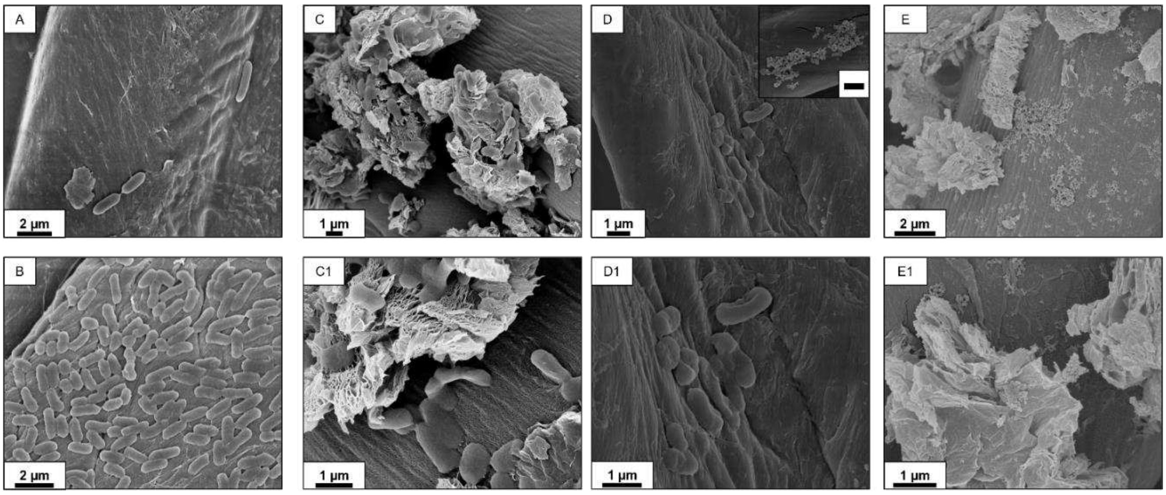

Fig.4.6: *Representative SEM micrographs of UCot and modified cotton fabrics with nanomaterials storage for 60 days onto Cot. A) UCot after inoculation of E. coli at about 6.10±0.25CFU mL*$^{-1}$ *(15Kx); B) UCot after 24 h of incubation (8.80±0.23CFU mL*$^{-1}$*) (15Kx). SEM micrographs collected at different magnifications of C-C1) Cot/His-RGO (8.90±0.29 CFU mL*$^{-1}$*) (15Kx, 30Kx), D-D1) and inset of D) Cot/Ag NPs (7.91±0.32CFU mL*$^{-1}$*) (15Kx, 30Kx) (inset of D, 30 Kx), E-E1) Cot/His-RGO/Ag NPs (0.00±0.00 CFU mL*$^{-1}$*) (15Kx, 30Kx) after 24 h of incubation, at 37°C and with high-humidity (more than 70% RH atmospheric condition) according to ISO 20743:2021 method.*

The high-resolution spectra of the Ag 3d component were reported in Fig.4.7. The spectrum of the Cot/Ag NPs sample (Fig.4.7, panel A) shows a single characteristic peak at 368.4 eV, attributed to Ag^+ (green line), in contrast, the spectrum of the Cot/His-RGO/Ag NPs sample (Fig.4.7, panel B) that consists of two components located at 368.4 eV and 367.2 eV, corresponding to Ag^+ (magenta line) and Ag^0 (green line), respectively.

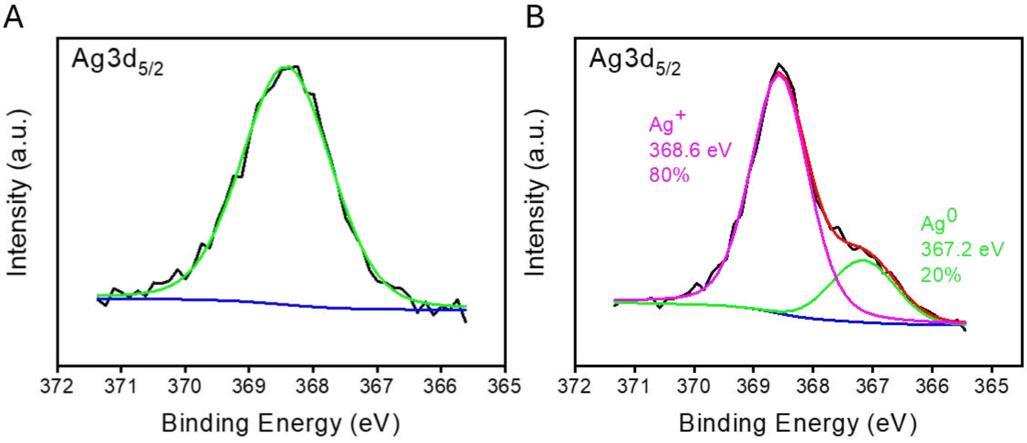

Fig.4.7: *$Ag3d_{5/2}$ high resolution XPS spectra of A) Cot/AgNPs and B) Cot/His-RGO/AgNPs samples aged for 60 days.*

The XPS spectrum of the aged Cot/Ag NPs sample indicates that the Ag NPs have undergone oxidation over time, as evidenced by the presence of only one component in the spectrum attributed to Ag^+. Conversely, the presence of the Ag^0 component (Fig.4.7, panel B, green line) in the spectrum of the aged Cot/His-RGO/Ag NPs sample confirms the role of RGO, acting as a stabilizer against the oxidation of metallic Ag NPs due to its oxygen and moisture barrier properties, thereby slowing down the oxidation process of the NPs. [10] Formation of the oxide passivation layer at the Ag NPs surface is a crucial point because slows down their dissolution kinetics in Ag^+ ions, inhibiting their antimicrobial activity. [10]

4.4 Conclusions

A novel hybrid nanocomposite formed of citrate coated Ag NPs anchored onto histidine (His) modified RGO sheets, has been fabricated by a simple and reproducible *in situ* colloidal chemical approach. RGO sheets have been achieved by liquid-phase-exfoliation with His, which intercalates among RGO multilayers and anchors onto the RGO basal plane by aromatic π-π stacking interactions, allowing RGO dispersion in water. The heteronucleation of the citrate-coated Ag NPs onto the -COO, imidazole and $-NH_2$ groups of His results in the dense decoration of the RGO sheets with Ag NPs of 24 ± 4 nm in size. The synthesis has been found to occur by an aggregative growth process affected by the $AgNO_3$:citrate and $AgNO_3$:borohydride molar ratio and by the pH of the synthesis solution. The process is assisted mainly by citrate and borohydride, the former behaving as a strong coordinating ligand, the latter, acting as a strong reducing agent and as a coordinating ligand sole at the early stages of the synthesis. The pH controls the negative charge of the citrate ligands that, undergoing electrostatic repulsions at the surface of the Ag clusters, slow down their aggregative growth yielding to Ag NPs with small size.

The developed nanocomposite has demonstrated a strong biocidal effect against *E. coli* bacteria upon deposition onto cotton. Its antimicrobial activity, tested by the standard ISO protocol method (ISO 20743:2021), improves with respect to that of His-RGO, that, on the contrary, favours their growth, and lasts longer than that of the neat Ag NPs of comparable size and surface chemistry. The nanocomposite has been observed to undergo morphology changes on the textile, because it slowly aggregates in time, but preserves its antimicrobial activity for times longer than those of the neat Ag NPs, thanks to the capability of His-RGO to slow down aggregation and oxidation. Investigations of the cytotoxicity of the nanocomposite are currently in progress to test its biocompatibility, in order to target the material in applications of wound dressing, medical equipment and food packaging.

References

[1] R.E. Siegel, “Emerging gram-negative antibiotic resistance: daunting challenges, declining sensitivities, and dire consequences,” Respir Care, 2008. 53(4): p. 471-9.

[2] X.-Z. Tang, et al., “Synthesis of graphene decorated with silver nanoparticles by simultaneous reduction of graphene oxide and silver ions with glucose,” Carbon, 2013. 59: p. 93–99.

[3] R. Khojasteh-Taheri, et al., “Green Synthesis of Silver Nanoparticles Using Salvadora persica and Caccinia macranthera Extracts: Cytotoxicity Analysis and Antimicrobial Activity Against Antibiotic-Resistant Bacteria,” Applied Biochemistry and Biotechnology, 2023. 195(8): p. 5120-5135.

[4] R.A.N. Chmielewski and J.F. Frank, “Biofilm Formation and Control in Food Processing Facilities,” Compr Rev Food Sci Food Saf, 2003. 2(1): p. 22-32.

[5] J. Harrison, et al., “A new understanding of these microbial communities is driving a revolution that may transform the science of microbiology,” Am. Sci., 2005. 93.

[6] C. Marambio-Jones and E.M.V. Hoek, “A review of the antibacterial effects of silver nanomaterials and potential implications for human health and the environment,” Journal of Nanoparticle Research, 2010. 12(5): p. 1531-1551.

[7] Y. Xiong, et al., “The role of surface chemistry on the toxicity of Ag nanoparticles,” Small, 2013. 9(15): p. 2628-38.

[8] R. Weiner, et al., “Assessment of Mass Transfer from Poly(ethylene) Nanocomposites Containing Noble-Metal Nanoparticles: A Systematic Study of Embedded Particle Stability,” ACS Applied Nano Materials, 2018. 1.

[9] Y. Li, et al., “Surface-Coating-Dependent Dissolution, Aggregation, and Reactive Oxygen Species (ROS) Generation of Silver Nanoparticles under Different Irradiation Conditions,” Environmental Science & Technology, 2013. 47(18): p. 10293-10301.

[10] B. Le Ouay and F. Stellacci, “Antibacterial activity of silver nanoparticles: A surface science insight,” Nano Today, 2015. 10(3): p. 339-354.

[11] H.M. Hegab, et al., “The controversial antibacterial activity of graphene-based materials,” Carbon, 2016. 105: p. 362-376.

[12] S. Liu, et al., “Antibacterial activity of graphite, graphite oxide, graphene oxide, and reduced graphene oxide: membrane and oxidative stress,” ACS Nano, 2011. 5(9): p. 6971-80.

[13] A. ElMekawy, et al., “Applications of graphene in microbial fuel cells: The gap between promise and reality,” Renewable and Sustainable Energy Reviews, 2017. 72: p. 1389-1403.

[14] Y. Hernandez, et al., “High-yield production of graphene by liquid-phase exfoliation of graphite,” Nature Nanotechnology, 2008. 3(9): p. 563-568.

[15] C. Ingrosso, et al., “Au nanoparticle in situ decorated RGO nanocomposites for highly sensitive electrochemical genosensors,” Journal of Materials Chemistry B, 2019. 7(5): p. 768-777

[16] E. Pinho, et al., “Antimicrobial activity assessment of textiles: standard methods comparison,” Annals of Microbiology, 2011. 61(3): p. 493-498.

[17] M.R. Das, et al., “The synthesis of citrate-modified silver nanoparticles in an aqueous suspension of graphene oxide nanosheets and their antibacterial activity,” Colloids and Surfaces B: Biointerfaces, 2013. 105: p. 128-136.

[18] S. He, et al., “Functionalization of cotton by reduced graphene oxide for improved electrical conductivity,” Textile Research Journal, 2019. 89(6): p. 1038-1050.

[19] Q. Wang, et al., “In situ synthesis of silver or selenium nanoparticles on cationized cellulose fabrics for antimicrobial application,” Mater Sci Eng C Mater Biol Appl, 2021. 121: p. 111859.

[20] C. Ingrosso, et al., “Solvent dispersible nanocomposite based on Reduced Graphene Oxide and in-situ decorated gold nanoparticles,” Carbon, 2019.

[21] L. Catarinucci, et al., “Smart IoT system empowered by customized energy-aware wireless sensors integrated in graphene-based tissues to improve workers thermal comfort,” Journal of Cleaner Production, 2022.

[22] L. Zhang, et al., “Surface-assisted assembly of a histidine-rich lipidated peptide for simultaneous exfoliation of graphite and functionalization of graphene nanosheets,” Nanoscale, 2019. 11(6): p. 2999-3012.

[23] J.G. Mesu, et al., “Host-guest chemistry of copper(II)-histidine complexes encaged in zeolite,” Y. Chemistry, 2006. 12(27): p. 7167-77.

[24] C.K. Chua and M. Pumera, “Chemical reduction of graphene oxide: a synthetic chemistry viewpoint,” Chemical Society Reviews, 2014. 43(1): p. 291-312.

[25] F. Vischio, et al., “Au nanoparticles decorated nanographene oxide-based platform: Synthesis, functionalization and assessment of photothermal activity,” Biomaterials Advances, 2022. 145: p. 213272.

[26] C. Ingrosso, et al., “PbS nanocrystals decorated Reduced Graphene Oxide for NIR responsive capacitive cathodes,” Carbon, 2021. 182: p. 57-69.

[27] J. Tang, et al., “Chemical-etched silver nanowires with tunable rough shape for surface enhanced Raman scattering,” Colloids and Surfaces A: Physicochemical and Engineering Aspects, 2021. 630: p. 127521.

[28] A. Amirjani, F. Firouzi, and D.F. Haghshenas, “Predicting the Size of Silver Nanoparticles from Their Optical Properties,” Plasmonics, 2020. 15(4): p. 1077-1082.

[29] X. Dong, et al., “Shape Control of Silver Nanoparticles by Stepwise Citrate Reduction,” Journal of Physical Chemistry C, 2009. 113: p. 6573-6576.

[30] D.L. Van Hyning, et al., “Silver Nanoparticle Formation: Predictions and Verification of the Aggregative Growth Model,” Langmuir, 2001. 17(11): p. 3128-3135.

[31] Q. Zhang, et al., “A Systematic Study of the Synthesis of Silver Nanoplates: Is Citrate a “Magic” Reagent?” Journal of the American Chemical Society, 2011. 133(46): p. 18931-18939.

[32] X. Dong, et al., “Synthesis of Triangular Silver Nanoprisms by Stepwise Reduction of Sodium Borohydride and Trisodium Citrate,” Journal of Physical Chemistry C, 2010. 114: p. 2070-2074.

[33] A.A. Mirzaei, et al., “Characterization and optical studies of PVP-capped silver nanoparticles,” Journal of Nanostructure in Chemistry, 2017. 7: p. 37-46.

[34] Z.S. Pillai and P.V. Kamat, “What Factors Control the Size and Shape of Silver Nanoparticles in the Citrate Ion Reduction Method?” The Journal of Physical Chemistry B, 2004. 108(3): p. 945-951.

[35] A. Henglein and M. Giersig, “Formation of Colloidal Silver Nanoparticles: Capping Action of Citrate,” Journal of Physical Chemistry B, 1999. 103: p. 9533-9539.

[36] X. Li, et al., “Aggregation kinetics and dissolution of coated silver nanoparticles,” Langmuir, 2012. 28(2): p. 1095-104.

[37] T. Linnert, et al., “Long-lived nonmetallic silver clusters in aqueous solution: preparation and photolysis,” Journal of the American Chemical Society, 1990. 112: p. 4657-4664.

[38] W. Patungwasa and J.H. Hodak, “pH tunable morphology of the gold nanoparticles produced by citrate reduction,” Materials Chemistry and Physics, 2008. 108(1): p. 45-54.

[39] B.V. Derjaguin, N.V. Churaev, and V.M. Muller, The Derjagu

[40] J.A.V. Butler, “Theory of the Stability of Lyophobic Colloids,” Nature, 1948. 162(4113): p. 315-316.

[41] X. Yang, et al., “Mechanism of silver nanoparticle toxicity is dependent on dissolved silver and surface coating in Caenorhabditis elegans,” Environmental Science & Technology, 2012. 46(2): p. 1119-27.

[42] S. Li, et al., “Surface Al-doping for compromise between facilitating oxygen redox and enhancing structural stability of Li-rich layered oxide,” Energy Storage Materials, 2023. 55: p. 356-363.

[43] M. Chen, et al., “Preparation and Study of Polyacryamide-Stabilized Silver Nanoparticles through a One-Pot Process,” The Journal of Physical Chemistry B, 2006. 110(23): p. 11224-11231.

[44] D. Gao, et al., “Long-acting antibacterial activity on the cotton fabric,” Cellulose, 2021. 28(3): p. 1221-1240.

[45] P.R. More, et al., “Silver Nanoparticles: Bactericidal and Mechanistic Approach against Drug Resistant Pathogens,” Microorganisms, 2023. 11, DOI: 10.3390/microorganisms11020369.

[46] K. Markowska, et al., “Silver nanoparticles as an alternative strategy against bacterial biofilms,” Acta Biochimica Polonica, 2013. 60(4): p. 523-30.

[47] Y. Yu, et al., “Ag-Conjugated graphene quantum dots with blue light-enhanced singlet oxygen generation for ternary-mode highly-efficient antimicrobial therapy,” Journal of Materials Chemistry B, 2020. 8(7): p. 1371-1382.

Chapter 5

Green synthesis of Ag NW-decorated RGO nanocomposites via a combined in situ–ex situ approach deposited on paper for SERS detection of drugs and pollutants

5.1 Introduction

The contamination of various freshwater sources and wastewater by pharmaceuticals is a widespread environmental concern that necessitates routine monitoring of pollutants to implement proper countermeasures. For fulfilling such a purpose, conventional analytical methods (gas chromatography/mass spectrometry (GC/MS), atomic absorption spectroscopy (AAS), high-performance liquid chromatography (HPLC)) have been typically used and they allow to quantify trace levels of pharmaceuticals. However, such technologies are expensive, require long times of analysis, or the use of toxic reagents, and present challenges for *on-site* investigation, because are not portable and have a large size. In addition, these approaches require a phase of sample preparation, including separation and/or pre-concentration steps, that can be particularly time consuming and especially problematic for a range of polar pharmaceuticals [1]. Despite recent advancements in some techniques, such as solid phase microextraction, challenges remain with respect to detection accuracy, indicating the need for further optimization. Besides, fast and accurate simultaneous detection of a wide range of pharmaceuticals in complex matrices, [1] with high sensitivity, continues to be a significant issue. These challenges highlight the need to develop analytical methods based on less expensive and sophisticated instruments, which could also be employed for *on-site* investigation.

Raman spectroscopy and surface-enhanced Raman spectroscopy (SERS) have emerged as promising analytical alternatives for addressing such a challenge. SERS-based sensors, in fact, can enhance fingerprints of analyte molecules, resulting in a superior sensitivity, allowing detection of molecules at trace levels, overcoming also sensitivity limitations of conventional Raman spectroscopy, in which signals are typically weak due to the small scattering cross-section of molecules [2,3].

It is well-established that two amplification mechanisms contribute to the enhancement of the Raman signal in SERS: electromagnetic enhancement (EM) and chemical or charge-transfer enhancement (CE)[4]. In the EM mechanism, the electromagnetic field surrounding analyte molecules is intensified by the surface plasmon resonance (SPR) of metallic NPs such as Ag, Au, and Cu at the analyte-substrate interface.

Since both amplification mechanisms simultaneously contribute to the Raman signal enhancement, there is significant interest in developing SERS substrates that can exploit both phenomena concurrently.[5]

Significant efforts have been devoted to the fabrication of stable and reusable SERS substrates based on metallic nanostructures capable of providing reproducible and high SERS signal enhancements. Previous reports indicate that Ag NPs [6] offer greater advantages for SERS applications compared to Au and Cu NPs, owing to their stronger plasmonic properties and ease of synthesis [7]. However, reproducibility and stability of their SERS signal remains a challenge due to their tendency to oxidize, aggregate and dissolve in presence of atmospheric oxygen and water vapor [8]. This limitation can be overcome by coating Ag NPs with a protective layer that does not interfere with their SERS activity while preventing oxidation. Besides, to further improve their enhancement factors, the SPR of Ag nanostructures have been coupled with other nanomaterials, to merge their EM effect with the CE mechanisms [4] [9].

For this purpose, single layer graphene and its derivatives have attracted as SERS substrates for accomplishing Raman enhancement [9]. Graphene oxide (GO) and reduced graphene oxide (RGO) have been, in fact, widely used in such applications for their large surface area and high surface reactivity that open the venue to the preparation of a variety of novel nanocomposites with (bio)molecules and nanostructures, exhibiting interesting chemical physical functionalities. GO and RGO are desirable materials for fabricating SERS substrates, because of their fluorescence quenching, high adsorption capacity of analyte molecules by aromatic π-π stacking and hydrophobic interactions, and especially for their [10] stable SERS signals when in form of monolayers, originated from charge-transfer-induced mechanisms [9] [11]. Due to these interesting properties, recent research has focused on the fabrication of GO/RGO composites with noble metal NPs to enhance SERS performance by combining CE and EM effects.[11, 12]

For example, L. Zhang et al. developed a GO sandwich nanostructure with embedded Ag NPs by a simple self-assembly process which was particularly effective in pesticide monitoring, due to the generation of numerous hot spots on its surface [10] [13][16]. W. Fan et al. addressed the effectiveness of the morphology control of Ag NPs decorating GO sheets, in accomplishing ultrasensitive single-particle SERS detection. They demonstrated a substantial enhancement in Raman signals from hybrid nanostructures fabricated with Ag octahedra [13][13] [11, 12].

Particularly interesting is the integration of SERS active materials into natural substrates such as cotton, silk and wool fabrics, that have showed exceptional performances as supporting scaffolds for sensors [7] [10, 14], thanks to their surface reactivity, mechanical flexibility, biodegradability and biocompatibility, all properties extremely promising for the fabrication of sustainable wearable, biodegradable and flexible sensors. In this context, to the best of our knowledge, there is still a lack of comprehensive investigation into the applications of GO or RGO as SERS [12]substrates in cellulose-based materials as paper and cotton.

Herein, we report on a facile method for fabricating a novel, flexible and wearable SERS sensor, based on hydrophobic paper modified with histidine functionalized RGO sheets, decorated with Ag NWs (His-RGO/Ag NWs). The hybrid nanocomposite was synthesized by modifying the self-seeding polyol approach reported for synthesizing neat Ag NWs and consisting in the reduction of the $AgNO_3$ precursor by ethylene glycol (EG), in presence of polyvinylpyrrolidone (PVP) and sodium chloride (NaCl) salt, with the concurrent heteronucleation and growth of the NWs onto the functionalities of the His-RGO platform. In this synthesis, EG acts as a reducing agent of the Ag precursor and as a green solvent of the synthesis mixture, NaCl keeps low the concentration of Ag atoms in the reaction environment ensuring thermodynamic control of the process, and hence unidirectional growth of Ag in NWs, together with PVP, that acts as a structure-directing agent. PVP, favouring the growth along a preferred axis of the Ag clusters and controlling their morphology, serves also as a stabilizer to prevent their aggregation and precipitation during the synthesis, and coordinates the synthesized nanocomposite allowing dispersion in water or alcohols [55].

The intrinsic mechanical flexibility of both the RGO sheets and the Ag NWs make them materials suited for the modification of flexible substrates, to integrate in wearable devices and sensors. The paper substrates were modified by the His-RGO/Ag NWs nanocomposite, whose SERS activity was studied in the detection of typical SERS active model molecules, and tested in the detection of pharmaceutical pollutant molecules, also against paper substrates modified by neat Ag NWs. This work has been done in collaboration with the FunNanobio Group of the Departamento de Química Física y CINBIO Universidade de Vigo, led by Jorge Perez Juste.
For this purpose, at first, the deposition of His-RGO/Ag NWs on hydrophobic paper, using a dip-coating technique, was optimized. The SERS performance of the prepared substrates was then enhanced by increasing the number of drop-casting depositions. Following this, preliminary experiments were conducted to improve SERS parameters for detecting three model molecules: 1-naphthalenethiol (1-NaT), rhodamine 6G (R6G) and benzo[a]pyrene. [12, 15] In general, nanocomposites based on Ag NWs decorated graphene derivatives are expected to allow detection of molecules with specific functional groups that have an affinity for Ag, such as thiols, carboxyl groups, or amines, as well as molecules with aromatic rings that interact via aromatic π-π stacking with the basal plane of graphene and its derivatives. [15] Thus, the choice to study the nanocomposite's behaviour with different model molecules stems from the expected dependence of its chemical affinity with the analyte chemical structure, playing a crucial role in SERS detection. [15]

To increase sensitivity, accuracy, and stability of the SERS-based detection of the target molecules with respect to conventional measurements of average Raman intensities, where the quantification of average signals is given in conventional "analog" measurements, a new approach was implemented here, basically based on a digital assay, counting individual signal events upon signal binarization into "1" or "0" (i.e. positive/negative), that considers positive the signals above a predetermined threshold value. [16]Compared to analog measurements, [17] digitalization reduces background noise and increases sensitivity of the measurement at very low analyte concentrations, thereby offering a high sensitive quantitative method for detecting rare targets in samples. [18]

Finally, to improve the SERS signal of the model molecules, the PVP capping ligand coordinated at the surface of the Ag NWs anchored onto His-RGO, was removed from the NWs surface by three different methods[19]. PVP[20], in fact, form a 2-3 nm thick insulating layer, significantly limiting Ag NWs application in electronics, biosensors, (electro)chemical catalysis, and SERS detection. To address this concern, thermal annealing and plasmonic welding, have been tested in literature[19, 21]. Specifically, in the context of SERS activity, the Ag NWs-PVP-Ag NWs interface hinders the effective plasmonic coupling among the stacked Ag NWs, leading to weak SPR effects, when the Ag NW stacks are exposed to laser radiation. Therefore, complete removal of PVP is considered a viable method to enhance Ag NWs SERS activity, and it has been performed in literature by using a treatment with borohydride ($NaBH_4$), potassium iodine (KI)[22, 23] and plasma cleaning.[24] $NaBH_4$ effectively removes PVP from the Ag NWs – Ag NWs interface, facilitating direct welding in Ag NW stacks, thereby significantly enhancing SERS activity of their films[25]. The use of halide ions [26]induce NP aggregation, further improving SERS sensitivity. In the study of X. Song et al., the addition of I^- was found to increase SERS sensitivity by promoting more compact and stable Ag substrate. This aggregation results in an increase in "hot spots" [27]within the substrate, significantly enhancing Raman scattering on the Ag surface. Furthermore, separate detection of various target molecules revealed that I^- addition effectively increases the

Raman intensity for both anionic and cationic targets on the Ag substrates while suppressing Raman peaks of neutral analytes. Plasma cleaning, [28] a commonly used laboratory technique, effectively decomposes organic contaminants on solid surfaces into volatile small molecules. Previous research has demonstrated that plasma treatment can initiate self-limited welding of metallic nanomaterials, such as Ag inks, Au NPs, and Cu NWs, significantly improving conductivity of Ag NWs and graphene-Ag NW hybrids, without disrupting the network structure. With a clean surface and abundant welded NW/NW junctions, the resulting Ag NW films exhibits greatly enhanced their carrier transport properties, making them highly suitable for applications such as transparent heaters and electrodes in electron-only devices. [24]

In this work, we performed all the three different approaches to remove PVP from the surface of the Ag NWs in the nanocomposite, including treatment with $NaBH_4$, KI and plasma cleaning. In regards of the plasma treatment, we systematically explored the effect of a treatment consisting of a cycle of O_2-Ar plasma, followed by a cycle of H_2-Ar plasma, on the SERS activity of the His-RGO/Ag NW nanocomposite in the detection of R6G, as well as the propranolol (PRNL) drug, a real target molecule, widely used as a β-blocker for the treatment of various cardiovascular diseases and other conditions such as migraines, anxiety, essential tremors, and hyperthyroidism [29].

5.2 Materials and methods

Chemicals and Materials. Reduced graphene oxide (RGO) powder was purchased from Graphene Supermarket with flake sizes of 1–3 μm. Polyvinylpyrrolidone (PVP, Mw = 360 kDa), NaCl (>99.8%), ethylene glycol (EG), silver nitrate ($AgNO_3$, 99.9999%), acetone (>99.9%), ethanol (>99.9%), 1-octadecene (ODE), DL-histidine (His, >99%), potassium iodine (KI), sodium borohydride ($NaBH_4$), 1-naphthalenethiol (1-Nat), rhodamine 6G (R6G), benzo[a]pyrene and potassium iodide (KI), dodecenylsuccinic anhydride (DDSA) and propranolol hydrochloride (PRNL) were purchased from Sigma-Aldrich**.** Milli-Q water was used for the preparation of all aqueous solutions (18.2 MΩ·cm organic carbon content ≥ 4 μg L^{-1}) achieved by a Milli-Q gradient A-10 system.

Exfoliation and functionalization of RGO. Exfoliation and functionalization of RGO with histidine (His) were conducted involving alternating steps of stirring, sonication, and centrifugation of a mixture of His and RGO powder in Milli-Q water at neutral pH. The resulting His-RGO has a ζ-potential of -20.1±1.5 mV.

Specifically, the initial phase of the preparation of the His-RGO complex involves dispersing 100 mg of RGO and 160 mg of His in 16 mL of water. The resulting dispersion was stirred for one week to allow intercalation of His molecules between the RGO sheets [30]. Subsequently, the solution was sonicated for 5 h to promote exfoliation of the flakes and functionalization with His. It was then subjected to four purification cycles by centrifugation, each lasting 30 min at 40,000 rpm, to remove the excess of His, with the supernatant being removed after each wash and the isolated powder being re-dispersed in Milli-Q water. After purification, the dispersion was stirred overnight, sonicated for 3 h the following day, and again purified by four centrifugation cycles. The resulting His-RGO powder was dried in an oven at 70°C to remove residual water.

Synthesis of Ag NWs. Ag NWs were synthesized by the polyol synthesis approach reported by S. Coskun et al. [31]. In a typical experiment, a vial filled up with a solution of 250 mg of PVP (Mw= 360 KDa) and 3.5 mg of NaCl in 5 mL of EG, closed with a septum, was heated up to 170°C by immersion in an oil bath placed onto a hotplate, and stirred at 600 rpm. To this solution, ten injections of 0.25 mL of a 25 mg mL^{-1} $AgNO_3$ solution in EG, were added, every 6 min, by a syringe. At the end of the injections, the vial was allowed to stir at 600 rpm and at 170°C for 90 min, and then, was air-cooled down to room temperature, to stop the reaction.

The NWs were purified from the excess of PVP and EG by three cycles of centrifugation (10000 rpm, 30 min) with acetone and re-dispersion in ethanol, and were finally dispersed in ethanol.

Synthesis of His-RGO/Ag NWs. The His-RGO/Ag NWs nanocomposite was synthesized by modifying the colloidal approach used for the synthesis of neat Ag NWs [32], by injecting the His-RGO complex in the synthesis solution of the Ag NWs.

The synthesis was conducted by injecting a dispersion of His-RGO in 2 mL of pre-heated (170°C) EG into the synthesis solution containing PVP and 3.5 mg of NaCl in 5 mL of EG. This mixture was placed in a vial sealed with a septum, heated up to 170°C onto a hotplate via immersion in an oil bath, and subjected to stirring at 600 rpm. The injection of His-RGO occurred between the seventh and eighth of the ten 0.25 mL injections of the 2.5 mL of 25 mg mL^{-1} $AgNO_3$ solution in EG. Subsequently, the reaction was allowed to proceed for 6.5 h, and the vial was air-cooled down to room temperature to stop the synthesis.

The obtained hybrid nanocomposite underwent purification from excess PVP and EG through six cycles of centrifugation with acetone (10000 rpm, 10 min) and subsequent re-dispersion in ethanol. The resulting hybrid nanocomposite was then re-dispersed in ethanol.

Functionalization of chromatographic paper. A 0.5% (w/v) dodecenylsuccinic anhydride (DDSA) solution in 1-hexanol was prepared by weighing 789.6 mg of DDSA into 150 mL of 1-hexanol. The solution was stirred under a fume hood at 50°C for 1 h.[33]

Subsequently, a sheet of chromatography paper (Whatman 1CHR No. 3001-861) was cut into four parts, and one piece was immersed in a glass Petri dish containing 50 mL of the DDSA solution for 5 min. After 5 min, the paper was transferred to another glass container and placed in a thermostatically controlled oven set at 160°C for additional 5 min to ensure complete solvent evaporation. This cycle was repeated twice.

The surface modification of the chromatographic paper was evaluated by depositing three separate spots of 2 µl of water on the paper. If the droplet remained intact and evaporated without being absorbed by the paper, the functionalization was deemed successful. In this condition, a water contact angle of approximately 110° was estimated.

Preliminary Surface-Enhanced Raman Scattering (SERS) study of 1-NaT, R6G and benzo[a]pyrene. SERS measurements were conducted with a Renishaw InVia Reflex confocal system. The spectrograph used a high-resolution grating (1800 grooves per mm) with additional band-pass filter optics, a confocal microscope, and a 2D-CCD camera. SERS images were obtained using a point-mapping method with an 20x objective (N.A. 0.40) and spatial resolution of 2.6 μm^2. The spectral images were obtained by collecting the SERS spectrum of each pixel of the image, one at a time. Laser excitation was carried out at 785, 633 and 532 nm with a power of 12.90 mW and 0.5 and 1 s acquisition time. The SERS images of each well were decoded using the signal to baseline area of the highest Raman peak from the reporter molecules (RBITC, 1620-1660 cm^{-1}) using WiRE software V 4.1 (Renishaw, UK).

To select the suited laser excitation to achieve intense SERS spectra of 1-NT, R6G and benzo[a]pyrene target molecules, 4 μl of His-RGO/Ag NWs and Ag NWs were deposited via drop casting onto hydrophobic paper, and preliminary SERS tests were conducted with different excitation laser lines (532 nm, 633 nm, and 785 nm), at 5% power, acquisition time of 10 s, 1 accumulation, and a 20x objective. [12, 15]

The deposition of His-RGO/Ag NWs and Ag NWs onto hydrophobic paper was optimized by drop-casting four different volumes, 1, 4, 8, and 16 μl, of both the materials onto four different hydrophobic papers, adding 1 μl at a time. Following this deposition, a 4 μl of the model molecule 1-NaT was applied to each sample, and SERS measurements were performed using a 785 nm laser with 5% power, a 10 s acquisition time, 1 accumulation, and a 20x objective.

SERS signal dependency of the focal length along z-axis. To investigate possible dependence of the SERS signal of the His-RGO/Ag NWs and Ag NWs samples on the laser focus distance along the z-axis, SERS signals from R6G (10^{-6} M) were acquired from the same sample and the same area, while varying the focus along the z-axis at positions 0, 10, 15, and 20. The laser used was the 633 nm line with 5% power, acquisition time of 10 s, 1 accumulation, and a 20x objective.

Estimation of the limit of detection (LOD) of 1-NaT and R6G. 4 μl of His-RGO/Ag NWs and Ag NWs were deposited via drop casting onto hydrophobic paper, and SERS tests were conducted using 1-NaT and R6G as the target molecules. SERS measurements of 1-NaT and R6G were performed with a 785 nm laser line at 10% power and a 633 nm laser line at 5% power, respectively, working for both, with acquisition time of 10 s, 1 accumulation, and a 20x objective.

LOD of the target molecules was evaluated from three aqueous solutions at different concentrations (10^{-5} M, 10^{-6} M, and 10^{-7} M), achieved diluting a stock solution in ethanol at a concentration of 10^{-4} M.

Study of SERS signal variation due to degradation of 1-NaT and R6G over time. A study was conducted to evaluate the potential instability of the SERS signal of 1-NaT and R6G molecules due to their degradation over the course of a month. A 4 μl droplet of His-RGO/Ag NWs and Ag NWs, respectively was deposited on paper, followed by the application of two 2 μl drops of the target molecules, allowing the paper to dry between each deposition. The SERS signal was measured for both samples using a 785 nm laser (P=10%; 20X; 1ac; 10s; 1-NaT 10^{-5} M) for 1-NaT and a 633 nm laser (P=5%; 20X; 1ac; 10s; R6G 10^{-6} M) for R6G. The signal was recorded on the same sample at one-week intervals for a duration of one month.

Study of SERS signal variation of 1-NaT and R6G due to degradation of His-RGO/Ag NWs and Ag NWs samples. An analysis was conducted to explore the potential oxidation of Ag NWs and His-RGO/Ag NWs and corresponding variation of SERS signals for both 1-NaT and R6G target molecules due to this phenomenon.

Four drops of 4 µl each of both samples were deposited onto four different pieces of paper. The SERS signals of 1-NaT and R6G were evaluated for the samples aged one month using a 785 nm laser (P=10%; 20X; 1ac; 10s; 1-NaT 10^{-5} M) and a 633 nm laser (P=5%; 20X; 1ac; 10s; R6G 10^{-6} M), respectively. The signals were monitored over time using samples aged 1, 2, 3, and 4 weeks.

PVP removal from His-RGO/Ag NWs with KI solution and SERS evaluation using 1-NaT and R6G target molecules. 4 µl of His-RGO/Ag NWs were deposited dropwise onto three hydrophobic paper sheets, allowing the paper to dry between each deposition. The deposited nanocomposite was soaked in three different KI aqueous solutions for 30 s (0.048 mM; 0.032 mM; 0.024 mM). The excess KI was subsequently removed by rinsing with ethanol. Two drops of 2 µl of 1-NaT were then deposited by drop-casting, and the SERS signal was evaluated using a 785 nm laser (P=5%; 20X; 1ac; 10 s; 1-NaT 10^{-5} M).[26]

PVP removal from His-RGO/Ag NWs with $NaBH_4$ solution and SERS evaluation using 1-NaT. 4 µl of His-RGO/Ag NWs were deposited dropwise onto three hydrophobic paper sheets, allowing the paper to dry between each deposition. The deposited nanocomposite was soaked in three different aqueous $NaBH_4$ solutions (0.05 M; 0.03 M; 0.025 M) for 30 s. The excess $NaBH_4$ was subsequently removed by rinsing with ethanol. Two drops of 2 µl of 1-NaT were then deposited by drop-casting, and the SERS signal was evaluated using a 785 nm laser (P=5%; 20X; 1ac; 10s; 1-NaT 10^{-5} M).

PVP removal from His-RGO/Ag NWS using plasma treatment. Before introducing the samples into the plasma reactor, a cleaning step of the chamber of the reactor was performed by flushing it with Ar for 10 s. After placing the nanocomposite modified paper, which was fixed to glass slides into the sample holder, the chamber was evacuated, and a plasma cycle with 20% O_2 and Ar was initiated for 2 min. Following this cycle, a reduction step using a 20% H_2 and Ar plasma was performed for 2 min to restore oxidized Ag. The samples were subsequently tested using SERS, with R6G as a model molecule and PRNL. SERS measurements of PRNL were performed using a 633 nm excitation laser at the 10% power, acquisition time of 5 s, 1 accumulation, and a 20x objective.[28]

The acquired recorded SERS mappings for R6G and PRNL, deposited onto the nanocomposite after plasma treatment, were processed using the new digital SERS methodology and they were transformed to the binary format by setting a specific threshold based on the average intensity, plus 3 times the standard deviation above the mean measured in the control test without the target molecules.[44,50] The pixels with intensities at 1364 and 1384 cm^{-1}, respectively for R6G and PRNL, above the threshold were assigned to 1, whereas those equal or below were set to 0. The digitized version of the SERS mappings generated for R6G and PRNL concentrations, as indicated, represents the positive “1” and negative “0” events in grey-white and black, respectively.[1, 18]

A digital calibration curve was generated by plotting the number of digital counts versus the target molecule concentrations, and the digital counts follows a sigmoidal-shaped curve, that can be described by the four-parameter logistic (4PL) equation (mathematically similar to the Hill equation), commonly employed in immunoassays,[59] and represented by:

$$y = A_1 + \frac{(A_2 - A_1)X^p}{X_0^p + X^p}$$

where y is the number of digital counts and X the target molecules concentration. A_1 and A_2 are the values of the lower and upper asymptote respectively, p is the slope at the inflection point (also known as the Hill coefficient) and X_0 is the value of X corresponding to 50% of the maximum asymptote.[59] LOD from a 4PL model is commonly determined by adding three times the standard deviation of the background noise to the mean signal of the blank samples. [18]

Characterization techniques

UV-Vis-NIR Absorption Spectroscopy. UV-Vis-NIR absorption spectra were collected by a VARIAN CARY® 5000 UV-Vis-NIR Spectrophotometer.

Transmission Electron Microscopy (TEM). A JEOL JEM 1011 electron microscope, operating at an acceleration voltage of 100 kV and equipped with a CCD camera, was used. For the analyses, the samples were prepared by dipping a 400 mesh copper TEM grid, coated with carbon, into diluted solutions. Size statistical analysis of the Ag nanostructures average size was performed by the ImageJ analysis software.

Raman Spectroscopy. Raman spectra were recorded with a LabRAM HR Horiba-Jobin Yvon spectrometer using a continuous 532 nm laser excitation source, operating at low power (1 mW) to prevent sample damage.

Fourier Transform Infrared Spectroscopy with Attenuated Total Reflectance (FTIR-ATR). Infrared spectra (4000-600 cm^{-1}) were recorded with a Varian 670 FTIR spectrometer equipped with a DTGS (Deuterated Triglycine Sulfate) detector at a spectral resolution of 4 cm^{-1}. A 2 mm diameter diamond microprism was used as the internal reflective element

Field Emission Scanning Electron Microscopy (FE-SEM). FE-SEM measurements were performed by a Zeiss Sigma microscope (Carl Zeiss Co., Oberkochen, Germany) operating in the range of 0.5–20 KV and equipped with an in-lens secondary electron detector and an INCA Energy Dispersive Spectroscopy (EDS) detector. Samples were mounted onto stainless-steel sample holders by double-sided conductive carbon tape and grounded by silver paste.

5.3 Results and discussion

5.3.1 Exfoliation and functionalization of RGO basal plane by Histidine (His)

RGO was exfoliated and functionalized with histidine (His) through a non-covalent approach, consisting of cycles of stirring and sonication, resulting in the binding of His via aromatic π-π stacking interactions [30, 34] to the basal plane of RGO (Fig. 5.1 panel A), without altering its C sp^2 structure, and thus, its unique physicochemical structural properties. This route facilitates both the exfoliation and dispersion of RGO in water and concomitantly the His molecules anchored onto its basal plane provide coordination sites for the *in situ* growth of the Ag NWs at its carboxyl and N-based groups (Fig. 5.1 panel A).

The spectroscopic, chemical, and morphological properties of the obtained His-RGO complex were studied using transmission electron microscopy (TEM), UV-Vis-NIR absorption spectroscopy, and FTIR-ATR spectroscopy.

TEM analysis of the His-RGO complex at pH 11 reveals sheet-like structures few micrometers in size that are nearly transparent to the electron beam (Fig. 5.1 panel B). [35] The sheets display areas of high image contrast, reasonably attributed to rolled edges and/or folds in the RGO sheets. These mechanical deformations are induced by structural defects occurring during reduction of GO to RGO,[32] crumpling of sheets during the exfoliation and functionalization of RGO with His, or the evaporation of water following sample deposition onto the TEM grid. The TEM images do not show the presence of undissolved His crystals on the basal plane of RGO or isolated onto the grid, demonstrating the effectiveness of the purification procedure implemented after exfoliation. (Fig. 5.1 panel B) [35]

The UV-Vis-NIR absorption spectrum of the His-RGO complex, isolated from a neutral pH solution, exhibits an absorption peak at 277 nm (Fig. 5.1 panel C), attributed to the characteristic π-π transition of the -C=C- bond in RGO. [36]

The FTIR-ATR spectrum of the His-RGO complex prepared at neutral pH was compared with that of an aqueous solution of His at the same pH (Fig. 5.1 panel D). The comparison shows that in the higher wavenumber region, the spectrum displays the stretching of $-NH_2$ groups (νNH_2) of His at 3394 cm^{-1}, as well as the symmetric and asymmetric stretching of $-CH_2$ groups ($\nu s,asCH_2$) at 2988 cm^{-1} and 2901 cm^{-1}, respectively. [31]These peaks are evident when compared with the spectrum of pure His (Fig 5.1 panel E).

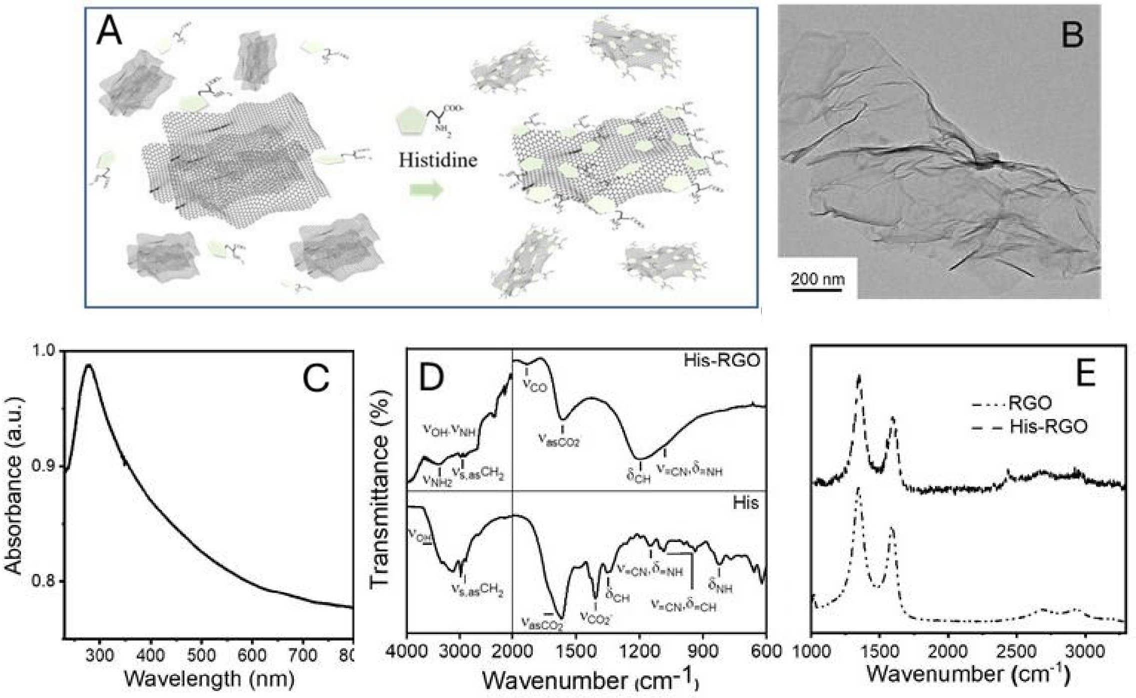

Fig. 5.1: *(A) Sketch of functionalization of RGO basal plane by His. (B) TEM image of His-RGO and (C) UV-Vis absorption spectrum of an aqueous solution of His-RGO at pH 7. (D) FTIR-ATR spectrum of an aqueous solution of His and His-RGO at pH 7. (E) Raman spectra of RGO and His-RGO*

The spectra of the His-RGO complex also show the asymmetric stretching of -COO$^-$ groups (νasCO_2^-) at 1564 cm^{-1} and a broad band between approximately 1380 and 695 cm^{-1} (Fig 5.1), attributable to the overlap of aliphatic -CH bending, imidazole =CN stretching (ν=CN), =NH group bending (δ=NH), and =CH group bending (δ=CH). These are centred at 1193 cm^{-1}, 1149 cm^{-1}, and 1086 cm^{-1} in the His spectrum, respectively (Fig 5.1 panel D), confirming the successful functionalization of RGO with His.

The Raman spectra of pristine RGO shows the D and G peaks at 1344 cm^{-1} and 1590 cm^{-1}, respectively (Fig. 5.1 panel E). The D peak is attributed to structural defects, including defects at the basal plane edges and grain boundaries, which may also involve functionalities containing oxygen atoms or heteroatoms such as nitrogen, or hydrocarbon chains from the GO reduction process [37]. The G peak is attributed to the breathing modes of sp^2 carbon atoms in the hexagonal rings [38]. These peaks are also observed in the Raman spectrum of His-RGO at 1347 cm^{-1} and 1597 cm^{-1}, respectively. The intensity ratio between the G and D peaks of RGO remains unchanged following the non-covalent functionalization with His, confirming that the procedure does not increase the density of structural defects of the RGO basal plane.

5.3.2 Synthesis mechanism and morphological and spectroscopical characterization of the nanocomposite His-RGO/AgNWs

The His-RGO/Ag NWs hybrid nanocomposite was synthesized by modifying the self-seeding polyol process of Xia et al. [39]The synthesis is performed by using His-RGO complex, which was isolated from aqueous solutions at pH 7 with ζ-potential of -20.1±1.5 mV, polyvinylpyrrolidone (PVP) acting as the coordinating and steric stabilizing agent for the NWs [32], ethylene glycol (EG) serving as the reductant for the $AgNO_3$ precursor and green solvent for the reaction, and sodium chloride (NaCl), responsible for buffering the concentration of Ag(I) ions in the reaction solution [40].

In a typical synthesis procedure, His-RGO was introduced into a mixture of PVP and NaCl in EG, which was homogenously stirred and heated up to 170°C. A 25 mg mL^{-1} $AgNO_3$ solution in EG [32] was then gradually added in ten aliquots of 0.25 mL at intervals of 6 min, to prevent the supersaturation of the reaction environment with Ag(I) ions.

The formation mechanism of His-RGO/Ag NWs was examined by monitoring its synthesis progress through withdrawal of aliquots of the synthesis solution after each $AgNO_3$ precursor injection, both before and after the addition of His-RGO. The spectroscopy and morphological properties of the resulting nanostructures in each aliquot were assessed after purification and isolation via centrifugation in acetone and subsequent re-dispersion in ethanol.

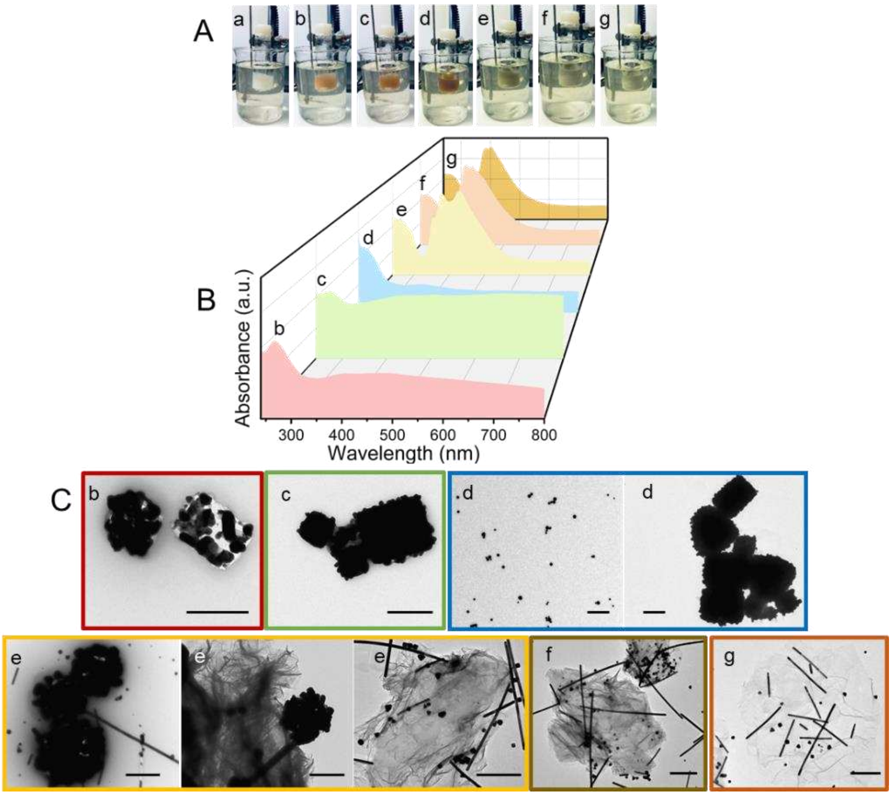

Fig. 5.2: *(A) Pictures of the synthesis mixture after the first (a), second (b), fourth (c), sixth (d), seventh (e), ninth (f) and tenth (g) $AgNO_3$ solution injection. (B) UV-Vis absorption spectra and (C) TEM micrographs of*

the aliquots withdrawn from the synthesis mixtures reported in the (b), (c), (d), (e), (f) and (g) photograph images of panel A. The synthesis was performed with the 10:1 $AgNO_3$:His-RGO w/w, 7.7:1 PVP:$AgNO_3$ molar ratio, at 170°C, PVP 360 kDa, stirring rate of 600 rpm, reaction time of 6.5 h, and His-RGO was added between the seventh and the eight injections of $AgNO_3$. Absorption spectra was registered in ethanol and normalized at the characteristic absorption peak of the PVP:Ag(I) complex at 270 nm .[41]

After the first injection of $AgNO_3$ into the solution of PVP and NaCl in EG, the reaction mixture turns milky white, indicating formation of AgCl nanocubes [40] (Fig. 5.2, panel A, photograph a), and after the second injection, it turns into a light orange color (photograph b), progressively darkening with subsequent injections of $AgNO_3$ up to the sixth (traces b-d).

The UV-Vis absorption spectra of the second and fourth aliquots exhibit a prominent plasmon peak spanning the entire visible spectrum, as depicted in traces b-c of Fig.5.2 panel B. This phenomenon persists even after the fifth injection and is likely attributable to the plasmon absorption of polydisperse Ag nanostructures. TEM images reveal that the nanostructures in the second, fourth, and sixth aliquots primarily comprise nodules composed of bright AgCl nanocubes [40] coated with Ag NPs exhibiting high image contrast, heteronucleated at their surface (trace b of Fig. 5.2 panel C), alongside few spherical Ag NPs of approximately 19 nm (data not shown). Subsequent aliquots (trace c of Fig. 5.2 panel C for the fourth, and data not shown for the fifth) also feature nodules, along with Ag NPs still around 19 nm in size, whose concentration appears to increase from the second to the fifth addition of the $AgNO_3$ precursor (data not shown).

Following the sixth injection of $AgNO_3$, the solution turns dark orange (trace d, Fig. 5.2 A), and the originally broad plasmon absorption band gets narrower and shifts towards higher energy, centring around 400 nm (trace d, Fig. 5.2 B), indicating primarily the formation of spherical Ag NPs (trace d, Fig.5.2 C), as confirmed by the TEM image that shows Ag NPs approximately 7 nm in size, along with nodules (trace d, Fig.5.2 C).

The absorption peak observed in the spectra of the second, fourth, and sixth aliquots at 270 nm is attributed to the absorption of the PVP:Ag^+ complex (Fig. 5.2 B).

After the seventh $AgNO_3$ injection and subsequent addition of His-RGO, the solution turns dark grey (trace e, Fig. 5.2 A), accompanied by significant changes in its absorption spectrum. A large plasmon absorption band emerges, with superimposed quadrupole resonance and transversal plasmon peaks of NWs at 350 nm and 380 nm [42] respectively, along with a LSPR peak of spherical Ag NPs at 430 nm (trace e, Fig. 5.2 B). These peaks persist in the subsequent additions of $AgNO_3$ up to the tenth injection (traces f-g, Fig. 5.2 B).

The TEM micrographs of the nanostructures isolated after the seventh injection show filaments protruding from the nodules homonucleated in the synthesis solution and from nodules anchored or wrapped by the His-RGO sheets, Ag NWs already anchored or wrapped onto the sheets, as well as homonucleated Ag NWs and Ag NPs of ca. 36 nm (trace e of Fig.5.2 panel C). These micrographs confirm that the addition of His-RGO after the seventh injection of $AgNO_3$, which is known as the primarily responsible for the NWs growth in the synthesis of neat Ag NWs, does not affect filaments initiation in solution, that starts also from the nodules anchored onto the His-RGO basal plane.

The TEM images of the ninth and tenth aliquots show that after the subsequent additions of $AgNO_3$, the NWs grow anchored onto the sheets and in the supernatant reaction solution, as well as the spherical Ag NPs that reach a final size of ca. 50 nm (traces f-g of Fig.5.2 panel C).

In view of these results, as for the synthesis of neat Ag NWs, it can be inferred that after the first injection of $AgNO_3$, AgCl nanocubes form, and, having the latter a solubility constant lower than that of $AgNO_3$ [43], they slowly release Ag^+ ions properly buffering their concentration in the reaction solution [40] for limiting Ag atoms nucleation events. These nucleation events occur through reduction with glycolaldehyde, which originates from the thermal oxidation of EG [40]. Indeed, in case of higher concentration of Ag(I) ions, it has been demonstrated that heteronucleation of small Ag clusters, which then dissolve and contribute to the formation of micrometer sized structures by Ostwald ripening, [32] occurs instead of the formation of more thermodynamically stable pentagonally twinned prisms, the seeds promoting the uniaxial growth of the NWs.

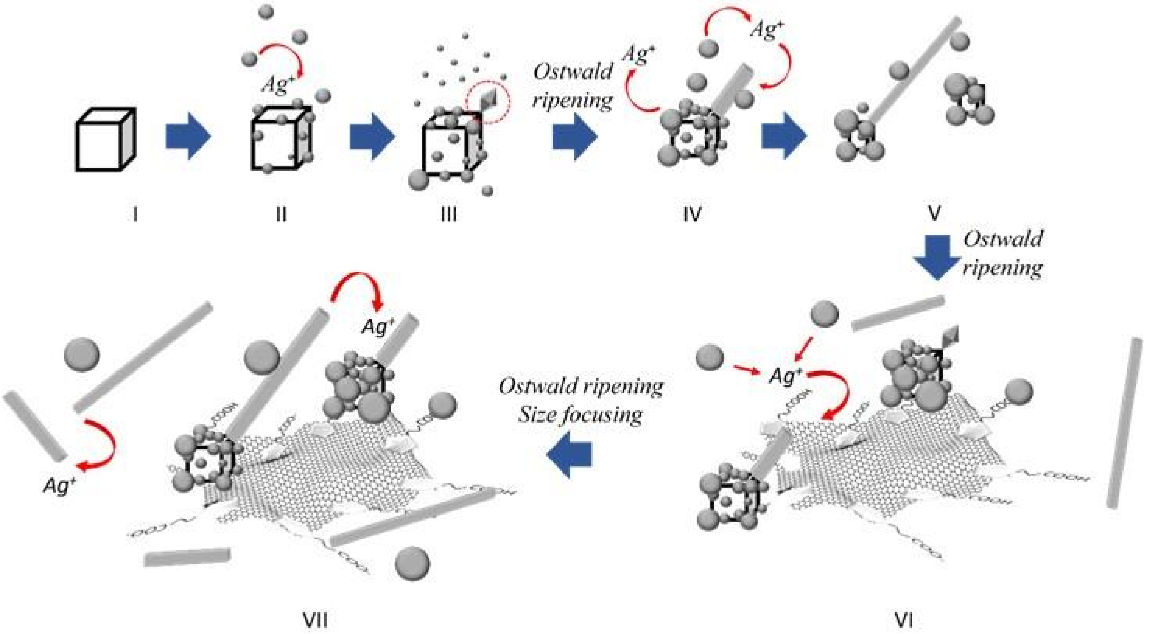

Fig.5.3: *Sketch of the synthesis reaction mechanism. (items not drawn to scale).*

Conversely, lower concentrations of Ag(I) ions lead to dissolution of small Ag NPs by Ostwald ripening, feeding larger Ag NPs and resulting in micrometer sized structures[32].

At the second injection of $AgNO_3$, the Ag atoms concentration overcomes supersaturation [44] reaching minimum nucleation concentration, and thus turns into the homonucleation of few Ag NPs. Under these conditions, the heteronucleation of Ag clusters concomitantly takes place at the surface of the AgCl nanocubes, thus generating the nodules, which are stabilized both electrostatically, via the electrostatic repulsions among the Cl^- ions chemisorbed at their surface, [45] and sterically by PVP (Fig.5.3, step II), coordinating their surface.

Such processes occur until the fifth injection, as the further addition of the Ag precursor, on one side increases the concentration of the Ag NPs that keeps their size constant over the additions, and, on the other side, contributes to the growth of the Ag nodules by deposition of metal monomers at their surface.

It has been inferred that the proper low concentration of Ag monomers in solution allows the reaction to proceed in thermodynamic control conditions, promoting onto the nodules surface, the heteronucleation of pentagonally twinned prisms (Fig.5.3, step III) which are the seeds initiating the anisotropic growth of the NWs, with formation of the filaments from the nodules (Fig.5.3, step IV) [40].

In literature, it has been reported that in this process, the temperature of the reaction is crucial to induce both the relatively fast thermal conversion of EG to glycolaldehyde [46] and to provide the thermal energy required for the conversion of some of the Ag nodules in the pentagonally twinned prisms, which are more thermodynamically stable [32]. The synthesis of the Ag NWs has been reported in literature for temperatures between 110°C and 200°C. At 110°C, the NWs form with long reaction times (12 h) [47], while for higher temperatures their formation is faster and occurs in few hours [45]. In this work, the temperature of 170°C has been selected, as it has been demonstrated to lead to Ag NWs in high yield [32], because, keeping fixed the $AgNO_3$ precursor concentration, a further increase of temperature would bring to a higher concentration of pentagonally twinned seeds, and therefore, to Ag NWs with lower aspect ratio [32].

The pentagonally twinned prisms have a face-centered cubic structure, with the {111} planes denser in atoms and in twin boundaries than the {100} facets, and hence, have a higher surface energy [39, 48]. As PVP preferentially adheres on the {100} planes restraining their growth kinetics, it promotes uniaxial elongation of the NWs by fast addition of Ag atoms to the {111} facets. The thermodynamic control of the synthesis process of the NWs is granted by the combination of the slow release of Ag^+ ions in solution, which keeps low the concentration of Ag atom monomers, and the selective coordination of PVP to the {100} facets of the prisms.

In the nanocomposite, the anisotropic growth of the Ag NWs was found dependent on the molecular weight of PVP, on the $AgNO_3$:PVP molar ratio, injection mode of the His-RGO complex and on its dissociation state. Neat Ag NWs have been effectively synthesized by using PVP at the Mw of 55 kDa [32], but in presence of His-RGO, such a low Mw was found ineffective in assisting and promoting the anisotropic growth of the NWs, likely due to: i. competition of the functionalities of His grafted on the sheets in coordinating the Ag NWs surface in growth, and ii. steric hindrance of His-RGO, that limits Ag atoms monomers diffusion in solution, resulting mostly in spherical and micrometer sized Ag nanostructures.

The results of Fig.5.2 showed that, until the sixth injection of $AgNO_3$, the Ag atom monomer concentration favours homonucleation of spherical Ag NPs, as well as of nodules (Fig.5.3, Steps II-III), and at the sixth injection, the concentration of the Ag NPs increases, while their size significantly decreases. At the seventh injection, it is likely that initiation of Ag filaments from the pentagonally twinned seeds occurs (Steps IV of Fig.5.3), thanks to the dissolution, by Oswald ripening [46], of the small Ag NPs (Steps V of Fig.5.3), which have a high surface energy due to their high surface to volume ratio, and hence, feed of Ag atoms the {111} facets of the pentagonally twinned filaments [46].

After the injection of the His-RGO complex, both the filaments in growth anchor the His-RGO basal plane by coordination to its carboxylic groups, as well as the Ag nodules initiators of the filament growth (Step VI Fig.5.3). In the following additions, the size of the Ag NPs increases due to Oswald ripening phenomena, as well as that of the NWs (Step VII Fig.5.3).

It worth noticing that for times of reaction between 5 h and 6.5 h, the monodispersion of the Ag NWs in the nanocomposite increases without resorting to any size separation, any change of the temperature of reaction, any step of separation by precipitation, redispersion in solvent, reflux, or addition of PVP [44]. This evidence, that, to the best of our knowledge, has never been discussed in literature for the synthesis of nanocomposites formed of graphene and Ag NWs, is reasonable due to the size focusing phenomenon (Fig.5.3, Step VII) [49]. This result allows to infer that, at the investigated temperature, the PVP ligand molecules coordinated at the NWs defect sites, which have higher chemical reactivity due to twinning boundaries and possessing strong microstress with lower lattice stabilization energy, promote an extensive transportation/exchange of ligated clusters/atoms from longer and larger NWs, that dissolve in the solvent and deposit on the shorter and thinner NWs, ultimately reaching an equilibrium between etching and redeposition processes, allowing the system to move toward the focusing conditions with the formation of monodisperse NWs (Fig.5.3,Step VII).

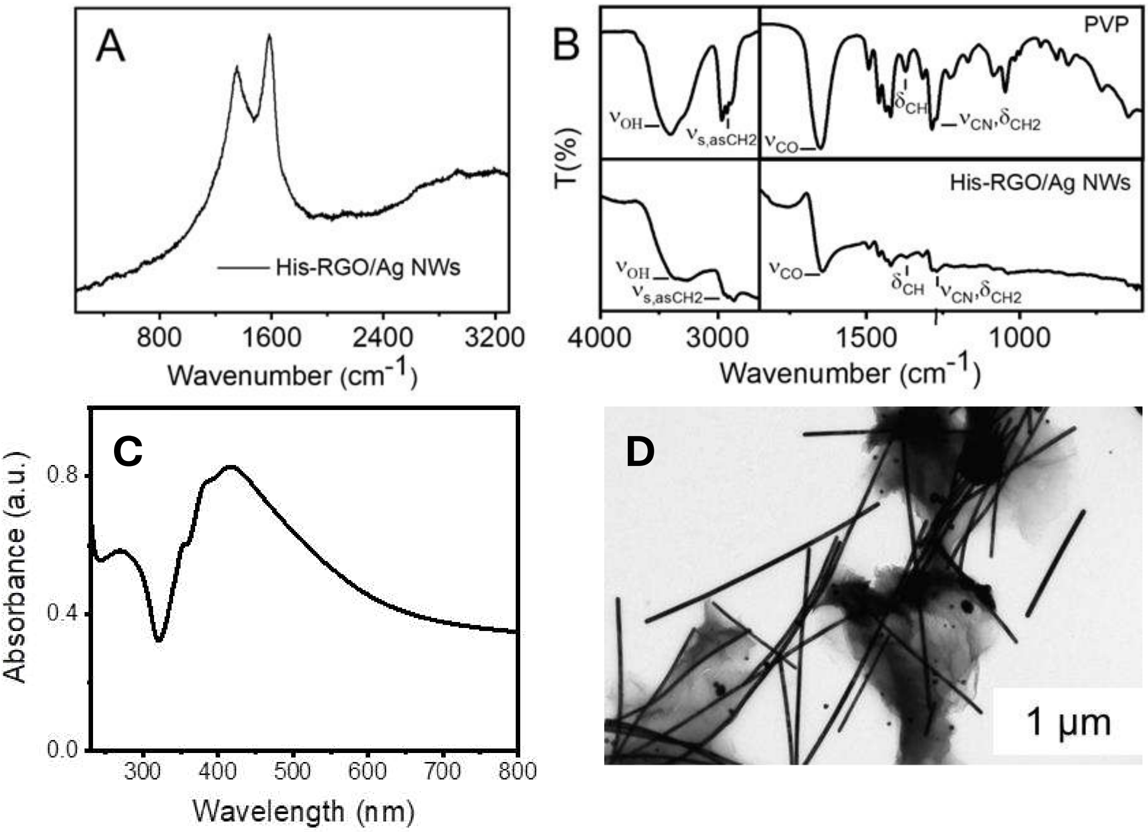

(A) Raman spectra of His-RGO/Ag NWs. (B) ATR-FTIR spectra of PVP (Mw= 360 KDa) and of His-RGO/Ag NWs (C) UV-Vis absorption spectra and (D) TEM micrograph of His-RGO/AgNWs

Fig.5.4: *(A) Raman spectra of His-RGO/Ag NWs. (B) ATR-FTIR spectra of PVP (Mw= 360 KDa) and of His-RGO/Ag NWs (C) UV-Vis absorption spectra and (D) TEM micrograph of His-RGO/AgNWs*

Fig. 5.4 (A) shows the Raman spectrum of the hybrid nanocomposite where the D and G peaks of RGO are clearly visible at approximately 1349 cm^{-1} and 1582 cm^{-1}, respectively. Since the ratio of intensity between the D and the G peak (I_D/I_G) is indicative of the defect density in the basal plane of RGO, comparing the Raman spectra of the bare His-RGO complex (Fig. 5.1E) with that of the nanocomposite, it can be noticed that it decreases with the *in situ* synthesis of the NWs. This evidence assesses the decrease of the defect density in RGO, likely due to EG, that not only reduces the Ag precursor, but also the residual GO domains of the RGO basal plane[50].

The FTIR-ATR spectrum of the nanocomposite shows a signal at 3322 cm^{-1} due to the stretching of the -OH group (ʋOH), which is visible also in the spectrum of neat PVP at 3400 cm^{-1}. The shift of this signal in the nanocomposite can be attributed to the establishment of a keto-enol equilibrium involving the carbonyl group of the pyrrolidone ring, leading to the formation of an enolic functional group in equilibrium with the ketone [51], thus confirming the presence of PVP in the hybrid. Additionally, the spectrum exhibits two peaks at 2865 cm^{-1} and 2940 cm^{-1}, corresponding to the symmetric and asymmetric stretching of -CH_2 groups (ʋs,as CH_2), respectively, that are also found in the spectrum of PVP at 2882 cm^{-1} and 2969 cm^{-1}, and in the spectrum of the His-RGO complex at 2889 cm^{-1} and 2981 cm^{-1}, respectively (Fig. 5.4 panel B).

Moreover, a peak around 1643 cm^{-1} is observed, which can be attributed to the stretching of the C=O group (ʋ C=O) of PVP, which is at a higher wavenumber (1652 cm^{-1}) in the spectrum of neat PVP. This peak provides further evidence of the presence of PVP in the nanocomposite, and its shift to lower wavenumbers confirms its coordination to the NW surface [51].

Finally, the spectrum of the nanocomposite also shows the CH bending (δCH) at 1367 cm^{-1} and the C-N wagging (ʋ C-N) at 1280 cm^{-1}, which are present in the spectrum of PVP at 1373 cm^{-1} and 1289 cm^{-1}, respectively. These vibrations are shifted compared to the pure PVP peaks due to the proximity of these functional groups to the surface of the Ag NWs. Other peaks of PVP, such as the C-C stretching (ʋC-C) at 934 cm^{-1}, the CH_2 rocking (ʋCH_2) at 843 cm^{-1}, and the breathing of the pyrrolidone ring at 880 cm^{-1}[51], are not visible in the spectrum of the His-RGO/Ag NW nanocomposite due to their low intensity.

The UV-Vis absorption spectrum of the achieved Ag NWs presents two peaks at 382 nm and 354 nm, which are ascribed to the transverse and quadrupolar longitudinal plasmon resonances (Fig. 5.4 panel C). TEM image shows Ag NWs with an average length and diameter of 5±3 μm and 0.10±0.03 μm (Figure 5.4 panel D), respectively, and an aspect ratio of 50.

5.3.3 His-RGO/AgNWs nanocomposite application in Surface-Enhanced Raman Scattering (SERS)

The achieved His-RGO/Ag NWs hybrid nanocomposite is expected to merge the intrinsic plasmonic properties of the Ag NWs, with the high surface area and chemical reactivity of RGO, its capability to enhance Raman signals of molecules by the chemical enhancement effect, in form of monolayer, and to stabilize the Ag NWs against oxidation, thanks to its oxygen and moisture barrier properties[52]. Thus, the nanocomposite was here preliminarily tested for the SERS detection of Raman active reference molecules, and then applied to the recognition of a drug molecule. For purpose of comparison, the same studies have been performed on neat Ag NWs working in the same experimental conditions.

We chose three model target molecules differing in their chemical structure, namely R6G, 1-Nat and benzo[a]pyrene, also using different concentrations of analyte solutions (10^{-5} M, 10^{-6} M and 10^{-7} M), to assess the effect of their chemical affinity with the nanocomposite, which is a crucial aspect for the effectiveness of the SERS detection [15,53]. The hypothesis is that RGO- and Ag-based nanocomposites can enable the detection of molecules with functional groups that have an affinity for Ag, such as 1-Nat, which is SERS-active due to its chemical binding to the Ag surface by the thiol group (SH) (Fig.5.5).

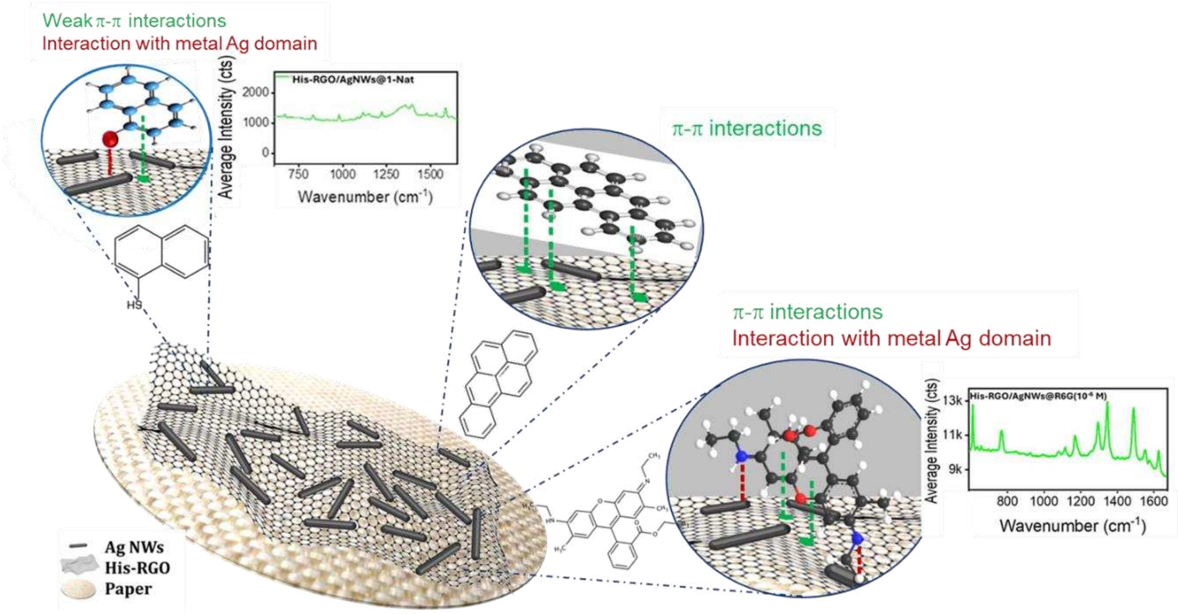

Fig.5.5: *Sketch illustrating the interaction between the His-RGO/Ag NWs nanocomposite deposited on hydrophobic paper and the functionalities of the model molecules 1-Nat (top left), benzo[a]pyrene (center), and R6G (bottom right).*

Also, molecules possessing functionalities able to bind RGO, such as R6G and benzo[a]pyrene, having aromatic rings that interact by aromatic π-π stacking interactions with RGO, can result SERS active, thanks to the chemical enhancement effect expected from RGO. In this case only R6G has been found SERS-active, because binds the Ag NWs, and its chemical adsorption onto RGO brings it close to the Ag NWs hot-spots. No SERS activity, instead, has been found for benzo[a]pyrene (Fig.5.5), which lacks functional groups chemically compatible with Ag, most likely because His-RGO does not provide the chemical enhancement effect.

Hydrophobic chromatographic paper (Fig.5.6) was chosen as a substrate for the SERS active materials in these measurements, because it presents a low fluorescence signal and a low Raman scattering background. [33]

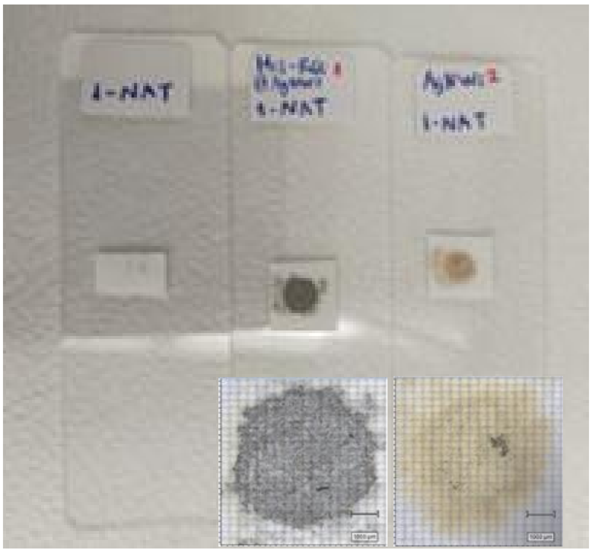

Fig.5.6: *Digital photograph images of hydrophobic paper modified by drop casting 1-Nat, His-RGO/Ag NWs and Ag NWs.*

Besides, the paper is composed of pure cellulose, being free from industrial additives and possible contaminants that could interfere with the SERS analysis[33].

The chromatographic paper was made hydrophobic by modification with DDSA, as reported in the experimental section of this chapter. DDSA is a widely used sizing agent due to its capability of promoting formation of a water resistance surface on paper [33]. The anhydride group of DDSA reacts with the hydroxyl groups of cellulose by esterification and enables grafting of aliphatic chains on the cellulose surface which reduces its wettability [33] .

5.3.4 Preliminary SERS Study for 1-NaT, R6G and benzo[a]pyrene

Detection of Rhodamine-6G (R6G)

R6G is a highly fluorescent dye, that is often used as a tracer dye in water to determine the rate and direction of water flow and transport, in biotechnology for fluorescence microscopy, flow cytometry, fluorescence correlation spectroscopy, and in SERS applications.

A preliminary study was conducted to assess the effective enhancement of the SERS signal of R6G, when deposited onto the nanocomposite substrate. The SERS spectra reveal a significant enhancement of the signal for R6G, demonstrating a 5-fold increase in intensity compared to pure R6G, when deposited onto the His-RGO/AgNWs nanocomposite substrate (Appendix 3, Fig.1).

The SERS properties of R6G deposited onto the His-RGO/Ag NWs nanocomposite and Ag NWs, both transferred onto paper substrates, were investigated in detail under laser line excitations of 633 nm and 785 nm.

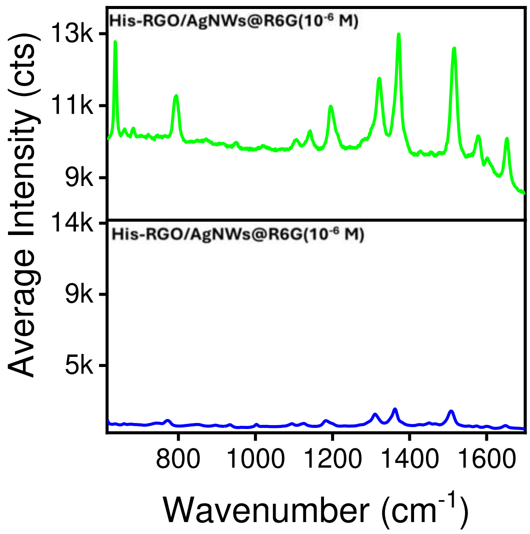

Fig.5.7: *SERS spectrum of His-RGO/AgNWs@R6G acquired using a 633 nm laser line (green line) and 785 nm laser line (blue line), at 5% power, acquisition time of 10 s, 1 accumulation, and a 20x objective.*

The comparison of the achieved SERS spectra showed that the best enhancement of the SERS signals of R6G is obtained for the 633 nm excitation (Fig. 5.7 green line).

The SERS spectra of R6G deposited onto His-RGO did not show any signal (data not reported). On the contrary, the SERS spectra of R6G deposited onto His-RGO/Ag NWs and Ag NWs substrates showed characteristic peaks at 1322, 1371, 1516, 1576, 1601, and 1652 cm^{-1} (Fig.5.7 panel B green line and panel A), which are assigned to the aromatic -C-C- stretching vibrations observed in the Raman spectra of R6G [12].

Panel B of Figure 5.8 (blue line) showed that the SERS spectrum of His-RGO/Ag NWs reports a shift in the peaks corresponding to the D and G bands of RGO at 1366 and 1637 cm^{-1}, respectively compared to those observed in the Raman spectrum of His-RGO/Ag NWs at 1349 and 1582 cm^{-1}, respectively (Fig. 5.3 (A)). This effect could be due to a change in the laser excitation wavelength, that, in the SERS spectrum was 633 nm while in the Raman spectrum was 532 nm, thus causing a shift in the SERS peaks.

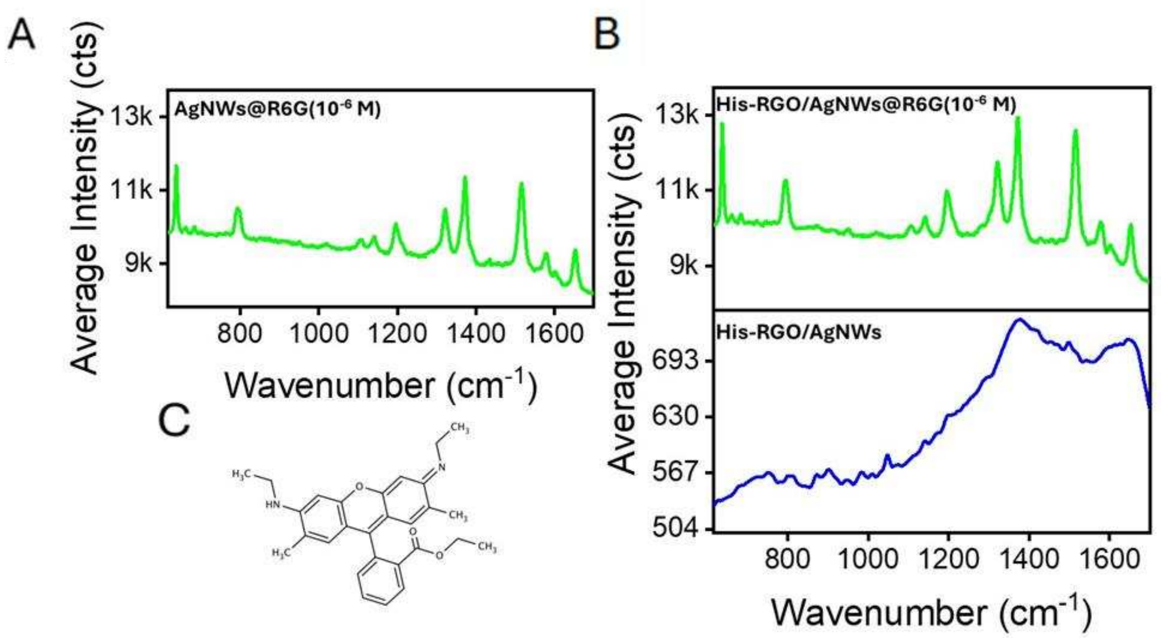

Fig.5.8: *SERS spectrum of (A) AgNWs@R6G, (B) His-RGO/AgNWs@R6G (green line) and His-RGO/AgNWs (blue line). C) Molecular structure of R6G. All SERS experiments were conducted with a 633 nm laser line at 5% power, an acquisition time of 10 s, 1 accumulation, and a 20x objective, respectively*.

This phenomenon occurs because the different energy of the incident laser resonates with different vibration modes of the sample molecules.

From the SERS spectra, it can be noted that the intensity of R6G peaks is higher in the nanocomposite with respect to the neat Ag NWs, due to the synergistic SERS enhancement effect of the Ag nanostructures and the RGO sheets. Since His-RGO did not provide any SERS signal (data not shown), therefore does not contribute by itself to increasing the signal of R6G, it follows that what actually generates the signal and enhances its intensity are the Ag NWs and the His-RGO two-dimensional platform that favours, with its large surface area and aromatic structure, the chemical adsorption of R6G bringing the molecules close to the Ag NWs hot-spots, quenching also their fluorescence emission, and helping to reduce the background noise [11].

Detection of 1-Naftalenthiol (1-Nat)

The SERS properties of 1-Nat upon deposition onto the His-RGO/Ag NWs nanocomposite and onto the Ag NWs, transferred onto paper, were investigated in detail under multiple laser line excitations (532, 633 and 785 nm). The study showed that the best enhancement of the SERS signals of 1-Nat is obtained for the 785 nm excitation (data not reported).

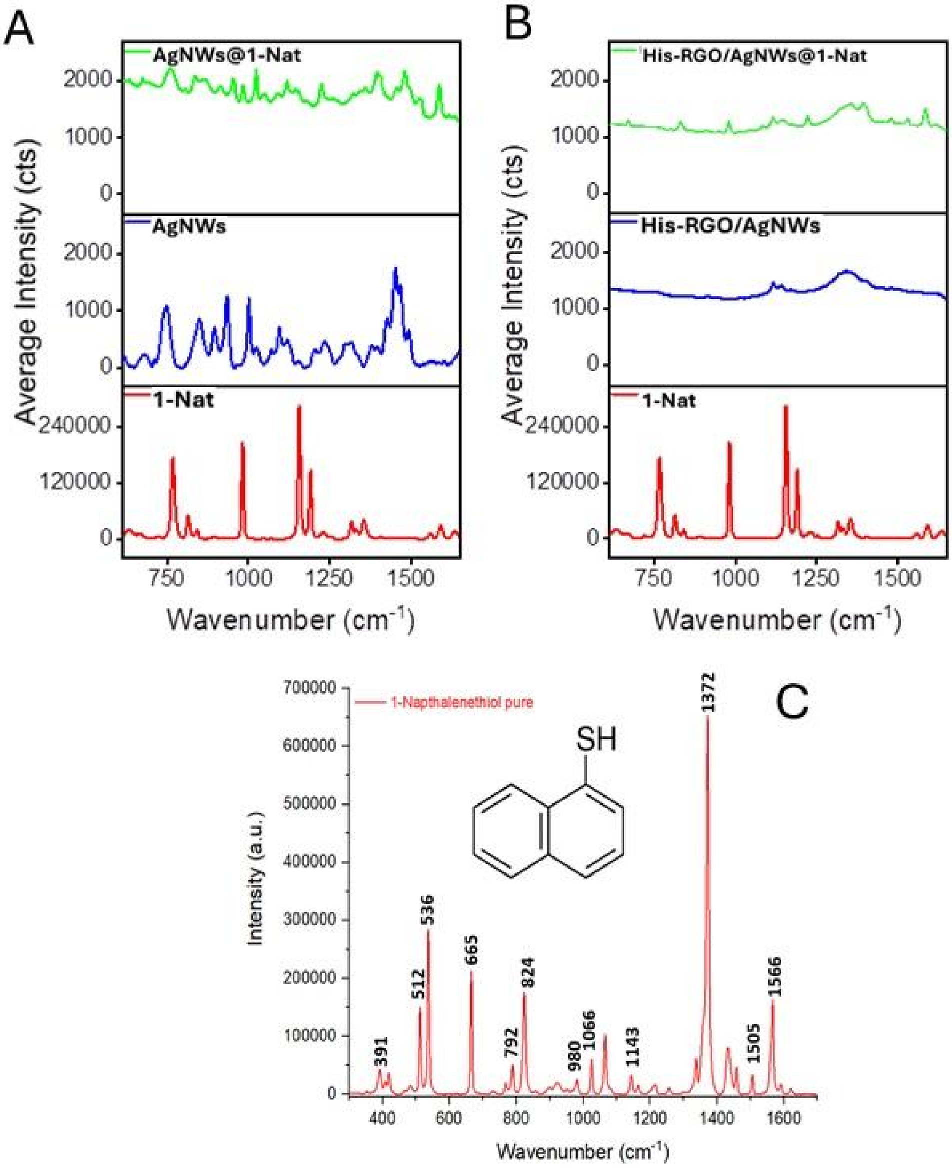

***Fig.5.9**: SERS spectrum of (A) AgNWs@1-Nat (green line), Ag NWs (blue line) and of 1-Nat (red line), (B) His-RGO/AgNWs@1-Nat (green line), His-RGO/Ag NWs (blue line), and 1-Nat (red line). C) Characteristic Raman spectrum of 1-Nat. All SERS experiments were conducted with a 785 nm laser line at 5% power, acquisition time of 10 s, 1 accumulation, and a 20x objective.*

The SERS spectrum of the Ag NWs (Fig.5.9 panel A blue line) [55] shows different peaks at around 1466 and 896 1395 and 1337 cm^{-1} which correspond to the stretching vibration modes of PVP, specifically the C-N, C-C and Ag-O bonds, that are due to the coordination with the Ag NWs. Also, peaks at 1451 and 1668 cm^{-1}, which can be likely due to the vibrations of C-N ring and C=O bonds, are observed [20].

The SERS spectrum of the nanocomposite (Fig.5.9 panel B blue line) shows the presence of a double peak at 1116 and 1142 cm^{-1}, which is also observed in the spectra of the Ag NWs. These peaks originate from the DSSA functionalized paper [33]. The SERS spectrum of the His-RGO/Ag NWs sample (Fig.5.9 panel B blue line) shows a shift in the peaks corresponding to the D and G bands of His-RGO to 1345 and 1550 cm^{-1}, compared to those observed in its Raman spectrum at 1349 and 1582 cm^{-1} (Fig.5.4, panel A). Additionally, SERS peaks were observed at 753, 860 and 945 cm^{-1}, that can be ascribed to the vibrational modes of PVP, specifically the N-C=O band vibration of the in-plane pyrrolidone ring breathing, the C-N stretching vibration, the weak ring CH_2 twist and the in-plane C-H band vibration. These peaks are shifted with respect to the Raman peaks of neat PVP due to the coordination to the Ag NWs surface (Fig.5.9 panel B blue line).

The SERS spectra of 1-Nat deposited onto the nanocomposite showed the characteristics peaks at 833 and 981 cm^{-1} that are due to its ring breathing, at 672 and 753 cm^{-1} due to its ring deformation, and at 1066 and 1143 cm^{-1} due to the C-H bending. The latter two peaks are merged with the peaks at 1116 and 1142 cm^{-1}, which are also observed in the SERS spectra of His-RGO/Ag NWs and Ag NWs, that can be attributed to the hydrophobic paper (Fig.5.9 panel B green line). [20].

Additionally, some Raman bands of 1-Nat on His-RGO/Ag NWs, which are associated with ring stretching at 1372, 1505, and 1584 cm^{-1} (Fig. 5.9 panel C), are shifted in the SERS spectrum at 1392, 1531, and 1584 cm^{-1} (Fig. 5.9 panel B). The bands at 1392 and 1531 cm^{-1} are merged with the D and G bands of RGO at 1345 cm^{-1} and 1550 cm^{-1}, resulting in a Raman shift in the spectrum.

The most striking observation is that the SERS spectra of 1-Nat on His-RGO/Ag NWs and Ag NWs showed a higher relative intensity peak at 1584 cm^{-1} compared to those obtained from pure 1-Nat. For this reason, this peak was considered as the reference in subsequent analyses.

Detection of Benzo[a]pyrene

The SERS properties of benzo[a]pyrene upon deposition onto the His-RGO/Ag NWs and Ag NWs samples transferred onto paper substrates, were investigated in detail under multiple laser line excitations (532, 633 and 785 nm). The studies conducted on the molecule deposited on the nanocomposite and tested at different laser excitation wavelengths did not show the characteristic SERS spectrum of benzo[a]pyrene (data not shown). Since it is anticipated that benzo[a]pyrene has chemical affinity with RGO, through its aromatic rings, and not with the Ag NWs, the lacks of signals in the SERS spectrum of benzo[a]pyrene, demonstrates that His-RGO is not SERS-active, and that SERS signals can be detected only for target molecules as R6G and 1-Nat, that bear functional moieties able to bind the Ag NWs surface.

5.3.5 Optimization of the deposition method

The SERS signals of 1-Nat deposited onto His-RGO/Ag NWs and Ag NWs substrates were also optimized in the volumes deposited by drop-casting onto the paper. For this purpose, four different volumes of each material, 1, 4, 8 and 16 µl, were deposited by drop-casting, 1 µl at a time, onto four paper slides, respectively.

From the color maps of the SERS signal collected at the integrated peak at 1584 cm^{-1}, it can be observed that, as the density of Ag increases in the Ag NWs sample, the signal also increases (Fig.5.10 SERS mappings on the top, panel A). Conversely, this trend is not observed in the nanocomposite (Fig.5.10 SERS mappings on the bottom, panel A).

This result is also evident in the graph showing the integrated peak at 1584 cm^{-1} relative to the baseline vs the density of Ag taken along the area of the deposited drop (Fig.5.10 panel B).

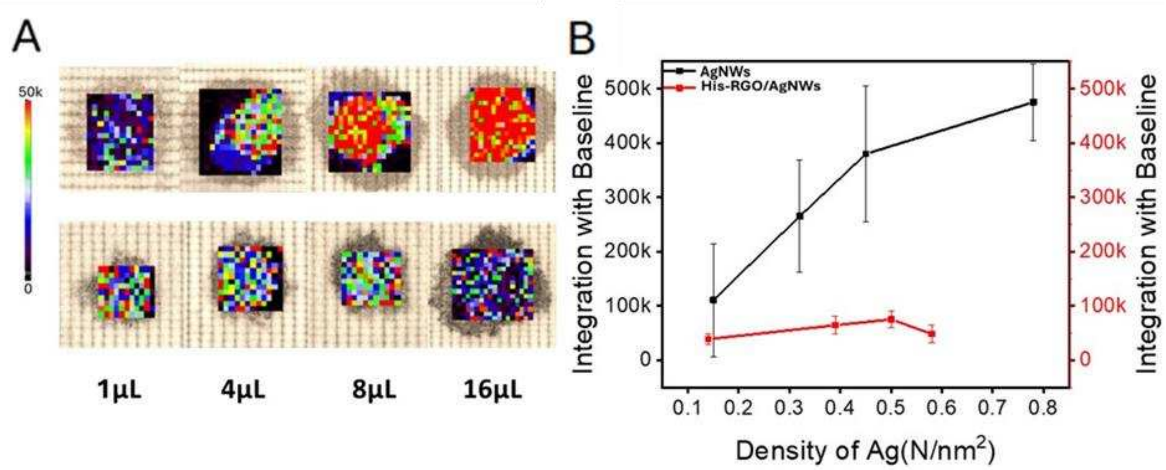

Fig.5.10: *(A) Representative SERS mappings measured using the peak intensity at 1584 cm^{-1} for four different volumes of His-RGO/AgNWs (on the bottom) and Ag NWs (on top) onto four different hydrophobic papers (1, 4, 8, and 16 µl). Followed deposition of 4-µl of 1-Nat (10^{-5}M) to each sample. All SERS measurements were carried out with a 785 nm laser, 5% power, 10 s acquisition time, 1 accumulation and a 20x objective. (B) Integrated peak at 1584 cm^{-1} relative to the baseline versus the density of Ag on the area of the deposited drop for Ag NWs (black line) and His-RGO/Ag NWs (red line).*

For Ag NWs, a maximum value of the SERS signal is reached upon deposition of 16 µl, beyond which the signal saturates (Fig.5.10 panel B black line). In contrast, for the nanocomposite, a maximum signal is reached for 8 µl, after which the signal decreases (Fig.5.10 panel B red line). This evidence is likely due to the layer-by-layer deposition hindering the access of the target molecule to the nanocomposite surface.

5.3.6 Dependence of the SERS signal on focal length along the z-axis

In the acquisition of SERS signals of target molecules, a variation in the background was experimentally observed, even though the signal always came from the same sample. [12] Therefore, the hypothetical dependence of the SERS signal on the laser focus distance, along the z-axis, was investigated for His-RGO/Ag NWs and Ag NWs.

For this purpose, the SERS signals of R6G (10^{-6} M) deposited onto His-RGO/AgNWs and AgNWs, were acquired using always the same sample and analyzing the same area while varying the focus along the Z-axis at the positions 0, 10, 15, and 20 (Fig.5.11). The results showed that the SERS spectra (Fig.5.11 panel B) and the related graphs of the integrated peak at 1365 cm^{-1} relative to the baseline versus the focus along the Z-axis (Fig.5.11 panel C), showed that, for both samples, the peak intensity does not change significantly with varying focus distance. Therefore, we can exclude a dependency of the acquired signal on the focal length along the z-axis.

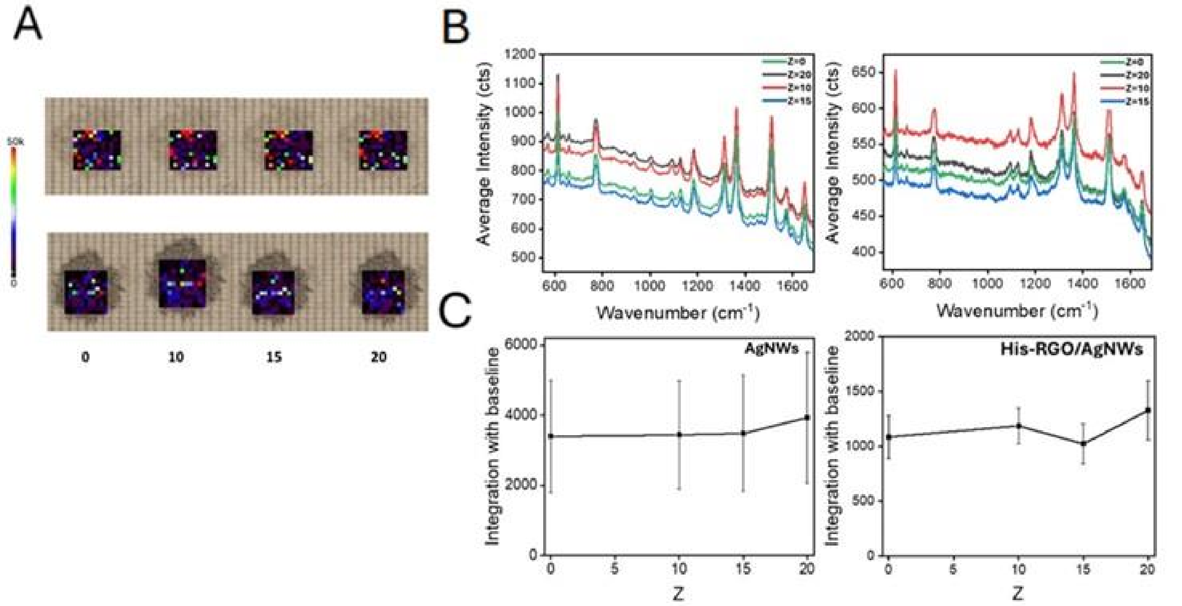

Fig.5.11:*(A) Representative SERS mappings of AgNWs@R6G (on the top) and of His-RGO/AgNWs@R6G (below), measured using the peak intensity at 1364 cm^{-1} (10^{-6} M). B) Representative average SERS spectra of AgNWs@R6G (left panel) and His-RGO/Ag NWs (right panel). C) Integrated peak at 1364 cm^{-1} relative to the baseline versus the focus along the Z-axis for AgNWs@R6G (left panel) and His-RGO/AgNWs@R6G (right panel). All SERS measurements were acquired using the same sample and analysing the same area while varying the focus along the Z-axis at positions 0, 10, 15, and 20 with the 633 nm laser line, 5% power, acquisition time of 10 s, 1 accumulation, and a 20x objective.*

5.3.7 Limit of detection (LOD) determination for 1-Nat and R6G for His-RGO/Ag NWs and Ag NWs.

To check the sensitivity of the investigated SERS substrates, His-RGO/AgNWs and AgNWs, towards 1-Nat and R6G molecules, and estimate their limit of detections (LODs), the intensity versus concentration graph for the 1584 cm^{-1} and 1365 cm^{-1} peaks, respectively, has been plotted (Fig.5.12, panel C and Fig.5.13, panel C).

In the SERS spectra of 1-Nat, the intensity of the peak at 1584 cm^{-1} decreases with the concentration both in presence of the nanocomposite and of the Ag NWs (Fig.5.12, panel B), as assessed also by the intensity trend for the peak at 1584 cm^{-1} versus concentration, collected in presence of the nanocomposite and of the Ag NWs (Fig.5.12, panel C black line and red line, respectively). In particular, the peak intensity value at the highest

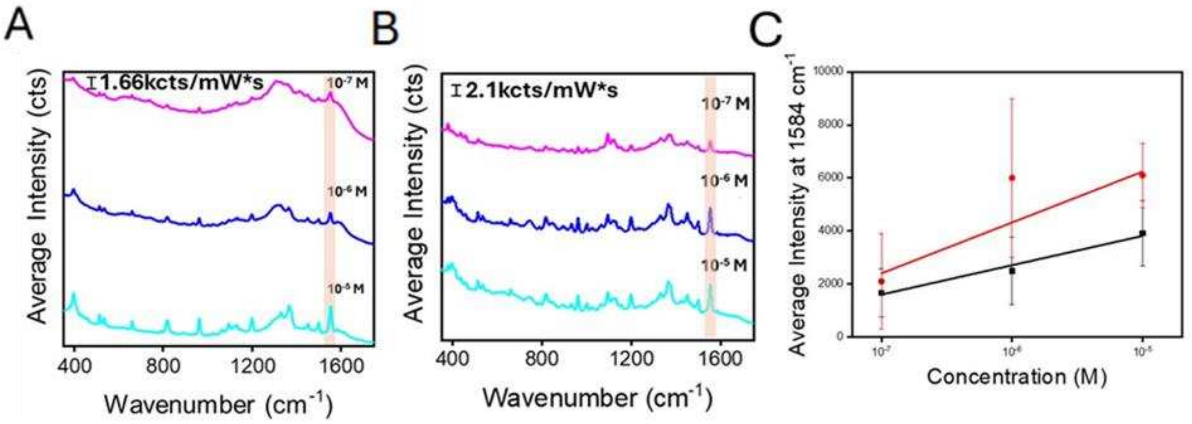

Fig.5.12: *(A) SERS spectrum of His-RGO/AgNWs@1-Nat acquired for three aqueous solutions at different concentrations (10^{-5} M, 10^{-6} M, and 10^{-7} M) and B) of AgNWs@1-Nat C) Average SERS intensity measured at 1584 cm^{-1} vs the 1-Nat concentration for His-RGO/Ag NWs samples (black line) and AgNWs samples (red line). SERS measurements were performed with a 785 nm laser line at 10% power, acquisition time of 10 s, 1 accumulation, and a 20x objective.*

concentration is greater with the neat Ag NWs (Fig.5.12, panel B-C red line) compared to the nanocomposite (Fig. 5.12 panel A-C, black line). This is because 1-Nat undergoes a sulphur-metal bond with the Ag NWs surface [56], enhancing its interaction with the NWs hotspots and hence increasing its SERS signals.

In case of the nanocomposite, it is likely that since the Ag NWs are bound to the functionalities of His anchored onto the RGO sheets, they are more spaced apart, losing their alignment along the longitudinal axis [57], which decreases the intensity of the electromagnetic field at the Ag NWs hotspots and accordingly the SERS signal.

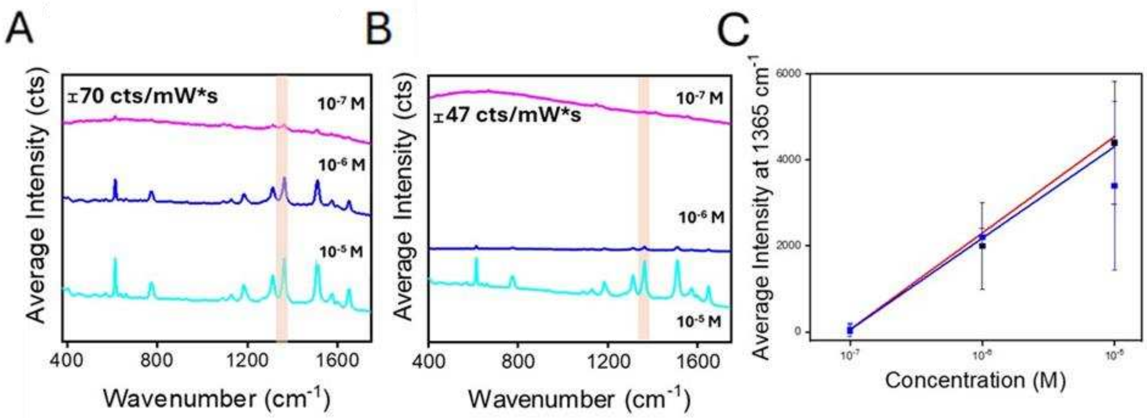

Fig.5.13*: SERS spectrum of (A) His-RGO/AgNWs@R6G acquired for three aqueous solutions at different concentrations (10^{-5} M, 10^{-6} M, and 10^{-7} M) and B) AgNWs@R6G. C) Average SERS intensity measured at 1365 cm^{-1} vs the R6G concentration for His-RGO/AgNWs (red line) and AgNWs (blue line). SERS measurements were performed with a 633 nm laser line at 5% power, an acquisition time of 10 s, 1 accumulation, and a 20x objective.*

Regarding R6G, also the intensity of its peak at 1365 cm⁻¹ decreases with the concentration both in presence of the nanocomposite and of the Ag NWs (Fig.5.13, panel B), as assessed also by the intensity trend for the peak at 1365 cm⁻¹ versus concentration (Fig.5.13, panel C black line and red line, respectively). This is because R6G exhibits chemical affinity not only towards Ag, but also towards RGO. R6G, in fact, is a molecule with aromatic rings capable of interacting with His-RGO through aromatic π-π stacking and it also possesses nitrogen-containing groups that interact with Ag NWs, creating a strong chemical bond with the nanocomposite (Fig.5.13).

Both molecules, 1-Nat and R6G, reach a limit of detection (LOD) of 10^{-7} M in presence of both samples, His-RGO/AgNWs and AgNWs, but from (Fig.5.12) and (Fig.5.13), it can be concluded that the different chemical interactions that 1-Nat and R6G undergo with the His-RGO/AgNWs and AgNWs, and the different chemical composition of the two SERS substrates, lead to a slightly different trend in intensities between the two molecules, not only in comparison with each other, but also when comparing the two materials. [15]

5.3.8 SERS signal variation of 1-NaT and R6G due to their degradation over time

A study was conducted to evaluate the hypothetical instability of the SERS signal induced by the degradation of 1-NaT and R6G over a month. A 4 µl droplet of His-RGO/Ag NWs and Ag NWs was deposited onto paper, followed by the deposition of two drops of 2 µl of the target molecules, allowing the paper to dry between each drop deposition.

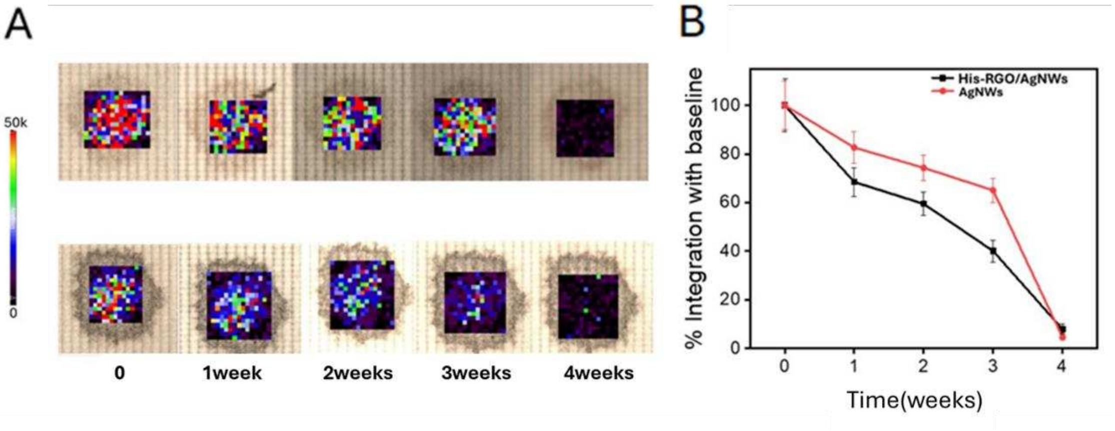

Fig.5.14*: A) Representative SERS mappings measured using the peak intensity at 1584 cm⁻¹ for AgNWs@1-Nat (10^{-5} M) (on the top) and His-RGO/AgNWs@1-Nat (on the bottom) acquired on the same sample at one-week intervals for a duration of one month. B) Integrated peak at 1584 cm⁻¹ relative to the baseline versus time of 1-Nat deposited onto Ag NWs (red line) and His-RGO/Ag NWs (black line).*

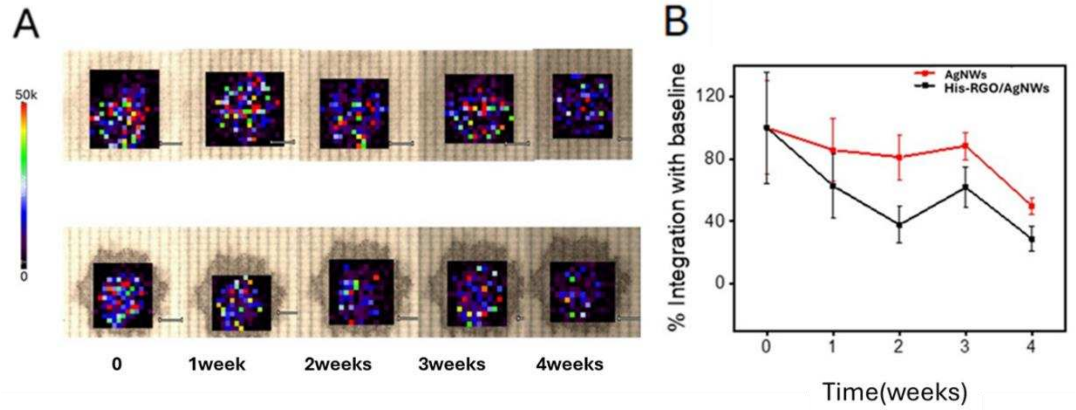

Fig.5.15*: A) Representative SERS mappings measured using the peak intensity at 1364 cm^{-1} for AgNWs@R6G (10^{-6} M) (on the top) and His-RGO/AgNWs@R6G (on the bottom) samples acquired on the same sample at one-week intervals for one month. B) Integrated peak at 1364 cm^{-1} relative to the baseline versus time of R6G deposited R6G onto Ag NWs (red line) and His-RGO/Ag NWs (black line).*

The molecule's signal was tested using a 785 nm laser for 1-NaT (Fig.5.14) and a 633 nm laser for R6G (Fig.5.15). The signal was studied on the same sample every week for a month.

His-RGO/Ag NWs and Ag NWs show a decrease in both target molecules signals over time, namely decrease the peaks at 1584 cm^{-1} for 1-NaT (Fig.5.14) and at 1365 (Fig.5.15) cm^{-1} for R6G. The signal loss, however, is more pronounced for 1-Nat compared to R6G in both samples.

These results assess that the nanocomposite enables detection of molecules with functional groups that have a chemical affinity for Ag, such as thiols, carboxylic acids, or amines, and with aromatic rings that interact via aromatic π-π stacking interactions with RGO; the aromatic π-π stacking interactions between RGO and R6G, keeps this molecule close to the Ag NWs hot-spots, stabilizing it over time against oxidation and enhancing its SERS signal.

5.3.9 SERS signal variation of 1-NaT and R6G due to the degradation of His-RGO/Ag NWs and Ag NWs over time

An analysis was conducted to explore the hypothetical oxidation phenomenon of Ag NWs and His-RGO/Ag NWs that can affect stability of their SERS signals. Four drops of 4 µl were deposited on four different pieces of paper for each sample. The signals of the samples aged 1, 2, 3, and 4 weeks from 1-Nat and R6G were monitored over time, using a 785 nm and a 633 nm laser, respectively. Both samples, His-RGO/AgNWs and AgNWs, showed a decrease in the signal of 1-Nat at 1584 cm^{-1}, (Fig.5.16) and only Ag NWs showed a decrease in the signal of R6G at 1365 cm^{-1} over time (Fig.5.17).

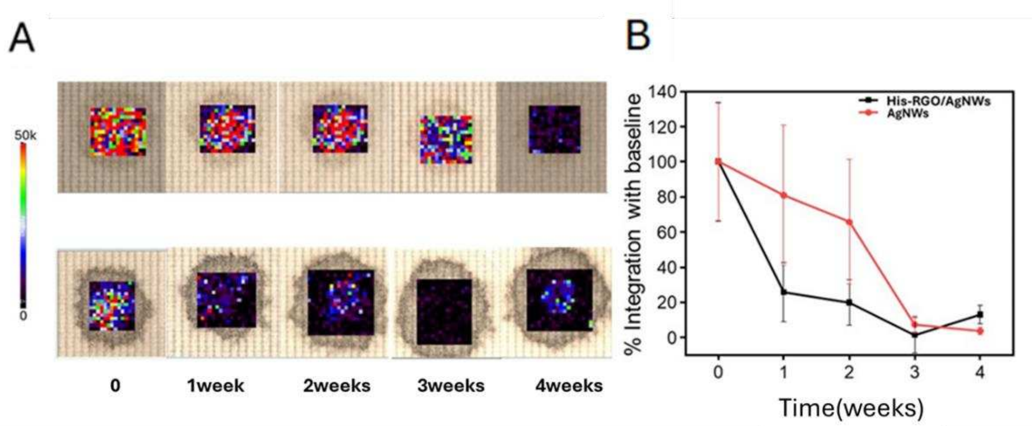

Fig.5.16: *A) Representative SERS mappings measured using the peak intensity at 1584 cm^{-1} for AgNWs@1-Nat (10^{-5} M) (on the top) and His-RGO/AgNWs@1-Nat (on the bottom) acquired using samples aged 1, 2, 3, and 4 weeks. B) Integrated peak at 1584 cm^{-1} relative to the baseline versus time of 1-Nat deposited onto aged Ag NWs (red line) and His-RGO/Ag NWs (black line).*

Thus, it is evident that His-RGO collaborates with this type of molecules like R6G in SERS detection mechanisms. Additionally, it is well-known that RGO also acts as a stabilizer against oxidation, as it slows down the oxidative processes of the Ag NWs occurring on its surface due to its oxygen and moisture barrier properties [52].

This aspect was further confirmed by comparing the stability experiments conducted over time for both molecules. For 1-Nat, a loss of signal over time is observed as the nanocomposite ages (Fig.5.16 panel B black line). This is because 1-Nat has an affinity only for Ag, which may have partially oxidized on the surface over time, leading to a decrease in the signal.

Conversely, for R6G, even after one month, the detection of the molecule remains almost the same (Fig.5.17 panel B black line). In this case, an explanation could be that R6G, having a dual affinity, is more strongly bound to the nanocomposite and therefore more stable and less susceptible to oxidative phenomena compared to when it is bound to the neat Ag NWs.

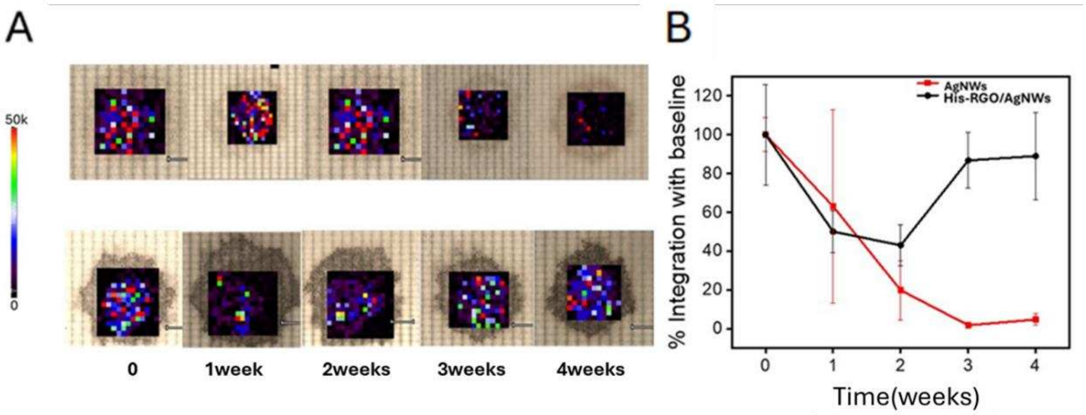

Fig.5.17: *A) Representative SERS mappings measured using the peak intensity at 1364 cm^{-1} for AgNWs@R6G (10^{-6} M) (top panel) and His-RGO/AgNWs@R6G (bottom panel) acquired using samples aged 1, 2, 3, and 4 weeks. B) Integrated peak at 1364 cm^{-1} relative to the baseline versus time of R6G deposited onto aged Ag NWs (red line) and His-RGO/Ag NWs (black line).*

5.3.10 PVP removal through wet chemistry methods

The PVP ligand cannot be removed by using the typical standard purification procedures that are applied to colloidal inorganic NPs and encompassing multiple washing steps, by dispersion in non-solvents and isolation by centrifugation. This is due to the strong Ag−O bond (50.9 kCal/mol) between its carbonyl groups and the Ag surface. Consequently, the removal of PVP from the nanocomposite was tested using a potassium iodide (KI) solution, sodium borohydride ($NaBH_4$) solution and plasma etching, and their efficacy were evaluated via SERS detection of 1-Nat and R6G target molecules.[19]

PVP removal with KI solution and SERS evaluation using 1-NaT and R6G target molecules

Initially, the PVP removal was tested by depositing 30 µl of the nanocomposite on a Si substrate via drop casting, followed by soaking the substrate in KI solutions at different concentrations (0.5 M, 0.16 M and 4.8 mM) for different times (60 and 120 s), and then rinsing with water and ethanol.[26]

The surface morphology of the nanocomposite was investigated before and after the treatment. SEM images of the as-prepared His-RGO/Ag NWs showed the typical surface morphology of RGO characterized by folded sheets-like structures with wrinkles, as well as elongated nanostructures that can be ascribed to the Ag NWs (Appendix 3, Fig.2 panel A).

After treatment with KI, at the highest concentration (Appendix 3, Fig.2 panel B), the SEM image showed a change of the surface morphology of the sample, exhibiting the formation of irregular structures having a low image contrast and coating the sample, that may be ascribed to residual PVP not removed in the rinsing step with water and ethanol. Such structures are detectable also in the SEM image collected on the sample of His-RGO/Ag NWs treated by 0.16 M KI (Appendix 3, Fig.2, panel C), while at the lower (4.8 mM) KI concentration (Appendix 3, Fig.2, panel D) are less evident. EDS spectra of the samples of panels C and E show the signal of

Ag and I elements, that can be likely due to the formation of AgI [26] that displaces PVP [23] coating the Ag NWs (Appendix 3,Fig.2 panel E-F).

This removal treatment was tested on the nanocomposite deposited onto hydrophobic paper, and its effect on the SERS detection of the model molecules R6G and 1-Nat was evaluated. (Appendix 3, Fig.3).

For the lower KI concentration (4.8 mM), a weak signal of 1-Nat at 1584 cm^{-1} was observed, accompanied by an increased background noise (Appendix 3, Fig. 3, panel B). The spectra showed that the treatment with KI did not enhance the signal of 1-Nat. Conversely, the SERS spectrum of R6G shows that, despite a noticeable reduction in background noise is noticed, no significant increase in its signal intensity was observed (Appendix 3, Fig.3, panel C green line) compared to the material tested without PVP removal treatment (Appendix 3, Fig.3,panel C blue line). This evidence can be likely accounted for by the strong adsorption of I^- at the Ag surface, preventing effective adsorption of neutral target molecules like 1-Nat on the nanocomposite surface and favouring instead that of molecules carrying a positive charge as R6G [26].

Thus, it can be concluded that the treatment with KI at the lower concentration partially removes PVP, as indicated by the slightly lower background observed, particularly for the R6G molecule (Appendix 3, Fig.3, panel C green line), but it does not enhance the signal intensity

PVP removal with $NaBH_4$ solution and SERS evaluation using 1-Nat

The PVP removal was tested by treating the nanocomposite with $NaBH_4$ solutions, varying its concentration and treatment duration. The proposed removal mechanism involves the decomposition of $NaBH_4$ by solvation, producing hydride ions that replace the carbonyl group of PVP to form Ag–H bonds [25].

Initially, 30 µl of the nanocomposite were deposited on a Si substrate via drop casting, and the removal was carried out by soaking the substrate in a 0.05 M $NaBH_4$ aqueous solution for 10 s and 30 s, followed by rinsing with ethanol. The surface morphology of the nanocomposite was investigated before and after the treatment. SEM images of as-prepared Si substrates modified with His-RGO/Ag NWs are shown in Appendix 3, Fig.4, panel A. The surface morphology of His-RGO/Ag NWs is confirmed by the presence of thin, wrinkled and folded sheets-like microstructures ascribed to RGO coating the elongated nanostructures of the Ag NWs. After treatment for 10 s and 30 s, any change of the surface morphology is detectable in the SEM images. (Appendix 3, Fig.4 panel A-B).

This treatment was, however, tested on hydrophobic paper modified with the nanocomposite, and its effect on the SERS detection of the model molecule 1-Nat was evaluated. (Appendix 3, Fig.4 panel C)

The treatment was conducted by directly soaking the paper modified with the nanocomposite in $NaBH_4$ solutions at different concentration, 0.05M; 0.03M; 0.025M, for 30 s. Immediately after the treatment, the paper lost its hydrophobicity, indicating that $NaBH_4$ penetrated the paper fibers affecting the initial functionalization of the paper with DDSA. Experimentally, this is evident from the behaviour of aqueous model molecule solutions, which tend to be absorbed and spread across the paper surface rather than remaining as droplets.

Furthermore, the SERS signals of the 1-NaT molecule indicate that the treatment is ineffective, as the molecule's SERS spectrum is not clearly visible (Appendix 3, Fig.4 panel C).

5.3.11 PVP removal using plasma treatment

Plasma treatment was tested to remove PVP from the His-RGO/AgNWs nanocomposite surface. For this purpose, a preliminary plasma treatment of 2 min with O_2 and Ar was performed to remove PVP, followed by an additional treatment of 2 min of reduction with H_2 to restore the Ag NWs.[24]

Various experiments were conducted varying the number of cycles of treatment with O_2/Ar and H_2/Ar plasma to optimize the SERS signal. Specifically, the material was tested after one cycle of O_2/Ar and one cycle of H_2/Ar, one cycle of O_2/Ar and two of H_2/Ar, two cycles of O_2/Ar and one of H_2/Ar, and two cycles of O_2/Ar and two of H_2/Ar (Fig.5.18).

The best result was obtained with one cycle of O_2/Ar and two cycles of H_2/Ar, as this provided a compromise between a low background and a sufficiently intense signal for R6G. The SERS spectrum of the nanocomposite after one cycle of O_2/Ar and two cycles of H_2 shows peaks at 1595, 1334, 1096, and 1004 cm^{-1}, attributed to the G and D bands of RGO, the CH_2 twist from the Ag-PVP bond, and the signals of paper (Fig.5.18).

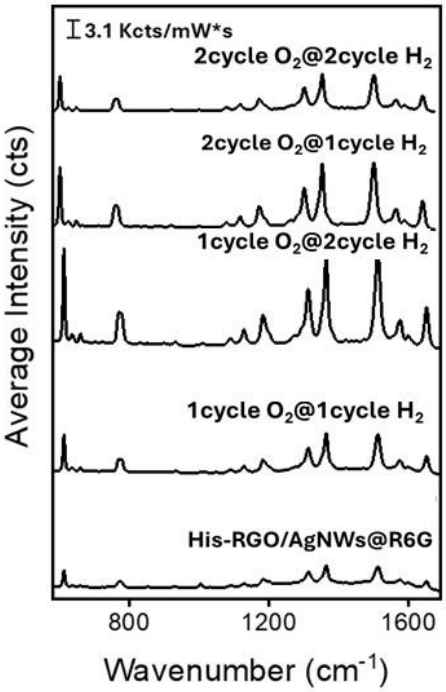

***Fig.5.18**: Representative SERS spectra of R6G deposited onto His-RGO/AgNWs samples after different cycles of plasma treatment.*

Indeed, it can be observed that the SERS spectrum of R6G, acquired after plasma treatment, shows characteristic peaks (1363 cm^{-1}) with higher intensities compared to the SERS spectrum of R6G acquired from the pristine nanocomposite (Fig.5.18)

Moreover, the LOD for the R6G, which was estimated considering the concentrations of 10^{-5} M, 10^{-6} M,10^{-7} M and 10^{-8} M, on the plasma-treated sample was 10^{-8} M, both when it was estimated with the average SERS intensity and with the digital analysis, The fact that the LOD achieved by both the investigated approaches is the same, is likely because the background of the SERS signal from which the threshold was estimated is high, and hence, it does not allow to decrease the sensitivity of the detection. This LOD is higher with respect to the LOD estimated for the same molecule from the untreated nanocomposite that was 10^{-7} M. (Fig.5.19).

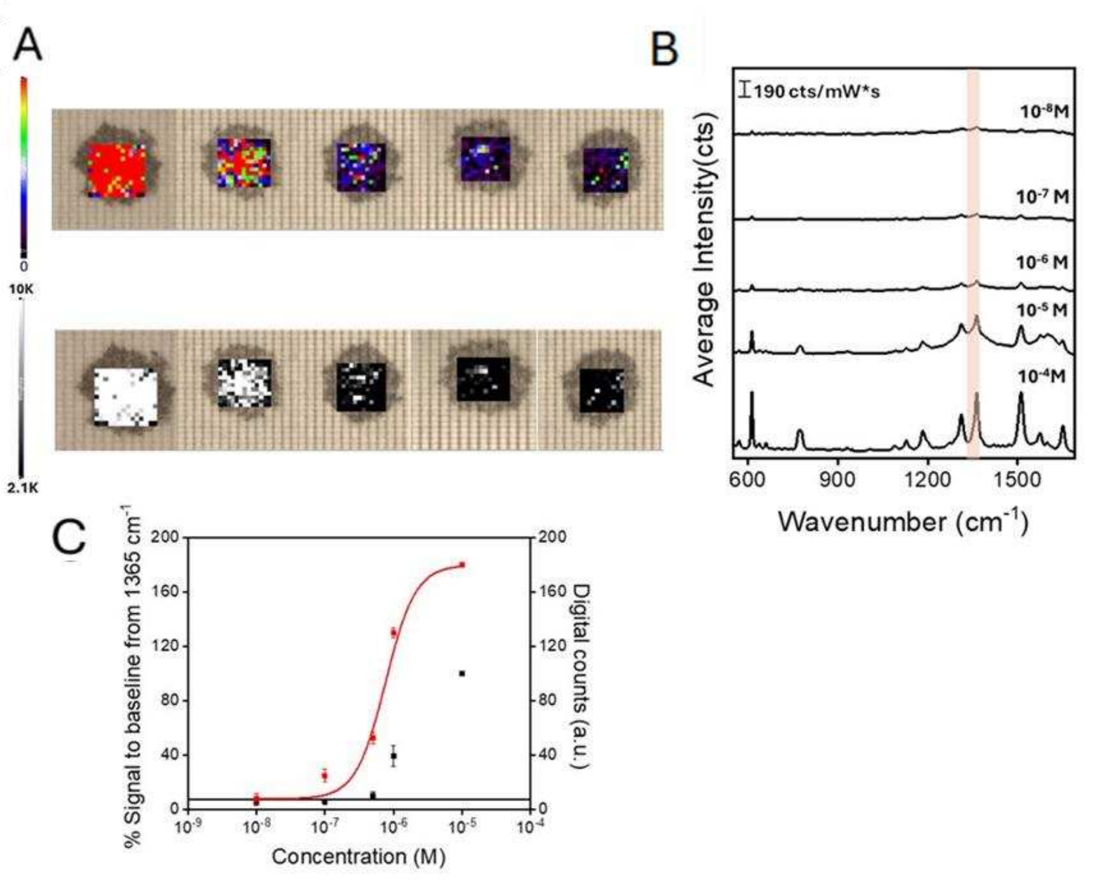

Fig.5.19: *(A) Representative SERS mappings measured using the peak intensity at 1365 cm^{-1} for different concentration of R6G deposited onto His-RGO/AgNWs sample after plasma treatment (on the top). Representative Digital SERS maps after applying the threshold limit value to the signal to baseline SERS maps. The grey/white and black squares correspond to positive and negative events, respectively (below). (B) LOD of R6G evaluated for four aqueous solutions at different concentrations (10^{-5} M, 10^{-6} M,10^{-7} M and 10^{-8} M) for His-RGO/AgNWs sample after plasma treatment C) Variation of the digital counts as function of the R6G concentration (red squares). The red curve represents the best fitting of a 4PL equation to the experimental data. As a guide, the measured average SERS intensity at 1365 cm^{-1} with the R6G concentration is also plotted*

(black squares). SERS measurements were obtained with a 633 nm laser line, 20× objective, 10% laser power, 10 s acquisition time.

To explain the increase of the LOD of the nanocomposite after plasma treatment, the surface morphology of the nanocomposite was investigated before and after the treatment. The sample was deposited on silicon and morphologically characterized by SEM after both the O_2/Ar treatment alone (Fig.5.20, panel B) and the treatment with H_2/Ar plasma (Fig.5.20, panel C).

Although the SEM images (Fig.5.20, panel C) show a morphological change compared to the pristine nanocomposite (Fig.5.20, panel A), the brighter irregular nanostructures could be attributed to Ag, that, due to the PVP removal, may have formed aggregates of varying sizes and shape. Elemental analysis, performed by EDS (Fig.5.20, panel D), confirmed the presence of Ag showing its Lα line at 2.984 keV. The spectroscopic properties of the plasma treated nanocomposite were also studied by UV-Vis absorption spectroscopy, showing a shift of the plasmon peaks of the Ag NWs at 293 nm and 320 nm and the formation of a band enlarging towards the low energy side of the spectral range that can be ascribed to polydisperse Ag NPs (Fig.5.20, panel D on the bottom).

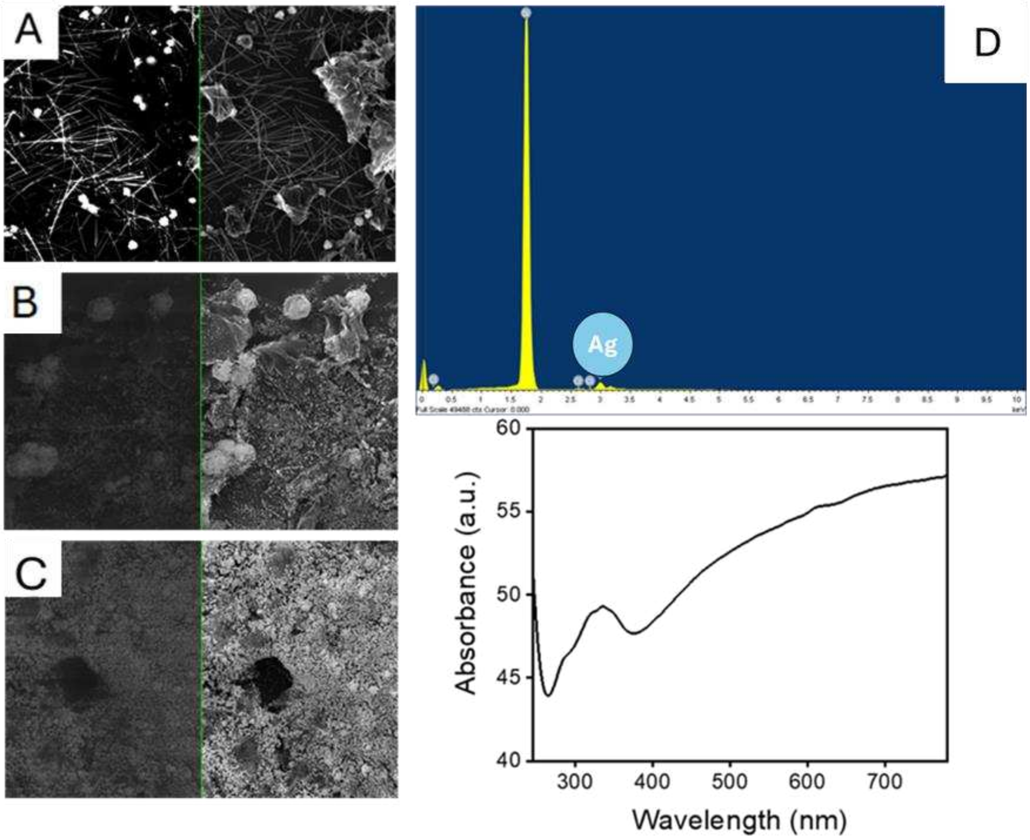

Fig.5.20: *SEM micrograph of 30 μl of His-RGO/AgNWs A) deposited onto Si substrate (11,24 KX), B) after O_2/Ar plasma treatment, and C) after O_2/Ar treatment and H_2/Ar plasma treatment (15 KX and 13 KX). D) EDS (on the top) and UV-Vis absorption spectra of of His-RGO/AgNWs after both plasma treatments (on the bottom).*

These results show that the plasma treatment leads to aggregation of the Ag NWs, significantly modifying the nanocomposite's morphology and enhancing LOD for R6G detection, likely because the intensity of the hot spots at the Ag nanostructures increases.

For this reason, it was decided to investigate also the potential degradation of the R6G signal over time (Fig.5.21, panel A on the top, and panel B red line) and the effect of aging of the plasma-treated nanocomposite samples (Fig.5.21, panel A on the bottom, and panel C red line) on the SERS intensity detection signal of R6G.

The SERS signal intensity of R6G deposited on the plasma-treated nanocomposite decreases over time (Fig. 5.21, panel A on the top, and panel B, red line). As shown in the graphs comparing the signal trends over time for R6G with plasma-treated (Fig. 5.21, panel B, red line) and untreated nanocomposites (Fig. 5.21, panel B, black line), the signal with the treated nanocomposite follows a similar trend as that of the untreated sample.

It can be observed that the intensity of the SERS signal of R6G deposited on the plasma-treated nanocomposite aged for one month remains constant over time (Fig. 5.21, panel C, red line). Therefore, it can be concluded that, in terms of signal stability, despite the morphological changes induced by plasma treatment, the well-known properties of RGO, acting as a stabilizer against oxidation of Ag NWs due to its oxygen and moisture barrier properties,[52] remain unaffected.

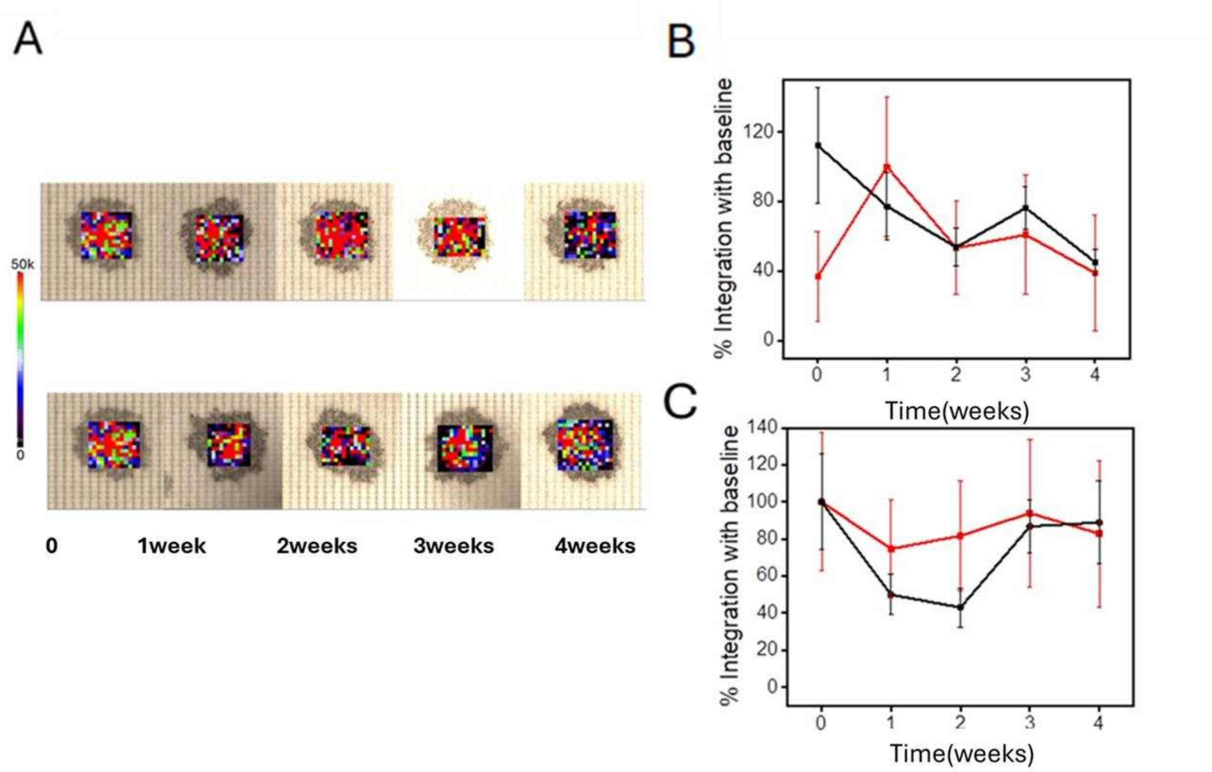

Fig.5.21: *A) Representative SERS mappings measured using the peak intensity at 1365 cm*$^{-1}$ *for R6G deposited onto His-RGO/AgNWs@plasmatreated samples (on the top) acquired on the same sample at one-week intervals for a duration of one month to evaluate potential oxidation of R6G, (on the bottom) aged 1, 2, 3, and 4 weeks, to evaluate the potential oxidation of the His-RGO/AgNWs@plasmatreated samples. B-C) Integrated peak at*

1364 cm^{-1} relative to the baseline versus time of B) R6G deposited onto the plasma treated His-RGO/AgNWs (red line) and untreated His-RGO/Ag NWs (black line), to evaluate the potential (B) degradation of R6G over time and C) oxidation of the plasma treated His-RGO/AgNWs over time.

5.3.12 Detection of propranolol (PRNL)

Finally, it was decided to test the performance of the nanocomposite material, as synthesized and treated by plasma, in the detection of a real target molecule.

For this purpose, propranolol (PRNL), a widely used β-blocker for the treatment of various cardiovascular diseases such as hypertension, angina pectoris, and tachycardia, as well as of other conditions such as migraines, anxiety, essential tremors, and hyperthyroidism, was investigated. [1] PRNL is a relevant target molecule both for biomedical purpose (e.g. for pharmacokinetic studies) and for environmental monitoring, as, like other pharmaceuticals, can enter water systems and impact aquatic life.

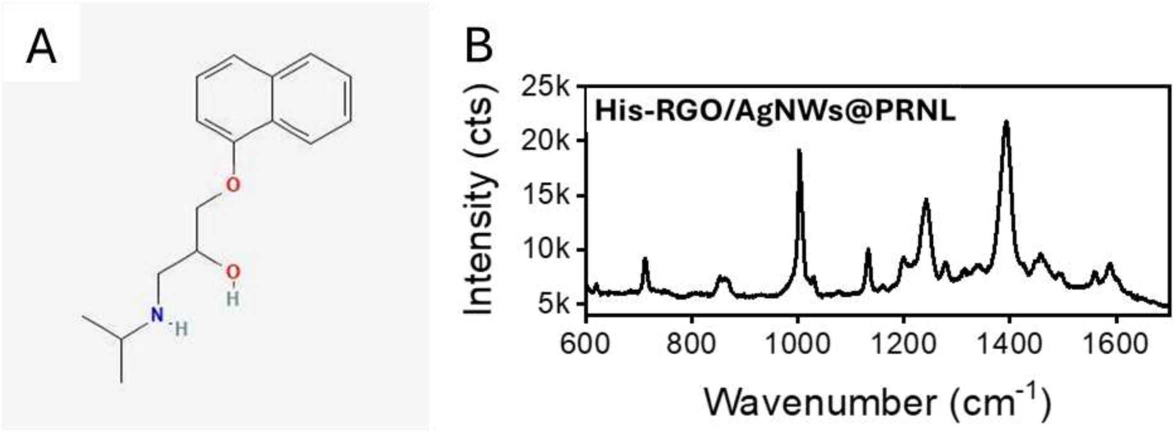

Fig.5.22: *A) Molecular structure of the* PRNL*: B) SERS spectrum of* PRNL *deposited onto His-RGO/AgNWs. The SERS measurements were performed using a 633 nm excitation laser at the 10% power, acquisition time of 5 s, 1 accumulation, and a 20x objective*

The SERS spectrum of PRNL acquired from the untreated nanocomposite showed only few weak intensity bands located at 1588, 1393, and 1002 cm^{-1}. The relative intensity of the 1002 cm^{-1} band in the SERS spectra obtained from PRNL on His-RGO/Ag NWs, could indicate the presence of carbon rings in cyclic or aromatic compounds, responsible for the ring-breathing mode of PRNL molecules (Fig. 5.22 panel B). [1]

To test the concentration-dependent SERS signal, 4 μL of the PRNL aqueous solutions prepared in the investigated concentrations (from 10^{-8} M to 10^{-4} M), were deposited onto the pristine and plasma treated His-RGO/Ag NWs substrate, and SERS measurements were performed using a 633 nm excitation laser at the 10% power, acquisition time of 5 s, 1 accumulation, and a 20x objective (Fig.5.23).

The most striking observation is that the spectra of PRNL on plasma-treated His-RGO/Ag NWs showed higher relative intensity at 1384 cm⁻¹ compared to the untreated nanocomposite, where the peak shifted up to 1393 cm⁻¹, and both modes have been previously assigned to ring-breathing vibrations and CH bending vibrations [1] (Fig.5.23).

The LOD for PRNL, determined on both untreated and plasma-treated SERS substrates, in the tested concentration range from 10^{-4} M to 10^{-8} M, was 10^{-4} M and 10^{-7} M, respectively.

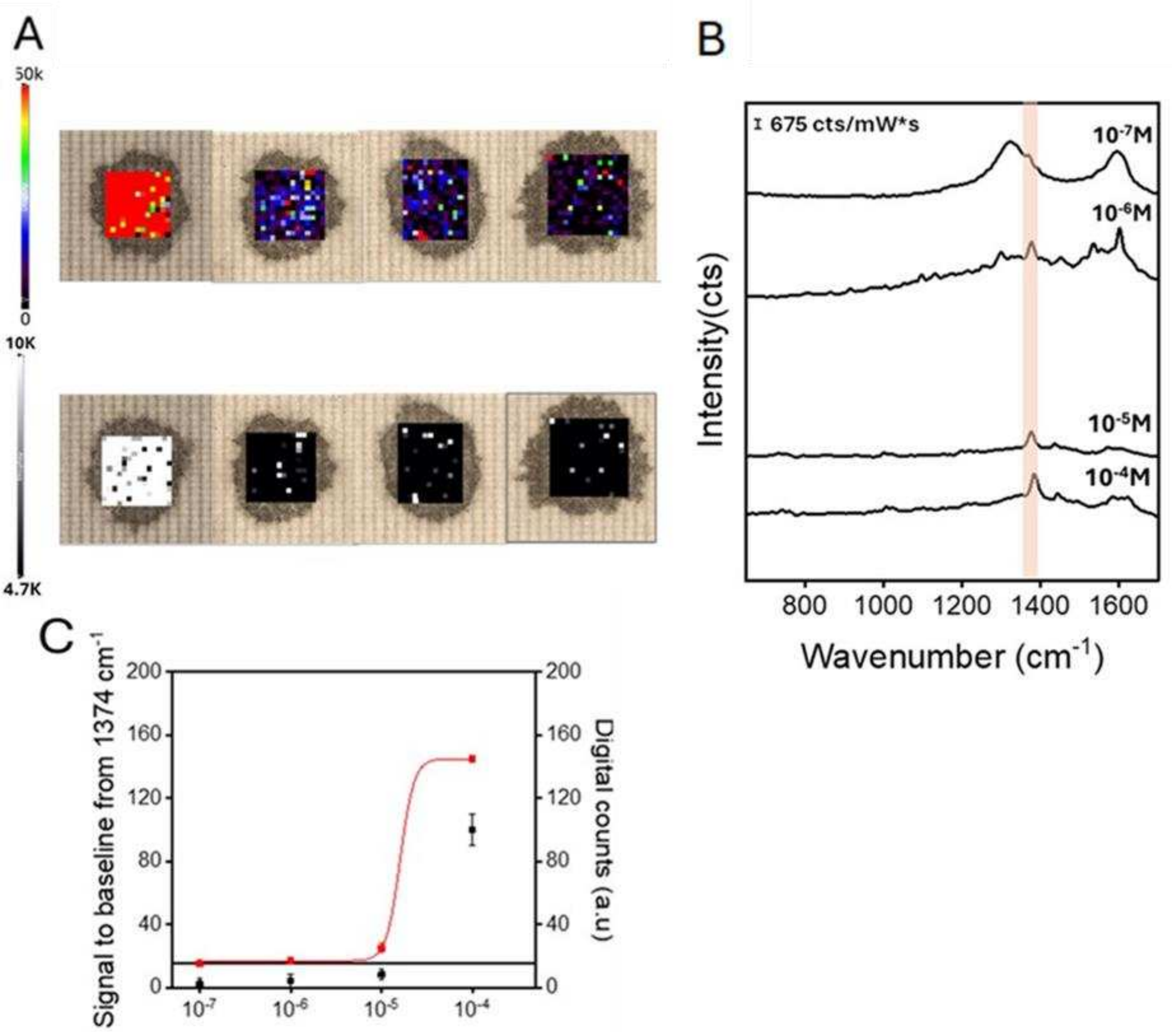

Fig.5.23:*(A) Representative SERS mappings measured using the peak intensity at 1384 cm^{-1} for different concentration of PRNL deposited onto His-RGO/AgNWs@plasmatreated (on the top). Representative digital SERS maps after applying the threshold limit value to the signal to baseline SERS maps. The grey/white and black squares correspond to positive and negative events, respectively (on the bottom). (B) LOD of PRNL evaluated with 4 PRNL aqueous solutions at different concentrations (10^{-5} M, 10^{-6} M,10^{-7} M and 10^{-8} M) for His-RGO/AgNWs sample after plasma treatment. C) Digital counts against PRNL concentrations (red squares). The red curve represents the best fitting of a 4PL equation to the experimental data. As a guide, the measured average SERS intensity at 1384 cm^{-1} with the PRNL concentration is also plotted (black squares). SERS*

measurements were obtained with a 633 nm excitation laser at the 10% power, acquisition time of 5 s, 1 accumulation, and a 20x objective.

5.4 Conclusions

In this work, a novel His-RGO/Ag NWs hybrid nanocomposite was tested against neat Ag NWs, as a substrate for the SERS detection of target molecules having a different chemical structure, namely 1-naphthalenethiol (1-Nat), rhodamine 6G (R6G), benzo[a]pyrene and tested for the SERS detection of propranolol hydrochloride (PRNL), a pharmaceutical molecule of interest.

1-Nat exhibited a high affinity for Ag, while R6G results in a spectrum with more intense SERS peaks compared to 1-Nat for both the materials. Benzo[a]pyrene did not generate any SERS signal, as it lacks functional groups having affinity for Ag. Although it interacts with RGO through aromatic rings, no SERS signal was produced, because RGO itself was demonstrated not SERS-active.

These results assess that i. the nanocomposite enables detection of molecules with functional groups that have a chemical affinity for Ag, such as thiols, carboxylic acids, or amines, and with aromatic rings that interact via aromatic π-π stacking interactions with RGO; ii. the aromatic π-π stacking interactions between RGO and R6G, keeps this molecule close to the Ag NWs hot-spots, stabilizing it over time against oxidation and enhancing its SERS signal, and iii. the number of the aromatic rings present in the molecular structure increases the signal, although the presence of functional groups with an affinity for Ag is necessary for SERS response.

To increase the SERS signal, removal of PVP was also investigated performing treatments with $NaBH_4$, KI and O_2/Ar and H_2/Ar plasma. In particular, the treatment of the nanocomposite deposited onto paper with $NaBH_4$ is not suitable, as it causes the detachment of the material from the paper, and it was not possible to detect the model molecules' spectra. After treatment with KI, the nanocomposite showed the SERS signal of R6G, but not that of 1-Nat, proving themself suitable for detecting charged target molecules, but not neutral ones. However, despite this, the R6G signal was not amplified. Finally, the plasma treatment performed by cycles with O_2/Ar and H_2/Ar, although changed significantly the sample's morphology, improved the R6G signal decreasing its LOD by one order of magnitude compared to the untreated nanocomposite, achieving for propranolol hydrochloride (PRNL), a pharmaceutical molecule of interest, a LOD of 10^{-7} M.

The obtained LOD of 1×10^{-7} M for propranolol is lower than the cytotoxicity limit recognized by legislation, set at 5.21×10^{-4} M (135 mg/kg), [58] demonstrating feasibility of the nanocomposite as a promising SERS substrate to integrate in flexible sensors for the detection of such a drug molecule down to the settled permissible environmental levels.

References

[1] C.M. Muntean, et al., “Gold vs. Silver Colloidal Nanoparticle Films for Optimized SERS Detection of Propranolol and Electrochemical-SERS Analyses,” Biosensors, 2023. 13, DOI: 10.3390/bios13050530.

[2] E. Roschi, et al., “Surface-Enhanced Raman Spectroscopy for Bisphenols Detection: Toward a Better Understanding of the Analyte–Nanosystem Interactions,” Nanomaterials, 2021. 11, DOI: 10.3390/nano11040881.

[3] A. Li, et al., “A SERS-active sensor based on heterogeneous gold nanostar core–silver nanoparticle satellite assemblies for ultrasensitive detection of aflatoxin B1,” Nanoscale, 2016. 8(4): p. 1873-1878.

[4] B. Chen, et al., “Tuning surface-enhanced Raman scattering activity of silver nanowires,” Optik, 2021. 244: p. 167537.

[5] L. Wang, et al., “SERS-based test strips: Principles, designs and applications,” Biosensors and Bioelectronics, 2021. 189: p. 113360.

[6] R. Pilot and M. Massari, “Silver nanoparticle aggregates: Wavelength dependence of their SERS properties in the first transparency window of biological tissues,” Chemical Physics Impact, 2021. 2: p. 100014.

[7] J. Yang, et al., “Flexible and reusable SERS substrate for rapid conformal detection of residue on irregular surface,” Cellulose, 2021. 28(2): p. 921-936.

[8] M. Rycenga, et al., “Controlling the Synthesis and Assembly of Silver Nanostructures for Plasmonic Applications,” Chemical Reviews, 2011. 111(6): p. 3669-3712.

[9] G.C. Olar, et al., “SERS-active substrates based on graphene oxide or reduced graphene oxide and silver nanoparticles,” Materials Today: Proceedings, 2020.

[10] D. Zhang, et al., “Advances in flexible surface-enhanced Raman scattering (SERS) substrates for nondestructive food detection: Fundamentals and recent applications,” Trends in Food Science & Technology, 2021. 109: p. 690-701.

[11] A.K. Nair, et al., “Multifunctional nitrogen sulfur co-doped reduced graphene oxide – Ag nano hybrids (sphere, cube and wire) for nonlinear optical and SERS applications,” Carbon, 2018. 132: p. 380-393.

[12] T.K. Naqvi, et al., “Silver nanoparticles decorated reduced graphene oxide (rGO) SERS sensor for multiple analytes,” Applied Surface Science, 2019. 478: p. 887-895.

[13] A. Shiohara, et al., “Recent approaches toward creation of hot spots for SERS detection,” Journal of Photochemistry and Photobiology C: Photochemistry Reviews, 2014. 21: p. 2-25.

[14] S. Bhattacharjee, et al., “Nanoparticles incorporated graphene-based durable cotton fabrics,” Carbon, 2020. 166: p. 148-163.

[15] X. Liu, et al., “Functionalizing metal nanostructured film with graphene oxide for ultrasensitive detection of aromatic molecules by surface-enhanced Raman spectroscopy,” ACS Applied Materials & Interfaces, 2011. 3(8): p. 2944-52.

[16] H. Noji, et al., “Enzyme-based digital bioassay technology – key strategies and future perspectives,” Lab on a Chip, 2022. 22(17): p. 3092-3109.

[17] Q. Huang, et al., “Critical Review: digital resolution biomolecular sensing for diagnostics and life science research,” Lab on a Chip, 2020. 20(16): p. 2816-2840.

[18] R. Gesztelyi, et al., “The Hill equation and the origin of quantitative pharmacology,” Archive for History of Exact Sciences, 2012. 66(4): p. 427-438.

[19] X. Zhang, et al., “A facile method in removal of PVP ligands from silver nanowires for high performance and reusable SERS substrate,” Spectrochimica Acta Part A: Molecular and Biomolecular Spectroscopy, 2019: p. 117733.

[20] S. Xu, et al., “Polyvinylpyrrolidine-functionalized silver nanoparticles for SERS based determination of copper (II),” Microchimica Acta, 2019. 186(8): p. 562.

[21] Y. Ge, et al., “Rapid Electrochemical Cleaning Silver Nanowire Thin Films for High-Performance Transparent Conductors,” Journal of the American Chemical Society, 2019. 141(31): p. 12251-12257.

[22] H. Kang, et al., “Halide Welding for Silver Nanowire Network Electrode,” ACS Applied Materials & Interfaces, 2017. 9(36): p. 30779-30785.

[23] J. Liu, et al., “Iodine ion modification enables Ag nanowire film with improved carrier transport properties and stability as high-performance transparent conductor,” Nano Research, 2022. 15(6): p. 5410-5417.

[24] J. Liu, et al., “Plasma Cleaning and Self-Limited Welding of Silver Nanowire Films for Flexible Transparent Conductors,” ACS Applied Nano Materials, 2021. 4(2): p. 1664-1671.

[25] Y. Ge, et al., “Direct Room Temperature Welding and Chemical Protection of Silver Nanowire Thin Films for High Performance Transparent Conductors,” Journal of the American Chemical Society, 2018. 140(1): p. 193-199.

[26] X. Song, et al., “Specific iodide effect on surface-enhanced Raman scattering for ultra-sensitive detection of organic contaminants in water,” Spectrochimica Acta Part A: Molecular and Biomolecular Spectroscopy, 2022. 272: p. 120950.

[27] M.S. Goh, et al., “A chemical route to increase hot spots on silver nanowires for surface-enhanced Raman spectroscopy application,” Langmuir, 2012. 28(40): p. 14441-1449.

[28] D.P.R. Thanu, et al., “Chapter 8 - Fundamentals and Applications of Plasma Cleaning, in Developments in Surface Contamination and Cleaning: Applications of Cleaning Techniques,” Elsevier, R. Kohli and K.L. Mittal, Editors. 2019, p. 289-353.

[29] C.M. Muntean, et al., “Gold vs. Silver Colloidal Nanoparticle Films for Optimized SERS Detection of Propranolol and Electrochemical-SERS Analyses,” Biosensors (Basel), 2023. 13(5).

[30] S. Elumalai, et al., “An experimental and steered molecular dynamics simulation approach to histidine assisted liquid-phase exfoliation of graphite into few-layer graphene,” Physical Chemistry Chemical Physics, 2020. 22(18): p. 9910-9914.

[31] Z. Najafi Rad, et al., “Surface functionalization of graphene nanosheet with poly (l-histidine) and its application in drug delivery: covalent vs non-covalent approaches,” Scientific Reports, 2022. 12(1): p. 19046.

[32] S. Coskun, et al., “Polyol Synthesis of Silver Nanowires: An Extensive Parametric Study,” Crystal Growth & Design, 2011. 11(11): p. 4963-4969.

[33] N.V. Godoy, et al., “Ultrasensitive inkjet-printed based SERS sensor combining a high-performance gold nanosphere ink and hydrophobic paper,” Sensors and Actuators B: Chemical, 2020. 320: p. 128412.

[34] C. Ingrosso, et al., “PbS nanocrystals decorated Reduced Graphene Oxide for NIR responsive capacitive cathodes,” Carbon, 2021. 182: p. 57-69.

[35] C.K. Chua, et al., “Chemical reduction of graphene oxide: a synthetic chemistry viewpoint” Chemical Society Reviews, 2014. 43(1): p. 291-312.

[36] F. Vischio, et al., “Au nanoparticles decorated nanographene oxide-based platform: Synthesis, functionalization and assessment of photothermal activity,” Biomaterials Advances, 2022. 145: p. 213272.

[37] A.C. Ferrari and J. Robertson, “Interpretation of Raman spectra of disordered and amorphous carbon,” Physical Review B, 2000. 61(20): p. 14095-14107.

[38] A.C. Ferrari, “Raman spectroscopy of graphene and graphite: Disorder, electron–phonon coupling, doping and nonadiabatic effects,” Solid State Communications, 2007. 143(1): p. 47-57.

[39] Y. Sun and Y.N. Xia, “Large-Scale Synthesis of Uniform Silver Nanowires Through a Soft, Self-Seeding, Polyol Process,” Advanced Materials, 2002. 14.

[40] W.M. Schuette and W.E. Buhro, “Silver chloride as a heterogeneous nucleant for the growth of silver nanowires,” ACS Nano, 2013. 7(5): p. 3844-3853.

[41] J. Tang, et al., “Chemical-etched silver nanowires with tunable rough shape for surface enhanced Raman scattering,” Colloids and Surfaces A: Physicochemical and Engineering Aspects, 2021. 630: p. 127521.

[42] T. Muhmood, et al., “Silver nanowires: a focused review of their synthesis, properties, and major factors limiting their commercialization,” Nano Futures, 2022. 6(3): p. 032006.

[43] K.E. Korte, et al., “Rapid synthesis of silver nanowires through a CuCl- or CuCl2-mediated polyol process,” Journal of Materials Chemistry, 2008. 18(4): p. 437-441.

[44] J.R. Shimpi, et al., “Digestive Ripening: A Fine Chemical Machining Process on the Nanoscale,” Langmuir, 2017. 33(38): p. 9491-9507.

[45] S.M. Bergin, et al., “The effect of nanowire length and diameter on the properties of transparent, conducting nanowire films,” Nanoscale, 2012. 4(6): p. 1996-2004.

[46] S.E. Skrabalak, et al., “On the polyol synthesis of silver nanostructures: glycolaldehyde as a reducing agent,” Nano Letters, 2008. 8(7): p. 2077-2081.

[47] J. Jiu, et al., “Facile synthesis of very-long silver nanowires for transparent electrodes,” Journal of Materials Chemistry A, 2014. 2(18): p. 6326-6330.

[48] B.J. Wiley, et al., “Shape-controlled synthesis of metal nanostructures: the case of silver,” Chemistry - A European Journal, 2005. 11(2): p. 454-463.

[49] S. Mozaffari, et al., “The role of nanoparticle size and ligand coverage in size focusing of colloidal metal nanoparticles,” Nanoscale Advances, 2019. 1(10): p. 4052-4066.

[50] Y. Song, et al., “Investigation into the fluorescence quenching behaviors and applications of carbon dots,” Nanoscale, 2014. 6(9): p. 4676-4682.

[51] C. Xu, et al., “Selective reduction of graphene oxide,” New Carbon Materials, 2014. 29(1): p. 61-66.

[52] X. Li, et al., “Silver silver protected by monolayer graphene as a stabilized substrate for surface enhanced Raman spectroscopy,” Carbon, 2014. 66: p. 713-719.

[53] E.A. Carrasco-Flores, et al., “Vibrational spectra and surface-enhanced vibrational spectra of 1-nitropyrene,” Applied Spectroscopy, 2004. 58(5): p. 555-561.

[54] C. Amicucci, et al., “Cost Effective Silver Nanowire-Decorated Graphene Paper for Drop-On SERS Biodetection,” Nanomaterials (Basel), 2021. 11(6).

[55] T. Zhang, et al., “Polyimide Aerogels Cross-Linked with Aminated Ag Nanowires: Mechanically Strong and Tough,” Polymers, 2017. 9, DOI: 10.3390/polym9100530.

[56] F. Sun, et al., “Multi-functional, thiophenol-based surface chemistry for surface-enhanced Raman spectroscopy,” Chemical Communications (Camb), 2017. 53(33): p. 4550-4561.

[57] M.S. Goh, et al., “A Chemical Route To Increase Hot Spots on Silver Nanowires for Surface-Enhanced Raman Spectroscopy Application,” Langmuir, 2012. 28(40): p. 14441-14449.

[58] D. Reith, et al., “Relative Toxicity of Beta Blockers in Overdose,” Journal of Toxicology: Clinical Toxicology, 1996. 34: p. 273-278.

Conclusions

This thesis presents a systematic study of the preparation and optimization of novel hybrid nanocomposites based on RGO sheets functionalized with His (His-RGO) and then decorated with Ag nanostructures of different morphology, including both Ag NPs and Ag NWs, that were synthesized by different solution-based routes. The ability to precisely control size and morphology of the Ag nanostructures anchored onto the His-RGO scaffold, suitably tuning the experimental parameters, has enabled application of the resulting nanocomposites in three distinct technological areas, that are the manufacturing of i. antimicrobial textiles, ii. thermally conductive coatings for cotton fabrics, and iii. SERS-active substrates for drug detection.

The ability to tailor the physicochemical properties of the hybrid nanocomposites was largely governed by optimizing key parameters during the synthesis, such as the Ag precursor concentration, pH of the reaction medium, and the use of appropriate reducing agents and stabilizers. By modifying these variables, it was possible to engineer the materials with specific functionalities, thereby achieving targeted performance across the aforementioned application domains.

The antimicrobial nanocomposite based on His-RGO/Ag NPs showed promising long-term biocidal activity when applied to cotton fabrics. The synergistic effect between His-RGO and Ag NPs resulted in an enhanced and higher long-term antimicrobial performance compared to neat Ag NPs, due to the stabilization provided by the RGO platform. This demonstrated the potential of the material for applications such as wound dressings, medical textiles, and food packaging.

In the case of thermally conductive cotton coatings, the *in situ* generation of Ag NPs onto His-RGO-modified cotton fabrics resulted in a nanocomposite with superior thermal conductivity, doubling thermal conductivity of untreated cotton. The method's sustainability, relying on the impregnation of the textile and on the UV-light induced photoreduction of the Ag precursor without the need for harsh chemicals, positions this approach as a scalable and eco-friendly alternative for developing advanced textile materials with improved heat conductivity, making them suitable for the fabrication of passive cooling applications for individual thermal comfort management.

Finally, the His-RGO/Ag NWs hybrid nanocomposite was effectively utilized as a SERS substrate for the sensitive detection of drug molecules, including propranolol hydrochloride (PRNL). The controlled growth of Ag NWs on the RGO sheets enhanced the SERS signal, and through plasma treatments, the detection limit was further lowered to 10^{-7} M, demonstrating the material's feasibility for use in flexible sensors aimed at environmental monitoring and drug detection.

In conclusion, the work demonstrated that by fine-tuning the synthesis parameters of the His-RGO/Ag nanocomposite, it was possible to create a versatile material applicable onto flexible cellulose based substrates in diverse application fields, including healthcare and sensor technologies. The findings underscore the potential of RGO-based hybrid nanocomposites in advancing sustainable nanotechnology solutions across multiple disciplines, with future work sets to focus on optimizing material durability and stability, improving mechanical properties, and exploring additional functionalities for broader fields of applications.

The ability to design and develop innovative nanomaterials that meet Industry 4.0 requirements—such as sustainability, compatibility, and combination of unique properties with high solution processability—has the potential to significantly drive innovation in the fields of wearable sensors and smart textiles.

Appendix 1

In Situ Decoration of RGO with Ag NPs:

Cotton Fabric Functionalization with a Thermally Conductive Coating

Fig.1 shows the UV-vis absorption spectra of supernatant solutions collected in the four ultracentrifuge cycles of the His-RGO dispersion with Milli-Q water, that were performed to purify RGO sheets from His in excess after their exfoliation and functionalization. The spectra of supernatants isolated after the first and second wash show a strong absorption shoulder at 263 nm and a large signal between 280-350 nm, reasonably ascribed to intramolecular π-π* transitions in the His imidazole ring [1] and intermolecular charge transfers among stacked His molecules [2], respectively. The latter band disappears in the supernatant solutions isolated after the third wash (Fig. 1) demonstrating the elimination of His aggregates, while the former significantly decreases in intensity after the second wash, disappearing almost at the fourth washing.

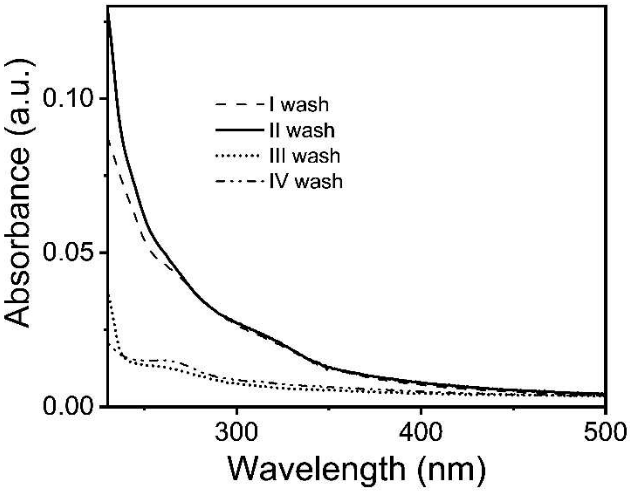

***Fig.1**. UV-Vis absorption spectra of supernatant solutions collected from the four cycles of ultracentrifugation of the His-RGO dispersions with Milli-Q water.*

Fig.2 reports the FTIR-ATR spectrum of cotton. The spectrum shows the typical band of stretching vibration of -OH groups ($\nu_{\text{-OH}}$) between ca. 3500-3000 cm^{-1}, the peak at 2899 cm^{-1} of the stretching mode of -CH$_2$- groups ($\nu_{\text{-CH2-}}$), the asymmetric -C-O-C- stretching ($\nu_{\text{as-C-O-C}}$) at 1156 cm^{-1} and the symmetric C-O-C stretching ($\nu_{\text{s-C-O-C}}$) at 1020 cm^{-1}.

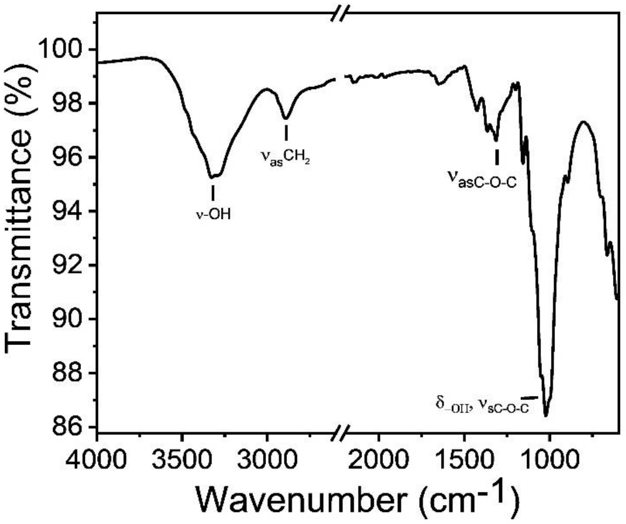

Fig.2: *FTIR-ATR of cotton.*

Figure 3 reports the absorption spectra of Cot/His-RGO and Cot/His-RGO/Ag fabrics.

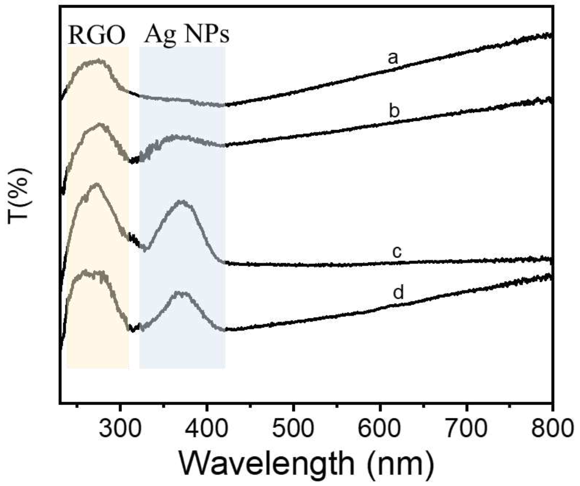

Fig.3: *UV-Vis absorption spectrum of (a) Cot/His-RGO, (b) Cot/His-RGO/Ag$_{\_1:1}$, (c) Cot/His-RGO/Ag$_{\_1:1,UV}$ and (d) Cot/His-RGO/Ag$_{\_9:1,UV}$.*

The C1s spectra of Cot/His-RGO, Cot/His-RGO$_{\_9:1,UV}$ and Cot/His-RGO/Ag$_{\_9:1,UV}$ were fitted with six components (Fig.4), specifically at 284.5 eV, 285.6 eV, 286.9 eV, 288.1 eV, 289.4 eV and 290.9 eV, that were ascribed to sp^2 C, sp^3 C, C-OH/R, C=O, C(O)OH/R and to π-π*, respectively.

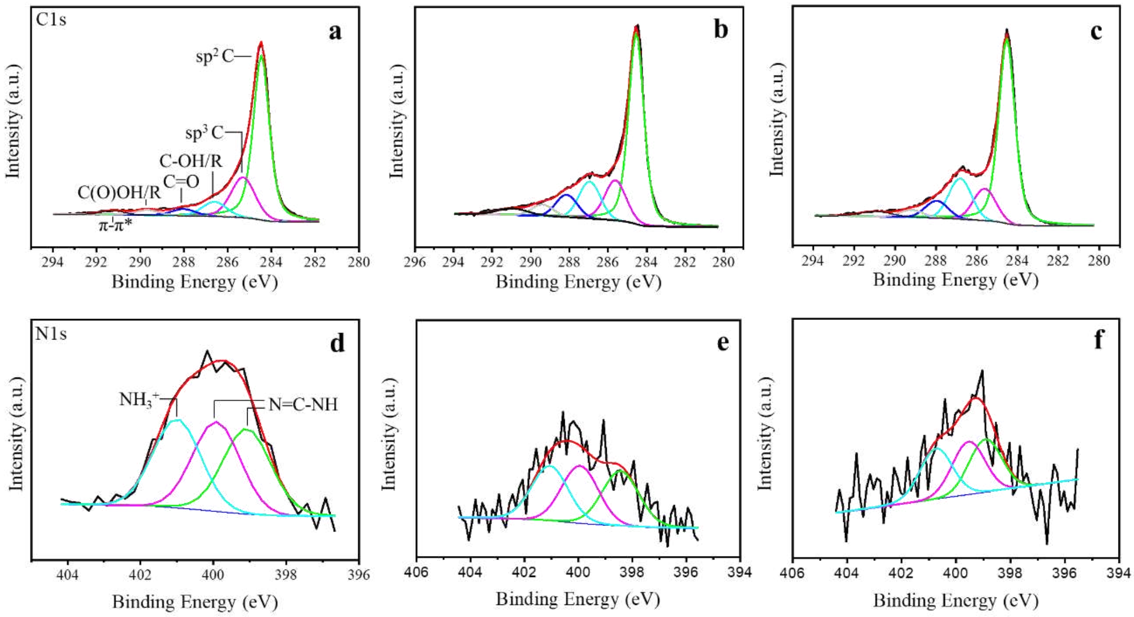

Fig.4: *XPS (a,b,c) C1s and (d,e,f) N1s high-resolution spectra of (a,d) Cot/His-RGO , (b,e) Cot/His-RGO*$_{\_9:1,UV}$ *(c,f) Cot/His-RGO/Ag*$_{\_9:1,UV}$.

The N1s high-resolution spectrum was curve-fitted with three peaks, namely the one at the lower binding energy of 399.0 eV, that is assigned to imidazole nitrogen ($\underline{N}$=C-NH), as well as the one at 400.0 eV (N=C-$\underline{N}$H) and the last component at 401.1 eV, that is instead due to the protonated His amine group (NH_3^+) (Fig.4d) [3]. In the N1s spectrum of the Cot/His-RGO$_{\_9:1,UV}$ sample, the peaks are at 398.4 eV, 399.9 eV and 401.1 eV, respectively (Fig.4e). With the addition of $AgNO_3$ and the heteronucleation of Ag NPs, the imidazole nitrogen shifts to 398.9 eV ($\underline{N}$=C-NH) and 399.5 eV (Fig.4f), likely due to the coordination with the metal NPs.

Fig.5 reports the Differential Scanning Calorimetry (DSC) curves of neat Cot fabrics, Cot/His-RGO samples and of Cot/His-RGO/Ag.

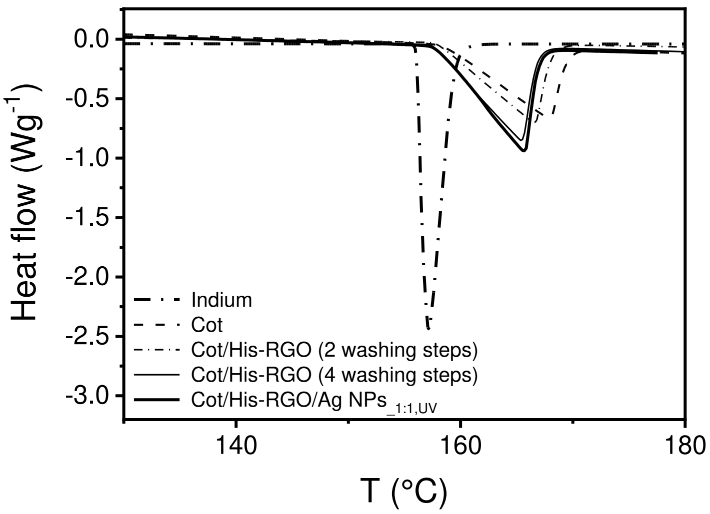

***Fig.5**: DSC curves of Indium, Cot, Cot/His-RGO achieved from His-RGO dispersions purified by two and four centrifuge cycles, and of Cot/His-RGO/Ag$_{\_1:1,UV}$.*

Table 1. TC of Cot/His-RGO, where the His-RGO dispersions were purified by two centrifuge washing steps, Cot/His-RGO$_{\_9:1,UV}$ and ot/His-RGO/Ag$_{\_9:1,UV}$.

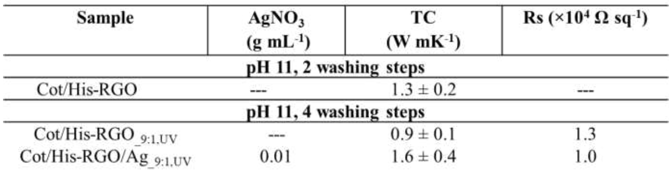

Sample	$AgNO_3$ (g mL^{-1})	TC (W mK^{-1})	Rs (×10^4 Ω sq^{-1})
		pH 11, 2 washing steps	
Cot/His-RGO	---	1.3 ± 0.2	---
		pH 11, 4 washing steps	
Cot/His-RGO$_{\_9:1,UV}$	---	0.9 ± 0.1	1.3
Cot/His-RGO/Ag$_{\_9:1,UV}$	0.01	1.6 ± 0.4	1.0

Table 2. C/O ratio of Cot/His-RGO/Ag$_{\_1:1,UV}$ estimated by EDS investigation.

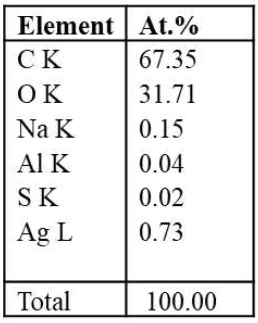

Element	**At.%**
C K	67.35
O K	31.71
Na K	0.15
Al K	0.04
S K	0.02
Ag L	0.73
Total	100.00

References

[1] E. Satheeshkumar, et al., “One-Step Simultaneous Exfoliation and Covalent Functionalization of MoS2 by Amino Acid Induced Solution Processes,” ChemNanoMat 3 (2017) 172-177

[2] O. Yamauchi, et al., “Structure-Stability Relationship in Ternary Copper(II) Complexes Involving Aromatic Amines and Tyrosine or Related Amino Acids. Intramolecular Aromatic Ring Stacking and Its Regulation through Tyrosine Phosphorylation,” J. Am. Chem. Soc. 107 (1985) 5938-5945

[3] O. Kostko, et al.,” Local electronic structure of histidine in aqueous solution,” Phys. Chem. Chem. Phys. 23 (2021) 8847-8853

Appendix 2

Silver Nanoparticle-Decorated RGO Hybrid Nanocomposites: Synthesis, Characterization, and Durable Antimicrobial Efficacy for Textile Coatings

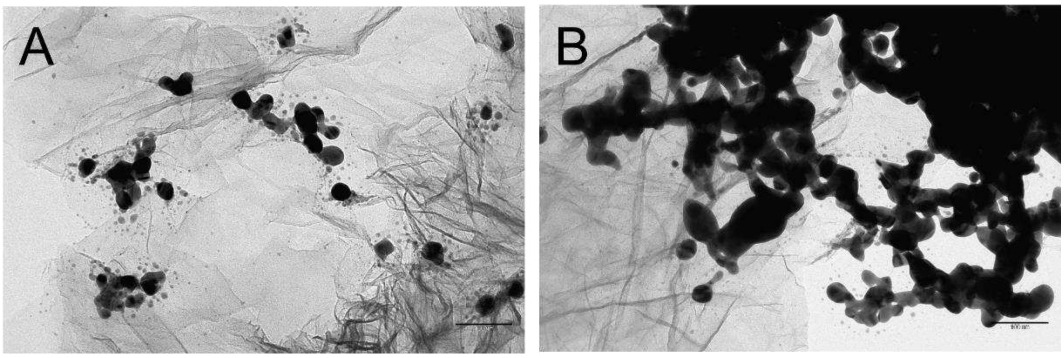

Fig.1. *TEM micrographs of the His-RGO/Ag NWs after 60 days of aging.*

Appendix 3

Green synthesis of Ag NW-decorated RGO nanocomposites via a combined in situ–ex situ approach deposited on paper for SERS detection of drugs and pollutants

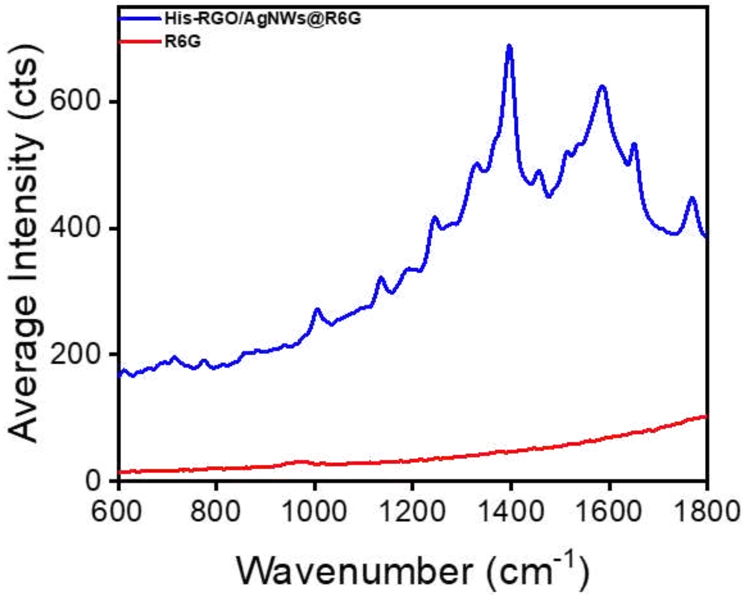

Fig.1: *SERS spectrum comparison of R6G at 10^{-3} M concentration, showing a 5-fold enhancement in signal when deposited on the nanocomposite substrate (blue line) with respect to pure R6G (red line). Spectra were acquired using a 633 nm laser line.*

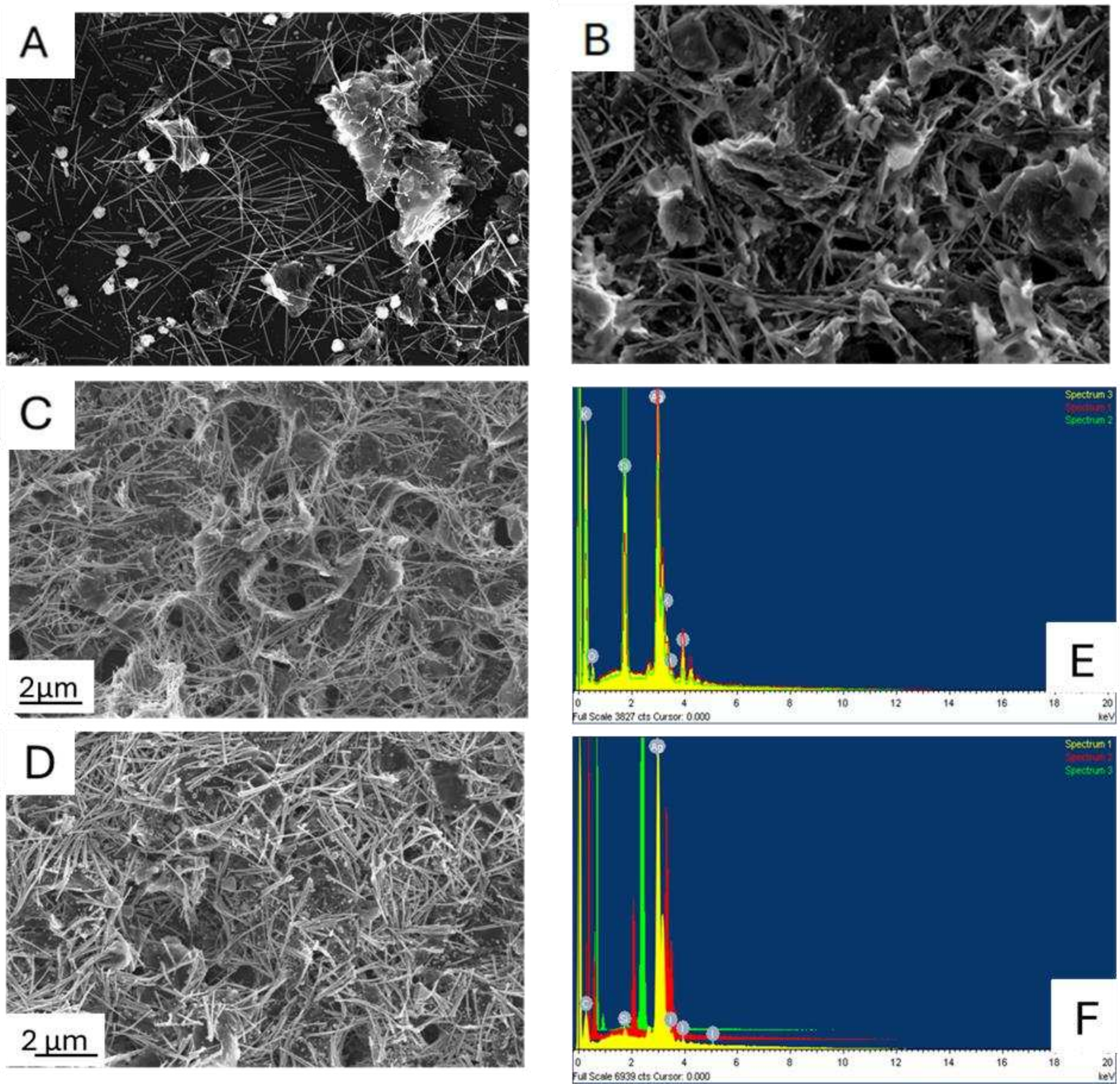

Fig.2: *(A-B) SEM micrographs of 30 μl of His-RGO/Ag NWs deposited on Si substrate and (B) treated by 0.5 M KI aqueous solution for 60 s (10,24 KX and 34 KX), (C) 0.16 M KI aqueous solution for 60 s (14,74 KX), (D) 4.48 mM KI aqueous solution for 120 s(17,65 KX). (E) EDS spectra of the samples reported in panels E and F.*

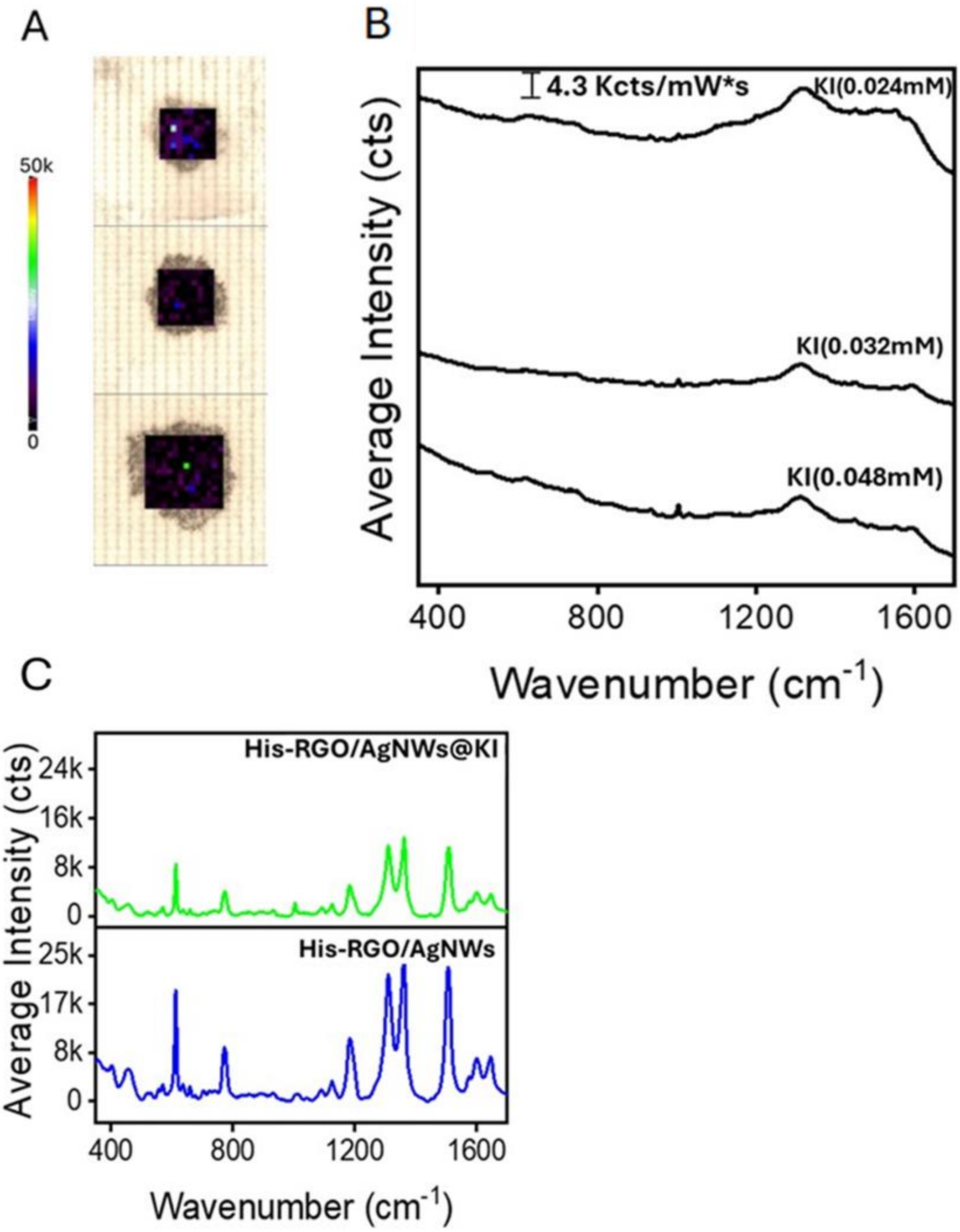

***Fig.3:**: C) Rappresentative average intensity of R6G SERS spectra onto His-RGO/AgNWssamples after PVP removal treatment with 0.032 mM aqueous KI solution for 30 s. The excess KI was subsequently removed by rinsing with ethanol.*

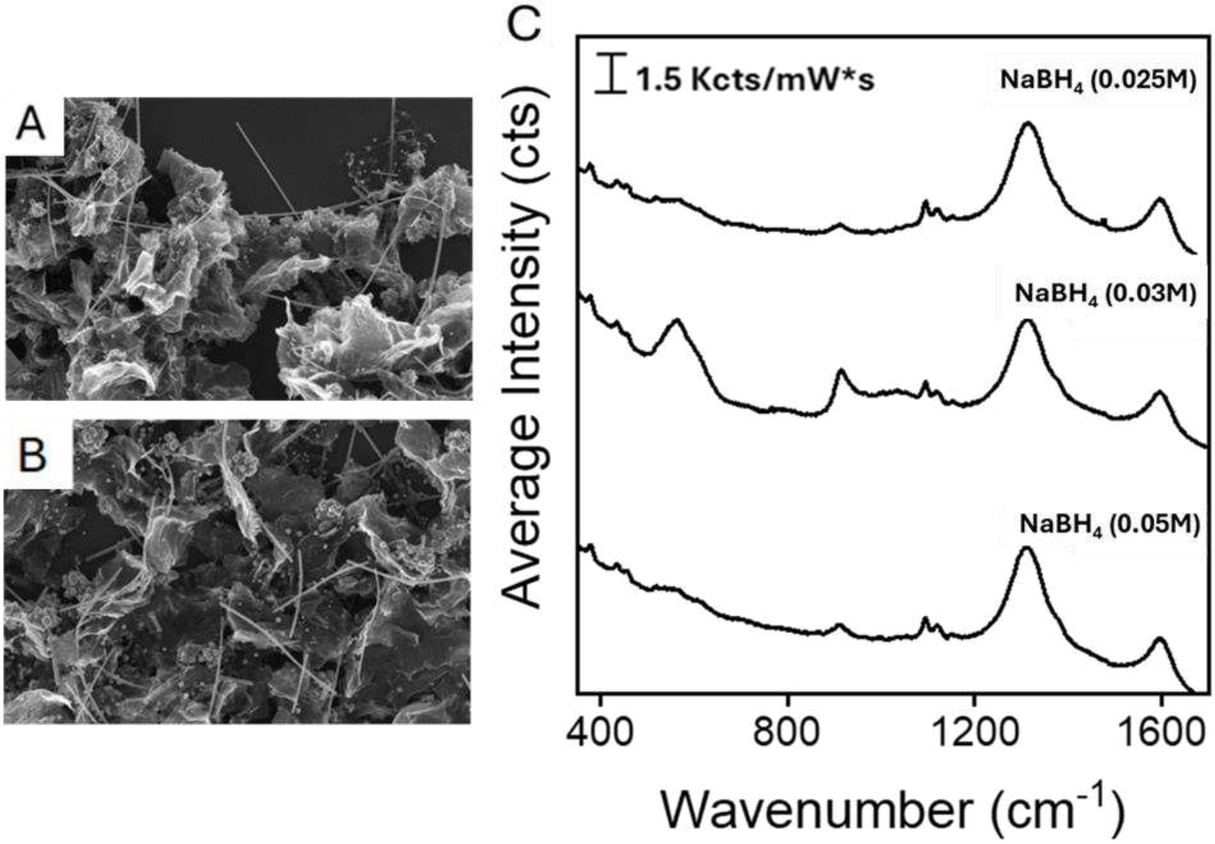

Fig.4: *SEM micrograph of 30 µl of His-RGO/AgNWs deposited on Si substrate treated by 0.05 M* $NaBH_4$ *aqueous solution for A) 10 s (16,78 KX) and B) 30 s (23,70 KX). C) Representative average intensity of 1-Nat SERS spectra onto His-RGO/AgNWs after PVP removal with* $NaBH_4$ *aqueous solutions at the 3 different investigated concentrations for 30 s (0.05M; 0.03M; 0.025M).*